Modelling of evolving microstructures at different scales

Der Fakultät Maschinenbau
der Technischen Universität Dortmund
zur Erlangung des akademischen Grades

Doktor-Ingenieur (Dr.-Ing.)

genehmigte Dissertation
von

Alexander Bartels

aus
Warendorf

Referent:	Prof. Dr.-Ing. J. Mosler
Korreferenten:	Prof. Dr. rer. nat. K. Hackl
	Prof. Dr.-Ing. A. Menzel

Tag der Einreichung:	27.01.2017
Tag der mündlichen Prüfung:	07.06.2017

© Alexander Bartels, 2017

This work is subject to copyright. All rights are reserved, whether the whole or part of the material is concerned, specifically the rights of translation, reprinting, reuse of illustrations, recitation, broadcasting, reproduction on microfilm or in any other way, and storage in data banks. Duplication of this publication or parts thereof is permitted in connection with reviews or scholarly analysis. Permission for use must always be obtained from the author.

Alle Rechte vorbehalten, auch das des auszugsweisen Nachdrucks, der auszugsweisen oder vollständigen Wiedergabe (Photographie, Mikroskopie), der Speicherung in Datenverarbeitungsanlagen und das der Übersetzung.

Als Manuskript gedruckt. Printed in Germany.

ISBN 978-3-921823-93-4

TO MY PARENTS

Acknowledgements

This thesis was generated during my stage at the Institute of Mechanics at TU Dortmund. During this time I grew in scientific and personal aspects which enabled me to successfully complete this thesis. I should like to take this opportunity to mention and thank some of the persons who accompanied and supported me during this time.

Probably the biggest part of my success I owe to my mentor and adviser Professor Jörn Mosler. He welcomed me in his team in February 2012 and inspired me with many interesting topics in the field of computational mechanics. Deeply convinced by the ”elegance of variational formulations” it was especially the scientific thinking which impressed and influenced me mostly. His motivative attitude and his confidence encouraged me to finalise this thesis successfully. Therefore, I express my sincere gratitude to him.

For agreeing to be the co-referee of my thesis I would like to thank Professor Klaus Hackl. It was at his chair at the Ruhr-Universität Bochum during my studies where I made my first steps within the theory of materials. Furthermore, I would like to thank Professor Andreas Menzel for acting as third referee of my thesis. I should also like to thank Professor Jochen Deuse, the chairman of the examination committee.

Special thanks go to the whole team of the Institute of Mechanics. During my time there I really enjoyed being a member of it. The reason for this was the amazing atmosphere and were my fantastic colleagues. To some of them I should like to express my gratitude with special thanks. For their outstanding administrative support I would like to thank the dream team ”Kerstin & Tina”, who organised various events like Christmas parties, breakfasts, institute trips and other parties resulting in a wonderful team spirit. Moreover, I thank Kerstin Walter for managing my administrative issues and Christina McDonagh for her professional translation support in writing papers, especially this thesis. I shall not forget Matthias (Mr. CentOS) Weiss, who professionally serviced my hardware and software. Thanks also go to Juniorprofessor Sandra Klinge. Due to her motivation during my master thesis I started strengthening my interest in the field of computational mechanics.

Next, I would like to express my sincere gratitude to my colleagues for their cordiality and friendship. The ”special” moments we had during and besides the work helped me to distract from mechanics crises and to motivate me to new ”mechanical high performances”. Especially the ”scientific” exchange of theories and information in the kitchen of the institute I will definitely miss. Under the guidance of Thorsten (Over-Engineer) Bartel, a lot of ingenious questions and topics were discussed together with Richard Ostwald, Raphael Holtermann, Tim (S04) Heitbreder, Guillermo (Tim-

Till) Diaz, Volker (The Pain) Fohrmeister, Christian (Fuchs) Sievers, Karsten (BCK) Buckmann, Dinesh Dusthakar and Rolf (Rolle) Berthelsen. The discussions, anger and fun we shared together I will definitely keep in good memories.

I would also like to thank my other colleagues and former colleagues Professor Björn Kiefer, Boadong Shi, Malek Homayonifar, Maniprakash Subramanian, Tim Furlan, Till Clausmeyer, Krishnendu Haldar, Professor Ralf Denzer, Muhammad Osman, Cesar Polindara, Tobias Asmanoglo, Robin Schulte, Markus Schewe, Lars Rose, Leon Sprave, Patrick Kurzeja, Kai Langenfeld and Serhat Aygün for their helpful and engaged teamwork. I hope we stay in touch.

Last but not least, I would like to thank my family and friends for their support, which was necessary for my graduation and for writing this thesis. My longtime "Jugo" friends from Sassenberg I thank for the many special weekends and holidays we had together. My girlfriend Malgorzata (Gosia) I thank for her patience and love especially in the end phase of this thesis. Finally, I gratefully thank my family, particularly my parents Ingrid and Wilfred, for their support during my whole education process. This thesis is dedicated to them.

Dortmund, Juni 2017 Alexander Bartels

Zusammenfassung

Die vorliegende Arbeit befasst sich mit der Entwicklung neuer Materialmodelle zur Abbildung der Evolution von Mikrostrukturen. Die Untersuchung von Mikrostrukturen ist essenziell für die Eigenschaftscharakterisierung von metallischen Werkstoffen, welche im Rahmen dieser Arbeit beschrieben werden. In Abhängigkeit der betrachteten Anwendung werden Mikrostrukturen auf der technologisch wichtigen Makroskala oder der materialwissenschaftlich wichtigen Mikroskala untersucht. Unabhängig von der zu untersuchenden Skala sind mechanische und thermische Belastungen die dominierenden Faktoren einer Mikrostrukturentwicklung. Das Ziel dieser Arbeit ist die Berücksichtigung von Mikrostrukturentwicklungen sowohl auf der Makroskala als auch auf der Mikroskala. Ein wesentlicher Aspekt einer makroskopisch motivierten Modellierung betrifft die Temperaturvorhersage in Metallen aufgrund plastischer Verformungen. Mit Hilfe eines neuen und allgemeinen Kopplungsansatzes, der auf einer angepassten Aufteilung gespeicherter und dissipativer Energieanteile basiert, wird eine realistischere Temperaturvorhersage gegenüber gewöhnlichen Kopplungsansätzen getroffen. Des Weiteren werden anisotrope Texturevolutionen durch ein verallgemeinertes Distorsionsverfestigungsgesetz berücksichtigt, welches auf Formänderung einer Fließfunktion beruht. Durch die Verbindung der neuen Temperaturkopplung und Distorsionsverfestigung werden die relevanten Mechanismen der Makroskala abgebildet. Um ein detaillierteres Verständnis von Mikrostrukturen zu bekommen, werden die Heterogenität von Mikrostrukturen und die damit verbundene Umwandlung von Phasen aufgrund von mechanischen Lasten zusätzlich zum zuvor beschriebenen makroskopischen Modell mittels Phasenfeldtheorien untersucht. Ein Problem in bisherigen Phasenfeldmodellen stellt dabei die Bestimmung der effektiven Eigenschaften im *Diffuse Interface* dar. Um Mikrostrukturen möglichst genau charakterisieren zu können, wird ein verallgemeinertes Phasenfeldmodell entwickelt, das sowohl etablierte als auch neue und effizientere Homogenisierungstheorien einbindet. Für die Phasenumwandlungsprozesse werden sowohl Allen-Cahn als auch Cahn-Hilliard ähnliche Modelle verwendet, so dass die wesentlichen Effekte einer Mikrostrukturentwicklung wiedergegeben werden.

Alle Materialmodelle sind dreidimensional für finite Verformungen entwickelt und basieren auf thermodynamisch konsistenten Ansätzen. Unter Berücksichtigung variationeller Modellierungsansätze folgen die Bilanz- und Evolutionsgleichungen aus Minimierungsprinzipien. Darauf basierend werden die hergeleiteten Modellformulierungen numerisch effizient in die Finite Elemente Methode implementiert und implizit monolithisch gelöst. Mittels geeigneter Beispiele werden die Eigenschaften aller Modelle veranschaulicht.

Abstract

This thesis deals with the development of novel material models that capture the evolution of microstructures. The analysis of microstructures is essential for the description of metallic material properties, which are considered in this thesis. Depending on the underlying application, microstructures are analysed on the technological relevant macroscale or on the materials science relevant microscale. Independent of the underlying scale, mechanical and thermal loadings are the most dominating factors of evolving microstructures. The objective of this work is to capture evolving microstructures for the technologically relevant macroscale as well as for the materials science relevant microscale.

A key aspect of a macroscopically motivated modelling is related to the temperature prediction in metals which are induced by plastic deformations. By means of a novel and generalised coupling, which is based on an adopted decomposition of stored and dissipative energy parts, a more realistic temperature prediction compared to standard coupling approaches is achieved. Furthermore, the anisotropic texture evolution in hardening processes is incorporated by a generalised distortional hardening model, which takes account of the distortion of a yield surface. Based on the novel thermomechanical coupling and distortional hardening, the relevant mechanisms are captured on the macroscale. In addition to the macroscopic modelling and in order to obtain a more detailed insight into microstructures, the heterogeneity of microstructures and the underlying transformation of phases is described by means of phase field theories. A problem in existing phase field models pertains the determination of effective properties in the *diffuse interface*. In order to describe microstructures as exactly as possible, a generalised phase field model is developed incorporating state-of-the-art as well as novel and more efficient homogenisation assumptions. For the phase transformations, Allen-Cahn-type and Cahn-Hilliard-type models are applied so that the most important effects of the evolution of microstructures are included.

All material models are derived three-dimensionally at finite strains and are based on thermodynamically consistent formulations. Considering an overall variational modelling, the balance and evolution equations follow jointly from underlying minimisation principles. The derived formulations are efficiently implemented in finite elements and are implicitly and monolithically solved. Demonstrative examples show the capability of the derived models.

Publications

The following list of articles were submitted or published during the preparation of this thesis. The articles of chapters 3, 5 and the first article of chapter 4 are peer-reviewed.

Chapter 3: A. Bartels, T. Bartel, M. Canadija, J. Mosler: *On the thermomechanical coupling in dissipative materials: a variational approach for generalized standard materials*, Journal of the Mechanics and Physics of Solids, 82:218–234, 2015, (Bartels et al. [11]).

Chapter 4: B. Shi, A. Bartels, J. Mosler: *On the thermodynamically consistent modeling of distortional hardening: A novel generalized framework*, International Journal of Plasticity, 63:170–182, 2014, (Shi et al. [114]).

Chapter 4: A. Bartels, J. Mosler: *On the numerical implementation of thermomechanically coupled distortional hardening*, International Journal of Plasticity, submitted for publication, 2016.

Chapter 5: A. Bartels, J. Mosler: *Efficient variational constitutive updates for Allen-Cahn-type phase field theory coupled to continuum mechanics*, Computer Methods in Applied Mechanics and Engineering, 317:55-83, 2017, (Bartels and Mosler [12]).

The contents of the listed articles have been partly modified in order to avoid unnecessary repetitions and to connect essential parts of this thesis. The articles were published together with one or more authors. Regarding the contribution of the articles, the author contributed essential parts of the underlying theories, the algorithmic formulations and the numerical analyses. Numerical analyses within the listed articles, which have not been carried out by the author, are not shown in this thesis.

Contents

1 Introduction **1**
1.1 Motivation 1
1.2 State of the art 2
1.2.1 Macroscopic models accounting for the evolution of microstructures 3
1.2.2 Explicit modelling of evolving microstructures by means of phase field theories 6
1.3 Structure of the thesis 9

2 Introduction to continuum mechanics **11**
2.1 Notation 11
2.2 Kinematics 13
2.3 Balance equations 15
2.4 Boundary conditions 19
2.5 Constitutive modelling 20
2.5.1 Hyperelasticity 20
2.5.2 Thermoelasticity 21
2.5.3 Thermo-elastoplasticity 24
2.6 Incremental variational updates 28
2.6.1 Hyperelasticity 29
2.6.2 Thermoelasticity 30
2.6.3 Thermo-elastoplasticity 32

3 Thermomechanical coupling in dissipative materials **37**
3.1 Analysis of internal dissipation 38
3.1.1 Isothermal plasticity theory 38
3.1.2 Thermomechanically coupled theory 40
3.1.3 A thermodynamically consistent prototype model 45
3.2 Variational framework 46
3.3 Uniaxial tension test of a bar made of Al 2024-T3 49
3.3.1 A thermomechanical prototype model 50
3.3.2 Isotropic hardening 51
3.3.3 Kinematic hardening 53

4 Numerical implementation of thermomechanically coupled anisotropic hardening 57
4.1 Generalised distortional hardening – isothermal setting 58
4.1.1 Prototype hardening model 58
4.1.2 Distortional hardening 60
4.1.3 Prototype model including isotropic, kinematic and distortional hardening 63
4.1.4 Distortional hardening with higher curvature in loading direction 65
4.2 Thermomechanically coupled setting 66
4.2.1 Fundamentals 66
4.2.2 Prototype model 68
4.3 Numerical implementation 68
4.3.1 Constitutive updates 70
4.3.2 Weak form – FEM implementation 73
4.4 Representative numerical examples 78
4.4.1 Uniaxial tension test of the aluminium alloy Al6061-T6511 – isothermal setting 79
4.4.2 Comparison of different hardening models for a uniaxial tension test of the aluminium alloy Al2024-T3 – thermomechanically coupled setting 81
4.4.3 Contact bending test – distortional hardening model 87
4.4.4 Inhomogeneous tension test - distortional hardening model with higher curvature of the yield function in loading direction 90
4.4.5 Necking of an axisymmetric bar - distortional hardening model . . 92

5 Allen-Cahn-type phase field theory coupled to continuum mechanics: Computation of effective material properties based on variational constitutive updates 99
5.1 Diffuse approximation of interfaces 100
5.2 A coupled phase field approach 102
5.2.1 Balance equations for a deformation driven phase field model . . . 102
5.2.2 Variationally consistent phase field modelling 105
5.3 Bulk response within the diffuse interface 108
5.3.1 Fundamentals of the homogenisation theory 108
5.3.2 Space of admissible jumps in the deformation gradient – different homogenisation assumptions 110
5.4 Numerical implementation 116
5.4.1 Incremental variational updates 116
5.4.2 Constrained optimisation 119
5.4.3 Finite element implementation 121
5.5 Numerical examples 125
5.5.1 Prototype phase field model 125

5.5.2 Comparison of the homogenisation assumptions – 3D computations 127
5.5.3 Further numerical analyses in 2D 130

6 Cahn-Hilliard-type phase field models coupled to continuum mechanics 137
6.1 Microstructural evolution based on a Cahn-Hilliard-type phase field model 138
6.1.1 Balance equations for a coupled deformation-diffusion driven phase field model 139
6.1.2 A variationally consistent phase field model coupled to elasticity and diffusion 141
6.1.3 Numerical implementation 146
6.1.4 Numerical example 151
6.2 A Cahn-Hilliard based phase field model for topology optimisation 157
6.2.1 Structural topology optimisation 158
6.2.2 Regularised topology optimisation based on Cahn-Hilliard-type phase field modelling 159
6.2.3 Numerical example 163

7 Conclusion and outlook 167
7.1 Concluding remarks 167
7.1.1 Macroscopic models accounting for the evolution of microstructures 167
7.1.2 Explicit modelling of evolving microstructures by means of phase field theories 168
7.2 Outlook 169

A Computation of internal energy 173
A.1 Computation of internal energy by means of Legendre transformation . . 173

B Implementation of thermomechanically coupled distortional hardening 175
B.1 Thermomechanically coupled algorithmic tangent 175
B.2 Enhanced assumed strain finite elements 176
B.3 Enhanced assumed strain formulation for axisymmetric elements 183

C Phase field modelling – Computation of properties within the diffuse interface 185
C.1 Computation of the relaxed energy and update of the stresses based on partial rank-1 homogenisation 185
C.2 Computation of the algorithmic tangent 186
C.3 Components of algorithmic tangent due to NCP functions 187

Bibliography 189

1 Introduction

1.1 Motivation

Most materials such as metallic alloys are heterogeneous at a certain microscale. For instance, by examining the structure of metallic alloys under the microscope, it can be observed that the microstructure is polycrystalline composed of different oriented and different sized single-crystals, grain boundaries and dislocations. These microstructures also evolve in time depending on the applied loading conditions. Obviously, the evolution of microstructure can be analysed on different scales since the underlying effects correspond to different microscales. Examples for scale dependent microstructures are related to the formation of texture in polycrystalline materials at the macroscopic scale or are related to the transformation of phases in single grains at the microscopic scale. Clearly, the form and design of evolving microstructures strongly depend on the applied processing condition and on the applied loading conditions. The most dominating loadings driving the evolution of microstructures are the deformation field and the temperature field. The effect of mechanical and thermal loadings are, for instance, the formation of grain boundary motion induced by plastic deformations or the temperature driven recrystallisation of crystal lattice. Mechanical and thermal loadings also influence the microstructure at a different microscale. For instance, the deformation of the crystallographic structure leads to a martensite-austenite phase transformation in TRIP steels. Thermal loadings are applied as well to overcome the energy barrier between phases in shape memory alloys. In summary, microstructures exhibit a complex topology and evolve due to applied loadings in time. These evolving microstructures, in turn, define the effective response of the considered material at the macroscale. Thus, the evolution of microstructure is essential for the resulting effective material properties which are relevant for large-scale technological processes.

The main objective of this thesis is to establish a link between the evolution of microstructures and the resulting macro-properties. For that purpose, two constitutive frameworks are elaborated in this thesis. The first one corresponds to the macroscale and, consequently, represents a natural connection to the scale for real technological processes. The second one is related to the microscale and thus shows a strong link to materials science.

Forming technologies such as deep drawing or sheet metal forming are the underlying focus of a macroscopic model. Due to high forming degrees, high plastic strains occur which lead to an anisotropic texture evolution and consequently to anisotropic hardening. Since isotropic and kinematic hardening cannot capture the anisotropic texture evolution, the more general framework of distortional hardening characterised by an evolution of the yield surface is necessary. Moreover, due to the high plastic deformations, energy dissipates which leads to a temperature increase within the material. For this reason, the anisotropic hardening model requires a thermomechanically coupled framework. A summary of the characteristic features of the model is given below.

- realistic prediction of temperatures caused by inelastic deformations
- generalised anisotropic/distortional hardening
- thermodynamical consistency
- efficient numerical implementation

In order to provide a deeper insight into the evolution of microstructures, the second part of the thesis deals with the analysis of phases at the microscale. The focus lies on phase transformation and precipitation in metallic alloys. Regarding such phenomena it is well-known that the governing driving force is strongly influenced by the mechanical field. In order to simulate mechanically driven phase transformations, phase field theories appear to be a natural choice. By using phase field theories, the evolution of phases is approximated in a diffuse manner, i.e. the interfaces are not considered to be sharp, but show a finite thickness. Although phase field theories are already well developed in the context of multi-physical coupling, some fundamental problems still exist. The problem addressed in this thesis is related to the exact definition of effective microstructural properties within the diffuse interface by means of homogenisation theories. Accordingly, the second part of the thesis deals with a unified and robust phase field framework fulfilling the following properties:

- geometrically exact description based on finite deformations
- unified phase field framework based on homogenisation schemes
- displacive as well as diffusion-driven phase transformations
- numerically robust algorithmic formulation.

1.2 State of the art

As mentioned before, this thesis mainly deals with the modelling of microstructures at different scales. While the first part deals with a new model for the realistic prediction of thermomechanically coupled anisotropic hardening, the second part focuses on a unified modelling framework for phase field theory. The following sections provide a concise state-of-the-art review on these two parts.

1.2.1 Macroscopic models accounting for the evolution of microstructures

The evolution of microstructures and its impact on macroscopic materials properties is governed, among others, by mechanical and thermal loadings. Concerning the latter, the understanding and the correct prediction of the thermomechanical coupling is of utmost importance in a broad variety of different scientific areas. From an engineering point of view, the coupling is for instance crucial for most production technologies of semi-finished parts such as extrusion or sheet metal forming, cf. Clausmeyer et al. [31], Parvizian et al. [102]. A more specific example is sheet forming of magnesium which can usually only be carried out at elevated temperatures (typically, above 200°C), cf. Mekonen et al. [82]. This is due to the temperature dependence of the dominant underlying deformation modes. To be more precise, forming of magnesium requires a sufficiently high twinning activity which, in turn, usually requires elevated temperatures, see Homayonifar and Mosler [56], Mekonen et al. [82]. For this reason, thermomechanical coupling is also crucial in materials science. In materials science, this coupling often represents the only way to investigate the irreversible mechanical response of solids, i.e., instead of measuring the dissipation directly, the temperature increase is monitored, cf. Jiang et al. [59], Oliferuk et al. [96]. An excellent overview in connection herewith is given in Bever et al. [17] and references cited therein.

The modelling of self-induced heating, i.e. temperature increase due to plastic deformations, can be modelled by using two fundamentally different approaches. These approaches are based either on thermodynamical considerations (see e.g. Simo [119]) or on the so-called *Taylor-Quinney* factor [130]. Focussing first on thermodynamical consistent modelling, the temperature evolution equation is provided by the first and second law of thermodynamics for given Helmholtz energy and suitable evolution equations. However, as shown in Chaboche [28, 29], Hodowany et al. [54], Nemat-Nasser and Kapoor [94], Rosakis et al. [109] the temperatures which are computed by this straightforward modelling are usually overestimated. The reason for the over-prediction of the temperature is the overestimation of the internal dissipation which is converted to heat. Therefore, the Taylor-Quinney factor is frequently applied. It correlates the work due to plastic deformations in an ad-hoc approach to the dissipation. Hence, this factor can be used to reduce the dissipation. Several experiments and numerical simulations such as Parvizian et al. [102], Simo and Miehe [121] show that the Taylor-Quinney factor often provides sufficiently accurate temperature predictions. Unfortunately, this ansatz is not consistent with the conservation of energy. It can be concluded that temperature predicting models based on thermodynamically consistent assumptions are still rare. First ideas towards a thermodynamically consistent temperature modelling can be found in the works of Ristinmaa et al. [108], Rosakis et al. [109]. In Rosakis et al. [109] a Helmholtz energy is computed which corresponds to the stored energy in cold work. However, in the proposed one-dimensional setting the dual variables do not follow from this energy. In Ristinmaa et al. [108] the evolution of isotropic hardening is modified. To be more precise, an offset is considered such that isotropic hardening does not start from a "virgin" state but from an initial history deformation. Based on these ideas, the first and second law of thermodynamics are fulfilled and the temperatures are decreased. However, the generalisation of these ideas in terms of kinematic hardening and finite strains is still missing. For this purpose, a novel thermodynamically consistent framework is elaborated which indeed allows a realistic prediction of temperature evolution.

As mentioned before, the evolution of microstructures in metals is governed by the interaction between mechanical and thermal loads. Often the evolution leads to a certain anisotropy at the macroscale - for instance, to the evolution of textures. To be more precise and as shown in several experiments, the microstructural dislocation motion and the macrostructural properties are highly connected, see e.g. Nesterova et al. [95] for steel alloys and Rauch et al. [107] for aluminium alloys. Experimentally it can be observed that, after a certain magnitude of mechanical loading, dislocation boundaries are activated leading to an anisotropic microstructure. For example, Fig. 1.1a) shows the evolution of microbands after an orthogonal loading with respect to the rolling direction. Along with the *Bauschinger* effect a cross hardening or softening effect can also often be observed. On the macroscopic scale the motion of grain boundaries can be studied by the evolution of yield surfaces, see e.g Ishikawa [58] for steel alloys and Khan et al. [62, 63, 64] for aluminium alloys. Consequently, the aforementioned microscopical anisotropies result in a distortion of the yield surface as shown in Fig. 1.1b).

Motivated by experiments in Fig. 1.1 the anisotropic evolution of texture can be described by two different modelling classes. These are crystal plasticity e.g. Agnew and Duygulu [1], Homayonifar and Mosler [56], Kalidindi and Anand [60], Miehe et al. [83] or purely macroscopic theories e.g. Baltov and Sawczuk [9], Feigenbaum and Dafalias [43], Haddidi et al. [52], Ortiz and Popov [101], Shi and Mosler [113]. By using crystal plasticity, the most relevant microscopical effects such as the plastic slip in individual slip planes are naturally captured in the constitutive assumptions. This makes crystal plasticity well applicable for the aforementioned texture evolution. However, since metallic alloys are polycrystalline in nature, the associated numerical effort is not practicable. For this reason, macroscopic theories are frequently applied due to their numerical efficiency. However, in order to capture effects of the atomic lattice rotation within the individual grains as well as the distortion and elongation of the grains macroscopically, the constitutive models become more complex. As noted in Haddidi et al. [52] isotropic and kinematic hardening cannot realistically capture the resulting macroscopic distortion of the yield surface. Models accounting for the distortion of the yield surface are referred to as *distortional hardening* models, cf. Baltov and Sawczuk [9], Haddidi et al.

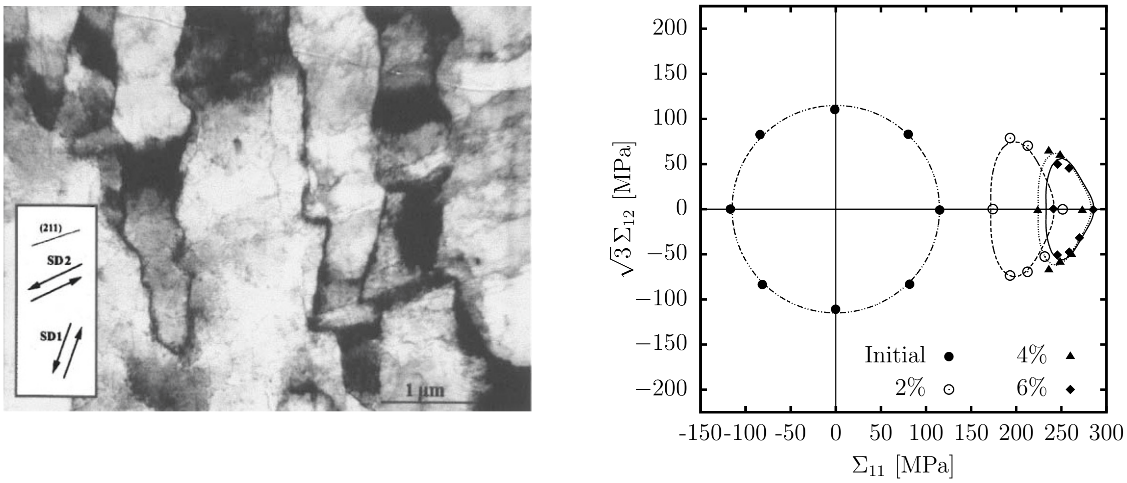

a) b)

Figure 1.1: Experiments associated with texture evolution. a) TEM microstructure of a Ti-killed IF steel. Anisotropic evolution after 10% shear loading in rolling direction followed by 20% shear loading at 135° in rolling direction. Reprinted from Nesterova et al. [95] with kind permission from Elsevier. b) Yield surface evolution for aluminium alloy 6061-T6511 subjected to simple tension of 2%, 4% and 6% strain loading. Experimental measurements are taken from Khan et al. [62].

[52], Ortiz and Popov [101]. Since the modelling of technologically relevant forming processes is analysed, distortional hardening is adopted here.

The modelling of evolving plastic anisotropies by means of macroscopic description goes back – at least – to the pioneering works of Baltov and Sawczuk [9], Ortiz and Popov [101]. In the cited publications, anisotropy is captured by evolving structural tensors entering the yield surface and – through the normality assumption – also the evolution equations. Examples which also contain state-of-the-art distortional hardening models can be found in Barthel et al. [15], Feigenbaum and Dafalias [43], Haddidi et al. [52], Shi and Mosler [113], Wang et al. [135] and references cited therein. The important physical effects that capture the distortion of the yield surface are dynamic and latent hardening or softening, see Barthel et al. [15], Wang et al. [135]. In models based on dynamic hardening, currently active dislocations lead to an elongation/shrinkage of the yield surface in loading direction. In addition to this effect, the orthogonal direction can also undergo cross hardening/softening. Particularly for materials showing a pronounced variation of the Lankford coefficient (r-value), an uncoupling of dynamic and latent hardening is important. In relation to physics, latent hardening is due to currently inactive dislocations which have to be crossed by the active ones, thereby providing additional hardening. Finally, for some materials such as high-strength aluminium alloys, a higher curvature of the yield function is observed in loading direction in contrast to the reverse direction, cf. Fig. 1.1b). Models taking account of this effect can be found in Feigenbaum and Dafalias [43], Ortiz and Popov [101], Pietryga et al. [105]. In general, the evolving plastic anisotropy is captured in Barthel et al. [15], Feigenbaum and Dafalias [43], Haddidi et al. [52], Pietryga et al. [105], Shi and Mosler [113], Wang et al. [135] by means of fourth-order tensors defining the equivalent stress in the yield function. Although the aforementioned physical effects can be captured in one evolution equation, see Baltov and Sawczuk [9], Feigenbaum and Dafalias [43, 44], Ortiz and Popov [101], Shi and Mosler [113], a decoupling of dynamic and latent hardening describes the cross hardening effect more realistically, see Barthel et al. [15], Haddidi et al. [52], Wang et al. [135].

Since essential physical aspects (thermodynamical consistency, boundedness and convexity of yield surfaces) are not sufficiently discussed in the cited works, a novel generalised distortional hardening model falling into the range of generalised standard materials is introduced, cf. Lemaitre [72], Mandel [80]. Another drawback of the cited works is the restriction to an isothermal setting. Since technological processes are eventually to be analysed, a thermomechanically coupled theory as discussed in the previous paragraphs is elaborated in the thesis. Furthermore, a numerically efficient algorithmic framework is advocated.

1.2.2 Explicit modelling of evolving microstructures by means of phase field theories

The models discussed before are usually based on evolution equations for fourth-order tensors. In order to derive or motivate these tensors, accompanying explicit simulations of the evolving microstructures are meaningful. For this purpose, both phase field theory and phase field modelling have become crucially important over the last years. Nowadays, phase field modelling can be found in many classic disciplines like fracture mechanics (see Bourdin et al. [21], Francfort and Marigo [46]), topology optimisation (see Bourdin and Chambolle [22], Wallin et al. [134]) and in materials science (see Chen [30], Steinbach [127]). The beginning of phase field theory goes back to the pioneering works of *Cahn and Hilliard* [24] ff. and by *Allen and Cahn* [2]. They proposed a smooth approximation of the sharp interface problem. *Modica and Mortola* [87] showed that this regularisation converges in the limiting case to the sharp interface (strictly speaking for time-invariant interfaces). Based on this description, structure and orientation of domains are identified and the evolution of the phase position is automatically tracked.

Originally, phase field models by Cahn and Hilliard [24] and Allen and Cahn [2] were introduced in metallurgy to describe the topology in binary alloy systems. A good overview of phase field modelling in the context of multi-phase alloys is also given in Moelans et al. [88] and Steinbach [127]. Although these works are restricted to phase transformations, phase field models are also suitable for the description of multi-physics. Focussing on physics in solid-solid transformations, phase field-type models can be found in the context of elastoplasticity (e.g. Ammar et al. [3], de Rancourt et al. [36]), chemical concentration (e.g. Steinbach and Apel [124]), and ferroelectrics (e.g. Schrade et al. [112], Zhang and Bhattacharya [140]) – to mention only a few.

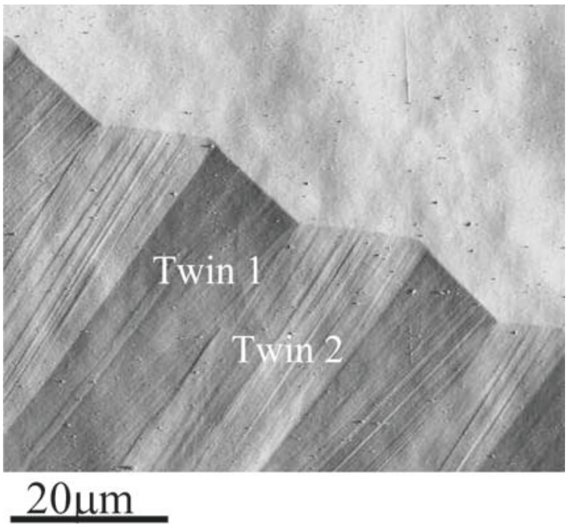

Figure 1.2: Atomic force microscope image of a Cu–14wt.% Al–3.4wt.% Ni alloy. Twinning of two martensitic twin volumes 1 and 2. Reprinted from Liu and Dunne [78] with kind permission from Elsevier.

In addition to thermal fields, phase transformations are often also strongly influenced by the mechanical problem. Experimentally, this can be observed for example in martensite twins of Cu-Al-Ni alloys as shown in Fig. 1.2. Phase transformations of this kind are intensively analysed and studied in the case of deformation induced martensite transformations by Levitas [73], Levitas et al. [76] and citations therein.

Although the aforementioned complex phenomena have already been analysed by using phase field models, some fundamental problems still exist. The problem considered in this thesis is associated with the computation of the effective mechanical bulk properties in the diffuse interface. These properties – in turn – define the driving force acting at the interface. Certainly, the effective bulk properties depend on the properties of the neighbouring bulk phases. However, the quantitative relation is not clear. In the literature, mainly two concepts can be found for the definition of the aforementioned effective properties. Regarding the first (see Khachaturyan [61]), one effective bulk energy is assumed in an ad-hoc manner. At the boundary of the diffuse interface, this energy converges to that of the neighbouring phases. This implies that the effective properties can be understood as an interpolation of the properties of the individual phases. Since this interpolation does not represent a homogenisation in general, an approach of Khachaturyan-type does not show the localisation property, i.e., the response of the individual phases defining the diffuse interface cannot be computed - for instance the stresses. Models of this type can be found in Clayton and Knap [32], Denoual et al. [39], Levitas [73], Levitas et al. [76]. From a physics point of view, Khachaturyan-type models are meaningful for very thin interfaces, for which the interface properties do not directly derive from the neighbouring bulk behaviour (by means of homogenisation).

Regarding the second class of models, each phase is characterised by an individual bulk energy, and the effective bulk properties in the diffuse interface follow naturally as a result from the homogenisation theory Mosler et al. [92], Steinbach and Apel [124, 125]. For this reason, this type of approach shows the localisation property. This type of model class which will be considered in the following is, from a physics point of view, meaningful for relatively thick interfaces.

The most frequently applied homogenisation assumptions for defining the effective properties of the bulk material in the diffuse interface are the Reuss/Sachs model and the Taylor/Voigt model (see Ammar et al. [3], Steinbach and Apel [124]). While Reuss/Sachs considers spatially constant stresses, Taylor/Voigt assumes spatially constant strains. Clearly, these two homogenisation assumptions are limiting cases in the sense of energies, i.e. they represent lower (Reuss/Sachs) and upper (Taylor/Voigt) energy bounds. Speaking in the sense of physics, the Reuss/Sachs model does not fulfil kinematic compatibility across the interface, while the Taylor/Voigt model does not fulfil static equilibrium at the interface. A good overview of these models and of the previously mentioned Khachaturyan model is given in Ammar et al. [3], de Rancourt et al. [36]. A novel homogenisation scheme simultaneously fulfilling kinematic compatibility as well as static equilibrium across the interface is presented in Mosler et al. [92]. For a geometrically linearised theory and linear elasticity, similar ideas can be found in Durga et al. [40, 41], Schneider et al. [111]. In Mosler et al. [92], kinematic compatibility is enforced by applying the *Cauchy & Hadamard* condition. The normal vector occurring in the Cauchy-Hadamard condition is computed from the spatial distribution of the phase field, while the vector associated with the deformation jump is computed by energy relaxation. It can be shown that this relaxation is equivalent to enforcing traction continuity across the interface.

The homogenisation scheme proposed in Mosler et al. [92] is inspired by the works of Aubry and Ortiz [6], Ortiz and Repetto [98], Bartels et al. [13], Levitas and Ozsoy [74, 75], Bartel and Hackl [10]. In contrast to Mosler et al. [92], the normal vector in the Cauchy-Hadamard condition as well as the phase fraction are locally relaxed and not related to a globally defined phase field parameter. From a mathematical point of view, the models in Aubry and Ortiz [6], Ortiz and Repetto [98], Bartels et al. [13], Levitas and Ozsoy [74, 75], Bartel and Hackl [10] are based on rank-1 convexification. Since the orientation of the normal vector is not locally relaxed in Mosler et al. [92], the respective model is termed partial rank-1 homogenisation. A generalised version of the model proposed in Mosler et al. [92] is elaborated in this thesis, which accounts for a locally defined normal vector – similar to the idea in rank-1 convexification frameworks Aubry and Ortiz [6], Ortiz and Repetto [98]. This generalised version is referred to as full rank-1 homogenisation.

In order to compare the state-of-the-art homogenisation assumptions of Taylor/Voigt and Reuss/Sachs to the novel assumptions based on rank-1 homogenisation, a unified framework is elaborated in this thesis. Independent of the underlying homogenisation assumption all models are presented in a unified variational structure where all unknowns follow jointly from energy minimisation. Following Fischer [45], see also Bartel and Hackl [10], Schmidt-Baldassari [110], the admissible range of the order parameter is enforced through nonlinear complementary conditions.

While martensitic phase transformations are displacive in nature, the formation of precipitates e.g. in NiTi shape memory alloys is driven by diffusion, cf. Bouville and Ahluwalia [23]. Displacive transformations are usually described by an *Allen-Cahn*-type phase field formulation (see Allen and Cahn [2]) as described in the previous paragraphs. By way of contrast, diffusion based phase transformations can be studied by a *Cahn-Hilliard*-type phase field model, cf. Cahn and Hilliard [24]. Mechanically induced phase segregation of Cahn-Hilliard-type can be found in Larché and Cahn [69], Onuki [97] and Maraldi et al. [81] and can be embedded into a variational format as shown in Miehe et al. [84]. Coupled Cahn-Hilliard-type phase field models can be found in the context of chemically induced swelling Miehe et al. [85] and elastoplasticity Anand [4] among others.

Since Cahn-Hilliard-type models naturally enforce conservation of volume and account for a rearrangement of material (see Gurtin [50]), they are also suitable for topology optimisation, as shown in Blank et al. [19], Dedè et al. [38], Wallin et al. [134]. The main goal in topology optimisation is the determination of the optimal material distribution. Based on the ideas given in Kotucha [67], Wallin and Ristinmaa [133], Wallin et al. [134] a model is presented for the optimisation of structures. By using the aforementioned nonlinear complementary conditions as proposed in Fischer [45] a robust and efficient implementation is proposed.

1.3 Structure of the thesis

This thesis is structured in two main parts which are associated with the macroscopic as well as with the microscopic scale. Starting with the fundamentals of continuum mechanics in Chapter 2, the relevant balance laws within this thesis are introduced. The focus of this chapter lies on the development of coupled constitutive models at finite strains. To be more precise, three material models covering hyperelasticity, thermoelasticity and thermoplasticity are discussed, where special emphasis is on the thermomechanical coupling in dissipative materials. Furthermore, the aforementioned constitutive models are presented in a variational format which serves as natural framework for thermomechanically coupled problems.

The correct prediction of temperatures and the correct thermomechanical coupling is addressed in Chapter 3. Particularly, the dissipation associated with plastic deformation influences the temperature evolution. For this reason, the dissipation is intensively analysed for standard dissipative materials as well as for generalised standard materials. Based on this analysis, a novel and generalised thermomechanical coupling is proposed, which accounts for an adequate split of energetic and dissipative parts. Interestingly, the advocated model shows a strong analogy to the ad-hoc ansatz of *Taylor-Quinney*.

As already pointed out in the previous section, the first main focus of the thesis is the development of a suitable material model for the technological relevant macroscale. Such a model is presented in Chapter 4, where the texture evolution is captured by means of a macroscopic distortional hardening model. For this purpose, a novel thermodynamically consistent distortional hardening model is proposed falling into the range of generalised standard materials. This novel model is incorporated into the generalised thermomechanical framework elaborated in the previous chapter. Regarding the numerical implementation of the coupled distortional hardening model, an efficient algorithmic formulation for the fourth-order evolution equations is developed, so that the numerical complexity is significantly reduced. Several numerical examples show the application for complex technological processes.

Chapter 5 represents the second main focus of the thesis, i.e. the efficient modelling of effective properties at the microscale. For this purpose, a unified Allen-Cahn-type phase field model is developed which includes homogenisation assumptions defining the mechanical response of the bulk material in the interface. The proposed framework includes state-of-the-art homogenisation schemes, such as the classic Taylor/Voigt and Reuss/Sachs assumptions as well as novel homogenisation schemes based on a rank-1 connection of the interface. As a key aspect of this chapter a robust numerical implementation is developed, such that admissible order parameters are guaranteed and the constrained optimisation is transferred into an unconstrained optimisation. The obtained algorithmic system of equations is implemented into a finite element scheme and the capability of the different homogenisation assumptions is investigated.

In Chapter 6 the Allen-Cahn-type phase field model as elaborated in Chapter 5 is adapted for a deformation-diffusion driven Cahn-Hilliard-type phase field model. Although the underlying Cahn-Hilliard equation driving the diffusion process is a fourth-order differential equation, the proposed model can efficiently be solved based on a mixed three-field formulation. It is shown that the constitutive assumptions inherit a natural variational structure, where the constitutive equations and the balance laws such as the mass conservation law follow jointly from the underlying minimisation principle. The resulting algorithmic formulation is implemented by using the aforementioned numerical framework in order to obtain an unconstrained optimisation. Based on the resulting model, the evolution of microstructures caused by the interaction between mechanics and diffusion are numerically analysed. A further point of this chapter deals with the prediction of the optimal design of structures. For this purpose, the Cahn-Hilliard-type phase field model which naturally enforces conservation of volume is adapted. The final system of governing equations shows a strong analogy to the evolution equation of the aforementioned coupled Cahn-Hilliard phase field model. The capability of the proposed model is demonstrated.

The present thesis is closed with a short summary and a short discussion of future perspectives.

2 Introduction to continuum mechanics

This chapter gives an introduction to continuum mechanics with focus on constitutive modelling. After introducing the notation of the underlying tensor operations in Section 2.1, the kinematics of the geometrically non-linear theory at finite strains is summarised in Section 2.2. Subsequently, the basic balance equations are derived in Section 2.3. Focussing on hyperelastic, thermoelastic and thermoplastic materials, the underlying constitutive equations are deduced in Section 2.5. Furthermore, Section 2.6 presents the constitutive models previously presented in Section 2.5 in a variational form.

It should be mentioned that the derived equations and relations are neither new nor completely presented in detail here. In fact, this chapter provides a basis for the following constitutive models and contains general equations and relations for the following chapters. A complete overview of classic continuum mechanics can be found for example in Holzapfel [55], Hutter and Jöhnk [57], Šilhavý [116].

2.1 Notation

The following notation is used throughout the entire thesis. If necessary, use is made of index notation which implies the Einstein summation rule. The Euclidean space $\mathbb{R}^3$ is spanned by the Cartesian vectors $\mathbf{e}_i$ for $i = \{1, 2, 3\}$ with $\mathcal{O}$ being the centre. For the sake of simplicity, all vectors and higher order tensors are spanned by Cartesian basis vectors. Accordingly, these basis vectors are omitted in the following. First order tensors are denoted by bold-face symbols, e.g. $\mathbf{a}$, $\mathbf{b}$, and second order tensors are denoted by bold-face symbols, e.g. $\mathbf{A}$, $\mathbf{B}$. Fourth order tensors are symbolised by blackboard-bold letters, e.g. $\mathbb{A}$, $\mathbb{B}$. Basic algebraic operations between these tensors are presented below.

Scalar products:

$$\begin{aligned}
\mathbf{a} \cdot \mathbf{b} &= [\mathbf{a}]_i \, [\mathbf{b}]_i \\
\mathbf{A} : \mathbf{B} &= [\mathbf{A}]_{ij} \, [\mathbf{B}]_{ij} \\
\mathbb{A} :: \mathbb{B} &= [\mathbb{A}]_{ijkl} \, [\mathbb{B}]_{ijkl}
\end{aligned}$$

The dots stand for the order of contraction. While $(\cdot)$ is a simple contraction, double dot $(:)$ and double-double dot $(::)$ stand for double contractions and fourth order contractions of indices, respectively. A generalised scalar product of two n-th order tensors $\mathcal{X}$, $\mathcal{Y}$ is denoted by the $(\circ)$ symbol, i.e. $\mathcal{X} \circ \mathcal{Y}$.

Standard and non-standard inner vector and tensor products:

$$\begin{aligned}
\left[\mathbf{A} \cdot \mathbf{b}\right]_i &= [\mathbf{A}]_{ij} \, [\mathbf{b}]_j \\
[\mathbf{A} \cdot \mathbf{B}]_{ij} &= [\mathbf{A}]_{im} \, [\mathbf{B}]_{mj} \\
[\mathbb{A} \cdot \mathbf{b}]_{ijk} &= [\mathbb{A}]_{ijkl} \, [\mathbf{b}]_l \\
[\mathbb{A} : \mathbf{B}]_{ij} &= [\mathbb{A}]_{ijkl} \, [\mathbf{B}]_{kl} \\
[\mathbb{A} : \mathbb{B}]_{ijkl} &= [\mathbb{A}]_{ijmn} \, [\mathbb{B}]_{mnkl} \\
[\mathbf{A} \odot \mathbb{B}]_{ijkl} &= [\mathbf{A}]_{im} \, [\mathbb{B}]_{jmkl} \\
[\mathbf{a} \bullet \mathbb{B}]_{ijk} &= [\mathbf{a}]_m \, [\mathbb{B}]_{imjk}
\end{aligned}$$

In this regard only the definitions of the operations $(\odot)$ and $(\bullet)$ are non-standard since they represent inner tensor products associated with the second index.

Standard and non-standard outer vector and tensor products:

$$\begin{aligned}
\left[\mathbf{a} \otimes \mathbf{b}\right]_{ij} &= [\mathbf{a}]_i \, [\mathbf{b}]_j \\
[\mathbf{A} \otimes \mathbf{B}]_{ijkl} &= [\mathbf{A}]_{ij} \, [\mathbf{B}]_{kl} \\
[\mathbf{A} \underline{\otimes} \mathbf{B}]_{ijkl} &= [\mathbf{A}]_{il} \, [\mathbf{B}]_{jk} \\
[\mathbf{A} \overline{\otimes} \mathbf{B}]_{ijkl} &= [\mathbf{A}]_{ik} \, [\mathbf{B}]_{jl} \, .
\end{aligned}$$

In this regard only the definitions of the operations $(\underline{\otimes})$ and $(\overline{\otimes})$ are non-standard in classic continuum mechanics.

Identity tensors:
By use of Kronecker Delta δ, the identity tensors

$$\begin{aligned}
[\mathbf{I}]_{ij} &= \delta_{ij} \\
[\mathbb{I}]_{ijkl} &= [\mathbf{I} \overline{\otimes} \mathbf{I}]_{ijkl} = \delta_{ik}\,\delta_{jl} \\
\left[\mathbb{I}^{\mathrm{dev}}\right]_{ijkl} &= \left[\mathbb{I} - \frac{1}{3}\mathbf{I} \otimes \mathbf{I}\right]_{ijkl} = \delta_{ik}\,\delta_{jl} - \frac{1}{3}\delta_{ij}\,\delta_{kl}
\end{aligned}$$

are defined, which exhibit the following identity properties. The trace of a second order tensor $\mathbf{A}$ is determined by $\mathrm{tr}\mathbf{A} = \mathbf{A} : \mathbf{I}$. The fourth order identity tensor $\mathbb{I}$ implies $\mathbb{I} : \mathbf{A} = \mathbf{A} \quad \forall\ \mathbf{A}$. Based on the deviatoric fourth order identity tensor $\mathbb{I}^{\mathrm{dev}}$, the deviatoric part of a second order tensor, i.e. $\mathrm{dev}\mathbf{A} = \mathbb{I}^{\mathrm{dev}} : \mathbf{A}$, and the deviatoric part of a fourth order tensor, i.e. $\mathrm{dev}\mathbb{A} = \mathbb{I}^{\mathrm{dev}} : \mathbb{A}$ are computed.

2.2 Kinematics

In this section the motion of a continuous body (Boltzmann continuum) is briefly summarised. A body $\mathcal{B}_0 \subset \mathbb{R}^3$ at time $t = 0$, which refers to the reference or undeformed configuration, is described by a set of material points or particles. Every material point P of $\mathcal{B}_0$ is defined by its coordinate $\mathbf{X}(P)$ in the Euclidean space $\mathbb{R}^3$. The body deforms under loading. This configuration of the body, also referred to as deformed or current configuration, is denoted by $\mathcal{B}_t$ for time $t > 0$. The underlying deformation of material points from $\mathcal{B}_0$ to $\mathcal{B}_t$ is described by the mapping

$$\boldsymbol{\varphi} : \begin{cases} \mathcal{B}_0 \times \tau \to \mathcal{B}_t \subset \mathbb{R}^3 \\ (\mathbf{X}, t) \mapsto \mathbf{x} = \boldsymbol{\varphi}(\mathbf{X}, t) \end{cases} . \tag{2.1}$$

The mapping indicates that to every material point in the reference configuration one coordinate $\mathbf{x} = \boldsymbol{\varphi}(\mathbf{X}, t)$ in the deformed configuration is assigned. The mapping is illustrated for an infinitesimal volume element in Fig. 2.1. For the sake of simplicity, identical Cartesian coordinates are chosen for the reference and current configuration. The difference between current and referential coordinate results in the displacement vector

$$\mathbf{u} = \mathbf{x} - \mathbf{X} . \tag{2.2}$$

In order to describe the deformation process locally, deformation gradient

$$\mathbf{F} = \frac{\partial \mathbf{x}}{\partial \mathbf{X}} = \frac{\partial \boldsymbol{\varphi}}{\partial \mathbf{X}} = \mathrm{GRAD}\boldsymbol{\varphi} \tag{2.3}$$

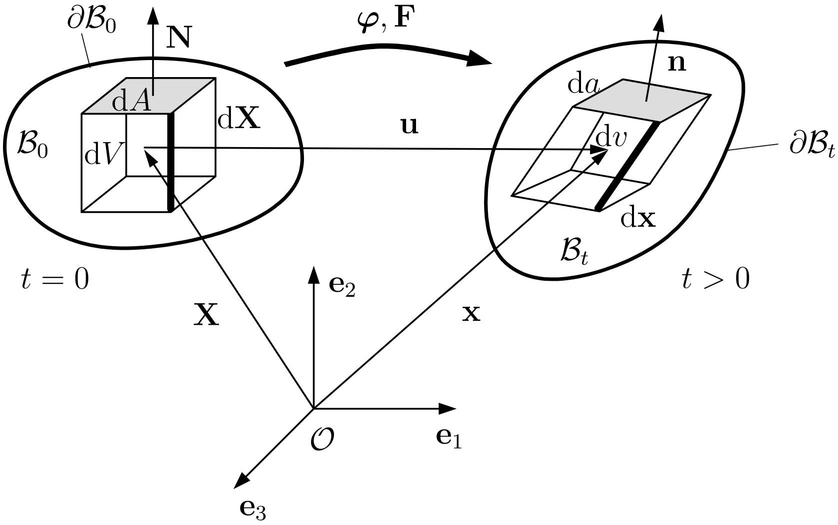

$\partial\mathcal{B}_0$
$\mathbf{N}$
$\varphi, \mathbf{F}$
$\mathbf{n}$
$\mathrm{d}a$
$\mathrm{d}A$
$\mathrm{d}\mathbf{X}$
$\mathbf{u}$
$\mathcal{B}_0$
$\mathrm{d}V$
$\mathrm{d}v$
$\partial\mathcal{B}_t$
$\mathrm{d}\mathbf{x}$
$\mathcal{B}_t$
$t = 0$
$t > 0$
$\mathbf{e}_2$
$\mathbf{X}$
$\mathbf{x}$
$\mathcal{O}$
$\mathbf{e}_1$
$\mathbf{e}_3$

Figure 2.1: Motion of a body. Reference and current configuration

is introduced. In this regard and throughout this thesis, derivatives with respect to the reference configuration are applied. Consequently, the gradient and the divergence for any tensor valued quantity $(\bullet)$ are defined as

$$\mathrm{GRAD}\,\bullet = \frac{\partial \bullet}{\partial \mathbf{X}}\,, \qquad \mathrm{DIV}\,\bullet = \mathrm{GRAD}\,\bullet : \mathbf{I}\,. \tag{2.4}$$

Based on the definition of $\mathbf{F}$, the mapping of line, surface and volume elements, as shown in Fig. 2.1, can be performed. The deformation gradient $\mathbf{F}$ maps a line segment $\mathrm{d}\mathbf{X}$ from the reference configuration to the current configuration $\mathrm{d}\mathbf{x}$ by means of

$$\mathrm{d}\mathbf{x} = \mathbf{F} \cdot \mathrm{d}\mathbf{X}\,. \tag{2.5}$$

Due to the invertibility constraint of material points, the Jacobian of $\mathbf{F}$ requires

$$J = \det\mathbf{F} > 0\,, \tag{2.6}$$

where (det) denotes the determinant of $\mathbf{F}$. A surface element is transformed from the reference to the deformed configuration by means of *Nanson* formula

$$\mathbf{n}\,\mathrm{d}a = J\,\mathbf{F}^{-\mathrm{T}} \cdot \mathbf{N}\,\mathrm{d}A\,. \tag{2.7}$$

As illustrated in Fig. 2.1, $\mathbf{n}$ and $\mathbf{N}$ are the normal vectors on the surface elements $\mathrm{d}a$ and $\mathrm{d}A$ for the reference and current configuration, respectively. The current volume element $\mathrm{d}v$ and the referential volume element $\mathrm{d}V$ are connected via

$$\mathrm{d}v = J\,\mathrm{d}V\,. \tag{2.8}$$

Since some material models rely on evolution equations, the rates of deformation-like quantities are also required. For that purpose, the spatial velocity gradient

$$\mathbf{l} = \dot{\mathbf{F}} \cdot \mathbf{F}^{-1} \tag{2.9}$$

is introduced where dot denotes the material time derivative. Following standard continuum mechanics notation, cf. Holzapfel [55], Hutter and Jöhnk [57], lower case letters are used to indicate variables belonging to the current configuration, and upper case letters are used to indicate variables belonging to the reference configuration. For the sake of simplicity, the balance equations and constitutive models are presented with respect to the reference configuration. However, balance laws can equivalently be formulated for the deformed configuration of the body. For more details with respect to continuum mechanics discussed in the context of deformed and undeformed configurations, the interested reader is referred to Holzapfel [55], Hutter and Jöhnk [57] and others.

2.3 Balance equations

This section gives a short overview of balance equations used within this thesis. Adopting the *cutting principle* (see Hutter and Jöhnk [57], p.51), the following balance laws are derived integrally for a control volume and control surface. The control volume and control boundary are denoted as subsets $\Omega_0 \subset \mathcal{B}_0$ and $\partial\Omega_0 \subset \partial\mathcal{B}_0$. Based on the integral formulations, the local balances, that are the balance of mass, linear momentum, energy and the entropy inequality, are derived.

Balance of mass:
For a generalised open system with a fixed body volume, mass can flow over the boundary or created by a source. Consequently, the mass balance in its referential configuration reads

$$\frac{\mathrm{d}}{\mathrm{d}t} \int\limits_{\Omega_0} \rho_0 \,\mathrm{d}V = - \int\limits_{\partial\Omega_0} \bar{H} \,\mathrm{d}A + \int\limits_{\Omega_0} M \,\mathrm{d}V \,. \tag{2.10}$$

The rate of the referential density $\rho_0 > 0$ is balanced by the mass flux $\bar{H}$ acting on the boundary and by mass source M. Similarly to *Stokes'* heat flux theorem (cf. Holzapfel [55] §4), the mass flux is linearly dependent on the normal vector, i.e. $H = \mathbf{H} \cdot \mathbf{N}$. The mass transfer is defined by the nominal mass flux vector $\mathbf{H}$. Within this work, no mass sources and fluxes over the boundary are considered, i.e. $M = 0$ and $\bar{H} = 0$. For the referential density $\rho_0(\mathbf{X}) > 0$ being only a function of the referential position $\mathbf{X}$ and independent on the time, the mass is conserved, i.e.

$$\frac{\mathrm{d}}{\mathrm{d}t}\rho_0 = \dot{\rho}_0 = 0 \,. \tag{2.11}$$

This corresponds to a closed system and is assumed for the following balance laws. Further information on mass balances in the context of open and closed systems can be found in Epstein and Maugin [42] and Kuhl [68].

Balance of linear momentum:
The conservation of linear momentum states that the time rate of momentum equals the sum of external forces acting on body $\mathcal{B}_0$. The external forces

$$\boldsymbol{\mathcal{F}} = \int\limits_{\Omega_0} \rho_0 \, \mathbf{B} \, \mathrm{d}V + \int\limits_{\partial\Omega_0} \bar{\mathbf{T}} \, \mathrm{d}A \tag{2.12}$$

are determined by the body force $\rho_0 \, \mathbf{B}$ and the prescribed tractions $\bar{\mathbf{T}}$ on the boundary. The linear momentum of the body is defined by

$$\mathbf{L} = \frac{\mathrm{d}}{\mathrm{d}t} \int\limits_{\Omega_0} \rho_0 \, \boldsymbol{\varphi} \mathrm{d}V \, . \tag{2.13}$$

Consequently, the linear momentum balance $\dot{\mathbf{L}} = \boldsymbol{\mathcal{F}}$ leads to

$$\int\limits_{\Omega_0} \rho_0 \, \ddot{\boldsymbol{\varphi}} \, \mathrm{d}V = \int\limits_{\Omega_0} \rho_0 \, \mathbf{B} \, \mathrm{d}V + \int\limits_{\partial\Omega_0} \bar{\mathbf{T}} \, \mathrm{d}A \, . \tag{2.14}$$

In this regard the double dot indicates the second material time derivative of the deformation map $\boldsymbol{\varphi}$. For stress vector $\mathbf{T}$ Cauchy's stress theorem is assumed. This theorem implies the linear dependency on the normal vector, i.e. $\mathbf{T} = \mathbf{P} \cdot \mathbf{N}$, where $\mathbf{P}$ denotes the first Piola-Kirchhoff stress tensor. Inserting this relation into Eq. (2.14) and applying the Gauss divergence theorem, the surface integral is converted into a volume integral. Consequently, for any material point $\mathbf{X} \in \mathcal{B}_0$, the momentum balance Eq. (2.14) is transformed into the local form

$$\rho_0 \, \ddot{\boldsymbol{\varphi}} = \mathrm{DIV}\mathbf{P} + \rho_0 \, \mathbf{B} \quad \text{on} \quad \mathcal{B}_0 \, . \tag{2.15}$$

If dynamic effects are neglected, the inertia term $\rho_0 \, \ddot{\boldsymbol{\varphi}}$ vanishes, and thus the balance of linear momentum results in

$$\mathrm{DIV}\mathbf{P} + \rho_0 \, \mathbf{B} = \mathbf{0} \quad \text{on} \quad \mathcal{B}_0 \, . \tag{2.16}$$

Remark 2.3.1: *From the balance of angular momentum it can be deduced that Cauchy stress tensor* $\boldsymbol{\sigma} = J^{-1} \, \mathbf{P} \cdot \mathbf{F}^{\mathrm{T}}$ *requires symmetry (for a classic Boltzmann continuum). This implies that* $\mathbf{P} \cdot \mathbf{F}^{\mathrm{T}} = \mathbf{F} \cdot \mathbf{P}^{\mathrm{T}}$ *has to hold. Similarly, it follows from the balance of angular momentum that the second Piola-Kirchhoff stress tensor* $\mathbf{S} = \mathbf{F} \cdot \mathbf{P}$ *is symmetrically.*

Balance of energy:
The balance of energy is equivalent with the first law of thermodynamics. From the physics point of view it states that the rate of kinetic energy K and internal energy E of a thermodynamic system equals the external mechanical power $\mathcal{P}_{\mathbf{F}}$, external thermal power $\mathcal{P}_{\Theta}$ and other external powers $\mathcal{P}_{\text{ext}}$ which are related to further macro- or micromechanical forces. Thus, the balance reads

$$\frac{\mathrm{d}}{\mathrm{d}t}\int\limits_{\Omega_0}\{K+E\}\,\mathrm{d}V=\mathcal{P}_{\mathbf{F}}+\mathcal{P}_{\Theta}+\mathcal{P}_{\text{ext}}\,. \tag{2.17}$$

Focussing on thermomechanically coupled Boltzmann continua, $\mathcal{P}_{\text{ext}}$ is currently skipped. For dynamic systems the kinetic energy $K=1/2\,\rho_0\,\|\dot{\boldsymbol{\varphi}}\|^2$ is taken into account, in which $\|\cdot\|$ denotes the Euclidean 2-norm. The external power of the mechanical system

$$\mathcal{P}_{\mathbf{F}}=\int\limits_{\partial\Omega_0}\bar{\mathbf{T}}\cdot\dot{\boldsymbol{\varphi}}\,\mathrm{d}A+\int\limits_{\Omega_0}\rho_0\,\mathbf{B}\cdot\dot{\boldsymbol{\varphi}}\,\mathrm{d}V \tag{2.18}$$

is determined by the tractions $\bar{\mathbf{T}}$ acting on the surface and the body force $\rho_0\,\mathbf{B}$. The external power of the thermal system is determined by the prescribed heat flux $\bar{\mathcal{Q}}$ acting on the surface and the volume specific heat source $\rho_0\,R_\Theta$, i.e.

$$\mathcal{P}_{\Theta}=-\int\limits_{\partial\Omega_0}\bar{\mathcal{Q}}\,\mathrm{d}A+\int\limits_{\Omega_0}\rho_0\,R_\Theta\,\mathrm{d}V\,. \tag{2.19}$$

For heat flux $\mathcal{Q}$, Stoke's heat flux theorem is postulated. Hence, $\mathcal{Q}$ is linearly dependent on the surface normal vector $\mathbf{N}$ and the heat flux vector $\boldsymbol{\mathcal{Q}}$, i.e. $\mathcal{Q}=\boldsymbol{\mathcal{Q}}\cdot\mathbf{N}$.

In order to obtain a local version of Eq. (2.17), Gauss's divergence theorem is applied for the transformation of surface into volume integrals. After insertion of balance of linear momentum (Eq. (2.15)), the resulting energy balance equation reads for all material points

$$\dot{E}=\mathbf{P}:\dot{\mathbf{F}}-\mathrm{DIV}\boldsymbol{\mathcal{Q}}+\rho_0\,R_\Theta\,, \tag{2.20}$$

where $\mathbf{P}:\dot{\mathbf{F}}$ denotes the stress power. Equation (2.20) refers to the local form of the first law of thermodynamics. It balances the mechanical and thermal energies inside and outside of a body $\mathcal{B}_0$. However, the direction of energy transformation cannot be governed from the first law of thermodynamics. To this end, the second law of thermodynamics is applied.

Remark 2.3.2: *For isothermal conditions, i.e. for constant temperature* $\Theta =$ const. *without considering heat flux* $\boldsymbol{\mathcal{Q}}$ *and heat source* R_Θ*, the balance of internal energy Eq.* (2.20) *reduces to*

$$\dot{E} = \mathbf{P} : \dot{\mathbf{F}} \,. \tag{2.21}$$

By means of the Legendre transformation (see Remark 2.5.1) this equation can be represented as

$$\dot{\Psi} + \Theta\,\dot{N} = \mathbf{P} : \dot{\mathbf{F}} \,. \tag{2.22}$$

Entropy inequality:
The direction of energy transfer is addressed in the entropy inequality, also known as the second law of thermodynamics. It states that the rate of entropy N is greater than the rate of entropy input. According to *Clausius-Duhem* the total production of entropy

$$\Gamma = \frac{\mathrm{d}}{\mathrm{d}t}\int\limits_{\Omega_0} N\,\mathrm{d}V + \int\limits_{\partial\Omega_0} \frac{\bar{\mathcal{Q}}}{\Theta}\,\mathrm{d}A - \int\limits_{\Omega_0} \frac{\rho_0\,R_\Theta}{\Theta}\,\mathrm{d}V \geq 0 \tag{2.23}$$

is defined. It requires that $\Gamma \geq 0$ is fulfilled for all possible processes. For $\Gamma = 0$, the process is termed reversible and for $\Gamma > 0$ the process is termed irreversible. Irreversible processes are associated with dissipation of energy. Moreover, the inequality is only valid for temperatures

$$\Theta : \begin{cases} \mathcal{B}_0 \times \tau \to \mathcal{B}_t \subset \mathbb{R}^+ \\ (\mathbf{X}, t) \mapsto \Theta(\mathbf{X}, t) \end{cases}, \tag{2.24}$$

i.e $\Theta > 0$, where the temperature is measured in Kelvin. In order to obtain a local form of Eq. (2.23) the surface integral is converted into a volume integral by means of Stoke's heat flux theorem. The resulting local form reads for all material points

$$\dot{N} + \frac{\mathrm{DIV}\boldsymbol{\mathcal{Q}}}{\Theta} - \frac{1}{\Theta^2}\boldsymbol{\mathcal{Q}} \cdot \mathrm{GRAD}\Theta - \frac{\rho_0\,R_\Theta}{\Theta} \geq 0 \,. \tag{2.25}$$

By multiplying this equation with Θ the second law of thermodynamics

$$\mathcal{D} = \Theta\,\dot{N} + \mathrm{Div}\boldsymbol{\mathcal{Q}} + \boldsymbol{\mathcal{Q}} \cdot \mathbf{G} - \rho_0\,R_\Theta \geq 0 \tag{2.26}$$

is obtained. The magnitude of irreversibility is denoted by dissipation $\mathcal{D}$. In this context, the generalised temperature gradient $\mathbf{G} = -\mathrm{GRAD}\Theta/\Theta$ is introduced. For the thermo-mechanically coupled version of the dissipation inequality, the term $\mathrm{Div}\boldsymbol{\mathcal{Q}} - \rho_0\,R_\Theta$ is replaced by the use of the balance of energy (2.20). Thus, the dissipation inequality reads for the thermomechanically coupled case

$$\mathcal{D} = \mathbf{P} : \dot{\mathbf{F}} + \Theta \, \dot{N} + \boldsymbol{\mathcal{Q}} \cdot \mathbf{G} - \dot{E} \geq 0 \,. \tag{2.27}$$

Again, $\mathbf{P} : \dot{\mathbf{F}}$ is the stress power. Furthermore, temperature Θ and entropy rate $\dot{N}$ are thermodynamically conjugated to one another, and heat flux $\boldsymbol{\mathcal{Q}}$ and normalised temperature gradient $\mathbf{G}$ are thermodynamically conjugated to one another. According to *Clausius-Planck*, a stronger form of Ineq. (2.27) requires that

$$\mathcal{D}_{\text{int}} = \mathbf{P} : \dot{\mathbf{F}} + \Theta \, \dot{N} - \dot{E} \geq 0 \,, \qquad \mathcal{D}_{\text{con}} = \boldsymbol{\mathcal{Q}} \cdot \mathbf{G} \geq 0 \tag{2.28}$$

are independently fulfilled. $\mathcal{D}_{\text{int}}$ denotes the internal dissipation and $\mathcal{D}_{\text{con}}$ denotes the dissipation due to heat conduction. This decomposition is inspired by the observation that heat flows from warm to cold zones even for thermoelastic processes where $\mathcal{D}_{\text{int}} = 0$. Clearly, the inequalities (2.28) need separately be proven for all constitutive material models, i.e. approaches for internal energies and heat conduction. Regarding the thermodynamical consistency of material models, the framework of Coleman and Noll [35], Coleman [33], Coleman and Gurtin [34], Truesdell and Noll [132] is usually considered. More details are given in the following chapters.

Remark 2.3.3: *For isothermal conditions, i.e. for constant temperatures* $\Theta > 0$ *without consideration of heat flux* $\boldsymbol{\mathcal{Q}}$ *and heat source* R_Θ*, the dissipation inequality Eq.* (2.27) *reduces to*

$$\mathcal{D} = \mathbf{P} : \dot{\mathbf{F}} + \Theta \, \dot{N} - \dot{E} \geq 0 \,. \tag{2.29}$$

By considering a Legendre transformation (see Remark 2.5.1) this equation reduces to

$$\mathcal{D} = \mathbf{P} : \dot{\mathbf{F}} - \dot{\Psi} \geq 0 \,. \tag{2.30}$$

2.4 Boundary conditions

In order to solve thermomechanically coupled boundary value problems or, to be more precise, the balance of linear momentum (Eq. (2.16)) and the energy balance (Eq. (2.20)), suitable boundary and initial conditions are required. To this end, boundary $\partial\mathcal{B}_0$ is decomposed into Dirichlet and Neumann boundaries for each field variable. For the mechanical boundary value problem, its boundary is decomposed into

$$\partial\mathcal{B}_0 = \partial\mathcal{B}_{0,\boldsymbol{\varphi}} \cup \partial\mathcal{B}_{0,\mathbf{T}} \,, \qquad \partial\mathcal{B}_{0,\boldsymbol{\varphi}} \cap \partial\mathcal{B}_{0,\mathbf{T}} = \emptyset \,. \tag{2.31}$$

The Dirichlet boundary $\partial\mathcal{B}_{0,\boldsymbol{\varphi}}$ and Neumann boundary $\partial\mathcal{B}_{0,\mathbf{T}}$ are determined by

$$\boldsymbol{\varphi} = \bar{\boldsymbol{\varphi}} \;\; \forall \mathbf{X} \in \partial\mathcal{B}_{0,\boldsymbol{\varphi}} \,, \qquad \mathbf{P} \cdot \mathbf{N} = \bar{\mathbf{T}} \;\; \forall \mathbf{X} \in \partial\mathcal{B}_{0,\mathbf{T}} \,, \tag{2.32}$$

where $\bar{\boldsymbol{\varphi}}$ denotes the prescribed deformation on the Dirichlet boundary and $\bar{\mathbf{T}}$ denotes the prescribed tractions on the Neumann boundary. The initial deformation map at time $t = 0$ is indicated by the index "0", i.e. $\boldsymbol{\varphi}(\mathbf{X}, t = 0) = \boldsymbol{\varphi}_0(\mathbf{X})$.

Analogously, the thermal boundary is decomposed into Dirichlet boundary $\partial\mathcal{B}_{0,\Theta}$ and Neumann boundary $\partial\mathcal{B}_{0,\mathcal{Q}}$, such that the boundaries fulfil

$$\partial\mathcal{B}_0 = \partial\mathcal{B}_{0,\Theta} \cup \partial\mathcal{B}_{0,\mathcal{Q}}\,, \qquad \partial\mathcal{B}_{0,\Theta} \cap \partial\mathcal{B}_{0,\mathcal{Q}} = \emptyset\,. \tag{2.33}$$

The respective boundary conditions are determined by the prescribed temperature $\bar{\Theta}$ and the prescribed heat flux $\bar{\mathcal{Q}}$, i.e. more precisely by

$$\Theta = \bar{\Theta}\ \forall \mathbf{X} \in \partial\mathcal{B}_{0,\Theta}\,, \qquad \boldsymbol{\mathcal{Q}} \cdot \mathbf{N} = \bar{\mathcal{Q}}\ \forall \mathbf{X} \in \partial\mathcal{B}_{0,\mathcal{Q}}\,. \tag{2.34}$$

Initial conditions for the temperature field are described by $\Theta(\mathbf{X}, t = 0) = \Theta_0(\mathbf{X})$, with Θ_0 being the initial temperature. Note, that in a thermomechanically coupled system thermal and mechanical boundaries can intersect.

2.5 Constitutive modelling

In order to define the material response of a body, constitutive relations need to be defined. Three constitutive models at finite strains are presented in the following. All models have in common that the existence of a Helmholtz energy Ψ is postulated.

2.5.1 Hyperelasticity

Focussing first on isothermal processes, the Helmholtz or free energy Ψ is solely a function of the deformation gradient $\mathbf{F}$

$$\Psi = \Psi(\mathbf{F})\,, \tag{2.35}$$

which demonstrates that the stored energy is locally defined. Postulating that the material fulfils objectivity or frame indifference (see Holzapfel [55] §6), the free energy satisfies

$$\Psi(\mathbf{F}) = \Psi(\boldsymbol{Q} \cdot \mathbf{F})\,. \tag{2.36}$$

It states that the stored energy is unaffected by any rigid body motion $\boldsymbol{Q} \in \mathcal{SO}(3)$. Equivalently, the stored energy can also be expressed in terms of the right Cauchy-Green tensor

$$\mathbf{C} = \mathbf{F}^{\mathrm{T}} \cdot \mathbf{F}\,, \tag{2.37}$$

i.e. $\Psi(\mathbf{F}) = \Psi(\mathbf{C})$. Since $\mathbf{C}$ is symmetric, objectivity implies automatically balance of angular momentum as well (see Simo and Hughes [120] §7). If the Helmholtz energy is assumed to be isotropic, meaning the material to behave identical in all directions, the relation $\Psi(\mathbf{F}) = \Psi(\mathbf{F}\cdot\boldsymbol{Q}^{\mathrm{T}})\ \forall\boldsymbol{Q}\in\mathcal{SO}(3)$ has to be fulfilled as well.

Hyperelastic material response is denoted as perfectly elastic behaviour, since the deformation process is not associated with dissipation. As a consequence, the local dissipation inequality (2.30) obtains $\mathcal{D} = 0$. By means of relation $\dot{\Psi} = \partial_{\mathbf{F}}\Psi : \dot{\mathbf{F}}$, Eq. (2.30) yields

$$\mathcal{D} = \mathbf{P} : \dot{\mathbf{F}} - \dot{\Psi} = \left[\mathbf{P} - \frac{\partial\Psi}{\partial\mathbf{F}}\right] : \dot{\mathbf{F}} = 0\,. \tag{2.38}$$

First, it can be deduced that stress power $\mathbf{P} : \dot{\mathbf{F}}$ equals the rate of the Helmholtz energy $\dot{\Psi}$. And secondly, for $\dot{\mathbf{F}}$ being arbitrary, the constitutive relation

$$\mathbf{P} = \frac{\partial\Psi}{\partial\mathbf{F}} \tag{2.39}$$

is derived. Within the framework of Coleman and Noll [35] and Coleman and Gurtin [34] the first Piola-Kirchhoff stress tensor or simply the Piola stress tensor $\mathbf{P}$ is referred to as thermodynamic force. The derivation of thermodynamic forces by means of the second law is also known as *Coleman & Noll* procedure.

2.5.2 Thermoelasticity

For thermoelastic material properties the Helmholtz energy depends locally on the deformation gradient $\mathbf{F}$ and the temperature $\Theta > 0$, i.e.

$$\Psi = \Psi(\mathbf{F},\Theta)\,. \tag{2.40}$$

To be more precise, an additive decomposition of Helmholtz energy (2.40) is assumed. A possible split of the Helmholtz energy

$$\Psi(\mathbf{F},\Theta) = \Psi^{\mathrm{el}}(\mathbf{F}) + M(\mathbf{F},\Theta) + T(\Theta) \tag{2.41}$$

contains the purely elastic contribution Ψ^{el}, the thermoelastic coupling $M(\mathbf{F},\Theta)$ and the purely thermal potential $T(\Theta)$. A purely hyperelastic material is obtained for the isothermal condition $\Psi(\mathbf{F}) = \Psi(\mathbf{F},\Theta)|_{\Theta=\mathrm{const}}$. For a stored energy, depending on the deformation gradient $\mathbf{F}$ and the entropy N, the internal energy E is considered. Ψ and E are connected via the Legendre transformation (Remark 2.5.1).

Remark 2.5.1: *The Helmholtz energy* $\Psi = \Psi(\bullet,\Theta)$ *and the internal energy* $E = E(\bullet, N)$ *as functions of a generalised variable set* $(\bullet)$ *are related via the Legendre transformation*

$$E(\bullet,N) = \Psi(\bullet,\Theta) + \Theta\,N\,. \tag{2.42}$$

Temperature Θ and entropy N are thermodynamically conjugated quantities.

The constitutive relations are subjected to the second law of thermodynamics, i.e. more precisely, the dissipation inequality $(2.28)_1$. For thermoelastic (perfect) materials the identity $\mathcal{D}_{\text{int}} = 0$ is postulated. Thus, inserting an internal energy of the form $E = E(\mathbf{F}, N)$ results in

$$\mathcal{D}_{\text{int}} = \mathbf{P} : \dot{\mathbf{F}} + \Theta\,\dot{N} - \dot{E} = \left[\mathbf{P} - \frac{\partial E}{\partial \mathbf{F}}\right] : \dot{\mathbf{F}} + \left[\Theta - \frac{\partial E}{\partial N}\right]\dot{N} = 0\,. \tag{2.43}$$

For arbitrary deformations and entropies, the Piola stress tensor $\mathbf{P}$ and the temperature Θ are obtained, i.e.

$$\mathbf{P} = \frac{\partial E}{\partial \mathbf{F}}\,, \qquad \Theta = \frac{\partial E}{\partial N}\,. \tag{2.44}$$

By means of the Legendre transformation (2.42) equation (2.43) is re-written into

$$\mathcal{D}_{\text{int}} = \mathbf{P} : \dot{\mathbf{F}} - \dot{\Theta}\,N - \dot{\Psi} = \left[\mathbf{P} - \frac{\partial \Psi}{\partial \mathbf{F}}\right] : \dot{\mathbf{F}} - \left[N + \frac{\partial \Psi}{\partial \Theta}\right]\dot{\Theta} = 0\,, \tag{2.45}$$

leading to the constitutive relations

$$\mathbf{P} = \frac{\partial \Psi}{\partial \mathbf{F}}\,, \qquad N = -\frac{\partial \Psi}{\partial \Theta}\,. \tag{2.46}$$

As can be seen, that N and Θ are thermodynamically conjugated to one another (Remark 2.5.1).

Temperature equation: The evolution of temperature is naturally defined by the first law of thermodynamics. For this purpose, the local energy balance (2.20) is considered. However, the process direction of the temperature is not included. Therefore, the Clausius-Planck relation for thermoelastic materials (2.43) is inserted into Eq. (2.20) leading to

$$\Theta\,\dot{N} = -\mathrm{DIV}\boldsymbol{\mathcal{Q}} + \rho_0\,R_\Theta\,. \tag{2.47}$$

Due to the dependency on $\mathbf{F}$ and Θ (see Eq. (2.46)) the entropy rate yields

$$\dot{N} = -\frac{\partial^2 \Psi}{\partial \Theta \partial \mathbf{F}} : \dot{\mathbf{F}} - \frac{\partial^2 \Psi}{\partial \Theta^2}\,\dot{\Theta}\,. \tag{2.48}$$

Multiplied by Θ, two quantities are derived i.e.

$$c = -\Theta\frac{\partial^2 \Psi}{\partial \Theta^2}\,, \qquad \mathcal{A} = \Theta\frac{\partial^2 \Psi}{\partial \Theta \partial \mathbf{F}} : \dot{\mathbf{F}}\,. \tag{2.49}$$

The heat capacity is denoted by c and is restricted to the constraint $c > 0$. The structural heating defined as $\mathcal{A}$ describes the thermoelastic response, which is also referred to as the *Gough-Joule* effect. Inserting these two relations into Eq. (2.47) yields the local temperature evolution equation

$$\dot{\Theta} = \frac{1}{c}\left[\mathcal{A} - \mathrm{DIV}\boldsymbol{\mathcal{Q}} + \rho_0\, R_\Theta\right] . \tag{2.50}$$

Constitutive relations for the heat flux are given in Remark 2.5.2 and Remark 2.5.3. They are based on a Fourier-type heat conduction. For adiabatic heat conditions (for $\boldsymbol{\mathcal{Q}} = \mathbf{0}$ and without consideration of heat sources $R_\Theta = 0$), the temperature equation reduces to

$$\dot{\Theta} = \frac{1}{c}\mathcal{A} . \tag{2.51}$$

Remark 2.5.2: *In this work a Fourier-type heat conduction is used. It is assumed that the constitutive heat flux vector* $\boldsymbol{\mathcal{Q}}$ *is given in the reference configuration as*

$$\boldsymbol{\mathcal{Q}} = -\mathbf{k}_0 \cdot \mathrm{GRAD}\Theta \, , \tag{2.52}$$

with $\mathbf{k}_0$ *being the thermal conductivity tensor. If* $\mathbf{k}_0$ *is positive definite, Eq.* (2.52) *automatically satisfies the conductivity related dissipation Ineq.* $(2.28)_2$. *For an isotropic conductivity tensor* $\mathbf{k}_0 = k_0\,\mathbf{I}$, *the heat conduction reduces to*

$$\boldsymbol{\mathcal{Q}} = -k_0\, \mathrm{GRAD}\Theta \, , \tag{2.53}$$

and the conductivity term of the dissipation yields

$$\mathcal{D}_{\mathrm{con}} = \boldsymbol{\mathcal{Q}} \cdot \mathbf{G} = \frac{k_0}{\Theta}\, \|\mathrm{GRAD}\Theta\|^2 > 0 \, . \tag{2.54}$$

Remark 2.5.3: *An alternative approach for the Fourier-type heat conduction is proposed in Yang et al. [139]. It is based on the convex potential*

$$\chi = \frac{1}{2}\frac{k_0}{\Theta_0}\|\mathbf{G}\|^2 \tag{2.55}$$

from which heat flux $\boldsymbol{\mathcal{Q}}$ *follows as thermodynamic force*

$$\boldsymbol{\mathcal{Q}} = \frac{\partial \chi}{\partial \mathbf{G}} = -\frac{k_0}{\Theta_0}\frac{\mathrm{GRAD}\Theta}{\Theta} \, . \tag{2.56}$$

Clearly, with $\Theta_0 > 0$ *being the referential temperature, dissipation inequality is automatically satisfied. Further constitutive assumptions of Fourier-type heat conduction can be found in Holzapfel [55] §4.5.*

Remark 2.5.4: *An alternative approach for the modelling of thermoelastic material is based on the decomposition of motion into a purely mechanical deformation and a purely thermal deformation. Accordingly, the deformation gradient*

$$\mathbf{F} = \mathbf{F}^{\mathrm{M}} \cdot \mathbf{F}^{\Theta} \tag{2.57}$$

is multiplicatively decomposed into the mechanical deformation gradient $\mathbf{F}^{\mathrm{M}}$ *and the thermal deformation gradient* $\mathbf{F}^{\Theta}$*. For further details the interested reader is referred to Holzapfel [55] §7.8. As a consequence of the thermoelastic deformation gradient the Helmholtz energy is given in the form*

$$\Psi(\mathbf{F}, \Theta) = \Psi^{\mathrm{el}}\left(\mathbf{F} \cdot \mathbf{F}^{\Theta^{-1}}\right) + T(\Theta)\,, \tag{2.58}$$

where the thermomechanical coupling is already included in the multiplicative split (2.57)*, cf. Eq.* (2.41)*.*

2.5.3 Thermo-elastoplasticity

Next, the thermoelastically coupled material model in Subsection 2.5.2 is extended to irreversible processes. For this purpose, plastic deformations are taken into account, where the classic work of Lee [70] is considered for the kinematical relations. In Lee [70] the deformation gradient is multiplicatively decomposed into an elastic and a plastic contribution. The decomposition yields

$$\mathbf{F} = \mathbf{F}^{\mathrm{e}} \cdot \mathbf{F}^{\mathrm{p}}\,, \qquad \det\mathbf{F}^{\mathrm{e}} > 0\,, \det\mathbf{F}^{\mathrm{p}} > 0 \tag{2.59}$$

with $\mathbf{F}^{\mathrm{e}}$ and $\mathbf{F}^{\mathrm{p}}$ being the elastic and plastic deformation gradient, respectively. Associated with this decomposition, the intermediate configuration is introduced as illustrated in Fig. 2.2. While the mapping $\mathbf{F}^{\mathrm{p}}$ is associated with purely plastic deformations, fully unloaded mechanical system, $\mathbf{F}^{\mathrm{e}}$ characterises the elastic part of the deformation. Experimental investigations show that for metal plasticity, which is assumed in the following, plastic deformation is isochoric. Based on these observations it is assumed that $\det\mathbf{F}^{\mathrm{p}} = 1$ holds. In standard plasticity theories $\mathbf{F}^{\mathrm{p}}$ is most frequently chosen as history-dependent, internal variable. The evolution of this variable can be determined by different rate equations. Therefore, and in analogy to the standard spatial velocity gradient in Eq. (2.9) the two additional velocity gradients

$$\mathbf{L}^{\mathrm{p}} = \dot{\mathbf{F}}^{\mathrm{p}} \cdot \mathbf{F}^{\mathrm{p}-1}\,, \qquad \mathbf{l}^{\mathrm{e}} = \dot{\mathbf{F}}^{\mathrm{e}} \cdot \mathbf{F}^{\mathrm{e}-1} \tag{2.60}$$

are also defined. Note, that $\mathbf{l}^{\mathrm{e}}$ is associated with the deformed configuration whereas $\mathbf{L}^{\mathrm{p}}$ refers to the intermediate configuration induced by the multiplicative split (2.59).

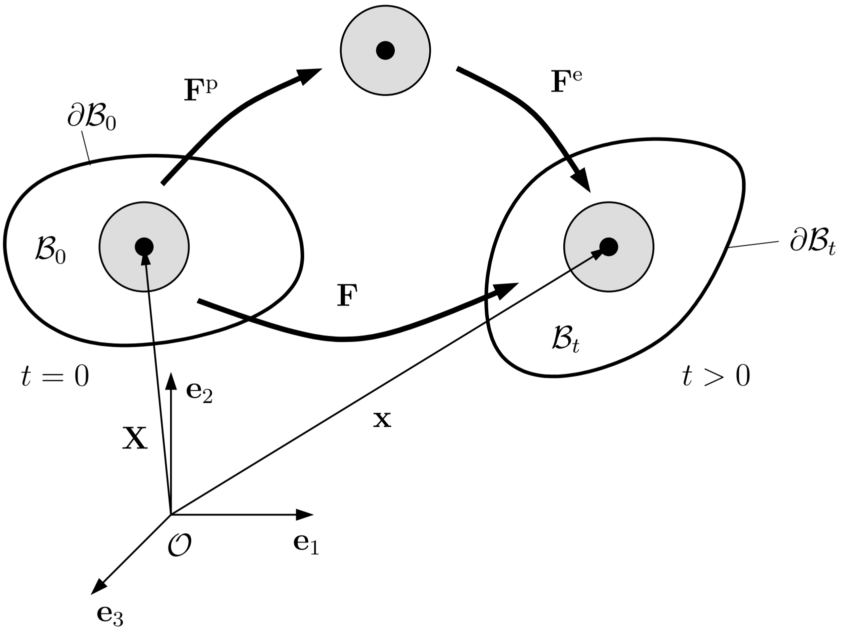

Figure 2.2: Multiplicative decomposed deformation gradient. Introduction of intermediate configuration.

Remark 2.5.5: *The multiplicative decomposition* (2.59) *is motivated by the micromechanical observation of the crystal lattice. While* $\mathbf{F}^{\mathrm{p}}$ *is responsible for the sliding of the crystal lattice,* $\mathbf{F}^{\mathrm{e}}$ *represents the distortion and rotation of the crystal lattice. Referring to Lubliner [79] §8.2, the plastic distortion rate* $\mathbf{L}^{\mathrm{p}}$ *depends on i-slip systems which are spanned by the slip unit vectors* $\mathbf{n}_i$ *and the slip directions* $\mathbf{m}_i$ *and are weighted by the shear rates* $\dot{\gamma}$*, i.e.*

$$\mathbf{L}^{\mathrm{p}} = \sum_i \dot{\gamma}_i \, \mathbf{m}_i \otimes \mathbf{n}_i \,. \tag{2.61}$$

Based on the thermoelastic Helmholtz energy given in the previous subsection, the material is extended to irreversible plastic behaviour. The thermo-elastoplastic material is defined by the Helmholtz energy

$$\Psi = \Psi(\mathbf{F}, \mathbf{F}^{\mathrm{p}}, \Theta, \boldsymbol{\alpha}) \,. \tag{2.62}$$

To be more precise, the underlying Helmholtz energy is additively decomposed into

$$\Psi(\mathbf{F}, \mathbf{F}^{\mathrm{p}}, \Theta, \boldsymbol{\alpha}) = \Psi^{\mathrm{el}}\left(\mathbf{F} \cdot \mathbf{F}^{\mathrm{p}-1}\right) + \Psi^{\mathrm{pl}}(\boldsymbol{\alpha}, \Theta) + M(\mathbf{F}, \Theta) + T(\Theta) \,. \tag{2.63}$$

The argument $\boldsymbol{\alpha} \in \mathbb{R}^n$ of the plastic energy Ψ^{pl} is a generalised set of internal variables associated with hardening related phenomena. Ψ^{pl} may also be a function of the temperature. The elastic energy Ψ^{el} depends solely on the elastic part of the deformation gradient $\mathbf{F}^{\mathrm{e}} = \mathbf{F} \cdot \mathbf{F}^{\mathrm{p}-1}$.

The second law of thermodynamics imposes restrictions on the constitutive assumptions. Inserting Helmholtz energy (2.63) into the Clausius-Planck inequality $(2.28)_1$ yields

$$\begin{aligned} \mathcal{D}_{\mathrm{int}} &= \mathbf{P} : \dot{\mathbf{F}} - \dot{\Theta}\, N - \dot{\Psi} \\ &= \left[\mathbf{P} - \frac{\partial \Psi}{\partial \mathbf{F}}\right] : \dot{\mathbf{F}} - \left[N + \frac{\partial \Psi}{\partial \Theta}\right] \dot{\Theta} - \frac{\partial \Psi}{\partial \mathbf{F}^{\mathrm{p}}} : \dot{\mathbf{F}}^{\mathrm{p}} - \frac{\partial \Psi}{\partial \boldsymbol{\alpha}} \circ \dot{\boldsymbol{\alpha}} \geq 0\,. \end{aligned} \tag{2.64}$$

For a purely elastic material response ($\dot{\boldsymbol{\alpha}} = \mathbf{0}$, $\dot{\mathbf{F}}^{\mathrm{p}} = \mathbf{0}$), Piola stress $\mathbf{P} = \partial_{\mathbf{F}} \Psi$ and entropy $N = -\partial_{\Theta} \Psi$ are deduced, cf. Eqs. (2.46). For inelastic deformations the re-insertion of these constitutive relations leads to the reduced dissipation inequality

$$\mathcal{D}_{\mathrm{int}} = \boldsymbol{\Sigma} : \mathbf{L}^{\mathrm{p}} + \mathbf{Q} \circ \dot{\boldsymbol{\alpha}} > 0\,. \tag{2.65}$$

The reduced dissipation is determined by the plastic work rate $\boldsymbol{\Sigma} : \mathbf{L}^{\mathrm{p}}$ and the hardening related power $\mathbf{Q} \circ \dot{\boldsymbol{\alpha}}$. In detail, the stress-like hardening variable

$$\mathbf{Q} = -\frac{\partial \Psi}{\partial \boldsymbol{\alpha}} = -\frac{\partial \Psi^{\mathrm{pl}}}{\partial \boldsymbol{\alpha}} \tag{2.66}$$

is thermodynamically conjugated to the generalised set of internal variables $\boldsymbol{\alpha}$. The plastic power is derived by

$$\boldsymbol{\Sigma} : \mathbf{L}^{\mathrm{p}} = -\frac{\partial \Psi}{\partial \mathbf{F}^{\mathrm{p}}} : \dot{\mathbf{F}}^{\mathrm{p}} = \left[\mathbf{F}^{\mathrm{eT}} \cdot \frac{\partial \Psi^{\mathrm{el}}}{\partial \mathbf{F}^{\mathrm{e}}}\right] : \left[\dot{\mathbf{F}}^{\mathrm{p}} \cdot \mathbf{F}^{\mathrm{p}-1}\right]\,, \tag{2.67}$$

in which the intermediate configurational Mandel stress tensor is defined as

$$\boldsymbol{\Sigma} = \mathbf{F}^{\mathrm{eT}} \cdot \frac{\partial \Psi^{\mathrm{el}}}{\partial \mathbf{F}^{\mathrm{e}}}\,. \tag{2.68}$$

For an isotropic and hyperelastic energy Ψ^{el}, the Mandel stress tensor $\boldsymbol{\Sigma}$ is symmetric and the stress space is six-dimensional. For an un-symmetric $\boldsymbol{\Sigma}$, the stress space is nine-dimensional. This property is important for the definition of the space of admissible stresses. In order to distinguish between fully elastic and elastoplastic states, a level set or more precisely a convex yield function $\phi(\boldsymbol{\Sigma}, \mathbf{Q}, \Theta) \leq 0$ is introduced. The respective stress space is defined by the set

$$\mathbb{E}_{\boldsymbol{\Sigma}} = \{(\boldsymbol{\Sigma}, \mathbf{Q}, \Theta) \in \mathbb{R}^{9+n+1} | \phi(\boldsymbol{\Sigma}, \mathbf{Q}, \Theta) \leq 0\}\,. \tag{2.69}$$

The elastic domain is determined by $\phi < 0$. Stress states outside of $\mathbb{E}_{\boldsymbol{\Sigma}}$ are not permissible.

In order to fulfil the dissipation Ineq. (2.65), appropriate evolution equations are required. By applying the principle of maximum dissipation (see Simo and Hughes [120] §2.6), associative flow rules and hardening laws are derived. In this case, the flow rule $\mathbf{L}^{\mathrm{p}}$ and the associative hardening law $\dot{\boldsymbol{\alpha}}$ read

$$\mathbf{L}^{\mathrm{p}} = \lambda \, \frac{\partial \phi}{\partial \boldsymbol{\Sigma}} \, , \qquad \dot{\boldsymbol{\alpha}} = \lambda \, \frac{\partial \phi}{\partial \mathbf{Q}} \, , \tag{2.70}$$

where λ denotes the *plastic multiplier*. An admissible elastoplastic solution is obtained if loading/unloading conditions

$$\lambda \geq 0 \, , \qquad \phi \leq 0 \, , \qquad \lambda \, \phi = 0 \tag{2.71}$$

are fulfilled. Constitutive modelling of plasticity, which follows the associativity of flow rule and hardening law is also referred to as *standard materials*. Flow rules and hardening laws which are not proportional to the normality rule of the yield function ($\partial_{\boldsymbol{\Sigma}} \phi$ or $\partial_{\mathbf{Q}} \phi$) can often be described by the framework of *generalised standard materials* (see Lemaitre [72], Mandel [80]). Within this framework, a plastic potential $g = g(\boldsymbol{\Sigma}, \mathbf{Q}, \Theta)$ is introduced and the evolution equations are postulated together with the loading/unloading conditions in Eq. (2.71) as

$$\mathbf{L}^{\mathrm{p}} = \lambda \, \frac{\partial g}{\partial \boldsymbol{\Sigma}} \, , \qquad \dot{\boldsymbol{\alpha}} = \lambda \, \frac{\partial g}{\partial \mathbf{Q}} \, . \tag{2.72}$$

Clearly, for a detailed derivation of evolution equations specific assumptions are required, e.g. for the Helmholtz energy, for the yield surface and if necessary for the plastic potential. Examples of such models are presented in Chapters 3 and 4.

Temperature equation: Similar to the thermoelastic material, the temperature evolution equation for the elastoplastic material is subjected to the first and second law of thermodynamics. The combination of Eq. (2.20) and Clausius-Planck relation (2.64) yields

$$\Theta \, \dot{N} = \mathcal{D}_{\mathrm{int}} - \mathrm{DIV} \boldsymbol{\mathcal{Q}} + \rho_0 \, R_\Theta \, . \tag{2.73}$$

Since the entropy is a function of $\{\mathbf{F}, \Theta, \boldsymbol{\alpha}\}$, its corresponding rate yields

$$\dot{N} = - \frac{\partial^2 \Psi}{\partial \Theta \partial \mathbf{F}} : \dot{\mathbf{F}} - \frac{\partial^2 \Psi}{\partial \Theta \partial \boldsymbol{\alpha}} \circ \dot{\boldsymbol{\alpha}} - \frac{\partial^2 \Psi}{\partial \Theta^2} \, \dot{\Theta} \, . \tag{2.74}$$

The multiplication of this rate with the temperature defines the heat capacity $c = -\Theta \, \partial_{\Theta\Theta} \Psi > 0$ and the structural heating

$$\mathcal{A} = \Theta \, \partial_\Theta \left\{ \mathbf{P} : \dot{\mathbf{F}} + \mathbf{Q} \circ \dot{\boldsymbol{\alpha}} \right\} \, . \tag{2.75}$$

In contrast to the purely elastic structural heating in Eq. (2.49), the structural heating in Eq. (2.75) consists of elastic and plastic contributions. The self-heating is determined by

$$\mathcal{H}_\Theta = \mathcal{A} + \mathcal{D}_\text{int} = \Theta \, \partial_\Theta \left\{ \mathbf{P} : \dot{\mathbf{F}} + \mathbf{Q} \circ \dot{\boldsymbol{\alpha}} \right\} + \mathcal{D}_\text{int} \, . \tag{2.76}$$

Accordingly, the local temperature equation yields

$$\dot{\Theta} = \frac{1}{c} \left[\mathcal{H}_\Theta - \mathrm{DIV} \boldsymbol{\mathcal{Q}} + \rho_0 \, R_\Theta \right] \, . \tag{2.77}$$

Since for metals the influence of the structural heating is comparably small, the temperature approximation

$$\dot{\Theta} \approx \frac{1}{c} \left[\mathcal{D}_\text{int} - \mathrm{DIV} \boldsymbol{\mathcal{Q}} + \rho_0 \, R_\Theta \right] \tag{2.78}$$

can be assumed, see Hodowany et al. [54]. Furthermore, if adiabatic heat conditions are assumed, the temperature evolution depends solely on the dissipation. Thus, the prediction of the internal dissipation is of utmost importance for a realistic temperature prediction during plastic deformations, see Chapter 3.

2.6 Incremental variational updates

The subsequent section deals with the constitutive modelling in the context of variational principles. It is well-known that variational principles play an important role in mechanics, e.g. for stability analyses. Variational formulations contain the intrinsic characteristic that all "information" of a system is included in one potential. This information includes balance laws, evolution equations of internal variables and Neumann boundary conditions. The stationarity point of the potential corresponds to the underlying Euler-Lagrange equations. Consequently, all unknowns follow jointly from minimisation/stationarity of the potential. Apart from the alternative derivation of balance equations, variational formulations provide a basis for mesh adaptivity in finite elements (e.g. Mosler and Ortiz [91]), for homogenisation theory (e.g. Miehe et al. [83]) and for the analysis of evolving microstructures (e.g. Bartels et al. [13]). The existence of solutions is also linked to the existence of a variational potential, which is an interesting aspect from a mathematical point of view. Due to its canonical structure, variational formulations inherit a natural symmetry. This symmetry becomes beneficial when Newton-type solution schemes are applied. Hence, symmetric solvers can be applied which requires less data storage. Within this section the framework of Ortiz and Stainier [99] is applied, in which a rate dependent potential is transferred into an *incremental variational potential.* Since the focus is on material modelling, the following subsections are restricted to the quasi-static case.

2.6.1 Hyperelasticity

Variational principles have gained a huge popularity in the context of the finite element method. Especially in the case of hyperelastic materials variational principles are widely used. The cornerstone of a variational principle is that the equilibrium point corresponds to the minimum of the underlying potential energy. In contrast to classic literature on the minimum of potential energy, a rate form is considered here. The reason for this unusual choice is the coupling to additional phenomena such as temperature and phase field in the following sections and chapters. Accordingly, the rate potential of the hyperelastic problem is defined as

$$\dot{\mathcal{I}} = \int\limits_{\mathcal{B}_0} \dot{\Psi}(\mathbf{F})\mathrm{d}V - \mathcal{P}_{\mathbf{F}}(\dot{\boldsymbol{\varphi}})\,. \tag{2.79}$$

Assuming deformation independent loads for body force $\rho_0\,\mathbf{B}$ and the prescribed tractions $\bar{\mathbf{T}}$, the external power is linearly dependent on the deformation rate $\dot{\boldsymbol{\varphi}}$, i.e.

$$\mathcal{P}_{\mathbf{F}} = \int\limits_{\mathcal{B}_0} \rho_0 \mathbf{B}\cdot\dot{\boldsymbol{\varphi}}\,\mathrm{d}V + \int\limits_{\partial\mathcal{B}_0} \bar{\mathbf{T}}\cdot\dot{\boldsymbol{\varphi}}\,\mathrm{d}A\,. \tag{2.80}$$

A state of equilibrium is found for the stationary point $\delta\dot{\mathcal{I}} = 0$. A straightforward calculation yields

$$\begin{aligned}\delta_{\dot{\varphi}}\mathcal{I} &= \int\limits_{\mathcal{B}_0} \frac{\partial\Psi}{\partial\mathbf{F}} : \delta\dot{\mathbf{F}}\,\mathrm{d}V - \int\limits_{\mathcal{B}_0} \rho_0\mathbf{B}\cdot\delta\dot{\boldsymbol{\varphi}}\,\mathrm{d}V - \int\limits_{\partial\mathcal{B}_0} \bar{\mathbf{T}}\cdot\delta\dot{\boldsymbol{\varphi}}\,\mathrm{d}A \\ &= -\int\limits_{\mathcal{B}_0} \left\{\mathrm{DIV}\left(\frac{\partial\Psi}{\partial\mathbf{F}}\right) + \rho_0\,\mathbf{B}\right\}\cdot\delta\dot{\boldsymbol{\varphi}}\,\mathrm{d}V + \int\limits_{\partial\mathcal{B}_0} \left\{\frac{\partial\Psi}{\partial\mathbf{F}}\cdot\mathbf{N} - \bar{\mathbf{T}}\right\}\cdot\delta\dot{\boldsymbol{\varphi}}\,\mathrm{d}A = 0\,.\end{aligned} \tag{2.81}$$

The virtual displacement field, also known as test function, is denoted as $\delta\boldsymbol{\varphi}$ while the virtual deformations are denoted as $\delta\mathbf{F} = \mathrm{GRAD}\delta\boldsymbol{\varphi}$. Clearly, in Eq. (2.81) use is made of partial integration and the Gauss divergence theorem. If arbitrary deformation rates $\delta\dot{\boldsymbol{\varphi}}$ are considered and if the constitutive relation $\mathbf{P} = \partial_{\mathbf{F}}\Psi$ is substituted, Eq. (2.81) is equivalent to the principle of virtual work. Consequently, the local balance of linear momentum (2.16) and the Neumann boundary condition (2.32)

$$\begin{aligned}\mathrm{DIV}\mathbf{P} + \rho_0\,\mathbf{B} &= \mathbf{0} \quad \text{on} \quad \mathcal{B}_0\,, \\ \mathbf{P}\cdot\mathbf{N} &= \bar{\mathbf{T}} \quad \text{on} \quad \partial\mathcal{B}_{0,\mathbf{T}}\,,\end{aligned} \tag{2.82}$$

are obtained. Since functional (2.79) is linearly dependent on the deformation rate, it does not strictly represent a minimisation principle. A minimisation principle can be achieved if the time-continuous potential (2.79) is written into a time-discrete potential. Following Ortiz and Stainier [99] an incremental variational potential is derived by integrating over the time interval $\tau = [t_n, t_{n+1}]$ leading to

$$\Delta\mathcal{I} = \int_{\tau} \dot{\mathcal{I}}\,\mathrm{d}t = \int_{\mathcal{B}_0} \{\Psi_{n+1}(\mathbf{F}_{n+1}) - \Psi_n(\mathbf{F}_n)\}\ \mathrm{d}V - \mathcal{P}_{\mathbf{F}}(\boldsymbol{\varphi}_{n+1}) + \mathcal{P}_{\mathbf{F}}(\boldsymbol{\varphi}_n)\,. \tag{2.83}$$

Index $n+1$ denotes all configurations at time t_{n+1} and the index n denotes all known configurations at time t_n. Finally, the unknown deformation map $\boldsymbol{\varphi}_{n+1}$ follows from the minimisation

$$\boldsymbol{\varphi}_{n+1} = \arg \inf_{\boldsymbol{\varphi}_{n+1}} \Delta\mathcal{I}\,. \tag{2.84}$$

2.6.2 Thermoelasticity

Next, the thermoelastic material model proposed in Subsection 2.5.2 is presented in a variational structure. The variational treatment of thermoelastic problems goes back to the pioneering works of Biot [18]. The demands on a variational description of a thermoelastic material are that the underlying stationarity conditions with respect to the deformation and the temperature correspond to the balance of linear momentum and the energy balance. In order to guarantee a variationally consistent formulation an enhanced Hu-Washizu-type potential is proposed where equilibrium temperature and external temperature are distinguished.

Following Yang et al. [139], the starting point is the definition of the mixed potential

$$\dot{\mathcal{I}} = \int_{\mathcal{B}_0} \Big\{\dot{E}(\mathbf{F}, N) - \Theta\,\dot{N} - \chi(\Theta, \mathrm{GRAD}\Theta)\Big\}\,\mathrm{d}V - \mathcal{P}_{\mathbf{F}}(\dot{\boldsymbol{\varphi}}) - \mathcal{P}_T(\Theta)\,, \tag{2.85}$$

in which both, the external temperature Θ and the thermodynamically conjugated entropy N appear. Furthermore, potential (2.85) depends on the deformation field $\boldsymbol{\varphi}$ and on the rates $\dot{\boldsymbol{\varphi}}$ and $\dot{N}$. Since the constitutive model is usually defined in terms of Helmholtz energy Ψ, the internal energy E is obtained by means of Legendre transformation (2.42). Thermal conduction is captured by means of the convex potential χ, where the choice of constitutive assumptions is restricted to the Fourier-type conductivity in Eq. (2.55). The externally applied thermal forces, i.e. the prescribed heat fluxes $\bar{\mathcal{Q}}$ and the heat source $\rho_0\,R_\Theta$, are summarised in the external potential (cf. Eq. (2.19))

$$\mathcal{P}_T(\Theta) = \int_{\partial\mathcal{B}_0} \bar{\mathcal{Q}}\,\ln\left(\frac{\Theta}{\Theta_0}\right)\mathrm{d}A - \int_{\mathcal{B}_0} \rho_0\,R_\Theta\,\ln\left(\frac{\Theta}{\Theta_0}\right)\mathrm{d}V\,. \tag{2.86}$$

The canonical structure of potential (2.85) is elaborated next. For this reason, the stationarity condition $\delta\dot{\mathcal{I}} = 0$ is evaluated. For the variation with respect to the deformation rate, the weak formulation (cf. Eq. (2.81))

$$\begin{aligned} \delta_{\dot{\boldsymbol{\varphi}}}\dot{\mathcal{I}} &= \int\limits_{\mathcal{B}_0} \frac{\partial E}{\partial \mathbf{F}} : \delta\dot{\mathbf{F}}\,\mathrm{d}V - \int\limits_{\mathcal{B}_0} \rho_0 \mathbf{B}\cdot\delta\dot{\boldsymbol{\varphi}}\,\mathrm{d}V - \int\limits_{\partial\mathcal{B}_0} \bar{\mathbf{T}}\cdot\delta\dot{\boldsymbol{\varphi}}\,\mathrm{d}A \\ &= -\int\limits_{\mathcal{B}_0} \left\{ \mathrm{DIV}\left(\frac{\partial E}{\partial \mathbf{F}}\right) + \rho_0\,\mathbf{B} \right\} \cdot \delta\dot{\boldsymbol{\varphi}}\,\mathrm{d}V + \int\limits_{\partial\mathcal{B}_0} \left\{ \frac{\partial E}{\partial \mathbf{F}}\cdot\mathbf{N} - \bar{\mathbf{T}} \right\}\cdot\delta\dot{\boldsymbol{\varphi}}\,\mathrm{d}A = 0 \end{aligned} \tag{2.87}$$

is obtained. By inserting the Piola stress tensor $(2.44)_1$ into Eq. (2.87), the stationarity condition corresponds to the balance of linear momentum and Neumann boundary condition (cf. Eq. (2.82)).

As mentioned before, the proposed potential is based on a distinction of external temperatures and equilibrium temperatures. The equivalence of these quantities is obtained by the variation

$$\delta_{\dot{N}}\dot{\mathcal{I}} = \int\limits_{\mathcal{B}_0} \left\{ \frac{\partial E}{\partial N} - \Theta \right\} \delta\dot{N}\,\mathrm{d}V = 0 \quad \Leftrightarrow \quad \frac{\partial E}{\partial N} - \Theta = 0\,, \tag{2.88}$$

where $\partial_N E$ is denoted as equilibrium temperature. At equilibrium, Eq. (2.88) confirms the constitutive relation $(2.44)_2$.

Furthermore, the variation with respect to the temperature leads to

$$\delta_\Theta\dot{\mathcal{I}} = \int\limits_{\mathcal{B}_0} \left\{ -\dot{N}\,\delta\Theta - \frac{\partial\chi}{\partial\mathbf{G}}\cdot\delta\mathbf{G} + \frac{\rho_0 R_\Theta}{\Theta}\,\delta\Theta \right\} \mathrm{d}V - \int\limits_{\partial\mathcal{B}_0} \frac{\bar{\mathcal{Q}}}{\Theta}\,\delta\Theta\,\mathrm{d}A = 0\,. \tag{2.89}$$

By using the relation $\mathbf{G} = -\mathrm{GRAD}\Theta/\Theta$, chain rule

$$\partial_{\mathbf{G}}\chi\cdot\delta\mathbf{G} = -\mathrm{DIV}\left(\frac{\partial_{\mathbf{G}}\chi}{\Theta}\,\delta\Theta\right) + \frac{\mathrm{DIV}\left(\partial_{\mathbf{G}}\chi\right)}{\Theta}\,\delta\Theta \tag{2.90}$$

and the divergence theorem, the variation (2.89) is re-written into

$$\begin{aligned} \delta_\Theta\dot{\mathcal{I}} = &\int\limits_{\mathcal{B}_0} \left\{ -\dot{N} - \frac{\mathrm{DIV}\left(\partial_{\mathbf{G}}\chi\right)}{\Theta} + \frac{\rho_0 R_\Theta}{\Theta} \right\} \delta\Theta\,\mathrm{d}V \\ &+ \int\limits_{\partial\mathcal{B}_0} \left\{ \frac{\partial_{\mathbf{G}}\chi\cdot\mathbf{N}}{\Theta} - \frac{\bar{\mathcal{Q}}}{\Theta} \right\} \delta\Theta\,\mathrm{d}A = 0\,. \end{aligned} \tag{2.91}$$

For arbitrary virtual temperatures $\delta\Theta$, the brace expressions in (2.91) vanish. If the constitutive heat flux according to Eq. (2.56) is used, the resulting local balance equation and Neumann boundary conditions are

$$\begin{aligned} -\dot{N} - \frac{\mathrm{DIV}\boldsymbol{\mathcal{Q}}}{\Theta} + \frac{\rho_0 R_\Theta}{\Theta} &= 0 \quad \text{on} \quad \mathcal{B}_0\,, \\ \boldsymbol{\mathcal{Q}} \cdot \mathbf{N} &= \bar{\mathcal{Q}} \quad \text{on} \quad \partial\mathcal{B}_{0,\mathcal{Q}}\,. \end{aligned} \tag{2.92}$$

Evidently, the stationarity condition $(2.92)_1$ is equivalent to the temperature equation (2.47). Thus, it can be stated, that the Euler-Lagrange equations of rate potential (2.85) are equivalent to the balance of linear momentum and the energy balance.

Next, the proposed rate potential (2.85) is transferred into a time-discrete minimisation problem. Furthermore, the underlying three-field formulation can efficiently be reduced to a two-field formulation by condensation of the balance equation (2.88). For that purpose, the rate potential (2.85) is integrated in the time interval $\tau = [t_n, t_{n+1}]$. This results the time-discrete potential

$$\Delta\mathcal{I} = \int\limits_{\tau} \dot{\mathcal{I}}\,\mathrm{d}t = \int\limits_{\mathcal{B}_0} \Delta\mathcal{E}\,\mathrm{d}V - \mathcal{P}_{\mathbf{F}}(\boldsymbol{\varphi}_{n+1}) + \mathcal{P}_{\mathbf{F}}(\boldsymbol{\varphi}_n) - \Delta t\,\mathcal{P}_T(\Theta_{n+1})\,, \tag{2.93}$$

in which the time increment is denoted as $\Delta t = t_{n+1} - t_n$ and the incremental potential $\Delta\mathcal{E}$ is determined as

$$\begin{aligned} \Delta\mathcal{E} = {} & E_{n+1}(\mathbf{F}_{n+1}, N_{n+1}) - E_n(\mathbf{F}_n, N_n) - \Theta_{n+1}\,[N_{n+1} - N_n] \\ & - \Delta t\,\chi(\Theta_{n+1}, \mathrm{GRAD}\Theta_{n+1})\,. \end{aligned} \tag{2.94}$$

Since the entropy (N_{n+1}, N_n) is locally defined in all material points, the incremental potential can be reduced by the minimisation

$$\Delta\mathcal{E}_{\mathrm{red}} = \inf_{N_{n+1}} \Delta\mathcal{E}\,. \tag{2.95}$$

Based on this reduced potential, the update of the deformation map and the temperature follow jointly from the saddle-point problem

$$(\boldsymbol{\varphi}_{n+1}, \Theta_{n+1}) = \arg \inf_{\boldsymbol{\varphi}_{n+1}} \sup_{\Theta_{n+1}} \Delta\mathcal{I}_{\mathrm{red}}\,. \tag{2.96}$$

2.6.3 Thermo-elastoplasticity

The extension of a thermoelastic variational principle to a thermomechanically coupled variational formulation for dissipative materials is not straightforward. The variational formulation for a class of dissipative materials goes back to the works of Hackl [51], Ortiz and Stainier [99]. However, the cited works are restricted to the isothermal case.

Although the mechanical and the thermal problem show independently a variational structure (see Simo and Miehe [121]), the thermomechanically coupled system of equations shows no symmetry and therefore no variational structure at first glance. In fact, a straightforward derivation of associated Hessian matrix shows an unsymmetric structure, i.e., the coupled problem does not show a variational structure. A symmetrisation of the thermomechanically coupled dissipative materials is investigated in Yang [138] and Yang et al. [139]. Without going into too much detail, the cornerstones of the respective model are the previously presented Hu-Washizu-type enhanced variational principle and a suitable integrating factor. Based on these ideas, an incremental potential is derived which defines every aspect of the coupled problem, i.e., all unknown state variables follow jointly and canonically from the stationarity of the potential. The following theory is in line with Yang et al. [139], Stainier and Ortiz [123] and Canadija and Mosler [25].

Starting point of the variational formulation is the extension of the thermoelastic potential given in Eq. (2.85). Based on this formulation, the thermomechanically coupled potential for dissipative materials reads

$$\dot{\mathcal{I}} = \int\limits_{\mathcal{B}_0} \dot{\mathcal{E}}(\mathbf{F}, \mathbf{F}^{\mathrm{p}}, \boldsymbol{\alpha}, N, \Theta, \mathrm{GRAD}\Theta)\, \mathrm{d}V - \mathcal{P}_{\mathbf{F}}(\dot{\boldsymbol{\varphi}}) - \mathcal{P}_T(\Theta) \tag{2.97}$$

with

$$\dot{\mathcal{E}} = \dot{E}(\mathbf{F}, \mathbf{F}^{\mathrm{p}}, \boldsymbol{\alpha}, N) - \Theta\, \dot{N} + f\, \zeta(\dot{\mathbf{F}}^{\mathrm{p}}, \dot{\boldsymbol{\alpha}}) - \chi(\Theta, \mathrm{GRAD}\Theta)\,. \tag{2.98}$$

The internal energy E may also be a function of a generalised set of internal variables $\boldsymbol{\alpha}$ (together with $\mathbf{F}^{\mathrm{p}}$) as proposed in Sec 2.5.3. Furthermore, the dissipation potential ζ can depend on the temperature and on the rates of internal variables. For the sake of simplicity, it depends only on $\{\dot{\mathbf{F}}^{\mathrm{p}}, \dot{\boldsymbol{\alpha}}\}$. In the case of a rate independent material, the dissipation potential ζ is equivalent to a positively homogeneous dissipation $\mathcal{D}_{\mathrm{int}}$ of degree one with respect to stress-like internal variables. Note, that not all dissipative materials are covered by a potential formulation, see also Remark 2.6.1.

Following Yang et al. [139], the integration factor f is chosen as

$$f = \frac{\Theta}{\partial_N E}\,. \tag{2.99}$$

For an equilibrium state $f = 1$, the absolute temperature Θ equals the equilibrium temperature $\partial_N E$. Therefore, the integration factor is strongly related to the proposed Hu-Washizu principle. For dissipative material models, the concept of external and equilibrium temperature is in line with the stability of thermomechanically coupled processes presented in Petryk [103, 104].

The effect of the integration factor becomes evident if one computes the stationary conditions of rate potential (2.97). For the sake of conciseness, the variation with respect to the deformation rate is neglected here (cf. Eq. (2.87)).

Likewise to the purely thermoelastic problem, the variation with respect to entropy rate yields

$$\delta_{\dot{N}}\dot{\mathcal{I}} = \int\limits_{\mathcal{B}_0} \left\{ \frac{\partial E}{\partial N} - \Theta \right\} \delta\dot{N}\,\mathrm{d}V = 0 \quad \Leftrightarrow \quad \frac{\partial E}{\partial N} - \Theta = 0\,, \tag{2.100}$$

which confirms the equilibrium statement of the integration factor f. The importance of integration factor f becomes evident for the stationary condition

$$\delta_{\Theta}\dot{\mathcal{I}} = \int\limits_{\mathcal{B}_0} \left\{ -\dot{N}\,\delta\Theta + \frac{\delta\Theta}{\partial_N E}\,\zeta - \frac{\partial\chi}{\partial\mathbf{G}} \cdot \delta\mathbf{G} + \frac{\rho_0 R_\Theta}{\Theta}\,\delta\Theta \right\} \mathrm{d}V - \int\limits_{\partial\mathcal{B}_0} \frac{\bar{\mathcal{Q}}}{\Theta}\,\delta\Theta\,\mathrm{d}A = 0\,. \tag{2.101}$$

Using chain rule in Eq. (2.90) and Gauss divergence theorem, the weak form

$$\begin{aligned} \delta_{\Theta}\dot{\mathcal{I}} = &\int\limits_{\mathcal{B}_0} \left\{ -\dot{N} + \frac{\zeta}{\partial_N E} - \frac{\mathrm{DIV}\,(\partial_{\mathbf{G}}\chi)}{\Theta} + \frac{\rho_0 R_\Theta}{\Theta} \right\} \delta\Theta\,\mathrm{d}V \\ &+ \int\limits_{\partial\mathcal{B}_0} \left\{ \frac{\partial_{\mathbf{G}}\chi \cdot \mathbf{N}}{\Theta} - \frac{\bar{\mathcal{Q}}}{\Theta} \right\} \delta\Theta\,\mathrm{d}A = 0 \end{aligned} \tag{2.102}$$

is derived. This equation is equivalent to the local temperature equation and Neumann boundary condition

$$\begin{aligned} -\dot{N} + \frac{\zeta}{\partial_N E} - \frac{\mathrm{DIV}\boldsymbol{\mathcal{Q}}}{\Theta} + \frac{\rho_0 R_\Theta}{\Theta} &= 0 \quad \text{on} \quad \mathcal{B}_0\,, \\ \boldsymbol{\mathcal{Q}} \cdot \mathbf{N} &= \bar{\mathcal{Q}} \quad \text{on} \quad \partial\mathcal{B}_{0,\mathcal{Q}}\,. \end{aligned} \tag{2.103}$$

Herein, the heat flux $\boldsymbol{\mathcal{Q}} = \partial_{\mathbf{G}}\chi$ (see Eq. (2.56)) is applied again. For $\zeta = \mathcal{D}_{\mathrm{int}}$, and if equilibrium condition (2.100) is inserted, the temperature equation $(2.103)_1$ is equivalent to Eq. (2.73). Thus, integration factor f is crucially important for the variational structure of dissipative materials.

Furthermore, and without further derivation, the variations with respect to the inelastic deformations $\{\dot{\mathbf{F}}^{\mathrm{p}}, \dot{\boldsymbol{\alpha}}\}$ yield

$$\begin{aligned} \delta_{\dot{\mathbf{F}}^{\mathrm{p}}}\dot{\mathcal{I}} = 0 \qquad &\Leftrightarrow \qquad \boldsymbol{\Sigma} = \mathbf{F}^{\mathrm{eT}} \cdot \frac{\partial E}{\partial \mathbf{F}^{\mathrm{e}}}\,, \\ \delta_{\dot{\boldsymbol{\alpha}}}\dot{\mathcal{I}} = 0 \qquad &\Leftrightarrow \qquad \mathbf{Q} = -\frac{\partial E}{\partial \boldsymbol{\alpha}}\,. \end{aligned} \tag{2.104}$$

Within the framework of incremental variational updates all unknowns are determined by minimisation or maximisation of a time-discretised potential. To this end, the rate potential (2.97) is integrated in time (cf. Eq. (2.93)), such that

$$\begin{aligned}\Delta\mathcal{E} = {} & E_{n+1}(\mathbf{F}_{n+1}, \mathbf{F}^{\mathrm{p}}_{n+1}, \boldsymbol{\alpha}_{n+1}, N_{n+1}) - E_n(\mathbf{F}_n, \mathbf{F}^{\mathrm{p}}_n, \boldsymbol{\alpha}_n, N_n) - \Theta_{n+1}\,[N_{n+1} - N_n] \\ & + \frac{\Theta_{n+1}}{\partial_N E(\mathbf{F}_{n+1}, \mathbf{F}^{\mathrm{p}}_{n+1}, \boldsymbol{\alpha}_{n+1}, N_{n+1})}\,\Delta\zeta(\mathbf{F}^{\mathrm{p}}_{n+1}, \boldsymbol{\alpha}_{n+1}) - \Delta t\,\chi(\Theta_{n+1}, \mathrm{GRAD}\Theta_{n+1})\end{aligned} \tag{2.105}$$

is obtained, where $\Delta\zeta$ denotes the integrated dissipation potential and where Δt denotes the time increment. Since $\mathbf{F}^{\mathrm{p}}_{n+1}, \boldsymbol{\alpha}_{n+1}$ and N_{n+1} are gradient-free, $\Delta\mathcal{E}$ is locally reduced by the minimisation

$$\Delta\mathcal{E}_{\mathrm{red}} = \inf_{\mathbf{F}^{\mathrm{p}}_{n+1}, \boldsymbol{\alpha}_{n+1}, N_{n+1}} \Delta\mathcal{E}\,, \tag{2.106}$$

in which the updated unknowns are the minimiser of the potential.

It should be emphasised that the chosen parametrisation cannot be utilised without further restrictions. Depending on the chosen material model, $\mathbf{F}^{\mathrm{p}}_{n+1}$ and $\boldsymbol{\alpha}_{n+1}$ are linearly dependent on one another, leading to a singular Hessian matrix. Furthermore, the plastic constraint $\det\mathbf{F}^{\mathrm{p}}_{n+1} > 0$ is variationally not enforced. Hence, in order to obtain a numerically unconstrained minimisation principle, an admissible parametrisation of the internal variables is required. This problem is pertained in Section 3 and is also addressed in Mosler and Bruhns [90] and Bleier and Mosler [20].

For a reduced potential (2.106) the global field variables, i.e. the deformation and the temperature, follow jointly from the saddle-point problem (cf. Eq. (2.96))

$$(\boldsymbol{\varphi}_{n+1}, \Theta_{n+1}) = \arg \inf_{\boldsymbol{\varphi}_{n+1}} \sup_{\Theta_{n+1}} \Delta\mathcal{I}_{\mathrm{red}} \tag{2.107}$$

based on

$$\Delta\mathcal{I}_{\mathrm{red}} = \int_{\mathcal{B}_0} \Delta\mathcal{E}_{\mathrm{red}}\,\mathrm{d}V - \mathcal{P}_{\mathbf{F}}(\boldsymbol{\varphi}_{n+1}) + \mathcal{P}_{\mathbf{F}}(\boldsymbol{\varphi}_n) - \Delta t\,\mathcal{P}_T(\Theta_{n+1})\,. \tag{2.108}$$

Remark 2.6.1: *A variational structure is not obvious for all class of dissipative material models. A class of material models which shows a variational structure is presented in Ortiz and Stainier [99] and Mosler and Bruhns [90]. Those materials belong to the so-called standard dissipative materials (Lubliner [79] p.129), where the flow rule and hardening law are often associated. Even for non-associative kinematic hardening a variational principle can be found as presented in Mosler [89]. However, generally non-associative or anisotropic hardening cannot be symmetrised such that a variational structure is obtained, e.g. distortional hardening models as derived in Chapter 4.*

3 Thermomechanical coupling in dissipative materials

One of the main objective of this thesis is to capture the dominating effects driving the macroscopic scale. As mentioned before, the macroscale is essentially influenced by the deformation and the temperature, where special attention lies on the thermomechanical coupling, known as self-heating effect. A more detailed discussion regarding the thermomechanical coupling in dissipative materials is given in this chapter.

The modelling of thermomechanics seems to be straightforward and fully understood at a first glance: Once the Helmholtz energy and suitable evolution equations fulfilling the second law of thermodynamics are defined, the coupling is provided by the first law of thermodynamics. However, the temperature predicted from such a straightforward viewpoint is usually too high, cf. Chaboche [28, 29], Hodowany et al. [54], Nemat-Nasser and Kapoor [94], Rosakis et al. [109]. For this reason, the so-called *Taylor-Quinney factor* is frequently applied, see Taylor and Quinney [130]. Essentially, this factor reduces the part of the dissipation which converts to heat. Several experiments and numerical simulations such as Simo and Miehe [121] show that the Taylor-Quinney factor often gives sufficiently accurate temperature predictions. The disadvantage of this ad-hoc approach is that the first law of thermodynamics is not considered at all. To be more precise, it is completely unclear where the other part of the dissipation remains, which is not converted to heat. That can lead to a violation of the second law of thermodynamics, e.g., in the case of kinematic hardening. In summary, thermodynamically sound models which predict the temperature increase realistically as a result of plastic deformation are still rare. First ideas towards such models can be found in Ristinmaa et al. [108], Rosakis et al. [109]. The ideas proposed in the cited papers will be discussed in detail later.

Having briefly discussed the fundamentals of thermomechanically coupled plasticity theory in Subsection 2.5.3, the dominating factor leading to an over-prediction of the temperature is identified: the internal dissipation. A more detailed discussion on the internal dissipation is given in Section 3.1. Adopting an energetical point of view, the definition of the internal dissipation is equivalent to the decomposition of the total energy into dissipative and stored parts. That leads to the crucial question whether a certain phenomenon is energetic (Helmholtz or internal energy) or dissipative in nature.

Based on this question, all hardening models are partitioned accordingly. Interestingly, this partition shows strong analogies to the Taylor-Quinney approach. Due to the importance of the energy within the advocated viewpoint, incremental energy minimisation seems to be the natural framework for the thermomechanically coupled problem. Such a variational setting is introduced in Section 3.2. The predictive capabilities of the final model are demonstrated in Section 3.3.

3.1 Analysis of internal dissipation

This section deals with the analysis of the internal dissipation and the resulting local temperature prediction.

3.1.1 Isothermal plasticity theory

For the isothermal case, the set of internal variables is defined according to $\boldsymbol{\alpha} = \{\mathbf{F}^{\mathrm{p}}, \boldsymbol{\alpha}^{\mathrm{k}}, \alpha^{\mathrm{i}}\}$ where $\boldsymbol{\alpha}^{\mathrm{k}}$ and α^{i} denote strain-like variables which account for kinematic and isotropic hardening. A frequently made assumption for such plasticity models (cf. Section 2.5.3) is a Helmholtz energy of the type

$$\Psi = \Psi^{\mathrm{el}}(\mathbf{F}, \mathbf{F}^{\mathrm{p}}) + \Psi^{\mathrm{pl}}(\boldsymbol{\alpha}^{\mathrm{k}}, \alpha^{\mathrm{i}})\,. \tag{3.1}$$

In addition to the Mandel stresses $\boldsymbol{\Sigma} = [\mathbf{F}^{\mathrm{e}}]^{\mathrm{T}} \cdot \partial_{\mathbf{F}^{\mathrm{e}}} \Psi$ which define the thermodynamically conjugated forces with respect to the velocity gradient $\mathbf{L}^{\mathrm{p}}$, one introduces

$$\mathbf{Q}^{\mathrm{k}} = -\partial_{\boldsymbol{\alpha}^{\mathrm{k}}} \Psi = -\partial_{\boldsymbol{\alpha}^{\mathrm{k}}} \Psi^{\mathrm{pl}} \qquad , \qquad Q^{\mathrm{i}} = -\partial_{\alpha^{\mathrm{i}}} \Psi = -\partial_{\alpha^{\mathrm{i}}} \Psi^{\mathrm{pl}} \tag{3.2}$$

as stress-like quantities conjugated to $\boldsymbol{\alpha}^{\mathrm{k}}$ and α^{i}. Note, that the definition of Ψ^{pl} as contribution to the total energy renders hardening effects as purely energetic. With this assumption and the introduced notations, the internal dissipation is now given by

$$\mathcal{D}_{\mathrm{int}} = \boldsymbol{\Sigma} : \mathbf{L}^{\mathrm{p}} + \mathbf{Q}^{\mathrm{k}} : \dot{\boldsymbol{\alpha}}^{\mathrm{k}} + Q^{\mathrm{i}}\, \dot{\alpha}^{\mathrm{i}} \geq 0\,. \tag{3.3}$$

For the sake of simplicity, the theory will be restricted to rate-independent processes. In this setting, the constitutive behaviour is conveniently defined by a suitable *yield function* $\phi = \widehat{\phi}(\boldsymbol{\Sigma}, \mathbf{Q}^{\mathrm{k}}, Q^{\mathrm{i}})$. The family of material models discussed here is based on the following assumptions:

- ϕ is convex in $(\boldsymbol{\Sigma} - \mathbf{Q}^{\mathrm{k}}, Q^{\mathrm{i}})$ and exhibits the form

  $$\phi = \Sigma^{\mathrm{eq}}(\boldsymbol{\Sigma} - \mathbf{Q}^{\mathrm{k}}) - Q^{\mathrm{i}} - y_0\,, \tag{3.4}$$

  where y_0 reflects the *initial yield limit.*

- The equivalent stress measure Σ^{eq} is a positively homogeneous function of degree one, i.e. in particular

  $$\left[\boldsymbol{\Sigma} - \mathbf{Q}^{\text{k}}\right] : \partial_{[\boldsymbol{\Sigma}-\mathbf{Q}^{\text{k}}]}\Sigma^{\text{eq}} = \Sigma^{\text{eq}} \,. \tag{3.5}$$

  Since $\partial_{[\boldsymbol{\Sigma}-\mathbf{Q}^{\text{k}}]}\Sigma^{\text{eq}} = \partial_{\boldsymbol{\Sigma}}\Sigma^{\text{eq}}$ holds, this is equivalent to

  $$\left[\boldsymbol{\Sigma} - \mathbf{Q}^{\text{k}}\right] : \partial_{\boldsymbol{\Sigma}}\Sigma^{\text{eq}} = \Sigma^{\text{eq}} \,. \tag{3.6}$$

The evolution of the introduced internal variables is governed by evolution equations. Those can for example be derived via the postulate of maximum dissipation as introduced in Section 2.70. The evaluation yields

$$\mathbf{L}^{\text{p}} = \lambda\,\partial_{\boldsymbol{\Sigma}}\phi = \lambda\,\partial_{\boldsymbol{\Sigma}}\Sigma^{\text{eq}} \,, \tag{3.7}$$

$$\dot{\boldsymbol{\alpha}}^{\text{k}} = \lambda\,\partial_{\mathbf{Q}^{\text{k}}}\phi = \lambda\,\partial_{\mathbf{Q}^{\text{k}}}\Sigma^{\text{eq}} \,, \tag{3.8}$$

$$\dot{\alpha}^{\text{i}} = \lambda\,\partial_{Q^{\text{i}}}\phi = -\lambda \,, \tag{3.9}$$

with λ as plastic multiplier. The solution of these equations is subjected to the fulfilment of the loading-unloading conditions (2.71). Inserting (3.7), (3.8), (3.9) into Ineq. (3.3) and additionally taking into account the identity $\partial_{\mathbf{Q}^{\text{k}}}\Sigma^{\text{eq}} = -\partial_{\boldsymbol{\Sigma}}\Sigma^{\text{eq}}$ and (3.6) results in

$$\mathcal{D}_{\text{int}} = \lambda\,\left[\Sigma^{\text{eq}} - Q^{\text{i}}\right] \,. \tag{3.10}$$

Since $\phi = 0$ has to hold for an inelastic equilibrium state (otherwise $\lambda = 0$), it finally follows that

$$\mathcal{D}_{\text{int}} = \lambda\, y_0 \tag{3.11}$$

according to Eq (3.4). From this equation it becomes apparent, that the initial yield stress y_0 plays a crucial role for predicting the temperature evolution. However, in this context, it has to be emphasised that the determination of this quantity from experiments is on the one hand subjected to specific uncertainties and can therefore usually not be performed with a satisfying accuracy. On the other hand, most constitutive models start from a “virgin” state of the material which is a rather unrealistic idealisation. In fact, one could assume that the initial state of the material under consideration is already a result of certain inelastic processes associated with hardening effects. These might have been occurred during the forming process of the considered workpiece. If it is assumed that such pre-hardening effects are “measured” by an initial accumulated equivalent plastic strain, i.e. $\alpha^{\text{i}}(t_0)$, this would give rise to an initially existing isotropic hardening quantity $Q^{\text{i}}_0 = Q^{\text{i}}(\alpha^{\text{i}}(t_0)) > 0$. As a consequence, the redefined yield limit $\widetilde{y}_0$ would then be given by

$$\widetilde{y}_0 = y_0 - Q^{\text{i}}_0 \,. \tag{3.12}$$

Following (3.11), one would obtain

$$\mathcal{D}_{\text{int}} = \lambda\, \widetilde{y}_0 = \lambda\, \left[y_0 - Q^{\text{i}}_0\right] < \lambda\, y_0 \tag{3.13}$$

for the dissipation rate density. Accordingly, the standard approach would lead to a greater dissipated power. To generalise this idea, one may also introduce a weighting factor $\beta^{\mathcal{D}} \in [0,1]$ such that

$$\mathcal{D}_{\text{int}} = \lambda\, \widetilde{y}_0 = \lambda\, \beta^{\mathcal{D}}\, y_0\,, \quad \widetilde{y}_0 = \beta^{\mathcal{D}}\, y_0\,. \tag{3.14}$$

By enforcing the first law of thermdynamics (energy equivalence), the energy contribution related to plastic hardening has to be enhanced in the case of Eq. (3.14) in terms of

$$\Psi^{\text{pl}}(\boldsymbol{\alpha}^{\text{k}}, \alpha^{\text{i}}) = \Psi^{\text{kin}}(\boldsymbol{\alpha}^{\text{k}}) + \Psi^{\text{iso}}(\alpha^{\text{i}}) - [1 - \beta^{\mathcal{D}}]\, \alpha^{\text{i}}\, y_0\,. \tag{3.15}$$

Here, Ψ^{kin} and Ψ^{iso} denote the energy contributions related to kinematic and isotropic hardening that will still evolve — and thus will result in hardening effects concerning the effective material response — whereas the term $[1 - \beta^{\mathcal{D}}]\, \alpha^{\text{i}}\, y_0$ reflects the offset energy due to pre-hardening. Note, that in this framework $\alpha^{\text{i}} < 0$ holds in general and hence the last term in (3.15) is always positive. From Eq. (3.15) one particularly obtains

$$Q^{\text{i}} = -\partial_{\alpha^{\text{i}}}\Psi = -\partial_{\alpha^{\text{i}}}\Psi^{\text{iso}} + [1 - \beta^{\mathcal{D}}]\, y_0\ , \tag{3.16}$$

which finally leads to

$$\widetilde{y}_0 + Q^{\text{i}} = y_0 - \partial_{\alpha^{\text{i}}}\Psi^{\text{iso}}\ . \tag{3.17}$$

The resulting yield function for the isothermal case is now given by

$$\phi = \Sigma^{\text{eq}}(\boldsymbol{\Sigma} - \mathbf{Q}^{\text{k}}) - Q^{\text{i}} - \widetilde{y}_0 = \Sigma^{\text{eq}}(\boldsymbol{\Sigma} + \partial_{\boldsymbol{\alpha}^{\text{k}}}\Psi^{\text{kin}}) - y_0 + \partial_{\alpha^{\text{i}}}\Psi^{\text{iso}}\ , \tag{3.18}$$

which is independent of $\beta^{\mathcal{D}}$. Thus, the introduction of the factor $\beta^{\mathcal{D}}$ has practically no effect within an isothermal setting (except for the dissipation). The significance of the factor $\beta^{\mathcal{D}}$ can only be verified by considering the thermomechanical coupling.

3.1.2 Thermomechanically coupled theory

3.1.2.1 A concise review of existing models

In a thermodynamically consistent setting, the first law of thermodynamics governs the temperature increase due to inelastic deformation. However, as illustrated in Figure 3.1, a straightforward application of this coupling usually leads to a significant overprediction of the temperature. According to the previous sections, such an overprediction is a

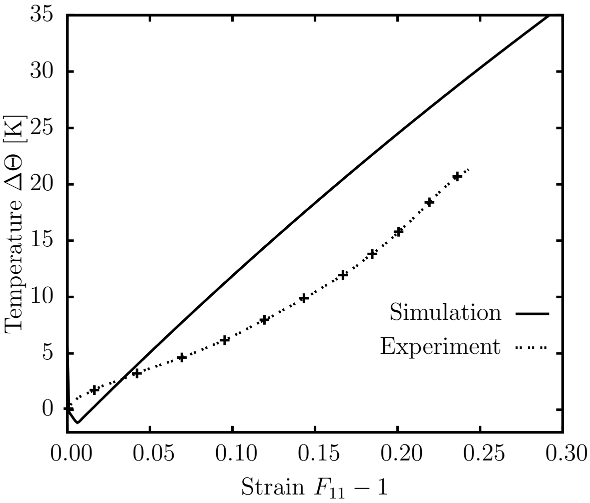

Figure 3.1: Temperature evolution for Al-2024 under uniaxial stretch. The experimental data was taken from Hodowany et al. [54]. The simulations are based on a standard plasticity model with exponential-saturation-type isotropic hardening, where the temperature increase during plastic deformations is clearly overestimated.

result of an overprediction of the internal dissipation. This observation suggests to simply decrease the internal dissipation. An idea in line with this thought was already proposed in the beginning of the last century. To be more precise, Taylor and Quinney [130] noticed in experiments that only a certain fraction of the plastic power

$$\dot{W}^{\mathrm{p}} = \boldsymbol{\Sigma} : \mathbf{L}^{\mathrm{p}} \tag{3.19}$$

is transformed into heat. For this reason, the Taylor-Quinney factor $\beta^{\mathrm{TQ}} \in [0,1]$ was introduced and only the part

$$\dot{\tilde{W}}^{\mathrm{p}} = \beta^{\mathrm{TQ}}\, \boldsymbol{\Sigma} : \mathbf{L}^{\mathrm{p}} \tag{3.20}$$

was assumed to be transformed into heat. Conceptually, this modification can be included into the framework discussed before by setting the internal dissipation identical to the reduced plastic power, i.e., by

$$\mathcal{D}_{\mathrm{int}} = \dot{\tilde{W}}^{\mathrm{p}} = \beta^{\mathrm{TQ}}\, \boldsymbol{\Sigma} : \mathbf{L}^{\mathrm{p}}\ . \tag{3.21}$$

Apparently, such a modification does neither guarantee that the first nor the second law of thermodynamics is fulfilled. However, assumption (3.21) is not necessarily thermodynamically inconsistent. To be more precise, a Taylor-Quinney factor complying with the restrictions imposed by thermodynamics can be derived by enforcing that Eq. (3.21) is identical to the real internal dissipation (3.3). This leads to the thermodynamically consistent Taylor-Quinney factor

$$\beta^{\mathrm{TQ}} = \frac{\mathcal{D}_{\mathrm{int}}}{\dot{W}^{\mathrm{p}}}, \tag{3.22}$$

In the case of the model defined by Eq. (3.3), this yields

$$\beta^{\mathrm{TQ}} = 1 + \frac{\mathbf{Q}^{\mathrm{k}} : \dot{\boldsymbol{\alpha}}^{\mathrm{k}} + Q^{\mathrm{i}}\,\dot{\alpha}^{\mathrm{i}}}{\boldsymbol{\Sigma} : \mathbf{L}^{\mathrm{p}}}\,. \tag{3.23}$$

By considering a monotonic loading test starting from the "virgin" state, the numerator $\mathbf{Q}^{\mathrm{k}} : \dot{\boldsymbol{\alpha}}^{\mathrm{k}} + Q^{\mathrm{i}}\,\dot{\alpha}^{\mathrm{i}}$ is always negative (in the case of hardening), while the denominator $\boldsymbol{\Sigma} : \mathbf{L}^{\mathrm{p}}$ is positive. Thus, the Taylor-Quinney factor predicted by thermodynamics is usually less than one. Furthermore, it depends on the internal variables and consequently, it is not constant, but deformation-dependent. However, usually a constant Taylor-Quinney factor is considered.

In summary, choosing an ad-hoc Taylor-Quinney factor often violates fundamental thermodynamical principles, while choosing the thermodynamically consistent definition (3.22) leads to an overprediction of the temperature — fully analogously to the underlying thermodynamical sound model.

The model proposed in Ristinmaa et al. [108] is among the first where the weighting of cold work for heat generation is incorporated in a thermodynamically consistent framework. In this work, the authors establish the idea that the effectively accumulated equivalent plastic strain does not necessarily has to coincide with the internal variable associated with isotropic hardening. More precisely, the difference between both quantities may be exemplified by an offset in terms of isotropic hardening which is in agreement with the above mentioned discussion. However in the present chapter, this idea is generalised in terms of kinematic hardening and the incorporation of the model into a variational framework which will be discussed in detail in the following sections.

An alternative model for a consistent prediction of the thermomechanically coupled problem is presented in Rosakis et al. [109]. In contrast to Ristinmaa et al. [108], it is restricted to a one-dimensional setting and linearised kinematics are considered. The underlying idea of this model is a proper computation of that part of the Helmholtz energy which is related to cold work. However, this energy does not define the relation between dual variables (the internal stress-like variables are not the negative derivative of the energy with respect to the dual strain-like variables). This is significantly different compared to the framework in Ristinmaa et al. [108] and also to the model advocated in this chapter. Due to this non-standard uncoupling between the Helmholtz energy and the internal variables, the mechanical response is essentially uncoupled from the temperature increase due to plastic deformation and the thermomechanically constitutive model can be fitted better.

3.1.2.2 A novel constitutive model

As a prerequisite, the model formulation presented in Subsection 3.1.1 is enhanced by the introduction of further coefficients β^{k} and β^{i} which affect the plastic energy contribution, cf. (3.15), in terms of

$$\widetilde{\Psi}^{\mathrm{pl}}(\boldsymbol{\alpha}^{\mathrm{k}}, \alpha_{\mathrm{i}}) = [1-\beta^{\mathrm{k}}]\,\Psi^{\mathrm{kin}}(\boldsymbol{\alpha}^{\mathrm{k}}) + [1-\beta^{\mathrm{i}}]\,\Psi^{\mathrm{iso}}(\alpha^{\mathrm{i}}) - [1-\beta^{\mathcal{D}}]\,\alpha^{\mathrm{i}}\,Q_0^{\mathrm{eq}}(y_0)\,, \tag{3.24}$$

where $Q_0^{\mathrm{eq}}(y_0)$ denotes a generalised yield limit depending on the initial value y_0 as well as other quantities such as temperature. The purely mechanical response is supposed to be unaffected by this enhancement, thus

$$\phi = \Sigma^{\mathrm{eq}}(\boldsymbol{\Sigma} + \partial_{\boldsymbol{\alpha}^{\mathrm{k}}}\Psi^{\mathrm{kin}}) + \partial_{\alpha^{\mathrm{i}}}\Psi^{\mathrm{iso}} - Q_0^{\mathrm{eq}} \tag{3.25}$$

still holds for the yield function. As a consequence, the evolution equations (3.7) to (3.9) still apply. The enhancement of the model becomes apparent in terms of the redefined reduced dissipation rate density. Starting from

$$\mathcal{D}_{\mathrm{int}} = \boldsymbol{\Sigma} : \mathbf{L}^{\mathrm{p}} - \partial_{\boldsymbol{\alpha}^{\mathrm{k}}}\widetilde{\Psi}^{\mathrm{pl}} : \dot{\boldsymbol{\alpha}}^{\mathrm{k}} - \partial_{\alpha^{\mathrm{i}}}\widetilde{\Psi}^{\mathrm{pl}}\,\dot{\alpha}^{\mathrm{i}} \tag{3.26}$$

and taking into account the evolution equations (3.7) to (3.9) one obtains

$$\mathcal{D}_{\mathrm{int}} = \lambda\left[\boldsymbol{\Sigma} : \partial_{\boldsymbol{\Sigma}}\Sigma^{\mathrm{eq}} + [1-\beta^{\mathrm{k}}]\,\mathbf{Q}^{\mathrm{k}} : \partial_{\mathbf{Q}^{\mathrm{k}}}\Sigma^{\mathrm{eq}} - [1-\beta^{\mathrm{i}}]\,Q^{\mathrm{i}} - [1-\beta^{\mathcal{D}}]\,Q_0^{\mathrm{eq}}\right] \tag{3.27}$$

with the redefined conjugate forces

$$\mathbf{Q}^{\mathrm{k}} = -\partial_{\boldsymbol{\alpha}^{\mathrm{k}}}\Psi^{\mathrm{kin}}\,, \qquad Q^{\mathrm{i}} = -\partial_{\alpha^{\mathrm{i}}}\Psi^{\mathrm{iso}}\,. \tag{3.28}$$

Furthermore, the relations $\partial_{\mathbf{Q}^{\mathrm{k}}}\Sigma^{\mathrm{eq}} = -\partial_{\boldsymbol{\Sigma}}\Sigma^{\mathrm{eq}}$, $\partial_{\boldsymbol{\Sigma}}\Sigma^{\mathrm{eq}} = \partial_{\boldsymbol{\Sigma}-\mathbf{Q}^{\mathrm{k}}}\Sigma^{\mathrm{eq}}$, $[\boldsymbol{\Sigma} - \mathbf{Q}^{\mathrm{k}}] : \partial_{\boldsymbol{\Sigma}-\mathbf{Q}^{\mathrm{k}}}\Sigma^{\mathrm{eq}} = \Sigma^{\mathrm{eq}}$ and $\phi = 0$ (in the case of elastoplastic loading) lead to the conclusion, that all terms in Ineq. (3.27) which are independent of the β-factors cancel out. Thus, one finally obtains

$$\mathcal{D}_{\mathrm{int}} = \lambda\left[\beta^{\mathrm{k}}\,\mathbf{Q}^{\mathrm{k}} : \partial_{\boldsymbol{\Sigma}}\Sigma^{\mathrm{eq}} + \beta^{\mathrm{i}}\,Q^{\mathrm{i}} + \beta^{\mathcal{D}}\,Q_0^{\mathrm{eq}}\right] \tag{3.29}$$

for the reduced dissipation rate density. Analogously, it can be shown that

$$\begin{aligned} \partial_t\widetilde{\Psi}^{\mathrm{pl}} + \mathcal{D}_{\mathrm{int}} &= \lambda\,\left[\boldsymbol{\Sigma} : \partial_{\boldsymbol{\Sigma}}\Sigma^{\mathrm{eq}} - [\Sigma^{\mathrm{eq}} - Q^{\mathrm{i}} - Q_0^{\mathrm{eq}}]\right] \\ &\overset{\phi=0}{=} \lambda\,\boldsymbol{\Sigma} : \partial_{\boldsymbol{\Sigma}}\Sigma^{\mathrm{eq}} = \boldsymbol{\Sigma} : \mathbf{L}^{\mathrm{p}} \end{aligned} \tag{3.30}$$

and therewith, this term is independent of the β-factors. Together with the general relation

$$\partial_t\Psi^{\mathrm{el}} = \mathbf{P} : \dot{\mathbf{F}} - \boldsymbol{\Sigma} : \mathbf{L}^{\mathrm{p}}\;, \tag{3.31}$$

the rate of total energy (for fixed temperatures)

$$\partial_t \Psi^{\mathrm{el}} + \partial_t \widetilde{\Psi}^{\mathrm{pl}} + \mathcal{D}_{\mathrm{int}} = \mathbf{P} : \dot{\mathbf{F}} \tag{3.32}$$

is equal to the stress power and thus unaffected by the aforementioned approach. The significance of this enhancement becomes obvious by the comparison with the original Taylor-Quinney approach. As indicated above, the internal dissipation rate density is therein determined by

$$\mathcal{D}_{\mathrm{int}}^{\mathrm{TQ}} = \beta^{\mathrm{TQ}}\, \dot{W}^{\mathrm{p}} = \beta^{\mathrm{TQ}}\, \boldsymbol{\Sigma} : \mathbf{L}^{\mathrm{p}} = \beta^{\mathrm{TQ}}\, \lambda\, \boldsymbol{\Sigma} : \partial_{\boldsymbol{\Sigma}} \Sigma^{\mathrm{eq}} \;. \tag{3.33}$$

By using the identity

$$\boldsymbol{\Sigma} : \partial_{\boldsymbol{\Sigma}} \Sigma^{\mathrm{eq}} = \left[\boldsymbol{\Sigma} - \mathbf{Q}^{\mathrm{k}}\right] : \partial_{\boldsymbol{\Sigma}} \Sigma^{\mathrm{eq}} + \mathbf{Q}^{\mathrm{k}} : \partial_{\boldsymbol{\Sigma}} \Sigma^{\mathrm{eq}} = \Sigma^{\mathrm{eq}} + \mathbf{Q}^{\mathrm{k}} : \partial_{\boldsymbol{\Sigma}} \Sigma^{\mathrm{eq}}. \tag{3.34}$$

one obtains

$$\mathcal{D}_{\mathrm{int}}^{\mathrm{TQ}} = \beta^{\mathrm{TQ}}\, \lambda\, \left[\Sigma^{\mathrm{eq}} + \mathbf{Q}^{\mathrm{k}} : \partial_{\boldsymbol{\Sigma}} \Sigma^{\mathrm{eq}}\right] \;. \tag{3.35}$$

Furthermore, it follows from $\phi = 0$ that

$$\Sigma^{\mathrm{eq}} = Q^{\mathrm{i}} + Q_0^{\mathrm{eq}} \tag{3.36}$$

and hence

$$\mathcal{D}_{\mathrm{int}}^{\mathrm{TQ}} = \lambda\, \beta^{\mathrm{TQ}}\, \left[\mathbf{Q}^{\mathrm{k}} : \partial_{\boldsymbol{\Sigma}} \Sigma^{\mathrm{eq}} + Q^{\mathrm{i}} + Q_0^{\mathrm{eq}}\right] \;. \tag{3.37}$$

By the comparison of dissipation (3.29) and dissipation (3.37) one can conclude that the enhanced model coincides with the Taylor-Quinney approach if $\beta^{\mathcal{D}} = \beta^{\mathrm{k}} = \beta^{\mathrm{i}} = \beta^{\mathrm{TQ}}$. In this regard, (3.24) represents a generalisation of the Taylor-Quinney approach. This remarkable conclusion, however, represents a significant drawback of the presented framework due to the fact that it might violate the second law of thermodynamics as will be discussed now.

Thermodynamical consistency can only be ensured if the dissipation rate density (3.29) is greater than or equal to zero, i.e.

$$\lambda\, \left[\beta^{\mathrm{k}}\, \mathbf{Q}^{\mathrm{k}} : \partial_{\boldsymbol{\Sigma}} \Sigma^{\mathrm{eq}} + \beta^{\mathrm{i}}\, Q^{\mathrm{i}} + \beta^{\mathcal{D}}\, Q_0^{\mathrm{eq}}\right] \geq 0 \,. \tag{3.38}$$

Since $\lambda \geq 0$ holds in general, it remains to show that

$$\beta^{\mathrm{k}}\, \mathbf{Q}^{\mathrm{k}} : \partial_{\boldsymbol{\Sigma}} \Sigma^{\mathrm{eq}} \geq -\beta^{\mathcal{D}}\, Q_0^{\mathrm{eq}} - \beta^{\mathrm{i}}\, Q^{\mathrm{i}} \,, \tag{3.39}$$

where focus is laid on the critical part related to kinematic hardening. Considering a worst-case scenario characterised by

$$\partial_{\boldsymbol{\Sigma}} \Sigma^{\mathrm{eq}} = -\mathbf{Q}^{\mathrm{k}} / \|\mathbf{Q}^{\mathrm{k}}\| \quad , \quad \beta^{\mathcal{D}} = 1 \quad , \quad \beta^{\mathrm{i}} = 0 \quad , \quad \beta^{\mathrm{k}} = 1 \, , \tag{3.40}$$

this restriction can be reformulated as

$$\|\mathbf{Q}^{\mathrm{k}}\| \leq Q_0^{\mathrm{eq}} \, . \tag{3.41}$$

For associated flow rules, this condition cannot be fulfilled in general since the internal variable $\boldsymbol{\alpha}^{\mathrm{k}}$ and with it the thermodynamically conjugated force $\mathbf{Q}^{\mathrm{k}}$ related to kinematic hardening are not bounded. To circumvent this issue, non-associated theories ensuring the validness of restriction (3.41) have to be considered which will be discussed in the following section.

As a preliminary conclusion, the following aspects about the developed framework shall be pointed out: Standard plasticity models treat hardening effects as purely energetic. As a consequence, the predicted local temperature increase due to plastic deformations is overestimated to a significant extent. The theory presented here solves this problem by the introduction of scaling parameters. These factors are associated with the scaling of the initial yield limit as well as the scaling of the hardening-related contributions to the total energy. It can be shown, that this generalised model indeed is equivalent to the Taylor-Quinney-ansatz for a special case. However, even if it fulfils the first law of thermodynamics, it may contradict the second law. To overcome this problem, the model for kinematic hardening has to be extended to a saturation-type ansatz which is only possible via non-associated relations.

3.1.3 A thermodynamically consistent prototype model

As discussed in the previous section, the presented framework has to be extended to non-associated plasticity rules in order to unconditionally fulfil the second law of thermodynamics. To this end, an Armstrong-Frederick-type model for kinematic hardening is introduced exemplified by

$$\Psi^{\mathrm{kin}} = \frac{1}{2} c^{\mathrm{k}} \boldsymbol{\alpha}^{\mathrm{k}} : \boldsymbol{\alpha}^{\mathrm{k}} \, , \qquad \dot{\boldsymbol{\alpha}}^{\mathrm{k}} = \lambda \, \partial_{\mathbf{Q}^{\mathrm{k}}} g \, , \qquad g = \phi + \frac{1}{2} \frac{b^{\mathrm{k}}}{c^{\mathrm{k}}} \mathbf{Q}^{\mathrm{k}} : \mathbf{Q}^{\mathrm{k}} \, . \tag{3.42}$$

Here, g denotes an inelastic potential and b^{k}, c^{k} are the parameters associated with the Armstrong-Frederick-type ansatz. The extended dissipation rate density then reads

$$\mathcal{D}_{\mathrm{int}} = \lambda \left[\beta^{\mathrm{k}} \mathbf{Q}^{\mathrm{k}} : \partial_{\boldsymbol{\Sigma}} \Sigma^{\mathrm{eq}} + [1 - \beta^{\mathrm{k}}] \frac{b^{\mathrm{k}}}{c^{\mathrm{k}}} \mathbf{Q}^{\mathrm{k}} : \mathbf{Q}^{\mathrm{k}} + \beta^{\mathrm{i}} Q^{\mathrm{i}} + \beta^{\mathcal{D}} Q_0^{\mathrm{eq}} \right] . \tag{3.43}$$

Note, that isotropic hardening always has a stabilising effect since $Q^{\mathrm{i}} \leq 0$. In a similar manner as before, a worst case is constructed via $\partial_{\boldsymbol{\Sigma}} \Sigma^{\mathrm{eq}} = -\mathbf{Q}^{\mathrm{k}}/\|\mathbf{Q}^{\mathrm{k}}\|$, $\beta^{\mathrm{k}} = 1$, $\beta^{\mathrm{i}} = 0$ and $\beta^{\mathcal{D}} = 1$ which yields

$$\mathcal{D}_{\mathrm{int}} = \lambda \left[-\|\mathbf{Q}^{\mathrm{k}}\| + Q_0^{\mathrm{eq}} \right] . \tag{3.44}$$

The extension to an Armstrong-Frederick-type approach for kinematic hardening now makes it possible to determine a maximum value — namely, the saturated value — for $\|\mathbf{Q}^{\mathrm{k}}\|$. This is achieved by setting $\|\dot{\boldsymbol{\alpha}}^{\mathrm{k}}\| = 0$, which together with Eq. (3.42) results in

$$\frac{b^{\mathrm{k}}}{c^{\mathrm{k}}} \|\mathbf{Q}^{\mathrm{k}}\| = \|\partial_{\boldsymbol{\Sigma}} \Sigma^{\mathrm{eq}}\| = 1 \qquad \Leftrightarrow \qquad \|\mathbf{Q}^{\mathrm{k}}\| = \frac{c^{\mathrm{k}}}{b^{\mathrm{k}}} \tag{3.45}$$

for $\lambda \neq 0$. Thus, one can define restrictions on the Armstrong-Frederick parameters via

$$\mathcal{D}_{\mathrm{int}} = \lambda \left[-\frac{c^{\mathrm{k}}}{b^{\mathrm{k}}} + Q_0^{\mathrm{eq}} \right] \geq 0 \tag{3.46}$$

which finally yields

$$\frac{c^{\mathrm{k}}}{b^{\mathrm{k}}} \leq Q_0^{\mathrm{eq}} . \tag{3.47}$$

This condition guarantees the fulfilment of the second law of thermodynamics. As a summary, it is possible to deduce such restrictions for the specific kinematic hardening related parameters for each material model based on non-associated hardening rules. These guarantee, that also the second law of thermodynamics is unconditionally fulfilled. Altogether, the proposed theory offers a fully thermodynamically consistent framework. It will be shown that it also accounts for the realistic prediction of the local temperature evolution.

3.2 Variational framework

Using an energetic approach as given by the proposed framework facilitates the introduction of a variational framework. Although the novel thermomechanical coupling in Subsection 3.1.2.2 is not restricted to a specific model or framework, variational principles show a natural decomposition of energetic and dissipative parts, and are therefore favoured here. According to the fundamentals presented in Subsection 2.6.3, the functional

$$\dot{\mathcal{I}} = \int_{\mathcal{B}_0} \dot{\mathcal{E}} \, \mathrm{d}V - \mathcal{P}_{\mathbf{F}} - \mathcal{P}_T \quad \text{with} \quad \dot{\mathcal{E}} = \dot{E} - \Theta \, \dot{N} + f \, \zeta - \chi \tag{3.48}$$

is introduced for that purpose (cf. Eq. (2.97)). Again, the convex potential χ in Eq. (2.55) and the external forces $\mathcal{P}_{\mathbf{F}}$ and $\mathcal{P}_T$ in Eq. (2.80)) and Eq. (2.86) are applied.

According to the framework presented in the previous sections, the internal energy density E is defined as

$$E = E^{\mathrm{el}}(\mathbf{F}^{\mathrm{e}}, N) + E^{\mathrm{pl}}(\boldsymbol{\alpha}^{\mathrm{k}}, \alpha^{\mathrm{i}}) \tag{3.49}$$

with

$$E^{\mathrm{pl}} = [1-\beta^{\mathrm{k}}]\, E^{\mathrm{kin}}(\boldsymbol{\alpha}^{\mathrm{k}}) + [1-\beta^{\mathrm{i}}]\, E^{\mathrm{iso}}(\alpha^{\mathrm{i}}) - [1-\beta^{\mathcal{D}}]\, \alpha^{\mathrm{i}}\, Q_0^{\mathrm{eq}}(y_0)\,. \tag{3.50}$$

Analogously, the dissipation functional ζ — which is known to be identical to the reduced internal dissipation rate density $\mathcal{D}_{\mathrm{int}}$ for rate-independent processes — is decomposed according to

$$\zeta = \mathcal{D}_{\mathrm{int}} = \lambda \left[\beta^{\mathrm{k}}\, \mathbf{Q}^{\mathrm{k}} : \partial_{\boldsymbol{\Sigma}} \Sigma^{\mathrm{eq}} + [1-\beta^{\mathrm{k}}]\, \frac{b^{\mathrm{k}}}{c^{\mathrm{k}}}\, \mathbf{Q}^{\mathrm{k}} : \mathbf{Q}^{\mathrm{k}} + \beta^{\mathrm{i}}\, Q^{\mathrm{i}} + \beta^{\mathcal{D}}\, Q_0^{\mathrm{eq}}\right], \tag{3.51}$$

focussing on an Armstrong-Frederick-type modelling of kinematic hardening, cf. dissipation (3.43). Again, the functional $\dot{\mathcal{I}} = \dot{\mathcal{I}}(\dot{\boldsymbol{\varphi}}, \dot{\boldsymbol{F}}^{\mathrm{p}}, \dot{\boldsymbol{\alpha}}^{\mathrm{k}}, \dot{\alpha}^{\mathrm{i}}, \dot{N}, \Theta)$ represents a Hu-Washizu-type functional depending on the rates of state variables except for the temperature Θ. In order to receive the underlying stationarity conditions, the variations with respect to the given arguments need to be derived. Since they have already been discussed in Subsection 2.6.3, the derivations are omitted here but can also be found in Yang et al. [139], Stainier and Ortiz [123], Canadija and Mosler [25].

Following the framework of incremental variational updates as introduced in Section 2.6, the rate dependent and time-continuous potential (3.48) is converted into a time-discrete incremental potential (cf. Eq. (2.105)). As a result, the time-discrete incremental potential

$$\begin{aligned}
\Delta\mathcal{E} = {} & E_{n+1}(\mathbf{F}^{\mathrm{e}}_{n+1}, N_{n+1}, \boldsymbol{\alpha}^{\mathrm{k}}_{n+1}, \alpha^{\mathrm{i}}_{n+1}) - E_n(\mathbf{F}^{\mathrm{e}}_n, N_n, \boldsymbol{\alpha}^{\mathrm{k}}_n, \alpha^{\mathrm{i}}_n) - \Theta_{n+1}\,[N_{n+1} - N_n] \\
& + \frac{\Theta_{n+1}}{\partial_N E(\mathbf{F}^{\mathrm{e}}_{n+1}, N_{n+1}, \boldsymbol{\alpha}^{\mathrm{k}}_{n+1}, \alpha^{\mathrm{i}}_{n+1})}\, \Delta\zeta(\mathbf{F}^{\mathrm{p}}_{n+1}, \boldsymbol{\alpha}^{\mathrm{k}}_{n+1}, \alpha^{\mathrm{i}}_{n+1}) \\
& - \Delta t\, \chi(\Theta_{n+1}, \mathrm{GRAD}\Theta_{n+1})\,,
\end{aligned} \tag{3.52}$$

is derived. Based on this potential, the unknowns at time t_{n+1} are updated according to

$$(\boldsymbol{\varphi}_{n+1}, \Theta_{n+1}, \mathbf{F}^{\mathrm{p}}_{n+1}, N_{n+1}, \boldsymbol{\alpha}^{\mathrm{k}}_{n+1}, \alpha^{\mathrm{i}}_{n+1}) = \arg \inf_{\boldsymbol{\varphi}_{n+1}, \mathbf{F}^{\mathrm{p}}_{n+1}, N_{n+1}, \boldsymbol{\alpha}^{\mathrm{k}}_{n+1}, \alpha^{\mathrm{i}}_{n+1}} \sup_{\Theta_{n+1}} \Delta\mathcal{I}\,. \tag{3.53}$$

In order to reduce the number of unknown state variables, focus is now on the parametrisation of the underlying evolution equations. For this purpose, the equations (3.7)-(3.9) are time integrated by a Backward-Euler scheme leading to the time-discretised values

$$
\begin{aligned}
\int_{t_n}^{t_{n+1}} \mathbf{L}^{\mathrm{p}} \, \mathrm{d}t \quad &\Rightarrow \quad \Delta\mathbf{L}^{\mathrm{p}} = \Delta\lambda \, \frac{\partial\phi}{\partial\boldsymbol{\Sigma}} \, , \\
\int_{t_n}^{t_{n+1}} \dot{\boldsymbol{\alpha}}^{\mathrm{k}} \, \mathrm{d}t \quad &\Rightarrow \quad \boldsymbol{\alpha}^{\mathrm{k}}_{n+1} = \frac{\boldsymbol{\alpha}^{\mathrm{k}}_{n} - \Delta\mathbf{L}^{\mathrm{p}}}{1 + b^{\mathrm{k}} \, \Delta\lambda} \, , \\
\int_{t_n}^{t_{n+1}} \dot{\alpha}^{\mathrm{i}} \, \mathrm{d}t \quad &\Rightarrow \quad \alpha^{\mathrm{i}}_{n+1} = \alpha^{\mathrm{i}}_{n} - \Delta\lambda \, ,
\end{aligned}
\tag{3.54}
$$

where the incremental plastic multiplier is given as $\Delta\lambda = \int_{t_n}^{t_{n+1}} \lambda \, \mathrm{d}t$. Values at the previous time step are denoted by index $(\bullet)_n$ and values at the current time step are denoted by index $(\bullet)_{n+1}$. Moreover, the evolution of the plastic deformation gradient requires a time-discretisation. Using an implicit time integration, the updated deformation gradient is computed by the now standard exponential mapping

$$
\mathbf{F}^{\mathrm{p}}_{n+1} = \mathrm{EXP}(\Delta\mathbf{L}^{\mathrm{p}}) \cdot \mathbf{F}^{\mathrm{p}}_{n} \, . \tag{3.55}
$$

Based on this equation, the elastic deformation gradient yields

$$
\mathbf{F}^{\mathrm{e}}_{n+1} = \mathbf{F}^{\mathrm{e}}_{\mathrm{trial}} \cdot \mathrm{EXP}(-\Delta\mathbf{L}^{\mathrm{p}}) \, , \tag{3.56}
$$

with $\mathbf{F}^{\mathrm{e}}_{\mathrm{trial}} = \mathbf{F}_{n+1} \cdot \mathbf{F}^{\mathrm{n}-1}_{n}$ being the trial value for the elastic deformation and with EXP denoting the exponential map (see Remark 3.2.1).

Since the yield function is of a von Mises-type and positively homogeneous of degree one in $\boldsymbol{\Sigma}$, the flow direction features the property $\|\partial_{\boldsymbol{\Sigma}}\phi\| = \|\partial_{\boldsymbol{\Sigma}}\Sigma^{\mathrm{eq}}\| = 1$. Consequently, the incremental plastic multiplier can be computed by the norm of the flow rule

$$
\Delta\lambda = \|\Delta\mathbf{L}^{\mathrm{p}}\| = \Delta\lambda \left\| \frac{\partial\phi}{\partial\boldsymbol{\Sigma}} \right\| . \tag{3.57}
$$

Due to the fact that $\Delta\mathbf{L}^{\mathrm{p}}$ is deviatoric (and symmetric), the number of unknowns for the evolution equations reduces to $\dim(\Delta\mathbf{L}^{\mathrm{p}}) = 5$ independent coefficients. In order to incorporate the deviatoric constraint of the flow rule, one may substitute $\Delta L^{\mathrm{p}}_{33}$ by $-\Delta L^{\mathrm{p}}_{11} - \Delta L^{\mathrm{p}}_{22}$. A more detailed discussion regarding the parametrisation of evolution equations is given in Bleier and Mosler [20]. Regarding the dissipation functional, ζ

is now completely parametrised by $\Delta\mathbf{L}^{\mathrm{p}}$. For a plastic state the potential (3.52) is expressed now by

$$\begin{aligned}\Delta\mathcal{E} = {} & E_{n+1}(\mathbf{F}_{n+1}, N_{n+1}, \Delta\mathbf{L}^{\mathrm{p}}) - E_n(\mathbf{F}^{\mathrm{e}}_n, N_n, \boldsymbol{\alpha}^{\mathrm{k}}_n, \alpha^{\mathrm{i}}_n) - \Theta_{n+1}\left[N_{n+1} - N_n\right] \\ & + \frac{\Theta_{n+1}}{\partial_N E(\mathbf{F}_{n+1}, N_{n+1}, \Delta\mathbf{L}^{\mathrm{p}})}\Delta\zeta(\Delta\mathbf{L}^{\mathrm{p}}) - \Delta t\,\chi(\Theta_{n+1}, \mathrm{GRAD}\Theta_{n+1})\,.\end{aligned} \tag{3.58}$$

Due to the occurrence of global and local variables (for global variables, their gradients also enter the potential), a two step optimisation is performed as suggested in Eq. (2.106). While in a first step the global variables $(\boldsymbol{\varphi}_{n+1}, \Theta_{n+1})$ are kept fixed, $\Delta\mathcal{E}$ is minimised with respect to the internal variables $(N_{n+1}, \Delta L^{\mathrm{p}}_{11}, \Delta L^{\mathrm{p}}_{12}, \Delta L^{\mathrm{p}}_{13}, \Delta L^{\mathrm{p}}_{22}, \Delta L^{\mathrm{p}}_{23})$. Thus, the reduced potential depending only on the global variables reads

$$\Delta\mathcal{E}_{\mathrm{red}} = \inf_{N_{n+1}, \Delta L^{\mathrm{p}}_{11}, \Delta L^{\mathrm{p}}_{12}, \Delta L^{\mathrm{p}}_{13}, \Delta L^{\mathrm{p}}_{22}, \Delta L^{\mathrm{p}}_{23}} \Delta\mathcal{E}\,. \tag{3.59}$$

In the subsequent second step the global saddle-point problem

$$(\boldsymbol{\varphi}_{n+1}, \Theta_{n+1}) = \arg \inf_{\boldsymbol{\varphi}_{n+1}} \sup_{\Theta_{n+1}} \Delta\mathcal{I}_{\mathrm{red}} \tag{3.60}$$

is resolved, in which the reduced potential is defined as

$$\Delta\mathcal{I}_{\mathrm{red}} = \int\limits_{\mathcal{B}_0} \Delta\mathcal{E}_{\mathrm{red}}(\boldsymbol{\varphi}_{n+1}, \Theta_{n+1})\,\mathrm{d}V - \mathcal{P}_{\mathbf{F}}(\boldsymbol{\varphi}_{n+1}) + \mathcal{P}_{\mathbf{F}}(\boldsymbol{\varphi}_n) - \Delta t\,\mathcal{P}_T(\Theta_{n+1})\,. \tag{3.61}$$

Remark 3.2.1: *The exponential map of a tensor* $\mathbf{A}$*, here a two-point tensor, is computed by use of the Taylor series expansion (see Ortiz et al. [100]). Since the exponential map enters the potential energy, gradient or Newton-type solution schemes of this potential energy require first and second derivatives of the exponential map* $\mathrm{EXP}(\mathbf{A})$*. While the first derivative of the exponential map* $\mathrm{DEXP}(\mathbf{A}) = \partial_{\mathbf{A}}\mathrm{EXP}(\mathbf{A})$ *yields a fourth-order tensor, the second derivative of the exponential map* $\mathrm{D}^2\mathrm{EXP}(\mathbf{A}) = \partial_{\mathbf{AA}}\mathrm{EXP}(\mathbf{A})$ *results in a sixth-order tensor. For the numerical computation, the recursion property of the exponential map can be used. Further details are omitted here, but can be found in Ortiz et al. [100].*

3.3 Uniaxial tension test of a bar made of Al 2024-T3

The predictive capabilities of the proposed framework and the fundamental features of the thermomechanical coupling are demonstrated here by means of a representative numerical example. For that purpose, a uniaxial tensile test is considered and the response predicted by the model is compared to the results observed in the experiments reported by Hodowany et al. [54].

3.3.1 A thermomechanical prototype model

The constitutive model employed in the computations is briefly summarised in this section. In contrast to the variational framework discussed in Section 3.2, the model is defined by means of the Helmholtz energy Ψ. From that representation, the internal energy E is computed by applying a standard Legendre transformation of the type (2.42). An explicit computation of the internal energy based on the following Helmholtz energy is given in Appendix A.1. Starting from an additive decomposition of the energy into parts related to elastic deformation (Ψ^{el}) and those corresponding to plastic work (Ψ^{pl}), the thermoelastic response of the prototype model is specified by

$$\Psi^{\text{el}} = W(\bar{\mathbf{C}}^{\text{e}}) + U(J) + M(J,\Theta) + T(\Theta)\,. \tag{3.62}$$

Concerning the individual parts in Eq. (3.62), they are chosen as

$$\begin{aligned} W(\bar{\mathbf{C}}^{\text{e}}) &= \frac{1}{2}\,\mu\,\left[\text{tr}\bar{\mathbf{C}}^{\text{e}} - 3\right], \quad \text{with} \quad \bar{\mathbf{C}}^{\text{e}} = J^{-2/3}[\mathbf{F}^{\text{e}}]^{\text{T}}\cdot\mathbf{F}^{\text{e}}\,, && (3.63)\\ U(J) &= \frac{1}{2}\,\kappa\,\left[\frac{1}{2}[J^2-1] - \ln J\right], && (3.64)\\ M(J,\Theta) &= [\Theta-\Theta_0]\,[-3\,\alpha_0\,\partial_J U]\,, && (3.65)\\ T(\Theta) &= c_0\left[\Theta - \Theta_0 - \Theta\ln\frac{\Theta}{\Theta_0}\right]. && (3.66) \end{aligned}$$

They are associated with the purely mechanical deviatoric response W, with the purely mechanical volumetric response U, with the thermoelastic coupling M and with the thermal potential T. κ and μ are the bulk and the shear modulus, α_0 is the thermal expansion coefficient (assumed as constant), c_0 is the thermal heat capacity (assumed as constant) and Θ_0 is a reference temperature.

Next, the constitutive assumptions regarding plastic deformations are summarised. It is assumed that such deformations are only possible, if the von Mises-type yield function

$$\phi = \|\text{dev}\boldsymbol{\Sigma} - \mathbf{Q}_{\text{k}}\| - Q^{\text{i}} - Q_0^{\text{eq}} \tag{3.67}$$

vanishes to zero. In order to capture thermal softening effects, the initial yield stress Q_0^{eq} within the yield function is temperature dependent. To be more precise, the linear thermal softening function

$$Q_0^{\text{eq}}(\Theta) = y_0\,[1-\omega_0[\Theta-\Theta_0]] \tag{3.68}$$

is adopted. Herein, y_0 describes a reference flow stress, ω_0 is a model parameter related to the slope of softening and Θ_0 denotes a reference temperature. The model is completed by an associative flow rule and hardening models. Concerning the latter, the following models will be considered:

- Model 1 (M1) – Associative isotropic hardening with exponential saturation

$$\Psi^{\mathrm{pl}} = c^{\mathrm{i}} \left[\frac{1}{b^{\mathrm{i}}} \exp(b^{\mathrm{i}}\, \alpha^{\mathrm{i}}) - \alpha^{\mathrm{i}} \right], \quad \dot{\alpha}^{\mathrm{i}} = \lambda\, \partial g / \partial \alpha^{\mathrm{i}}, \quad g = \phi \tag{3.69}$$

- Model 2 (M2): Non-associative isotropic hardening with exponential saturation

$$\Psi^{\mathrm{pl}} = \frac{1}{2}\, c^{\mathrm{i}}\, {\alpha^{\mathrm{i}}}^2, \quad \dot{\alpha}^{\mathrm{i}} = \lambda\, \partial g / \partial \alpha^{\mathrm{i}}, \quad g = \phi + \frac{1}{2}\, \frac{b^{\mathrm{i}}}{c^{\mathrm{i}}}\, {Q^{\mathrm{i}}}^2 \tag{3.70}$$

- Model 3 (M3): Non-associative kinematic hardening with exponential saturation (Armstrong-Frederick model)

$$\Psi^{\mathrm{pl}} = \frac{1}{2}\, c^{\mathrm{k}}\, \boldsymbol{\alpha}^{\mathrm{k}} : \boldsymbol{\alpha}^{\mathrm{k}}, \quad \dot{\boldsymbol{\alpha}}^{\mathrm{k}} = \lambda\, \partial g / \partial \boldsymbol{\alpha}^{\mathrm{k}}, \quad g = \phi + \frac{1}{2}\, \frac{b^{\mathrm{k}}}{c^{\mathrm{k}}}\, \mathbf{Q}^{\mathrm{k}} : \mathbf{Q}^{\mathrm{k}}. \tag{3.71}$$

Here, c^{i}, c^{k}, b^{i} and b^{k} are model parameters. They control the hardening rate (b) and the saturation of the stresses (c/b). The models are designed such that they lead under isothermal conditions to the same uniaxial stress-strain response for monotonic loading (for the choice $c^{\mathrm{i}} = c^{\mathrm{k}}$ and $b^{\mathrm{i}} = b^{\mathrm{k}}$). The hardening-independent model parameters are summarised in Tab. 3.1.

Name	Symbol	Value	Unit
Shear modulus	μ	28	[GPa]
Bulk modulus	κ	73	[GPa]
Thermal expansion	α_0	$2.4 \cdot 10^{-5}$	[K^{-1}]
Heat capacity	c_0	2.4325	[MPa/K]
Thermal heat softening	ω_0	0.002	[K^{-1}]

Table 3.1: Material parameters for Al 2024-T3 at $\Theta_0 = 293$ K (the respective parameters related to the hardening models are summarised in Tab. 3.2 and Tab. 3.3)

3.3.2 Isotropic hardening

The remaining model parameters y_0 (reference yield stress), b and c are computed from a standard least-squares fit in which the difference between the experimentally measured stress-strain and strain-temperature response and the numerically predicted counterparts are minimised. The calibrated model parameters are summarised in Tab. 3.2, while the computed strain-temperature response is given in Fig. 3.2. The diagram in Fig. 3.2 corresponds to purely energetic hardening ($\beta^{\mathrm{i}} = 0$ and $\beta^{\mathcal{D}} = 1$).

associative hardening (M1)		
b^{i} [-]	c^{i} [MPa]	y_0 [MPa]
4.07	305.77	322.83

non-associative hardening (M2)		
b^{i} [-]	c^{i} [MPa]	y_0 [MPa]
4.05	1259.11	322.91

Table 3.2: Material parameters for Al 2024-T3: Isotropic hardening models for purely energetic hardening

non-associative hardening (M3)		
b^{i} [-]	c^{i} [MPa]	y_0 [MPa]
4.05	1259.11	322.91

Table 3.3: Material parameters for Al 2024-T3: Kinematic hardening model for purely energetic hardening (model M3 on page 51)

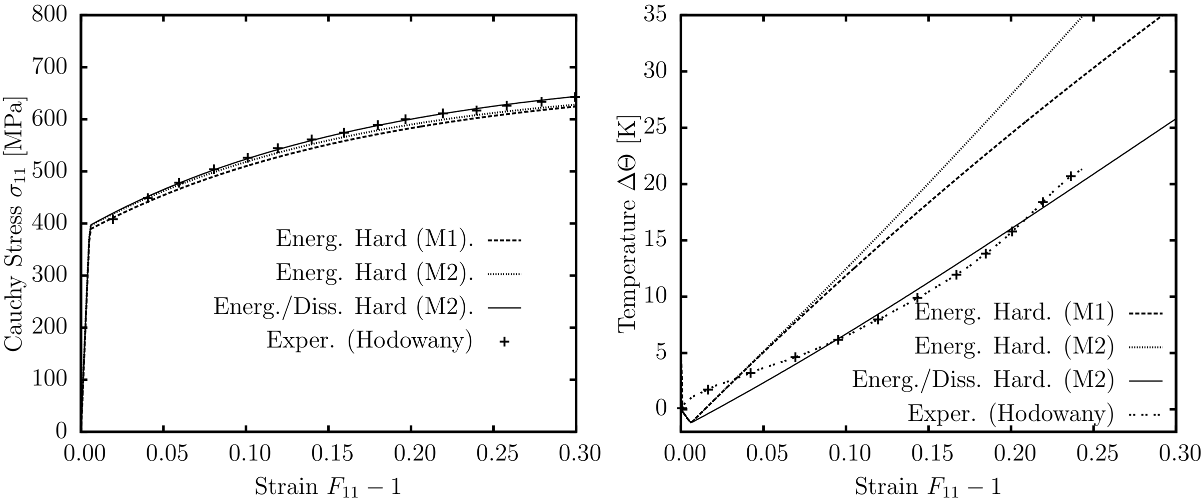

Figure 3.2: Uniaxial tension test of a bar made of Al 2024-T3 (adiabatic heat conditions): stress-strain response (left); temperature increase for isotropic hardening (right). Model 1 (M1) associative and purely energetic hardening [$\beta^{\text{i}} = 0$, $\beta^{\mathcal{D}} = 1$]. Model 2 (M2) non-associated hardening and purely energetic hardening [$\beta^{\text{i}} = 0$, $\beta^{\mathcal{D}} = 1$] and model M2 with optimised diss./energ. hardening [$\beta^{\text{i}} = 0.25$, $\beta^{\mathcal{D}} = 0.57$]

According to Tab. 3.2 and in contrast to the isothermal setting, the model parameters related to the two different isotropic hardening models are not identical anymore. Although both models (M1 and M2; see page 51) show a good agreement with the experimentally measured stress-strain response, they significantly over-predict the temperature increase induced by plastic deformation. This over-prediction is even more pronounced in the case of the non-associative model (M2). That is consistent with the larger internal dissipation of this model ($\mathcal{D}_{\text{int}} = \lambda\, Q_0^{\text{eq}}$ for model M1; $\mathcal{D}_{\text{int}} = \lambda\, Q_0^{\text{eq}} + \lambda\, b^{\text{i}}/c^{\text{i}}\, {Q^{\text{i}}}^2$ for model M2).

Next, the advocated decomposition of hardening into energetic and dissipative parts is considered. For that purpose, the parameters β^{i} and $\beta^{\mathcal{D}}$ of model M2 are optimised by a least-squares approach in which the error of the predicted temperature evolution is monitored. The objective function $\mathcal{F}^{\mathrm{err}} = 1/2\,||\Theta_{\mathrm{exp}} - \Theta_{\mathrm{sim}}||^2$ defining the error is plotted in Fig. 3.3. Form this figure, the dependence of the predicted temperature on the advocated decomposition into energetic and dissipative parts is evident. Furthermore, the choice of the model parameters related to the energetic-dissipative-decomposition does not seem to be unique. This observation is in line with the work Ristinmaa et al. [108]. The thermomechanical response of the model with optimised parameters β^{i} and $\beta^{\mathcal{D}}$ is given in Fig. 3.2. Now, the model predictions are in good agreement with the experimental measurements.

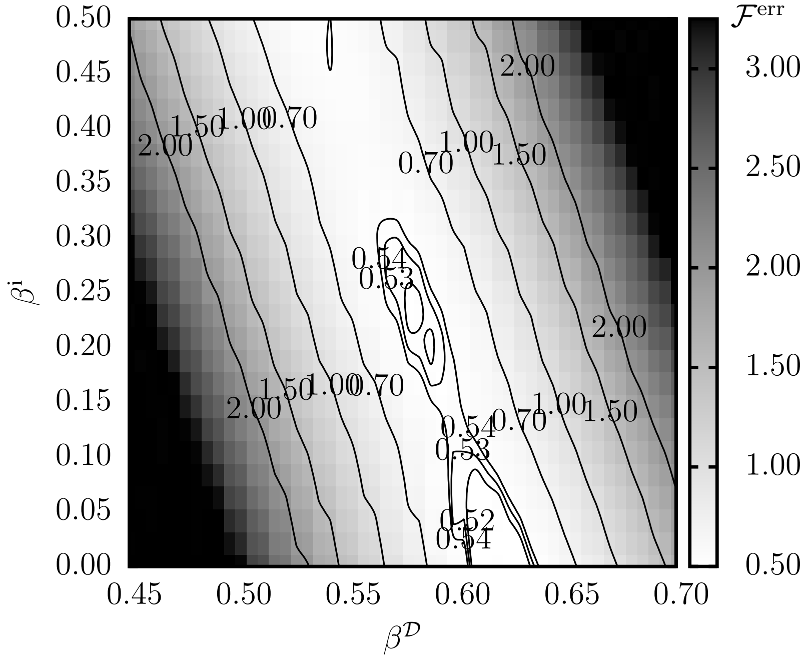

Figure 3.3: Uniaxial tension test of a bar made of Al 2024-T3 (adiabatic heat conditions): Error in temperature prediction for isotropic hardening and model M2. Error is defined as $\mathcal{F}^{\mathrm{err}} = 1/2\,||\Theta_{\mathrm{exp}} - \Theta_{\mathrm{sim}}||^2$

3.3.3 Kinematic hardening

The example is re-analysed using a kinematic hardening model (see model M3 on page 51). The model parameters defining the initial flow stress and the hardening response for a purely energetic description are summarised in Tab. 3.3 ($\beta^{\mathrm{k}} = 0$ and $\beta^{\mathcal{D}} = 1$). A comparison between the numerically predicted and the measured thermomechanical response is given in Fig. 3.4.

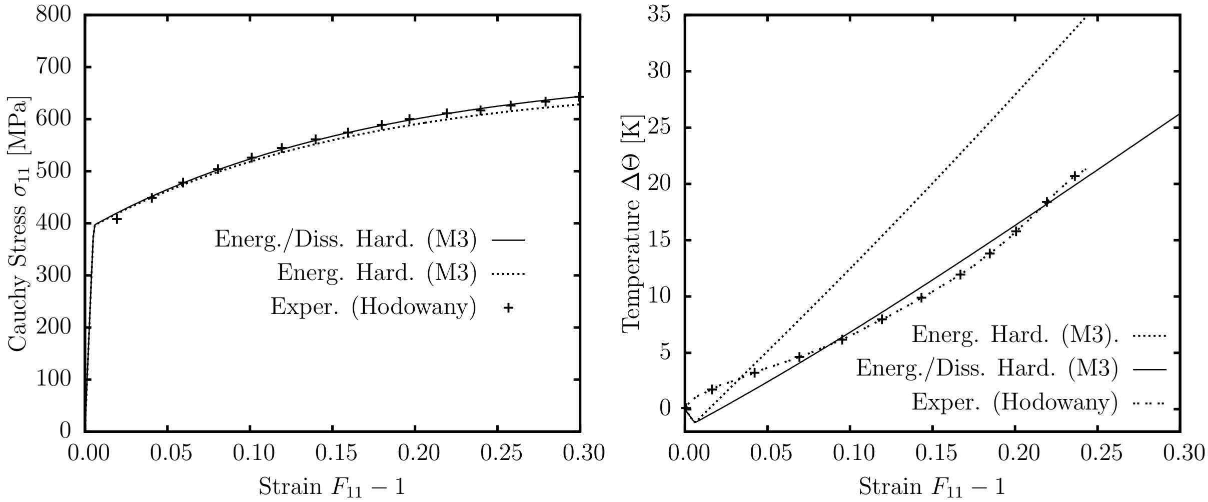

Figure 3.4: Uniaxial tension test of a bar made of Al 2024-T3 (adiabatic heat conditions): stress-strain response (left); temperature increase for kinematic hardening (right). Non-associative hardening model M3 for purely energetic hardening [$\beta^{\mathrm{k}} = 0$, $\beta^{\mathcal{D}} = 1$] and for diss./energ. hardening [$\beta^{\mathrm{k}} = 0.25$, $\beta^{\mathcal{D}} = 0.57$]; material parameters according to Tab. 3.3.

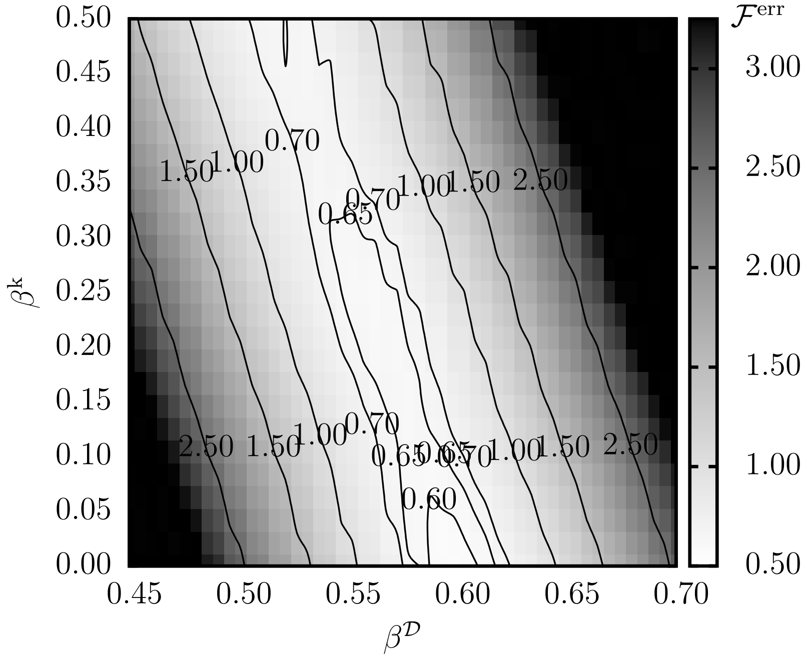

Figure 3.5: Uniaxial tension test of a bar made of Al 2024-T3 (adiabatic heat conditions): Error in temperature prediction for kinematic hardening (model M3 on page 51). Error is defined as $\mathcal{F}^{\mathrm{err}} = 1/2\,||\Theta_{\mathrm{exp}} - \Theta_{\mathrm{sim}}||^2$

In line with the isotropic model, the purely energetic approach leads to an overprediction of the temperature increase. Again, a significant improvement is obtained by the decomposition of the hardening model into energetic and dissipative parts. The error in temperature depending on this decomposition is shown in Fig. 3.5. Similar to isotropic hardening, the choice of the parameters β^{k} and $\beta^{\mathcal{D}}$ does not seem to be unique. The thermomechanical response predicted by setting $\beta^{\mathrm{k}} = 0.25$ and $\beta^{\mathcal{D}} = 0.57$ is given in Fig. 3.4. Again, a significant improvement in the temperature prediction is evident.

4 Numerical implementation of thermomechanically coupled anisotropic hardening

---

The development of a material model, which accounts of the most relevant effects of the macroscale, requires along with a realistic temperature prediction, as discussed in the previous chapter, the consideration of anisotropic texture evolutions. The incorporation of anisotropic hardening is especially relevant for technological forming processes.

However, the classic isotropic and kinematic hardening cannot account for anisotropic hardening. For this purpose, the more general framework of distortional hardening characterised by an evolution of the yield surface's shape can capture the effect of texture evolution on the macroscopic response and is elaborated therefore in the following.

Anisotropic plastic evolution by means of distortional hardening can be found in the state-of-the-art works Barthel et al. [15], Feigenbaum and Dafalias [43], Haddidi et al. [52], Shi and Mosler [113], Wang et al. [135] and references therein. However, the cited distortional hardening models are restricted to an isothermal setting, i.e., a thermomechanically coupled framework, important for most technologically relevant forming processes is not considered. Moreover, the thermodynamcial consistency and the underlying physical bounds (i.e. boundedness and convexity of the yield surface) are missing in most of the cited works.

In this chapter a novel distortional hardening model is presented which falls into the range of generalised standard materials (see Lemaitre [72], Mandel [80]), and is therefore thermodynamically consistent. Based on a novel potential, two independent fourth-order evolution equations capturing dynamic and latent hardening are introduced. Furthermore, the effect of a higher curvature of the yield surface in loading direction can be incorporated into this model.

As shown in Chapter 3, a naive and straightforward extension of an isothermal elastoplasticity model to the thermomechanically coupled setting usually leads to unrealistic temperature predictions. For this purpose, the advocated idea of Subsection 3.1.2.2 is adopted for the thermomechanical coupling to distortinal hardening. Since the initial yield stress is the dominating factor in the temperature over-estimation, it is decomposed into a purely dissipative part and a purely energetic part. The energetic part does not enter the first law of thermodynamics and thus does not result in a temperature increase due to plastic deformations.

For the resulting model, an efficient numerical implementation is proposed. A return-mapping scheme for updating the fourth-order evolution equations is derived which is based on a novel exponential time integration scheme. The resulting implicit return-mapping scheme for updating the internal variables shows the same numerical complexity as a return-mapping scheme for purely isotropic hardening. This efficient return-mapping scheme is finally incorporated into a thermomechanically coupled finite element formulation, and the resulting set of equations is fully implicitly and monolithically solved by means of a Newton-type iteration.

The chapter is organised as follows: A prototype distortional hardening model including isotropic and kinematic hardening is elaborated in Section 4.1. The extension of this anisotropic hardening model to the fully thermomechanically coupled setting is the focus of Section 4.2. An efficient numerical implementation of the resulting framework is proposed in Section 4.3. The predictive capabilities of the advocated constitutive framework as well as the numerical efficiency and robustness of the elaborated finite element formulation are demonstrated in Section 4.4 by means of several numerical examples.

4.1 Generalised distortional hardening – isothermal setting

This section deals with a generalised anisotropic hardening model. Whereas a by now standard setting for the modelling of elastoplasticity including isotropic and kinematic hardening is introduced in Subsection 4.1.1, extensions necessary for distortional hardening are addressed in Subsection 4.1.2. For the sake of simplicity, this section is restricted to the isothermal case.

4.1.1 Prototype hardening model

In order to model isotropic and kinematic hardening, the set of strain-like internal variables $\boldsymbol{\alpha}$ is chosen as $\boldsymbol{\alpha} = \{\mathbf{F}^{\mathrm{p}}, \alpha^{\mathrm{i}}, \boldsymbol{\alpha}^{\mathrm{k}}\}$ and a Helmholtz energy of the type

$$\Psi = \Psi^{\mathrm{el}}(\mathbf{F}^{\mathrm{e}}) + \Psi^{\mathrm{iso}}(\alpha^{\mathrm{i}}) + \Psi^{\mathrm{kin}}(\boldsymbol{\alpha}^{\mathrm{k}}) \tag{4.1}$$

is assumed, cf. Eq. (3.1). While an exponential saturation-type hardening is considered for isotropic hardening (Example 1), an Armstrong & Frederick-type nonlinear hardening is assumed for kinematic hardening (Example 2). Accordingly, the stress-like variables $\{\boldsymbol{\Sigma}, Q^{\mathrm{i}}, \mathbf{Q}^{\mathrm{k}}\}$ are derived in Section 3.2 as thermodynamical conjugate to the strain-like variables $\boldsymbol{\alpha}$. In order to distinguish elastic from plastic states, the space of admissible stresses

$$\mathbb{E}_{\boldsymbol{\Sigma}} = \{(\boldsymbol{\Sigma}, Q^{\mathrm{i}}, \mathbf{Q}^{\mathrm{k}}) \in \mathbb{R}^{9+n} | \phi(\boldsymbol{\Sigma}, Q^{\mathrm{i}}, \mathbf{Q}^{\mathrm{k}}) \leq 0\} \,. \tag{4.2}$$

is defined where ϕ denotes the yield function. At the beginning, the class of positively homogeneous yield functions of degree one spanned by

$$\phi = \Sigma^{\mathrm{eq}} - Q^{\mathrm{i}} - Q_0^{\mathrm{eq}} \quad \text{with} \quad \Sigma^{\mathrm{eq}} = \sqrt{[\mathrm{dev}\boldsymbol{\Sigma} - \mathbf{Q}^{\mathrm{k}}] : \mathbb{H} : [\mathrm{dev}\boldsymbol{\Sigma} - \mathbf{Q}^{\mathrm{k}}]} \,. \tag{4.3}$$

is considered with Q_0^{eq} being the equivalent yield stress again. The fourth-order Hill-type tensor $\mathbb{H}$ characterises the material symmetry, i.e., the shape of the field surface. Up to now, it is assumed as constant. Consequently, its material time derivative vanishes. Clearly, by setting $\mathbb{I}^{\mathrm{dev}} = \mathbb{I} - 1/3\,\mathbf{I} \otimes \mathbf{I}$, the yield surface ϕ degenerates to the classic von Mises surface, cf. 3.1.1. However, more complex material symmetries can certainly also be captured by means of Eq. (4.3). The respective yield surface should fulfil Drucker's postulate [79], i.e., the yield function needs to be convex in the stress space.

The model is completed by loading/unloading conditions and suitable evolution equations. Concerning the latter, they are derived by employing the framework of *generalised standard materials* proposed by [72, 80]. Accordingly, a convex plastic potential g is introduced and the evolution equations are postulated as gradients of this potential, i.e.,

$$\mathbf{L}^{\mathrm{p}} = \lambda \, \frac{\partial g}{\partial \boldsymbol{\Sigma}} \,, \quad \dot{\alpha}^{\mathrm{i}} = \lambda \, \frac{\partial g}{\partial Q^{\mathrm{i}}} \,, \quad \dot{\boldsymbol{\alpha}}^{\mathrm{k}} = \lambda \, \frac{\partial g}{\partial \mathbf{Q}^{\mathrm{k}}} \,, \quad \lambda \geq 0. \tag{4.4}$$

The solution of these equations is subjected to the loading/unloading conditions in Eq. (2.71).

Example 1: *Isotropic hardening with exponential saturation can be modelled by choosing the energy and plastic potential*

$$\Psi^{\mathrm{iso}} = c^{\mathrm{i}} \left[1/b^{\mathrm{i}} \exp(b^{\mathrm{i}}\, \alpha^{\mathrm{i}}) - \alpha^{\mathrm{i}} \right] \,, \qquad g = \phi \,, \tag{4.5}$$

together with the associative evolution equation

$$\dot{\alpha}^{\mathrm{i}} = -\lambda \,. \tag{4.6}$$

This leads to the stress-like internal variable

$$Q^{\mathrm{i}} = -c^{\mathrm{i}} \left[\exp(b^{\mathrm{i}}\, \alpha^{\mathrm{i}}) - 1 \right] \,. \tag{4.7}$$

The model parameters c^{i} and b^{i} define the saturation value of isotropic hardening and the hardening slope, respectively.

Example 2: *Nonlinear kinematic hardening of Armstrong & Frederick-type [5] is obtained by choosing*

$$\Psi^{\mathrm{kin}} = \frac{1}{2}\, c^{\mathrm{k}} \boldsymbol{\alpha}^{\mathrm{k}} : \boldsymbol{\alpha}^{\mathrm{k}} \tag{4.8}$$

and

$$g = \phi + \frac{1}{2}\,\frac{b^{\mathrm{k}}}{c^{\mathrm{k}}}\,\mathbf{Q}^{\mathrm{k}} : \mathbf{Q}^{\mathrm{k}}. \tag{4.9}$$

Again, the model parameters b^{k} and c^{k} are related to the saturation rate and the saturation value. More details regarding the thermodynamical forces are presented in Subsection 3.1.3.

4.1.2 Distortional hardening

4.1.2.1 Fundamentals

Having briefly introduced a standard framework for elastoplasticity including isotropic and kinematic hardening, the focus is now on the modelling of distortional hardening – a less standard hardening theory, cf. Barthel et al. [15], Feigenbaum and Dafalias [43], Haddidi et al. [52], Ortiz and Popov [101], Shi and Mosler [113], Wang et al. [135] and references cited therein. An illustration of different important distortional hardening effects is given in Fig. 4.1.

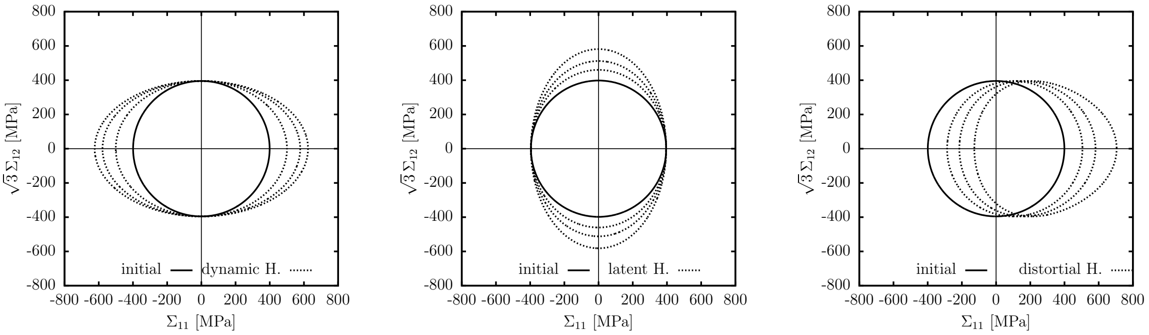

Figure 4.1: Yield surface evolution according to distortional hardening – uniaxial loading in 1-direction: (left) dynamic hardening – the diameter of the yield surface increases only in loading direction; (middle) latent hardening; – the diameter of the yield surface increases only in the direction orthogonal to the loading direction; (right) generalised distortional hardening showing dynamic hardening and a higher curvature in loading direction, cf. Feigenbaum and Dafalias [43].

According to the previous section, the shape of the yield function is implicitly defined by means of the fourth-order tensor $\mathbb{H}$ for the considered prototype model. Consequently, and following Barthel et al. [15], Feigenbaum and Dafalias [43], Shi and Mosler [113], the distortion of the yield surface can be modelled by a suitable evolution law for $\mathbb{H}$. In order to account for the different underlying physical mechanisms leading to distortional hardening, the evolution law for $\mathbb{H}$ is decomposed into one part related to latent hardening (captured by the fourth-order tensor $\mathbb{A}^{\mathrm{l}}$) and into another part related to dynamic hardening (captured by the fourth-order tensor $\mathbb{A}^{\mathrm{d}}$), i.e.,

$$\mathbb{H} = \mathbb{H}(\mathbb{A}^{\mathrm{d}}, \mathbb{A}^{\mathrm{l}}). \tag{4.10}$$

4.1.2.2 A novel distortional hardening model

The starting point of the constitutive distortional hardening model (see also Shi and Mosler [113]) is a Helmholtz energy of the type

$$\Psi = \Psi^{\mathrm{el}}(\mathbf{F}^{\mathrm{e}}) + \Psi^{\mathrm{dis}}(\mathbb{E}^{\mathrm{d}}, \mathbb{E}^{\mathrm{l}})\,. \tag{4.11}$$

Accordingly, the part due to cold work is enhanced by the additional term

$$\Psi^{\mathrm{dis}} = \frac{1}{2}\, c^{\mathrm{d}}\, \mathbb{E}^{\mathrm{d}} :: \mathbb{E}^{\mathrm{d}} + \frac{1}{2}\, c^{\mathrm{l}}\, \mathbb{E}^{\mathrm{l}} :: \mathbb{E}^{\mathrm{l}} \tag{4.12}$$

accounting for distortional hardening. The superscripts $\bullet^{\mathrm{d}}$ and $\bullet^{\mathrm{l}}$ highlight terms related to *dynamic hardening* and *latent hardening*, respectively. Furthermore, $\mathbb{E}^{\mathrm{d}}$ and $\mathbb{E}^{\mathrm{l}}$ are fourth-order tensors enhancing the set of internal variables and c^{d} and c^{l} can be interpreted as hardening moduli (see Eq. (4.8)). The variables energetically conjugated to $\mathbb{E}^{\mathrm{d}}$ and $\mathbb{E}^{\mathrm{l}}$ are introduced by means of

$$\mathbb{A}^{\mathrm{d}} = -\partial_{\mathbb{E}^{\mathrm{d}}} \Psi^{\mathrm{dis}} = -c^{\mathrm{d}}\, \mathbb{E}^{\mathrm{d}} \qquad \text{and} \qquad \mathbb{A}^{\mathrm{l}} = -\partial_{\mathbb{E}^{\mathrm{l}}} \Psi^{\mathrm{dis}} = -c^{\mathrm{l}}\, \mathbb{E}^{\mathrm{l}}\,. \tag{4.13}$$

Such tensors enter the yield surface through

$$\mathbb{H} = [1 - b^{\mathrm{d}} - b^{\mathrm{l}}]\, \mathbb{H}_0 + b^{\mathrm{d}}\, \mathbb{A}^{\mathrm{d}} + b^{\mathrm{l}}\, \mathbb{A}^{\mathrm{l}}\,. \tag{4.14}$$

Here, the fourth-order tensor $\mathbb{H}_0$ describes the symmetry (shape) of the initial yield surface and b^{d} and b^{l} are weighting factor for dynamic and kinematic hardening. Since

$$\dot{\mathbb{H}} = b^{\mathrm{d}}\, \dot{\mathbb{A}}^{\mathrm{d}} + b^{\mathrm{l}}\, \dot{\mathbb{A}}^{\mathrm{l}}\,, \tag{4.15}$$

the fourth-order tensors $\mathbb{A}^{\mathrm{d}}$ and $\mathbb{A}^{\mathrm{l}}$ indeed define the evolution of the material symmetry.

Next, the evolution equations $\dot{\mathbb{E}}^{\mathrm{l}}$ and $\dot{\mathbb{E}}^{\mathrm{d}}$ are defined. They have to fulfil the dissipation inequality

$$\mathcal{D}_{\mathrm{int}} = \mathbf{\Sigma} : \mathbf{L}^{\mathrm{p}} + \mathbb{A}^{\mathrm{d}} :: \dot{\mathbb{E}}^{\mathrm{d}} + \mathbb{A}^{\mathrm{l}} :: \dot{\mathbb{E}}^{\mathrm{l}} \geq 0\,. \tag{4.16}$$

In order to fulfil Ineq. (4.16), the framework of *generalised standard materials* is again employed and a quadratic and convex plastic potential of the type

$$g^{\mathrm{dis}} = \frac{1}{2}\left[[\mathbf{N}_{\Xi} \otimes \mathbf{N}_{\Xi}] :: \mathbb{A}^{\mathrm{d}}\right]^{2} + \frac{1}{2}\left[\left[\mathbb{I}^{\mathrm{dev}} - \mathbf{N}_{\Xi} \otimes \mathbf{N}_{\Xi}\right] :: \mathbb{A}^{\mathrm{l}}\right]^{2} \tag{4.17}$$

is introduced where $\mathbf{N}_{\Xi} = \mathrm{dev}\mathbf{\Sigma}/\|\mathrm{dev}\mathbf{\Sigma}\|$ is the direction of the deviatoric stress tensor. Application of the framework of *generalised standard materials* leads to the evolution equations

$$\begin{aligned} \dot{\mathbb{E}}^{\mathrm{d}} &= \lambda\, \partial_{\mathbb{A}^{\mathrm{d}}} g^{\mathrm{dis}} = \lambda\, [\mathbf{N}_{\Xi} \otimes \mathbf{N}_{\Xi}] :: \mathbb{A}^{\mathrm{d}}\, [\mathbf{N}_{\Xi} \otimes \mathbf{N}_{\Xi}]\ , \\ \dot{\mathbb{E}}^{\mathrm{l}} &= \lambda\, \partial_{\mathbb{A}^{\mathrm{l}}} g^{\mathrm{dis}} = \lambda\, \left[\mathbb{I}^{\mathrm{dev}} - \mathbf{N}_{\Xi} \otimes \mathbf{N}_{\Xi}\right] :: \mathbb{A}^{\mathrm{l}}\, \left[\mathbb{I}^{\mathrm{dev}} - \mathbf{N}_{\Xi} \otimes \mathbf{N}_{\Xi}\right] \end{aligned} \tag{4.18}$$

and consequently to the hardening related rates

$$\begin{aligned} \dot{\mathbb{A}}^{\mathrm{d}} &= -\lambda\, c^{\mathrm{d}}\, \partial_{\mathbb{A}^{\mathrm{d}}} g^{\mathrm{dis}} = -\lambda\, c^{\mathrm{d}}\, [\mathbf{N}_{\Xi} \otimes \mathbf{N}_{\Xi}] :: \mathbb{A}^{\mathrm{d}}\, [\mathbf{N}_{\Xi} \otimes \mathbf{N}_{\Xi}]\ , \\ \dot{\mathbb{A}}^{\mathrm{l}} &= -\lambda\, c^{\mathrm{l}}\, \partial_{\mathbb{A}^{\mathrm{l}}} g^{\mathrm{dis}} = -\lambda\, c^{\mathrm{l}}\, \left[\mathbb{I}^{\mathrm{dev}} - \mathbf{N}_{\Xi} \otimes \mathbf{N}_{\Xi}\right] :: \mathbb{A}^{\mathrm{l}}\, \left[\mathbb{I}^{\mathrm{dev}} - \mathbf{N}_{\Xi} \otimes \mathbf{N}_{\Xi}\right]\ . \end{aligned} \tag{4.19}$$

As a result, $\mathbb{E}^{\mathrm{d}}$ evolves in the loading direction $[\mathbf{N}_{\Xi} \otimes \mathbf{N}_{\Xi}]$ (dynamic hardening), while $\mathbb{E}^{\mathrm{l}}$ evolves in the orthogonal direction $\left[\mathbb{I}^{\mathrm{dev}} - \mathbf{N}_{\Xi} \otimes \mathbf{N}_{\Xi}\right]$ (latent hardening). Since $[\mathbf{N}_{\Xi} \otimes \mathbf{N}_{\Xi}] :: \left[\mathbb{I}^{\mathrm{dev}} - \mathbf{N}_{\Xi} \otimes \mathbf{N}_{\Xi}\right] = 0$ this decomposition is indeed orthogonal. Assuming an associated flow rule of the type

$$\mathbf{L}^{\mathrm{p}} = \lambda\, \partial_{\mathbf{\Sigma}} \phi = \lambda/\Sigma^{\mathrm{eq}}\, [\mathbb{H} : \Xi]\,, \tag{4.20}$$

thermodynamical consistency of the model can be checked in a straightforward manner. To be more precise, the dissipation inequality implied by the model reads

$$\mathcal{D}_{\mathrm{int}} = \lambda\, Q_0^{\mathrm{eq}} + \lambda\, 2\, g^{\mathrm{dis}} \geq 0. \tag{4.21}$$

The factor 2 occurring in this equation is a result of g being positively homogeneous of degree two with respect to $\mathbb{A}^{\mathrm{d}}$ and $\mathbb{A}^{\mathrm{l}}$. Along with the thermodynamical consistency, the yield surfaces saturate and the stress states are therefore bounded (see Remark 4.1.1).

Remark 4.1.1: *In the following, it is shown first that the yield function indeed converges to a limiting yield surface. For that purpose, an arbitrary loading path is approximated by piece wise radial loading paths. If the respective radial loading direction (normalized relative stress) is given by* $\mathbf{N}_{\Xi}$*, the evolution equation corresponding to dynamic hardening (cf. Eq.* (4.19)*) yields the analytical solution*

$$\mathbb{A}^{\mathrm{d}}(t) = \overset{8}{\mathrm{EXP}}\left(-\Delta\lambda\, c^{\mathrm{d}}\, [\mathbf{N}_{\Xi} \otimes \mathbf{N}_{\Xi}] \otimes [\mathbf{N}_{\Xi} \otimes \mathbf{N}_{\Xi}]\right) :: \mathbb{A}^{\mathrm{d}}_0\,, \tag{4.22}$$

where $\mathbb{A}^{\mathrm{d}}_0$ *represents the initial state of* $\mathbb{A}^{\mathrm{d}}(t)$ *and* $\Delta\lambda$ *is the integrated plastic multiplier. By a standard Taylor-series expansion (see Section 4.3.1) of the eighth-order exponential* *map* $\overset{8}{\mathrm{EXP}}$ *the evolution equation can be simplified. Inserting the derived equations* (4.61) *yields eventually for* $c^{\mathrm{d}} \geq 0$

$$\mathbb{A}^{\mathrm{d}} \overset{t\to\infty}{\to} \mathbb{A}^{\mathrm{d}}_0 - [\mathbf{N}_\Xi \otimes \mathbf{N}_\Xi] \otimes [\mathbf{N}_\Xi \otimes \mathbf{N}_\Xi] :: \mathbb{A}^{\mathrm{d}}_0 \,. \tag{4.23}$$

As a result, $\mathbb{A}^{\mathrm{d}}$ *indeed converges. Analogously, it can be shown that latent hardening converges to (if* $c^{\mathrm{l}} \geq 0$ *and* $\mathbb{A}^{\mathrm{l}}_0$ *being the initial latent state)*

$$\mathbb{A}^{\mathrm{l}} \overset{t\to\infty}{\to} \mathbb{A}^{\mathrm{l}}_0 - \frac{1}{7} \left[\mathbb{I}^{\mathrm{dev}} - \mathbf{N}_\Xi \otimes \mathbf{N}_\Xi\right] \otimes \left[\mathbb{I}^{\mathrm{dev}} - \mathbf{N}_\Xi \otimes \mathbf{N}_\Xi\right] :: \mathbb{A}^{\mathrm{l}}_0 \,. \tag{4.24}$$

Accordingly, the fourth-order tensor $\mathbb{H}$ *saturates.*

Remark 4.1.2: *If the initial values* ${\mathbb{A}^{\mathrm{d}}}_0 = {\mathbb{A}^{\mathrm{l}}}_0 = \mathbb{H}_0 = \mathbb{I}^{\mathrm{dev}}$ *are chosen, together with* $b^{\mathrm{d}} = b^{\mathrm{l}}$ *and* $c^{\mathrm{d}} = 7\, c^{\mathrm{l}}$*, the fourth-order tensor* $\mathbb{H}$ *in Eq.* (4.14) *reduces to*

$$\mathbb{H} = \left[1 - b^{\mathrm{d}} + b^{\mathrm{d}} \exp(-\Delta\lambda_t c^{\mathrm{d}})\right] \mathbb{I}^{\mathrm{dev}} \,. \tag{4.25}$$

According to Eq. (4.25)*, the distortional hardening model is then equivalent to isotropic hardening.*

4.1.3 Prototype model including isotropic, kinematic and distortional hardening

The fully coupled isothermal hardening model including isotropic, kinematic and distortional hardening shows the Helmholtz energy

$$\Psi(\mathbf{F}, \mathbf{F}^{\mathrm{p}}, \alpha^{\mathrm{i}}, \boldsymbol{\alpha}^{\mathrm{k}}, \mathbb{E}^{\mathrm{d}}, \mathbb{E}^{\mathrm{l}}) = \Psi^{\mathrm{el}}(\mathbf{F}^{\mathrm{e}}) + \Psi^{\mathrm{iso}}(\alpha^{\mathrm{i}}) + \Psi^{\mathrm{kin}}(\boldsymbol{\alpha}^{\mathrm{k}}) + \Psi^{\mathrm{dis}}(\mathbb{E}^{\mathrm{d}}, \mathbb{E}^{\mathrm{l}}) \tag{4.26}$$

and the yield function

$$\phi = \Sigma^{\mathrm{eq}} - Q^{\mathrm{i}} - Q^{\mathrm{eq}}_0 \quad \text{with} \quad \Sigma^{\mathrm{eq}} = \sqrt{[\mathrm{dev}\boldsymbol{\Sigma} - \mathbf{Q}^{\mathrm{k}}] : \mathbb{H} : [\mathrm{dev}\boldsymbol{\Sigma} - \mathbf{Q}^{\mathrm{k}}]} \,. \tag{4.27}$$

While isotropic hardening is still modelled by means of the associated ansatz (4.5) and (4.6) – in line with the flow rule – the slightly modified kinematic hardening evolution law

$$\dot{\boldsymbol{\alpha}}^{\mathrm{k}} = \lambda \left[-\partial_{\boldsymbol{\Sigma}}\phi + \frac{b^{\mathrm{k}}}{c^{\mathrm{k}}} \left\|\partial_{\boldsymbol{\Sigma}}\phi\right\| \mathbf{Q}^{\mathrm{k}}\right] \tag{4.28}$$

will be considered in the following, cf. Feigenbaum and Dafalias [43]. In sharp contrast to the original version (4.9), this evolution equation guarantees that the back stress tensor converges, i.e., $\|\mathbf{Q}^{\mathrm{k}}\| \to c^{\mathrm{k}}/b^{\mathrm{k}} < \infty$.

Finally, the distortional hardening model must also be adapted. According to the previous paragraph, the tensor $\mathbf{N}_\Xi = \mathrm{dev}\boldsymbol{\Sigma}/\|\mathrm{dev}\boldsymbol{\Sigma}\|$ defines the dynamic hardening direction. However, if kinematic hardening is present, the physically more relevant relative stresses show the direction

$$\mathbf{N}_\Xi = \frac{\mathrm{dev}\boldsymbol{\Sigma} - \mathbf{Q}^{\mathrm{k}}}{\|\mathrm{dev}\boldsymbol{\Sigma} - \mathbf{Q}^{\mathrm{k}}\|}\,. \tag{4.29}$$

For this reason, $\mathbf{N}_\Xi = \mathrm{dev}\boldsymbol{\Sigma}/\|\mathrm{dev}\boldsymbol{\Sigma}\|$ is replaced by direction (4.29) in the distortional hardening model.

Due to the additive structure of the Helmholtz energy (4.26), distortional hardening does not effect isotropic and kinematic hardening, and thus the considered isotropic and kinematic hardening models comply with the restrictions imposed by the second law of thermodynamics. A straightforward computation of the dissipation inequality for the resulting coupled hardening model yields

$$\mathcal{D}_{\mathrm{int}} = \lambda\, Q_0^{\mathrm{eq}} + \lambda\, \frac{b^{\mathrm{k}}}{c^{\mathrm{k}}}\, \|\partial_{\boldsymbol{\Sigma}}\phi\|\, \mathbf{Q}^{\mathrm{k}} : \mathbf{Q}^{\mathrm{k}} + \lambda\, 2\, g^{\mathrm{dis}} \geq 0\,, \tag{4.30}$$

and thus, the second law of thermodynamics is still fulfilled. Furthermore, simple constraints for modelling parameters b^{d} and b^{l} of the yield evolution can be derived by analysing the convexity of the yield surface. As proven in Remark 4.1.3 convexity of yield surfaces is satisfied for the case $b^{\mathrm{d}}, b^{\mathrm{l}} < 1$.

Remark 4.1.3: *Proving convexity of the yield function for arbitrary fourth-order tensors* $\mathbb{A}^{\mathrm{d}}$ *and* $\mathbb{A}^{\mathrm{l}}$ *is relatively difficult – it is at least difficult to derive simple constraints for the model parameters guaranteeing convexity. Within this model, the initial yield surface is characterised by a von Mises yield function* $\mathbb{H}_0 = \mathbb{A}_0^{\mathrm{d}} = \mathbb{A}_0^{\mathrm{l}} = \mathbb{I}^{\mathrm{dev}}$, *and saturated internal variables are assumed, cf. Eq.* (4.23) *and Eq.* (4.24). *In this case, the saturated fourth-order tensor yields*

$$\mathbb{H} = \mathbb{I}^{\mathrm{dev}} - b^{\mathrm{d}}\, \mathbf{N}_\Xi \otimes \mathbf{N}_\Xi - b^{\mathrm{l}}\, \left[\mathbb{I}^{\mathrm{dev}} - \mathbf{N}_\Xi \otimes \mathbf{N}_\Xi\right]\,. \tag{4.31}$$

Based on Eq. (4.31) *convexity can be analysed. For that purpose, the respective condition* $\mathbf{V} : \frac{\partial^2\phi}{\partial\boldsymbol{\Sigma}^2} : \mathbf{V} \geq 0$ *is computed where* $\mathbf{V}$ *is an arbitrary normalized deviatoric second-order tensor. After a lengthy but straightforward calculation, this inequality can be rewritten as*

$$\|\mathrm{dev}\boldsymbol{\Sigma} - \mathbf{Q}^{\mathrm{k}}\|\, \mathbf{V} : \frac{\partial^2\phi}{\partial\,\boldsymbol{\Sigma}^2} : \mathbf{V} = \frac{(1-\beta^2)(1-b^{\mathrm{l}})}{\sqrt{1-b^{\mathrm{d}}}} \geq 0. \tag{4.32}$$

Since $\beta = \mathbf{V} : \mathbf{N}_\Xi \in [-1, +1]$ *implying* $(1-\beta^2) \geq 0$, *two conditions have to be fulfilled in order to guarantee Ineq. (4.32). They are:*

$$b^{\mathrm{d}} < 1, \quad b^{\mathrm{l}} < 1, \tag{4.33}$$

These conditions are fulfilled for all models presented in Section 4.4.

4.1.4 Distortional hardening with higher curvature in loading direction

As written in Feigenbaum and Dafalias [43], some materials exhibiting dynamic distortional hardening show a higher curvature of the yield surface in loading direction compared to the opposite direction, see right diagram in Fig. 4.1. That can be taken into account by modifying Eq. (4.14) to

$$\mathbb{H} = [1 - b^{\mathrm{d}} - b^{\mathrm{c}}\,[\mathbf{N}_{\Xi} : \mathbf{Q}^{\mathrm{k}}] - b^{\mathrm{l}}]\,\mathbb{H}_0 + [b^{\mathrm{d}} + b^{\mathrm{c}}\,[\mathbf{N}_{\Xi} : \mathbf{Q}^{\mathrm{k}}]]\,\mathbb{A}^{\mathrm{d}} + b^{\mathrm{l}}\,\mathbb{A}^{\mathrm{l}}\,, \tag{4.34}$$

where the factor

$$\mathbf{N}_{\Xi} : \mathbf{Q}^{\mathrm{k}} \tag{4.35}$$

precisely captures the higher curvature in loading direction, cf. Feigenbaum and Dafalias [43]. It bears emphasis that this modification does not change the structure of the dissipation inequality. More explicitly, Ineq. (4.30) is still valid. It can be shown that the the additional material parameter b^{c} has to fulfil the inequality $1 - b^{\mathrm{d}} - b^{\mathrm{c}}\,c^{\mathrm{k}}/b^{\mathrm{k}} > 0$ (see Remark 4.1.4).

Remark 4.1.4: *Since simple constraints for guaranteeing convexity of the yield surface, i.e. Eq.* (4.34)*, are difficult to derive, the model is proven for saturated hardening variables. Within this model, the initial yield surface is characterised by an initial von Mises yield function with* $\mathbb{H}_0 = \mathbb{A}^{\mathrm{d}}_0 = \mathbb{A}^{\mathrm{l}}_0 = \mathbb{I}^{\mathrm{dev}}$*, leading to the saturated fourth-order tensor*

$$\mathbb{H} = \mathbb{I}^{\mathrm{dev}} - \left[b^{\mathrm{d}} + b^{\mathrm{c}}\,\frac{c^{\mathrm{k}}}{b^{\mathrm{k}}}\,\alpha\right]\mathbf{N}_{\Xi}\otimes\mathbf{N}_{\Xi} - b^{\mathrm{l}}\,\left[\mathbb{I}^{\mathrm{dev}} - \mathbf{N}_{\Xi}\otimes\mathbf{N}_{\Xi}\right], \tag{4.36}$$

cf. Eq. (4.14)*. In Eq.* (4.36)*, the saturated back stress*

$$\mathbf{Q}^{\mathrm{k}} \overset{t\to\infty}{\to} \frac{c^{\mathrm{k}}}{b^{\mathrm{k}}}\,\frac{\partial_{\mathbf{\Sigma}}\phi}{\|\partial_{\mathbf{\Sigma}}\phi\|} = \frac{c^{\mathrm{k}}}{b^{\mathrm{k}}}\,\mathbf{N}_{\phi}, \quad \mathbf{N}_{\phi} = \frac{\partial_{\mathbf{\Sigma}}\phi}{\|\partial_{\mathbf{\Sigma}}\phi\|}, \tag{4.37}$$

together with the abbreviation $\alpha = \mathbf{N}_{\Xi} : \mathbf{N}_{\phi}$*, has been inserted.*

Based on Eq. (4.37) *convexity can be analysed. For that purpose, the respective condition* $\mathbf{V} : \frac{\partial^2\phi}{\partial\mathbf{\Sigma}^2} : \mathbf{V} \geq 0$ *is computed with* $\mathbf{V}$ *being an arbitrary second-order tensor. This results into a lengthy inequality which is omitted here for readability. In contrast to a model without higher curvature* ($b^{\mathrm{c}} = 0$)*, simple conditions such as those in Ineq.* (4.33) *cannot be derived for a model exhibiting a higher curvature ($b^{\mathrm{c}} > 0$). However, the necessary condition for convexity*

$$1 - b^{\mathrm{d}} - b^{\mathrm{c}}\,\frac{c^{\mathrm{k}}}{b^{\mathrm{k}}}\,\alpha > 0 \tag{4.38}$$

needs to be satisfied. It can be shown that this condition is equivalent to $\mathbf{V} : \mathbb{H} : \mathbf{V} \geq 0$ for all $\mathbf{V}$. Since $b^{\mathrm{c}} \geq 0$ and $c^{\mathrm{k}}/b^{\mathrm{k}} \geq 0$, Ineq. (4.38) *is fulfilled, if (sufficient condition)*

$$1 - b^{\mathrm{d}} - b^{\mathrm{c}}\,\frac{c^{\mathrm{k}}}{b^{\mathrm{k}}} > 0. \tag{4.39}$$

This constraint is fulfilled by all models in Section 4.4.

4.2 Thermomechanically coupled setting

4.2.1 Fundamentals

According to Subsection 3.1.2.2, a direct coupling of an isothermal elastoplasticity model with the thermal problem through the first law of thermodynamics would generally lead to an over-prediction of the temperature increase due to plastic deformations. This effect is equivalent to an over-prediction of the internal dissipation. To be more precise, the temperature evolution (2.78) can be conveniently approximated for most metals under adiabatic conditions by means of

$$\dot{\Theta} \approx \frac{1}{c}\,\mathcal{D}_{\mathrm{int}}\,, \tag{4.40}$$

which clearly confirms the previous statement. Furthermore, if a positively homogeneous yield function of degree one (such as that defined in Eq. (4.3)) is used, combined with associative evolution equations, the internal dissipation simplifies to $\mathcal{D}_{\mathrm{int}} = \lambda\, Q_0^{\mathrm{eq}}$. This result confirms once again that the over-prediction of the temperature increase is often a result of an initial yield stress Q_0^{eq} which is too large. Similar arguments also hold in the more general case of non-associative evolution equations and the underlying dissipation, e.g. Eq. (4.30). However, the most dominant factor in the dissipation remains the yield stress Q_0^{eq}, which needs to be adjusted. Likewise to the novel thermomechanical coupling in Subsection 3.1.2.2 an adjustment of the Helmholtz energy is also advocated here.

The underlying idea of the thermomechanical framework advocated in Subsection 3.1.2.2 is to shift a certain portion of Q_0^{eq} into isotropic hardening, since only the non-energetic dissipative part of Q_0^{eq} enters the internal dissipation. For that purpose, the Helmholtz energy of the original model is changed to

$$\begin{aligned}\Psi(\mathbf{F},\mathbf{F}^{\mathrm{p}},\alpha^{\mathrm{i}},\boldsymbol{\alpha}^{\mathrm{k}},\mathbb{E}^{\mathrm{d}},\mathbb{E}^{\mathrm{l}}) = \Psi^{\mathrm{el}}(\mathbf{F}^{\mathrm{e}}) + \Psi^{\mathrm{iso}}(\alpha^{\mathrm{i}}) + \Psi^{\mathrm{kin}}(\boldsymbol{\alpha}^{\mathrm{k}}) + \Psi^{\mathrm{dis}}(\mathbb{E}^{\mathrm{d}},\mathbb{E}^{\mathrm{l}}) \\ + \left[\widetilde{Q}_0^{\mathrm{eq}} - Q_0^{\mathrm{eq}}\right]\alpha^{\mathrm{i}}\,,\end{aligned} \tag{4.41}$$

where the last term is new. This modification leads to the new isotropic stress-like hardening variable

$$Q^{\mathrm{i}} = -\frac{\partial\Psi}{\partial\alpha^{\mathrm{i}}} = -\partial_{\alpha^{\mathrm{i}}}\Psi^{\mathrm{iso}} - \widetilde{Q}_0^{\mathrm{eq}} + Q_0^{\mathrm{eq}}. \tag{4.42}$$

Consequently, if $\widetilde{Q}_0^{\mathrm{eq}}$ is assumed to be the initial yield stress, the yield function

$$\phi = \Sigma^{\mathrm{eq}} - Q^{\mathrm{i}} - \widetilde{Q}_0^{\mathrm{eq}} = \Sigma^{\mathrm{eq}} + \partial_{\alpha^{\mathrm{i}}}\Psi^{\mathrm{iso}} - Q_0^{\mathrm{eq}} \tag{4.43}$$

resulting from this modification is identical to that of the original model. Accordingly, the isothermal response of the model is not affected. A straightforward computation of the dissipation resulting from this modified model yields

$$\mathcal{D}_{\mathrm{int}} = \lambda\,\widetilde{Q}_0^{\mathrm{eq}} + \lambda\,\frac{b^{\mathrm{k}}}{c^{\mathrm{k}}}\,\|\partial_{\boldsymbol{\Sigma}}\phi\|\,\mathbf{Q}^{\mathrm{k}} : \mathbf{Q}^{\mathrm{k}} + \lambda\,2\,g^{\mathrm{dis}} \geq 0\,. \tag{4.44}$$

Since the first term in Eq. (4.44) is the most dominant one (for most metals), the internal dissipation can be conveniently controlled by changing $\widetilde{Q}_0^{\mathrm{eq}} < Q_0^{\mathrm{eq}}$. For a better interpretation, the factor

$$\beta^{\mathcal{D}} = \frac{\widetilde{Q}_0^{\mathrm{eq}}}{Q_0^{\mathrm{eq}}} \in [0,1] \tag{4.45}$$

is introduced by which the internal dissipation becomes

$$\mathcal{D}_{\mathrm{int}} = \lambda\,\beta^{\mathcal{D}}\,Q_0^{\mathrm{eq}} + \lambda\,\frac{b^{\mathrm{k}}}{c^{\mathrm{k}}}\,\|\partial_{\boldsymbol{\Sigma}}\phi\|\,\mathbf{Q}^{\mathrm{k}} : \mathbf{Q}^{\mathrm{k}} + \lambda\,2\,g^{\mathrm{dis}} \geq 0\,. \tag{4.46}$$

Again, $\beta^{\mathcal{D}}$ is related to the classic Taylor-Quinney factor. However, as deduced in Chapter 3 the presented modification is thermodynamically consistent: the first and the second law of thermodynamics are fulfilled. Furthermore, the energetic term $\widetilde{Q}_0^{\mathrm{eq}} - Q_0^{\mathrm{eq}}$ give rise to an initially existing pre-hardening due to an underlying manufacturing process, cf. p. 39.

4.2.2 Prototype model

A thermomechanically coupled distortional hardening framework is obtained by incorporating the isothermal distortional hardening models as discussed in Subsections 4.1.3 and 4.1.4 into the thermomechanical setting outlined in the previous subsection. This coupling leads to a Helmholtz energy of the type

$$\Psi = \Psi^{\mathrm{el}}(\mathbf{F}^{\mathrm{e}}, \Theta) + \Psi^{\mathrm{pl}}(\boldsymbol{\alpha}, \Theta)\,, \tag{4.47}$$

in which the two involved energies are chosen as

$$\Psi^{\mathrm{el}}(\mathbf{F}, \mathbf{F}^{\mathrm{p}}, \Theta) = \Psi^{\mathrm{el}}_{\mathrm{mech}}(\mathbf{F}^{\mathrm{e}}) + M(\mathbf{F}^{\mathrm{e}}, \Theta) + T(\Theta) \tag{4.48}$$

and

$$\begin{aligned} \Psi^{\mathrm{pl}}(\alpha^{\mathrm{i}}, \boldsymbol{\alpha}^{\mathrm{k}}, \mathbb{E}^{\mathrm{d}}, \mathbb{E}^{\mathrm{l}}, \Theta) = {} & \Psi^{\mathrm{iso}}(\alpha^{\mathrm{i}}) + \Psi^{\mathrm{kin}}(\boldsymbol{\alpha}^{\mathrm{k}}) + \Psi^{\mathrm{dis}}(\mathbb{E}^{\mathrm{d}}, \mathbb{E}^{\mathrm{l}}) \\ & + \left[\beta^{\mathcal{D}} - 1\right]\, Q_0^{\mathrm{eq}}(\Theta)\, \alpha^{\mathrm{i}}\,. \end{aligned} \tag{4.49}$$

In Eq. (4.48), $\Psi^{\mathrm{el}}_{\mathrm{mech}}$ corresponds to the purely mechanical part of Ψ^{el}, the energy M is associated with the thermoelastic coupling and T covers the purely thermal part. By comparing Eq. (4.49) to its isothermal counterpart (4.41), it can be seen that the only influence of the temperature on Ψ^{pl} is through the temperature-dependent yield stress $Q_0^{\mathrm{eq}}(\Theta)$. Certainly, temperature-dependent hardening could also be taken into account in a similar straightforward manner. However, this effect is not very pronounced for most metallic alloys in a temperature range of $0 - 100$ K, cf. Hodowany et al. [54], Rosakis et al. [109]. With regard to the temperature-dependent part, linear thermal softening is assumed, resulting in the yield stress

$$Q_0^{\mathrm{eq}} = y_0\,[1 - \omega_0\,[\Theta - \Theta_0]]\,. \tag{4.50}$$

In Eq. (4.50), y_0 is the yield stress at reference temperature Θ_0, while the coefficient ω_0 controls the thermal softening slope. It is subjected to constraint $\omega_0\,[\Theta - \Theta_0] \leq 1$. Otherwise, the effective temperature-dependent yield stress would be negative and the second law of thermodynamics would also be violated. A prototype model falling into the range of the coupled setting proposed here is summarised in Fig. 4.2.

4.3 Numerical implementation

The numerical implementation of the presented thermomechanically coupled framework suitable for distortional hardening is elaborated here. While the update of the internal variables and the computation of the stresses is outlined in Subsection 4.3.1, Subsection 4.3.2 is associated with an efficient finite element formulation for the solution of the thermomechanically coupled boundary value problem.

- Helmholtz energy:

$$
\begin{aligned}
\Psi &= \Psi^{\mathrm{el}}(\mathbf{F}^{\mathrm{e}},\Theta) + \Psi^{\mathrm{pl}}(\alpha^{\mathrm{i}},\boldsymbol{\alpha}^{\mathrm{k}},\mathbb{E}^{\mathrm{d}},\mathbb{E}^{\mathrm{l}},\Theta)\\
\Psi^{\mathrm{el}} &= \underbrace{W(\mathbf{F}^{\mathrm{e}})}_{\text{Eq.(4.87)}} + \underbrace{U(J)}_{\text{Eq.(4.88)}} + \underbrace{M(J,\Theta)}_{\text{Eq.(4.93)}} + \underbrace{T(\Theta)}_{\text{Eq.(4.94)}}\\
\Psi^{\mathrm{pl}} &= \underbrace{\Psi^{\mathrm{iso}}(\alpha^{\mathrm{i}})}_{\text{Eq.(4.5)}} + \underbrace{\Psi^{\mathrm{kin}}(\boldsymbol{\alpha}^{\mathrm{k}})}_{\text{Eq.(4.8)}} + \underbrace{\Psi^{\mathrm{dis}}(\mathbb{E}^{\mathrm{d}},\mathbb{E}^{\mathrm{l}})}_{\text{Eq.(4.12)}} + \left[\beta^{\mathcal{D}} - 1\right]\, Q_0^{\mathrm{eq}}(\Theta)\,\alpha^{\mathrm{i}}
\end{aligned}
$$

- Yield function:

$$
\phi = \Sigma^{\mathrm{eq}} - Q^{\mathrm{i}} - Q_0^{\mathrm{eq}}(\Theta) \qquad \text{with} \qquad \Sigma^{\mathrm{eq}} = \sqrt{\boldsymbol{\Xi} : \mathbb{H} : \boldsymbol{\Xi}}\,, \quad \boldsymbol{\Xi} = \mathrm{dev}\boldsymbol{\Sigma} - \mathbf{Q}^{\mathrm{k}}
$$

- Tensor defining the material symmetry:

$$
\begin{aligned}
&\mathbb{H} = [1 - b^{\mathrm{d}} - b^{\mathrm{c}}\,[\mathbf{N}_\Xi : \mathbf{Q}^{\mathrm{k}}] - b^{\mathrm{l}}]\,\mathbb{H}_0 + [b^{\mathrm{d}} + b^{\mathrm{c}}\,[\mathbf{N}_\Xi : \mathbf{Q}^{\mathrm{k}}]]\,\mathbb{A}^{\mathrm{d}} + b^{\mathrm{l}}\,\mathbb{A}^{\mathrm{l}}\,,\\
&\mathbf{N}_\Xi = \boldsymbol{\Xi}/\|\boldsymbol{\Xi}\|
\end{aligned}
$$

- Driving forces:

$$
\begin{aligned}
&\boldsymbol{\Sigma} = \mathbf{F}^{\mathrm{eT}} \cdot \partial_{\mathbf{F}^{\mathrm{e}}}\Psi\,, \qquad \mathbf{Q}^{\mathrm{k}} = -c^{\mathrm{k}}\,\boldsymbol{\alpha}^{\mathrm{k}}\,, \qquad Q^{\mathrm{i}} = -c^{\mathrm{i}}\,\left[\exp(b^{\mathrm{i}}\,\alpha^{\mathrm{i}}) - 1\right]\,,\\
&\mathbb{A}^{\mathrm{d}} = -c^{\mathrm{d}}\,\mathbb{E}^{\mathrm{d}}\,, \qquad \mathbb{A}^{\mathrm{l}} = -c^{\mathrm{l}}\,\mathbb{E}^{\mathrm{l}}
\end{aligned}
$$

- Evolution equations:

$$
\begin{aligned}
\dot{\mathbf{F}}^{\mathrm{p}} &= \mathbf{L}^{\mathrm{p}} \cdot \mathbf{F}^{\mathrm{p}} = \lambda\,\partial_{\boldsymbol{\Sigma}}\phi \cdot \mathbf{F}^{\mathrm{p}}\\
\dot{\alpha}^{\mathrm{i}} &= -\lambda\,,\\
\dot{\boldsymbol{\alpha}}^{\mathrm{k}} &= -\lambda\,\left[\partial_{\boldsymbol{\Sigma}}\phi + b^{\mathrm{k}}\,\|\partial_{\boldsymbol{\Sigma}}\phi\|\,\boldsymbol{\alpha}^{\mathrm{k}}\right]\,,\\
\dot{\mathbb{E}}^{\mathrm{d}} &= \lambda\,[\mathbf{N}_\Xi \otimes \mathbf{N}_\Xi] :: \mathbb{A}^{\mathrm{d}}\,[\mathbf{N}_\Xi \otimes \mathbf{N}_\Xi]\,,\\
\dot{\mathbb{E}}^{\mathrm{l}} &= \lambda\,\left[\mathbb{I}^{\mathrm{dev}} - \mathbf{N}_\Xi \otimes \mathbf{N}_\Xi\right] :: \mathbb{A}^{\mathrm{l}}\,\left[\mathbb{I}^{\mathrm{dev}} - \mathbf{N}_\Xi \otimes \mathbf{N}_\Xi\right]
\end{aligned}
$$

- State equations:
  First Piola-Kirchhoff stresses, entropy, specific heat capacity, heat flux, mechanically induced self-heating

$$
\begin{aligned}
&\mathbf{P} = \partial_{\mathbf{F}}\Psi = \partial_{\mathbf{F}^{\mathrm{e}}}\Psi \cdot \mathbf{F}^{\mathrm{p-T}}\,, \qquad N = -\partial_\Theta\Psi\,, \qquad c = -\Theta\,\partial_{\Theta\Theta}\Psi\,,\\
&\boldsymbol{\mathcal{Q}} = -k_0\,\mathrm{GRAD}\Theta \qquad \text{(see Eq. (2.53))}\\
&\mathcal{H}_\Theta = \mathcal{A} + \mathcal{D}_{\mathrm{int}} = \Theta\frac{\partial^2\Psi}{\partial J\partial\Theta}\,\dot{J}\\
&\qquad + \lambda\,\left[\beta^{\mathcal{D}}\,y_0\,\left[1 - \omega_0\,\left[\frac{\Theta}{\beta^{\mathcal{D}}} - \Theta_0\right]\right] + \frac{b^{\mathrm{k}}}{c^{\mathrm{k}}}\,\|\partial_{\boldsymbol{\Sigma}}\phi\|\,\mathbf{Q}^{\mathrm{k}} : \mathbf{Q}^{\mathrm{k}} + 2\,g^{\mathrm{dis}}\right]
\end{aligned}
$$

Figure 4.2: Thermomechanically coupled elastoplasticity model accounting for isotropic, kinematic and distortional hardening including a higher curvature of the yield surface in loading direction

4.3.1 Constitutive updates

A return-mapping-type algorithm for the computation of updated internal variables and stresses is presented here. In order to derive this algorithm, partition

$$\tau = \bigcup_{n=1}^{n_\tau} [t_n, t_{n+1}] \tag{4.51}$$

of the total time interval is considered. Furthermore, an elastic trial state in the considered time interval $[t_n, t_{n+1}]$ is introduced in standard manner, i.e., by means of

$$\mathbf{F}^{\mathrm{p}}_{n+1} = \mathbf{F}^{\mathrm{p}}_{n}, \quad \alpha^{\mathrm{i}}_{n+1} = \alpha^{\mathrm{i}}_{n}, \quad \boldsymbol{\alpha}^{\mathrm{k}}_{n+1} = \boldsymbol{\alpha}^{\mathrm{k}}_{n}, \quad \mathbb{A}^{\mathrm{d}}_{n+1} = \mathbb{A}^{\mathrm{d}}_{n}, \quad \mathbb{A}^{\mathrm{l}}_{n+1} = \mathbb{A}^{\mathrm{l}}_{n}. \tag{4.52}$$

Based on this state, the trial yield function

$$\phi_{\text{trial}} = \phi(\boldsymbol{\Sigma}_{\text{trial}}, \alpha^{\mathrm{i}}_{n}, \boldsymbol{\alpha}^{\mathrm{k}}_{n}, \mathbb{A}^{\mathrm{d}}_{n}, \mathbb{A}^{\mathrm{l}}_{n}) \quad \text{with} \quad \boldsymbol{\Sigma}_{\text{trial}} = {\mathbf{F}^{\mathrm{e}}_{\text{trial}}}^{\mathrm{T}} \cdot \partial_{\mathbf{F}^{\mathrm{e}}} \Psi \big|_{\mathbf{F}^{\mathrm{e}}_{\text{trial}}} \tag{4.53}$$

and

$$\mathbf{F}^{\mathrm{e}}_{\text{trial}} = \mathbf{F}_{n+1} \cdot {\mathbf{F}^{\mathrm{p}}_{n}}^{-1} \tag{4.54}$$

can be evaluated.
If plasticity occurs within the considered time interval $[t_n, t_{n+1}]$ by $\phi_{\text{trial}} > 0$, the evolution equations have to be integrated. For that purpose, a standard exponential integration scheme is applied to the flow rule yielding

$$\mathbf{F}^{\mathrm{p}}_{n+1} = \mathrm{EXP}\left(\Delta\lambda \, \partial_{\boldsymbol{\Sigma}} \phi|_{n+1}\right) \cdot \mathbf{F}^{\mathrm{p}}_{n} \,, \tag{4.55}$$

with EXP(•) being the exponential map for second-order tensors, whereas a backward Euler integration is adopted for the evolution equations of isotropic and kinematic hardening, i.e.,

$$\begin{aligned} \alpha^{\mathrm{i}}_{n+1} &= \alpha^{\mathrm{i}}_{n} - \Delta\lambda \,, \\ \boldsymbol{\alpha}^{\mathrm{k}}_{n+1} &= \frac{\boldsymbol{\alpha}^{\mathrm{k}}_{n} - \Delta\lambda \, \partial_{\boldsymbol{\Sigma}} \phi|_{n+1}}{1 + \Delta\lambda \, b^{\mathrm{k}} \, \|\partial_{\boldsymbol{\Sigma}} \phi|_{n+1}\|} \,. \end{aligned} \tag{4.56}$$

Regarding the fourth-order tensors $\mathbb{A}^{\mathrm{d}}$ and $\mathbb{A}^{\mathrm{l}}$, a different time integration is proposed, since a straightforward application of an implicit scheme would result in $2 \times 3 \times 3 \times 3 \times 3 = 162$ additional equations. Starting points of this integration scheme are the differential equations (see Eq. (4.19))

$$\begin{aligned} \dot{\mathbb{A}}^{\mathrm{d}} &= -\lambda \, c^{\mathrm{d}} \left[\mathbf{N}_{\Xi} \otimes \mathbf{N}_{\Xi}\right] :: \mathbb{A}^{\mathrm{d}} \left[\mathbf{N}_{\Xi} \otimes \mathbf{N}_{\Xi}\right] , \\ \dot{\mathbb{A}}^{\mathrm{l}} &= -\lambda \, c^{\mathrm{l}} \left[\mathbb{I}^{\mathrm{dev}} - \mathbf{N}_{\Xi} \otimes \mathbf{N}_{\Xi}\right] :: \mathbb{A}^{\mathrm{l}} \left[\mathbb{I}^{\mathrm{dev}} - \mathbf{N}_{\Xi} \otimes \mathbf{N}_{\Xi}\right] . \end{aligned} \tag{4.57}$$

Here, the notation

$$\mathbf{N}_\Xi = \frac{\mathbf{\Xi}}{\|\mathbf{\Xi}\|} = \frac{\mathrm{dev}\mathbf{\Sigma} - \mathbf{Q}^\mathrm{k}}{\|\mathrm{dev}\mathbf{\Sigma} - \mathbf{Q}^\mathrm{k}\|} \tag{4.58}$$

for the direction of the relative stresses has been used. By assuming a piece-wise constant approximation of $\mathbf{N}_\Xi$, the analytical solution of Eq. (4.57) reads

$$\begin{aligned} \mathbb{A}^\mathrm{d}(t) &= \overset{8}{\mathrm{EXP}}\left(-\Delta\lambda\, c^\mathrm{d}\,[\mathbf{N}_\Xi \otimes \mathbf{N}_\Xi] \otimes [\mathbf{N}_\Xi \otimes \mathbf{N}_\Xi]\right) :: \mathbb{A}^\mathrm{d}_0\,, \\ \mathbb{A}^\mathrm{l}(t) &= \overset{8}{\mathrm{EXP}}\left(-\Delta\lambda\, c^\mathrm{l}\left[\mathbb{I}^\mathrm{dev} - \mathbf{N}_\Xi \otimes \mathbf{N}_\Xi\right] \otimes \left[\mathbb{I}^\mathrm{dev} - \mathbf{N}_\Xi \otimes \mathbf{N}_\Xi\right]\right) :: \mathbb{A}^\mathrm{l}_0\,, \end{aligned} \tag{4.59}$$

with $\mathbb{A}^\mathrm{d}_0 = \mathbb{A}^\mathrm{d}(t_n)$ and $\mathbb{A}^\mathrm{l}_0 = \mathbb{A}^\mathrm{l}(t_n)$. If this assumption does not hold, Eq. (4.59) is a time-discrete approximation of Eq. (4.57). It bears emphasis that the by now standard exponential map for $\mathbf{F}^\mathrm{p}_{n+1}$ in Eq. (4.55) is based on the same idea. In Eq. (4.59), $\overset{8}{\mathrm{EXP}}(\bullet)$ denotes the exponential map of an eighth-order tensor $(\bullet)$. In order to reduce the extensive calculation of this exponential map, the identities

$$\mathbb{N} \otimes \mathbb{N} :: \mathbb{N} \otimes \mathbb{N} = \begin{cases} \mathbb{N} \otimes \mathbb{N} & \text{for} \quad \mathbb{N} = [\mathbf{N}_\Xi \otimes \mathbf{N}_\Xi] \\ 7\,\mathbb{N} \otimes \mathbb{N} & \text{for} \quad \mathbb{N} = \left[\mathbb{I}^\mathrm{dev} - \mathbf{N}_\Xi \otimes \mathbf{N}_\Xi\right] \end{cases} \tag{4.60}$$

are used within a Taylor series expansion of Eq. (4.59). Based on the identities (4.60), the exponential mappings (4.59) can be rewritten as

$$\begin{aligned} &\overset{8}{\mathrm{EXP}}\left(-\Delta\lambda\, c^\mathrm{d}\,[\mathbf{N}_\Xi \otimes \mathbf{N}_\Xi] \otimes [\mathbf{N}_\Xi \otimes \mathbf{N}_\Xi]\right) = \\ &\qquad \overset{8}{\mathbb{I}} + \left[\exp\left(-\Delta\lambda\, c^\mathrm{d}\right) - 1\right]\,[\mathbf{N}_\Xi \otimes \mathbf{N}_\Xi] \otimes [\mathbf{N}_\Xi \otimes \mathbf{N}_\Xi]\ , \\ &\overset{8}{\mathrm{EXP}}\left(-\Delta\lambda\, c^\mathrm{l}\left[\mathbb{I}^\mathrm{dev} - \mathbf{N}_\Xi \otimes \mathbf{N}_\Xi\right] \otimes \left[\mathbb{I}^\mathrm{dev} - \mathbf{N}_\Xi \otimes \mathbf{N}_\Xi\right]\right) = \\ &\qquad \overset{8}{\mathbb{I}} + \left[\frac{1}{7}\,\exp\left(-\Delta\lambda\, 7\, c^\mathrm{l}\right) - 1\right]\,\left[\mathbb{I}^\mathrm{dev} - \mathbf{N}_\Xi \otimes \mathbf{N}_\Xi\right] \otimes \left[\mathbb{I}^\mathrm{dev} - \mathbf{N}_\Xi \otimes \mathbf{N}_\Xi\right]\ , \end{aligned} \tag{4.61}$$

with $\overset{8}{\mathbb{I}}$ denoting the eighth-order identity tensor defined as $\overset{8}{\mathbb{I}} :: \mathbb{A} = \mathbb{A},\ \forall\mathbb{A}$. Accordingly, the numerically extensive exponential map for the eighth-order tensor has been replaced by means of the exponential function (exp) for scalars. Clearly, this modification significantly improves the numerical efficiency of the algorithm. Based on Eqs. (4.61), the time integration scheme (4.59) can be replaced by means of the equivalent equations

$$
\begin{aligned}
\mathbb{A}^{\mathrm{d}}(t) &= \mathbb{A}^{\mathrm{d}}_0 + \left[\exp\left(-\Delta\lambda\, c^{\mathrm{d}}\right) - 1\right] \Big\{ \left[\mathbf{N}_\Xi \otimes \mathbf{N}_\Xi\right] :: \mathbb{A}^{\mathrm{d}}_0 \Big\} \left[\mathbf{N}_\Xi \otimes \mathbf{N}_\Xi\right] , \\
\mathbb{A}^{\mathrm{l}}(t) &= \mathbb{A}^{\mathrm{l}}_0 + \frac{1}{7} \left[\exp\left(-\Delta\lambda\, 7\, c^{\mathrm{l}}\right) - 1\right] \Big\{ \left[\mathbb{I}^{\mathrm{dev}} - \mathbf{N}_\Xi \otimes \mathbf{N}_\Xi\right] :: \mathbb{A}^{\mathrm{l}}_0 \Big\} \left[\mathbb{I}^{\mathrm{dev}} - \mathbf{N}_\Xi \otimes \mathbf{N}_\Xi\right] .
\end{aligned}
\tag{4.62}
$$

Such equations are now used for any time interval resulting in the novel time integration

$$
\begin{aligned}
\mathbb{A}^{\mathrm{d}}_{n+1} &= \mathbb{A}^{\mathrm{d}}_n + \left[\exp\left(-\Delta\lambda\, c^{\mathrm{d}}\right) - 1\right] \Big\{ \\
&\qquad \left[\mathbf{N}_{\Xi,n+1} \otimes \mathbf{N}_{\Xi,n+1}\right] :: \mathbb{A}^{\mathrm{d}}_n \Big\} \left[\mathbf{N}_{\Xi,n+1} \otimes \mathbf{N}_{\Xi,n+1}\right] , \\
\mathbb{A}^{\mathrm{l}}_{n+1} &= \mathbb{A}^{\mathrm{l}}_n + \left[\frac{1}{7} \exp\left(-\Delta\lambda\, 7\, c^{\mathrm{l}}\right) - 1\right] \Big\{ \\
&\qquad \left[\mathbb{I}^{\mathrm{dev}} - \mathbf{N}_{\Xi,n+1} \otimes \mathbf{N}_{\Xi,n+1}\right] :: \mathbb{A}^{\mathrm{l}}_n \Big\} \left[\mathbb{I}^{\mathrm{dev}} - \mathbf{N}_{\Xi,n+1} \otimes \mathbf{N}_{\Xi,n+1}\right] .
\end{aligned}
\tag{4.63}
$$

Finally, the fourth-order tensor $\mathbb{H}$ defining the shape (distortion) of the yield surface can be computed by means of Eq. (4.63). By considering Eq. (4.34) for $\mathbb{H}_0 = \mathbb{I}^{\mathrm{dev}}$, the update

$$
\mathbb{H}_{n+1} = [1 - b^{\mathrm{d}} - b^{\mathrm{c}}\,[\mathbf{N}_{\Xi,n+1} : \mathbf{Q}^{\mathrm{k}}_n] - b^{\mathrm{l}}]\, \mathbb{I}^{\mathrm{dev}} + [b^{\mathrm{d}} + b^{\mathrm{c}}\,[\mathbf{N}_{\Xi,n+1} : \mathbf{Q}^{\mathrm{k}}_n]]\, \mathbb{A}^{\mathrm{d}}_{n+1} + b^{\mathrm{l}}\, \mathbb{A}^{\mathrm{l}_{n+1}} \tag{4.64}
$$

is advocated. It bears emphasis that the coupling $\mathbf{N}_\Xi : \mathbf{Q}^{\mathrm{k}}$ between kinematic and disproportional hardening, necessary if a higher curvature of the yield surface in loading direction is to be modelled, is approximated in a mixed explicit/implicit manner. To be more precise, $\mathbf{N}_{\Xi,n+1} : \mathbf{Q}^{\mathrm{k}}_{n+1} \approx \mathbf{N}_{\Xi,n+1} : \mathbf{Q}^{\mathrm{k}}_n$. This approximation turned out to improve the efficiency of the implementation without degrading the numerical accuracy, cf. Remark 4.3.1. However, this approximation is certainly not mandatory and a fully implicit scheme could also be used. Furthermore, if a higher curvature in loading direction is not modelled (factor $b^{\mathrm{c}} = 0$), Eq. (4.64) is indeed a fully implicit update scheme.

According to Eqs. (4.55)–(4.56) and Eqs. (4.63)–(4.64), the updated internal variables can be expressed in terms of the unknowns $\boldsymbol{\chi} = \{\Delta\lambda, \Xi_{n+1}\}$. They follow from the solution of the non-linear set of algebraic equations

$$
\mathbf{r}_\chi(\Delta\lambda, \Xi_{n+1}) = \begin{bmatrix} \phi \\ \mathbf{r}_\Xi \end{bmatrix} = \begin{bmatrix} \sqrt{\Xi_{n+1} : \mathbb{H}(\Delta\lambda, \Xi_{n+1}) : \Xi_{n+1}} - Q^{\mathrm{i}}(\Delta\lambda) - Q^{\mathrm{eq}}_0(\Theta_{n+1}) \\ \Xi_{n+1} - \mathrm{dev}\boldsymbol{\Sigma}(\mathbf{F}_{n+1}, \Theta_{n+1}, \Delta\lambda, \Xi_{n+1}) + \mathbf{Q}^{\mathrm{k}}(\Delta\lambda, \Xi_{n+1}) \end{bmatrix} = \mathbf{0} . \tag{4.65}
$$

The solution of the 7 (10) dimensional problem is computed by employing a Newton-type iteration (7 unknowns in the case of symmetric Mandel stresses, 10 unknowns in the case of non-symmetric Mandel stresses). It is noteworthy that the number of unknowns of the considered complex distortional hardening model is thus as small as the number of unknowns of standard isotropic hardening models. However, and in contrast to isotropic models where only 10 internal variables have to be stored ($\mathbf{F}^{\mathrm{p}}_n$ and α^{i}_n), a naive storage implementation would require $\{\mathbf{F}^{\mathrm{p}}_n, \alpha^{\mathrm{i}}_n, \boldsymbol{\alpha}^{\mathrm{k}}_n, \mathbb{A}^{\mathrm{d}}_n, \mathbb{A}^{\mathrm{l}}_n\}$, $9+1+9+81+81 = 181$ variables. By considering the initial conditions $\mathbb{A}^{\mathrm{d}}_0 = \mathbb{A}^{\mathrm{l}}_0 = \mathbb{I}^{\mathrm{dev}}$ as well as the minor and major symmetries of $\mathbb{A}^{\mathrm{d}}$ and $\mathbb{A}^{\mathrm{l}}$, the $81+81$ components of the fourth-order tensors $\mathbb{A}^{\mathrm{d}}$ and $\mathbb{A}^{\mathrm{l}}$ can be spanned by means of only $21+21$ independent history variables. If it is additionally taken into account that $\mathbb{A}^{\mathrm{d}}$ and $\mathbb{A}^{\mathrm{l}}$ are deviatoric tensors (projections), the $21{+}21$ independent variables can be further reduced to $15{+}15$. By doing so, the resulting algorithm is very efficient in terms of the computing time (only 7 (10) unknowns in the return-mapping scheme) and in terms of storage (only $9{+}1{+}9{+}15{+}15 = 49$ independent variables have to be stored).

A summary of the resulting return-mapping scheme is given in Fig. 4.3. Having computed the solution of Eq. (4.65), the updated internal variables as well as the updated stresses can be calculated.

Remark 4.3.1: *If a higher curvature of the yield surface in loading direction was considered by setting $b^{\mathrm{c}} \neq 0$, a fully implicit time integration, together with a fully implicit coupling factor of the type $\mathbf{N}_{\Xi,n+1} : \mathbf{Q}^{\mathrm{k}}_{n+1}$, would not allow to express the fourth-order tensor $\mathbb{H}_{n+1}$ only in terms of $\Delta\lambda$ and Ξ_{n+1}. Consequently, an additional fourth-order tensor would enter the set of unknowns, significantly worsening the numerical performance. However, numerical experiments showed that the approximation $\mathbf{N}_{\Xi,n+1} : \mathbf{Q}^{\mathrm{k}}_{n} \approx \mathbf{N}_{\Xi,n+1} : \mathbf{Q}^{\mathrm{k}}_{n+1}$ has only little influence on the numerical accuracy and, therefore, the approximation seems to be reasonable.*

4.3.2 Weak form – FEM implementation

While the updated internal variables and the stresses follow from the (local) return-mapping scheme, the computation of the primary fields $\boldsymbol{\varphi}$ and Θ requires the consideration of the global boundary value problem. The starting point of the finite element formulation to be elaborated is the weak form of balance of linear momentum

$$\delta W_{\boldsymbol{\varphi}} = \int\limits_{\mathcal{B}_0} \mathbf{P} : \delta\mathbf{F}\,\mathrm{d}V - \int\limits_{\partial\mathcal{B}_0} \delta\boldsymbol{\varphi}\cdot\mathbf{T}\,\mathrm{d}A - \int\limits_{\mathcal{B}_0} \delta\boldsymbol{\varphi}\cdot\rho_0\mathbf{B}\,\mathrm{d}V = 0 \qquad \forall\,\delta\boldsymbol{\varphi} \in \mathcal{H}^1_0(\mathcal{B}_0) \tag{4.66}$$

```
1. Given state:
   current global variables: $\{\mathbf{F}, \Theta\}$
   history variables at time $t_n$: $\boldsymbol{\Gamma}_n = \{\mathbf{F}^\mathrm{p}_n, \alpha^\mathrm{i}_n, \boldsymbol{\alpha}^\mathrm{k}_n, \mathbb{A}^\mathrm{d}_n, \mathbb{A}^\mathrm{l}_n\}$

2. Compute trial state:
   compute trial strains: $\mathbf{F}^\mathrm{e}_\text{trial} = \mathbf{F} \cdot {\mathbf{F}^\mathrm{p}_n}^{-1}$
   compute trial stresses: $\boldsymbol{\Sigma}_\text{trial} = {\mathbf{F}^\mathrm{e}_\text{trial}}^\mathrm{T} \cdot \partial_{\mathbf{F}^\mathrm{e}} \Psi(\mathbf{F}^\mathrm{e}_\text{trial})$, $\boldsymbol{\Xi}_\text{trial} = \mathrm{dev}\boldsymbol{\Sigma}_\text{trial} - \mathbf{Q}^\mathrm{k}_n$

3. Check yield condition:
   compute: $\phi_\text{trial} = \sqrt{\boldsymbol{\Xi}_\text{trial} : \mathbb{H}_n : \boldsymbol{\Xi}_\text{trial}} - Q^\mathrm{i}_n - Q^\mathrm{eq}_0(\Theta)$ with $\mathbb{H}_n = \mathbb{H}(\mathbb{A}^\mathrm{d}_n, \mathbb{A}^\mathrm{l}_n)$
   IF $\phi_\text{trial} \leq 0$ THEN
       set: $\boldsymbol{\Gamma} = \boldsymbol{\Gamma}_n$
       EXIT
   ELSE
       GO TO 4. (Return-mapping)
   ENDIF

4. Return-mapping:
   set: $\boldsymbol{\chi} = [\Delta\lambda, \boldsymbol{\Xi}]^\mathrm{T} = [0, \boldsymbol{\Xi}_\text{trial}]^\mathrm{T}$
   set: $\boldsymbol{\Gamma} = \boldsymbol{\Gamma}_n$ and $\{Q^\mathrm{i}, \mathbf{Q}^\mathrm{k}, \mathbb{H}\} = \{Q^\mathrm{i}_n, \mathbf{Q}^\mathrm{k}_n, \mathbb{H}_n\}$
   WHILE $\|\mathbf{r}_\chi\| > \mathrm{TOL}$
       compute: $\partial_{\boldsymbol{\chi}}\mathbf{r}$
       update: $\boldsymbol{\chi} \longleftarrow \boldsymbol{\chi} - \partial_{\boldsymbol{\chi}}\mathbf{r}_\chi \cdot \mathbf{r}_\chi$
       update: $\boldsymbol{\Gamma}(\boldsymbol{\chi})$    →    (Eq. (4.55)–Eq. (4.56))
       compute: $\{Q^\mathrm{i}, \mathbf{Q}^\mathrm{k}, \mathbb{H}\}$
       compute: $\mathbf{r}_\chi$    →    (Eq. (4.65))
   END
```

Figure 4.3: Return mapping algorithm of the proposed distortional hardening model

and the weak form of the first law of thermodynamics

$$\begin{aligned}\delta W_\Theta = &\int\limits_{\mathcal{B}_0} \left\{ \delta\Theta \left[c\,\dot{\Theta} - \mathcal{H}_\Theta \right] - \mathbf{H} \cdot \mathrm{GRAD}\delta\Theta \right\} \mathrm{d}V \\ &+ \int\limits_{\partial\mathcal{B}_0} \delta\Theta\, \bar{H}\, \mathrm{d}A - \int\limits_{\mathcal{B}_0} \delta\Theta\, \rho_0\, R_\Theta\, \mathrm{d}V = 0 \qquad \forall\, \delta\Theta \in \mathcal{H}^1_0(\mathcal{B}_0)\,.\end{aligned} \tag{4.67}$$

In theses equations, $\delta(\bullet)$ symbolises the virtual quantity of $(\bullet)$, and $\mathcal{H}^1_0$ denotes the space of admissible test functions. The rates (velocities) in Eq. (4.67) are approximated in the standard manner

$$\dot{\Theta} = \frac{\mathrm{d}\Theta}{\mathrm{d}t} \approx \frac{\Theta - \Theta_n}{\Delta t}\,, \qquad \dot{J} = \frac{\mathrm{d}J}{\mathrm{d}t} \approx \frac{J - J_n}{\Delta t}\,, \qquad \lambda \approx \frac{\Delta\lambda}{\Delta t}\,. \tag{4.68}$$

Accordingly, the time index $(\bullet)_{n+1}$ for the current time is omitted and only variables belonging to the previous time are highlighted by $(\bullet)_n$. With Eqs. (4.68), the first integral in Eq. (4.67) is approximated by

$$\int\limits_{\mathcal{B}_0} \left\{ \delta\Theta\, \frac{1}{\Delta t} \left[c\,[\Theta - \Theta_n] - \Delta\mathcal{H}_\Theta \right] - \mathbf{H} \cdot \mathrm{GRAD}\delta\Theta \right\} \mathrm{d}V\,, \tag{4.69}$$

where the self-heating-related term reads

$$\begin{aligned}\Delta\mathcal{H}_\Theta = &\,\Theta \frac{\partial^2\Psi}{\partial J \partial\Theta}\,[J - J_n] \\ &+ \Delta\lambda \left[\beta^{\mathcal{D}}\, y_0 \left[1 - \omega_0 \left[\frac{\Theta}{\beta^{\mathcal{D}}} - \Theta_0 \right] \right] + \frac{b^{\mathrm{k}}}{c^{\mathrm{k}}}\, \|\partial_{\boldsymbol{\Sigma}}\phi\|\, \mathbf{Q}^{\mathrm{k}} : \mathbf{Q}^{\mathrm{k}} + 2\, g^{\mathrm{dis}} \right].\end{aligned} \tag{4.70}$$

For the spatial discretisation, a finite element triangulation is used. For that purpose, the referential body $\mathcal{B}_0$ and the referential boundary of the body $\partial\mathcal{B}_0$ are approximated by

$$\mathcal{B}_0 \approx \mathcal{B}^{\mathrm{h}}_0 = \bigcup_{e=1}^{n_{\mathrm{el}}} \mathcal{B}^e_0\,, \qquad \partial\mathcal{B}^{\mathrm{h}}_0 = \bigcup_{e=1}^{n^{\partial\mathcal{B}}_{\mathrm{el}}} \partial\mathcal{B}^e_0\,. \tag{4.71}$$

Subsequently, the primary fields are interpolated in every finite element as

$$\mathbf{X}\big|_{\mathcal{B}^e_0} \approx \mathbf{X}^{\mathrm{h}} = \sum_{a=1}^{n_{\mathrm{en}}} N^a\, \mathbf{X}^a\,, \quad \boldsymbol{\varphi}\big|_{\mathcal{B}^e_0} \approx \boldsymbol{\varphi}^{\mathrm{h}} = \sum_{a=1}^{n_{\mathrm{en}}} N^a\, \boldsymbol{\varphi}^a\,, \quad \Theta\big|_{\mathcal{B}^e_0} \approx \Theta^h = \sum_{a=1}^{n_{\mathrm{en}}} N^a\, \Theta^a\,. \tag{4.72}$$

Here, $\mathbf{X}^a$, $\boldsymbol{\varphi}^a$ and Θ^a are the nodal values at node a and N^a are shape functions. Approximations (4.72) lead to the gradients

$$\mathbf{F}^h = \mathrm{GRAD}\boldsymbol{\varphi}^{\mathrm{h}} = \sum_{a=1}^{n_{\mathrm{en}}} \boldsymbol{\varphi}^a \otimes \mathrm{GRAD} N^a \,, \quad \mathrm{GRAD}\Theta^h = \sum_{a=1}^{n_{\mathrm{en}}} \Theta^a \, \mathrm{GRAD} N^a \,. \tag{4.73}$$

The variations of these gradients follow identical lines. To be more precise, with

$$\delta\boldsymbol{\varphi}\big|_{\mathcal{B}_0^e} \approx \delta\boldsymbol{\varphi}^{\mathrm{h}} = \sum_{a=1}^{n_{\mathrm{en}}} N^a \, \delta\boldsymbol{\varphi}^a \,, \quad \delta\Theta\big|_{\mathcal{B}_0^e} \approx \delta\Theta^h = \sum_{a=1}^{n_{\mathrm{en}}} N^a \, \delta\Theta^a \,, \tag{4.74}$$

one obtains

$$\delta\mathbf{F}^{\mathrm{h}} = \mathrm{GRAD}\delta\boldsymbol{\varphi}^{\mathrm{h}} = \sum_{a=1}^{n_{\mathrm{en}}} \delta\boldsymbol{\varphi}^a \otimes \mathrm{GRAD} N^a, \quad \mathrm{GRAD}\delta\Theta^h = \sum_{a=1}^{n_{\mathrm{en}}} \delta\Theta^a \otimes \mathrm{GRAD} N^a. \tag{4.75}$$

As can be seen, a Bubnov-Galerkin-type approximation is considered.

Finally, by inserting Eqs. (4.71)–(4.75) into the balance laws (4.66) and (4.67) (see also the time-discretised counterpart (4.69) and (4.70)), the contributions of each finite element to the weak forms of the balance laws can be derived. They are summarised in the compact notation

$$\begin{aligned} \delta W_{\boldsymbol{\varphi}}\big|_{\mathcal{B}_0^e} &= \sum_{a=1}^{n_{\mathrm{en}}} \delta\boldsymbol{\varphi}^a \cdot \left[\mathbf{f}^a_{\boldsymbol{\varphi},\mathrm{int}} - \mathbf{f}^a_{\boldsymbol{\varphi},\mathrm{sur}} - \mathbf{f}^a_{\boldsymbol{\varphi},\mathrm{vol}}\right] \,, \\ \delta W_{\Theta}\big|_{\mathcal{B}_0^e} &= \sum_{a=1}^{n_{\mathrm{en}}} \delta\Theta^a \left[f^a_{\Theta,\mathrm{int}} + f^a_{\Theta,\mathrm{sur}} - f^a_{\Theta,\mathrm{vol}}\right] \,, \end{aligned} \tag{4.76}$$

where the generalised forces are defined by

$$\begin{aligned} \mathbf{f}^a_{\boldsymbol{\varphi},\mathrm{int}} &= \int_{\mathcal{B}_0^e} \mathbf{P} \cdot \mathrm{GRAD} N^a \, \mathrm{d}V \,, \quad \mathbf{f}^a_{\boldsymbol{\varphi},\mathrm{sur}} = \int_{\partial\mathcal{B}_0^e} N^a \, \bar{\mathbf{T}} \, \mathrm{d}A \,, \quad \mathbf{f}^a_{\boldsymbol{\varphi},\mathrm{vol}} = \int_{\mathcal{B}_0^e} N^a \, \rho_0 \, \mathbf{B} \, \mathrm{d}V \,, \\ f^a_{\Theta,\mathrm{int}} &= \int_{\mathcal{B}_0^e} \left\{ N^a \, \frac{1}{\Delta t} \left[c\,[\Theta - \Theta_n] - \Delta\mathcal{H}_\Theta \right] - \mathrm{GRAD} N^a \cdot \mathbf{H} \right\} \mathrm{d}V \,, \\ f^a_{\Theta,\mathrm{sur}} &= \int_{\partial\mathcal{B}_0^e} N^a \, \bar{H} \, \mathrm{d}A \,, \quad f^a_{\Theta,\mathrm{vol}} = \int_{\mathcal{B}_0^e} N^a \, \rho_0 \, R_\Theta \, \mathrm{d}V \,. \end{aligned} \tag{4.77}$$

For the sake of simplicity, the mechanical forces $\mathbf{B}$ and $\bar{\mathbf{T}}$ and the thermal heat source R_Θ are assumed to be independent of the primary fields. By way of contrast, the prescribed heat flux $\bar{H}$ may depend on the temperature. The assembly over all finite elements yields the approximation of the fully coupled boundary value problem. For instance, by introducing the global assembly operator A, the contribution related to global node A reads

$$\mathbf{r}^A = \mathop{\mathsf{A}}_{e=1}^{n_{\text{el}}} \begin{bmatrix} \mathbf{r}^a_{\boldsymbol{\varphi}} \\ r^a_{\Theta} \end{bmatrix} = \mathbf{0} \quad \text{with} \quad \begin{bmatrix} \mathbf{r}^a_{\boldsymbol{\varphi}} \\ r^a_{\Theta} \end{bmatrix} = \begin{bmatrix} \mathbf{f}^a_{\boldsymbol{\varphi},\text{int}} - \mathbf{f}^a_{\boldsymbol{\varphi},\text{sur}} - \mathbf{f}^a_{\boldsymbol{\varphi},\text{vol}} \\ f^a_{\Theta,\text{int}} + f^a_{\Theta,\text{sur}} - f^a_{\Theta,\text{vol}} \end{bmatrix} . \tag{4.78}$$

In this chapter, the fully coupled non-linear system of equations is solved in a monolithic manner by employing Newton's scheme. Therefore, the nodal residuals $\mathbf{r}^a = [\mathbf{r}^a_{\boldsymbol{\varphi}}, r^a_{\Theta}]$ have to be linearised with respect to the unknowns $\mathbf{d}^b = [\boldsymbol{\varphi}^b, \Theta^b]$. The resulting element stiffness matrix can be written as

$$\mathbf{K}^{ab} = \frac{\mathrm{d}\mathbf{r}^a}{\mathrm{d}\mathbf{d}^b} = \begin{bmatrix} \mathbf{K}^{ab}_{\boldsymbol{\varphi}\boldsymbol{\varphi}} & \mathbf{K}^{ab}_{\boldsymbol{\varphi}\Theta} \\ \mathbf{K}^{ab}_{\Theta\boldsymbol{\varphi}} & K^{ab}_{\Theta\Theta} \end{bmatrix} , \tag{4.79}$$

with the sub-matrices

$$\begin{aligned}
\mathbf{K}^{ab}_{\boldsymbol{\varphi}\boldsymbol{\varphi}} &= \frac{\mathrm{d}\mathbf{r}^a_{\boldsymbol{\varphi}}}{\mathrm{d}\boldsymbol{\varphi}^b} = \int\limits_{\mathcal{B}^e_0} \mathrm{GRAD}N^a \bullet \frac{\mathrm{d}\mathbf{P}}{\mathrm{d}\mathbf{F}} \cdot \mathrm{GRAD}N^b \,\mathrm{d}V \,, \\
\mathbf{K}^{ab}_{\boldsymbol{\varphi}\Theta} &= \frac{\mathrm{d}\mathbf{r}^a_{\boldsymbol{\varphi}}}{\mathrm{d}\Theta^b} = \int\limits_{\mathcal{B}^e_0} N^b \,\frac{\mathrm{d}\mathbf{P}}{\mathrm{d}\Theta} \cdot \mathrm{GRAD}N^a \,\mathrm{d}V \,, \\
\mathbf{K}^{ab}_{\Theta\boldsymbol{\varphi}} &= \frac{\mathrm{d}r^a_{\Theta}}{\mathrm{d}\boldsymbol{\varphi}^b} = \int\limits_{\mathcal{B}^e_0} N^a \,\frac{\mathrm{d}\Delta\mathcal{H}_{\Theta}}{\mathrm{d}\mathbf{F}} \cdot \mathrm{GRAD}N^a \,\mathrm{d}V \,, \\
K^{ab}_{\Theta\Theta} &= \frac{\mathrm{d}r^a_{\Theta}}{\mathrm{d}\Theta^b} = \int\limits_{\mathcal{B}^e_0} \left\{ N^a \,\frac{1}{\Delta t} \left[c - \frac{\mathrm{d}\Delta\mathcal{H}_{\Theta}}{\mathrm{d}\Theta} \right] N^b + k_0 \,\mathrm{GRAD}N^a \cdot \mathrm{GRAD}N^b \right\} \mathrm{d}V \\
&\quad + \int\limits_{\partial\mathcal{B}^e_0} N^a \frac{\partial \bar{H}}{\partial \Theta} N^b \,\mathrm{d}V \,.
\end{aligned} \tag{4.80}$$

Due to the missing variational structure, the stiffness matrix is generally not symmetric, which is in contrast to the thermomechanical frameworks Canadija and Mosler [25, 26], Yang et al. [139]. Further details regarding the computation of sensitivities

$$\mathrm{d}\mathbf{P} = \frac{\partial \mathbf{P}}{\partial \mathbf{F}} : \mathrm{d}\mathbf{F} + \frac{\partial \mathbf{P}}{\partial \Theta} \mathrm{d}\Theta + \frac{\partial \mathbf{P}}{\partial \boldsymbol{\chi}} \cdot \mathrm{d}\boldsymbol{\chi} \tag{4.81}$$

and

$$\mathrm{d}\Delta\mathcal{H}_{\Theta} = \frac{\partial \Delta\mathcal{H}_{\Theta}}{\partial \mathbf{F}} : \mathrm{d}\mathbf{F} + \frac{\partial \Delta\mathcal{H}_{\Theta}}{\partial \Theta} \mathrm{d}\Theta + \frac{\partial \Delta\mathcal{H}_{\Theta}}{\partial \boldsymbol{\chi}} \cdot \mathrm{d}\boldsymbol{\chi} \tag{4.82}$$

can be found in Appendix B.1.

Remark 4.3.2: *It is well known that finite elements based on linear shape functions can lead to spurious locking effects in the nearly incompressible regime, e.g., in the case of isochoric plasticity. This effect is reduced here by using bi-quadratic and tri-quadratic shape functions: A 9-noded quadratic element has been implemented for the 2D simulations in the case of plain strain and axisymmetric analysis, whereas a 20-noded serendipity element has been derived for the 3D formulation. In addition to a standard two-field formulation in terms of the deformation and the temperature field, an enhanced assumed strain (EAS) approach is also used, cf. Appendix B.2 and Appendix B.3.*

Remark 4.3.3: *For polar axisymmetric problems, such as the boundary value problem presented in Subsection 4.4.5, the deformation gradient written in polar axisymmetric coordinates reads*

$$\mathbf{F} = \begin{bmatrix} \partial_R \boldsymbol{\varphi}_r & \partial_Z \boldsymbol{\varphi}_r & 0 \\ \partial_R \boldsymbol{\varphi}_z & \partial_Z \boldsymbol{\varphi}_z & 0 \\ 0 & 0 & r/R \end{bmatrix} . \tag{4.83}$$

Remark 4.3.4: *For polar axisymmetric problems, such as the boundary value problem presented in Subsection 4.4.5, the vector of internal forces can be written in matrix notation as*

$$\mathbf{f}^a_{\boldsymbol{\varphi},\mathrm{int}} = \int\limits_{\mathcal{B}^e_0} \mathbf{B}^{a\mathrm{T}} \cdot \widehat{\mathbf{P}} \, \mathrm{d}V \qquad \textit{with} \qquad \widehat{\mathbf{P}} = \begin{bmatrix} \mathbf{P}_{11} & \mathbf{P}_{12} & \mathbf{P}_{21} & \mathbf{P}_{22} & \mathbf{P}_{33} \end{bmatrix}^{\mathrm{T}} , \tag{4.84}$$

where

$$\mathbf{B}^a = \begin{bmatrix} \partial_R N^a & \partial_Z N^a & 0 & 0 & N^a/R \\ 0 & 0 & \partial_R N^a & \partial_Z N^a & 0 \end{bmatrix} . \tag{4.85}$$

4.4 Representative numerical examples

In this section, the predictive capabilities of the proposed generalised plasticity framework and the robustness and efficiency of the elaborated algorithmic formulation are demonstrated by means of several numerical examples.

In order to show the directive distortion of yield surfaces the aluminium alloy Al6061-T6511 is numerically investigated in Subsection 4.4.1. Therefore, experiments reported in Khan et al. [62] are identified for the isothermal setting, since temperature data for a thermomechanically coupled analysis is missing.

The thermomechanically coupled distortional hardening model is numerically analysed in Subsection 4.4.2 and its predictions are compared to the uniaxial tension test experiments reported in Hodowany et al. [54], Rosakis et al. [109] in which the aluminium alloy Al2024-T3 was characterised, see also Kintzel and Mosler [65]. Computations based on an isotropic and a kinematic hardening model are also presented for the sake of comparison. After a parameter identification of the different hardening models, the resulting distortional hardening models are subsequently used for more complex structural analyses: a contact bending test in Subsection 4.4.3, inhomogeneous tension test in Subsection 4.4.4 and necking of a bar in Subsection 4.4.5.

4.4.1 Uniaxial tension test of the aluminium alloy Al6061-T6511 – isothermal setting

4.4.1.1 Elastoplastic prototype model

For the elastoplastic response of the model, the elastic energy is defined next. The prototype Helmholtz energy is given by

$$\Psi^{\mathrm{el}} = W(\mathbf{F}^{\mathrm{e}}) + U(J)\,, \tag{4.86}$$

in which the elastic energy is split into an purely isochoric part W and a purely volumetric part U. More precisely, the parts are defined as

$$W(\mathbf{F}^{\mathrm{e}}) = \frac{1}{2}\mu\,\left[J^{-2/3}\mathbf{F}^{\mathrm{e}} : \mathbf{F}^{\mathrm{e}} - 3\right]\,, \tag{4.87}$$

$$U(J) = \frac{1}{2}\kappa\,\left[\frac{1}{2}[J^2 - 1] - \ln J\right]\,, \tag{4.88}$$

where $\mu = E/2/[1+\nu]$ is the shear modulus (depending on the Young's modulus E and Poisson's ratio ν), $\kappa = E/3/[1-2\,\nu]$ is the bulk modulus. Furthermore, the initial yield stress is equivalent to the yield limit y_0, i.e.

$$Q_0^{\mathrm{eq}} = y_0\,. \tag{4.89}$$

The elastic model parameters are summarised in Tab. 4.1.

Al 6061-T6511	Name	Symbol	Value	Unit
	Youngs modulus	E	74000	[MPa]
	Poisson ratio	ν	0.32	[–]

Table 4.1: Material parameters for the aluminium alloy Al 6061-T6511 at $\Theta_0 = 293$ K

4.4.1.2 Mechanical response

According to the experimental measurements reported in Khan et al. (2009), aluminium alloy Al6061-T6511 shows a pronounced distortion of the yield surface during deformation. Furthermore, the respective yield loci have a higher curvature in loading direction compared to the opposite reverse direction. Within the experiments reported in Khan et al. [62], a bar made of Al6061-T6511 is deformed under monotonic uniaxial tension (strain-controlled). In order to identify the material parameters of the hardening behaviour, a standard least square fit

$$\{y_0, c^{\mathrm{k}}, b^{\mathrm{k}}, b^{\mathrm{d}}, b^{\mathrm{l}}, b^{\mathrm{c}}\} = \arg \inf_{y_0, c^{\mathrm{k}}, b^{\mathrm{k}}, b^{\mathrm{d}}, b^{\mathrm{l}}, b^{\mathrm{c}}} \mathcal{F}_{\mathrm{err}} \tag{4.90}$$

with

$$\text{with} \qquad \mathcal{F}_{\mathrm{err}} = \frac{1}{2} \sum_{i=1}^{n} \|\boldsymbol{\sigma}_{\mathrm{Khan}}(F_{11}^{(i)}) - \boldsymbol{\sigma}_{\mathrm{model}}(F_{11}^{(i)})\|^2 \tag{4.91}$$

is applied. The stress states $\boldsymbol{\sigma}_{\mathrm{Khan}}$ taken from Khan et al. [62] are based on uniaxial stretches $F_{11}^{(i)}$. These stresses are numerically compared to stress states $\boldsymbol{\sigma}_{\mathrm{model}}$ of the proposed model. A summary of the identified hardening parameters are presented in Tab. 4.2.

Al 6061-T6511	Name	Symbol	Value	Unit
	Yield limit (∗)	y_0	93.9	[MPa]
	kinematic hard. mod. (∗)	c^{k}	18800	[MPa]
	kinematic sat. coef. (∗)	b^{k}	91.9	[–]
	dynamic hard. mod.	c^{d}	40.0	[–]
	dynamic sat. coef. (∗)	b^{d}	-44.5	[–]
	latent hard. mod.	c^{l}	5.0	[–]
	latent sat. coef. (∗)	b^{l}	-5.6	[–]
	curvature coef. (∗)	b^{c}	0.144	[MPa^{-1}]

Table 4.2: Uniaxial tensile test of the aluminium alloy Al 6061-T6511: Hardening associated parameters. Only the parameters highlighted by (∗) have been computed by means of the least square-type identification (4.90). Parameters c^{d} and c^{l} have been chosen beforehand.

The results of the novel model together with their experimentally measured counterparts are given in Fig. 4.4. Three yield surfaces corresponding to engineering strains of 2%, 4% and 6% are summarized in this figure. As can be seen, the surfaces predicted by the novel model are in excellent agreement with the experimental measurements. All characteristic features of the investigated aluminium alloy Al6061-T6511 are captured such as high curvature changes of the yield surface as well as an exceeding dynamic and latent softening. For a realistic prediction of technological processes, temperature effects need to be considered. Since temperature effects are not available for this material, the focus is in the following on a different aluminium alloy for which temperature data is available.

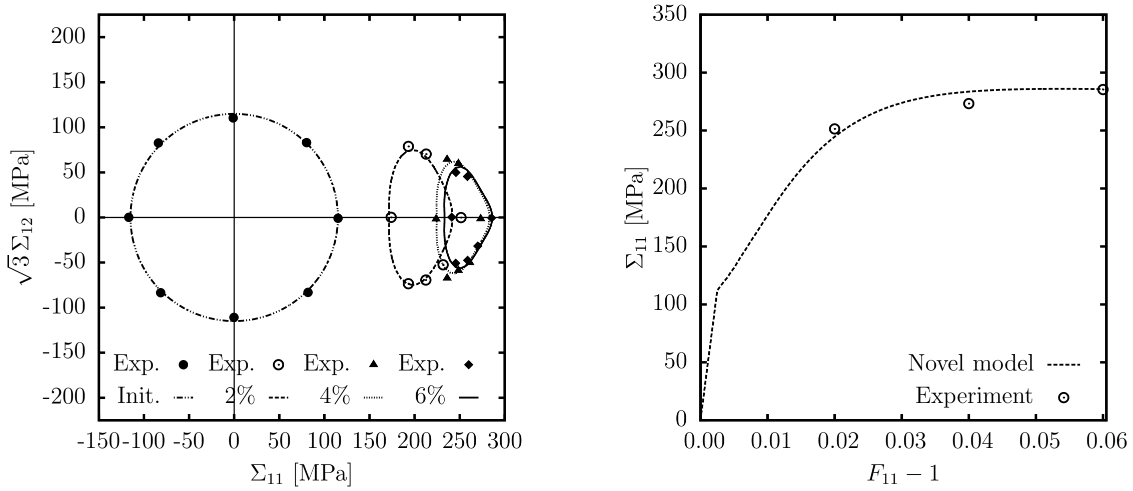

Figure 4.4: Evolution of the yield surface (left) for aluminium alloy 6061-T6511 subjected to simple tension of 2%, 4% and 6%. The respective stress-strain response is shown in the right diagram. Lines represent the predictions obtained from the novel model, while the symbols are associated with the experimental measurements reported in Khan et al. [62].

4.4.2 Comparison of different hardening models for a uniaxial tension test of the aluminium alloy Al2024-T3 – thermomechanically coupled setting

4.4.2.1 Thermo-elastoplastic prototype model

In the following, the hardening-independent structure of the considered thermo-elastoplastic prototype models is summarised. The underlying Helmholtz energy is given by

$$\Psi^{\mathrm{el}} = W(\mathbf{F}^{\mathrm{e}}) + U(J) + M(J,\Theta) + T(\Theta)\,, \tag{4.92}$$

where W and U are defined by Eqs. (4.87) and (4.88). The energy M is associated with the thermoelastic coupling and is assumed to be volumetric in nature. T covers the thermal part. Such individual energies are chosen as

$$\begin{aligned} M(J,\Theta) &= [\Theta - \Theta_0]\,[-3\,\alpha_0\,\partial_J U]\,, && (4.93)\\ T(\Theta) &= c_0\left[[\Theta - \Theta_0] - \Theta \ln \frac{\Theta}{\Theta_0}\right]\,, && (4.94) \end{aligned}$$

where α_0 is the (constant) thermal expansion coefficient, c_0 is the (constant) heat capacity and where Θ_0 denotes the reference temperature. Heat conduction is modelled by means of the isotropic Fourier's law (2.53). Furthermore, linear heat convection of the type

$$H_N = k_c \, [\Theta_0 - \Theta] \tag{4.95}$$

is considered at the thermal Neumann boundary $\partial \mathcal{B}_{0,\mathbf{H}}$. Finally, thermal-softening is included in the model by means of the temperature-dependent yield limit

$$Q_0^{\mathrm{eq}} = y_0 \, [1 - \omega_0 \, [\Theta - \Theta_0]] \, . \tag{4.96}$$

For the considered aluminium alloy Al2024-T3, the model parameters are summarised in Tab. 4.3.

Al 2024-T3	Name	Symbol	Value	Unit
	Youngs modulus	E	74000	[MPa]
	Poisson ratio	ν	0.32	[–]
	Thermal expansion	α_0	$2.4 \cdot 10^{-5}$	[K^{-1}]
	Heat capacity	c_0	2.4325	[MPa/K]
	Thermal conductivity	k_0	120	[W/(m K)]
	Yield limit	y_0	322.91	[MPa]
	Thermal yield softening	ω_0	0.003	[K^{-1}]
	Reference temperature	Θ_0	293	[K]
	Air temperature	Θ_∞	293	[K]
	Convection coefficient	k_c	0.0175	[N/(mm s K)]

Table 4.3: Material parameters for the aluminium alloy Al 2024-T3 at $\Theta_0 = 293$ K

4.4.2.2 Mechanical response

In the following, the four different hardening models

1. associative isotropic hardening – see Eq. (4.5)
2. non-associative kinematic hardening – see Eq. (4.8) and Eq. (4.9)
3. distortional hardening model 1 (M1)– see Eq. (4.12), Eq. (4.17) and Eq. (4.34)) with $b^{\mathrm{c}} = 0$
   kinematic hardening coupled to latent hardening and dynamic softening
4. distortional hardening model 2 (M2) – see Eq. (4.12), Eq. (4.17) and Eq. (4.34) with $b^{\mathrm{d}} = 0$
   kinematic hardening coupled to latent softening and dynamic hardening with high curvature in loading direction compared to the opposite direction

will be used in order to numerically analyse the uniaxial tension test as experimentally studied in Hodowany et al. [54]. The initial yield surface of all models is assumed to be of von Mises-type. Therefore, the material symmetry is described by $\mathbb{H}_0 = \mathbb{A}_0^{\mathrm{d}} = \mathbb{A}_0^{\mathrm{l}} = \mathbb{I}^{\mathrm{dev}}$ at time step $t = 0$. Furthermore, the other internal variables are initialised by $\mathbf{F}_0^{\mathrm{p}} = \mathbf{I}$, $\alpha_0^{\mathrm{i}} = 0$ and $\boldsymbol{\alpha}_0^{\mathrm{k}} = \mathbf{0}$ for all simulations. In order to compute the models' hardening parameters, a standard least-square method is employed. It is based on the minimisation principle

$$\{c, b\} = \arg\inf_{c,b} \mathcal{F}_{\mathrm{err}} \qquad \text{with} \qquad \mathcal{F}_{\mathrm{err}} = \frac{1}{2}\sum_{i=1}^{n} \|\sigma_{\mathrm{Hodowany}}(F_{11}^{(i)}) - \sigma_{\mathrm{model}}(F_{11}^{(i)})\|^2 \, , \tag{4.97}$$

where $\sigma_{\mathrm{Hodowany}}(F_{11}^{(i)})$ is the uniaxial tensile stress (of Cauchy-type) for the stretch $F_{11}^{(i)}$ measured in Hodowany et al. [54] and where $\sigma_{\mathrm{model}}(F_{11}^{(i)})$ denotes the numerically predicted counterpart (depending on the underlying hardening model). Within the first step, thermal softening is ignored ($\omega_0 = 0$) and only the purely mechanical response is considered in the material parameter identification process. A summary of the model parameters associated with the four different hardening models is given in Tab. 4.4.

Hardening model	Name	Symbol	Value	Unit
isotropic (associative)	isotropic hard. mod. $(*)$	c^{i}	266.02	[MPa]
	isotropic sat. coef. $(*)$	b^{i}	4.814	[–]
kinematic	kinematic hard. mod.$(*)$	c^{k}	1280.7	[MPa]
	kinematic sat. coef.$(*)$	b^{k}	4.814	[–]
distortional hard. model 1 (M1)	kinematic hard. mod. $(*)$	c^{k}	1430.7	[MPa]
	kinematic sat. coef. $(*)$	b^{k}	4.435	[–]
	dynamic hard. mod.	c^{d}	1.0	[–]
	dynamic sat. coef.	b^{d}	-1.0	[–]
	latent hard. mod.	c^{l}	1.0	[–]
	latent sat. coef.	b^{l}	0.2	[–]
	curvature coef.	b^{c}	0.0	[MPa^{-1}]
distortional hard. model 2 (M2)	kinematic hard. mod.$(*)$	c^{k}	1343.8	[MPa]
	kinematic sat. coef.$(*)$	b^{k}	6.758	[–]
	dynamic hard. mod.	c^{d}	1.0	[–]
	dynamic sat. coef.	b^{d}	0.0	[–]
	latent hard. mod.	c^{l}	1.0	[–]
	latent sat. coef.	b^{l}	-1.0	[–]
	curvature coef.	b^{c}	0.0035	[MPa^{-1}]

Table 4.4: Uniaxial tensile test of the aluminium alloy Al 2024-T3: Model parameters associated with the four different hardening models. Only the parameters highlighted by $(*)$ have been computed by means of the least square-type approach according to Eq. (4.97). The remaining parameters were chosen beforehand.

The mechanical response as predicted by the different hardening models is summarised in Fig. 4.5. According to Fig. 4.5a), all models are in good agreement with the experimental observations for loading. This is clearly not surprising since the respective stress-strain response served as the input for the model parameter identification process. However, the differences between the models become visible during unloading. Apart from the model based on isotropic hardening, all models show the Bauschinger effect.

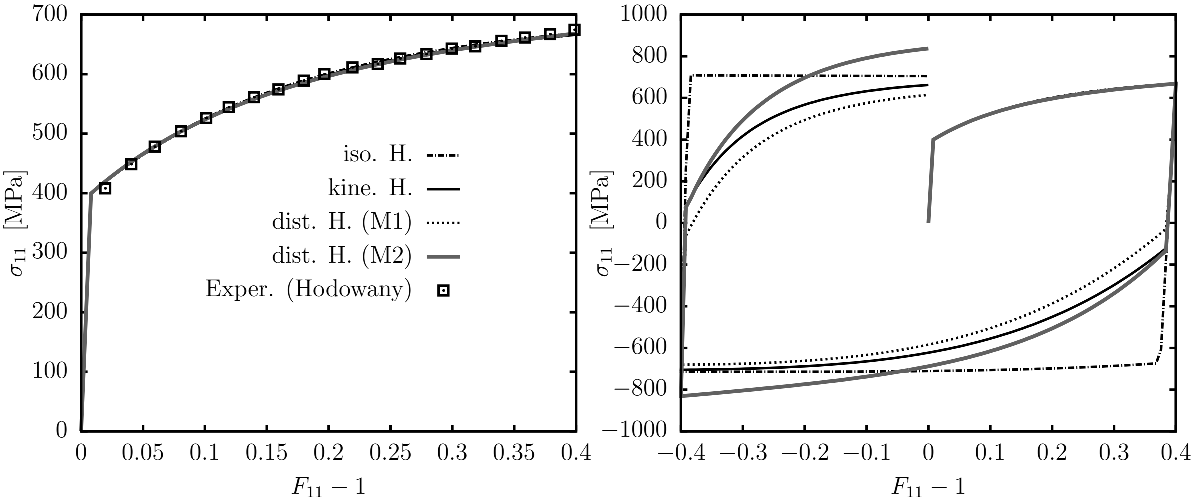

Figure 4.5: Uniaxial tensile test of the aluminium alloy Al 2024-T3: Stress vs. strain response for the different hardening models: a) (left) loading regime – used in the parameter identification. b) (right) loading-unloading-loading cycle

In order to make the differences between the hardening models visible during loading as well, the evolution of the yield surfaces are depicted in Fig. 4.6 – in the $\{\Sigma_{11}, \sqrt{3}\,\Sigma_{12}\}$ Mandel stress space. As can be seen in Fig. 4.6b), the initially circular yield function (see Fig. 4.6a) indeed evolves differently for the four hardening models. The models only agree in the loading direction. While the purely isotropic and the purely kinematic hardening model enforce the initial shape of the yield function, a distortion of the yield surface is captured by the distortional hardening models M1 and M2. Furthermore, the distortional hardening model M1 shows softening in loading direction (dynamic softening; the diameter of the initial yield surface decreases in loading direction) and hardening orthogonal to the loading direction (latent hardening; the diameter of the initial yield surface increases in the direction orthogonal to the loading direction). By way of contrast, model M2 leads to hardening in loading direction and to latent softening. Additionally, the curvature of the yield surface as predicted by model M2 is significantly higher in the loading direction than in the opposite direction.

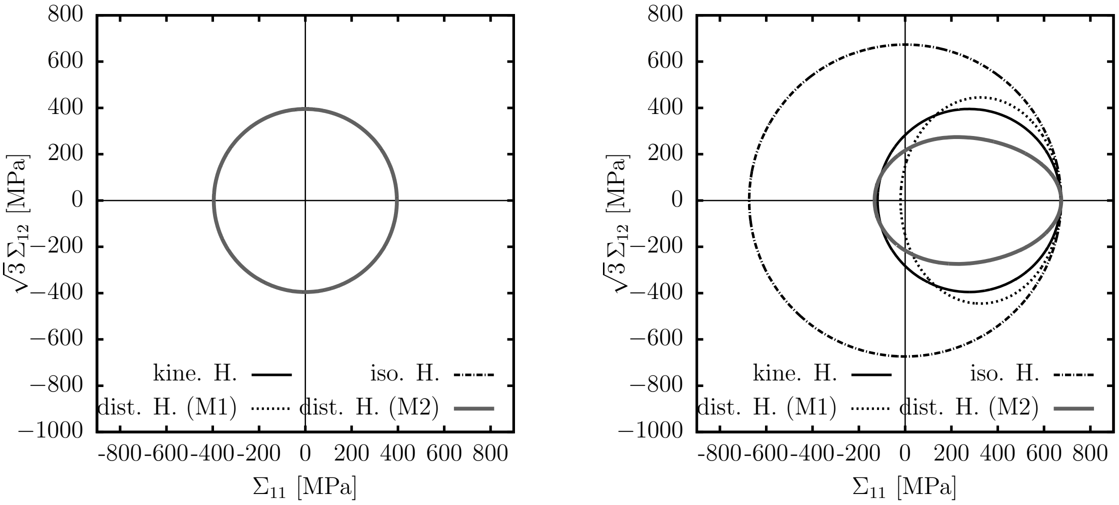

a) Initial b) Loading: $F_{11} - 1 = 0.4$

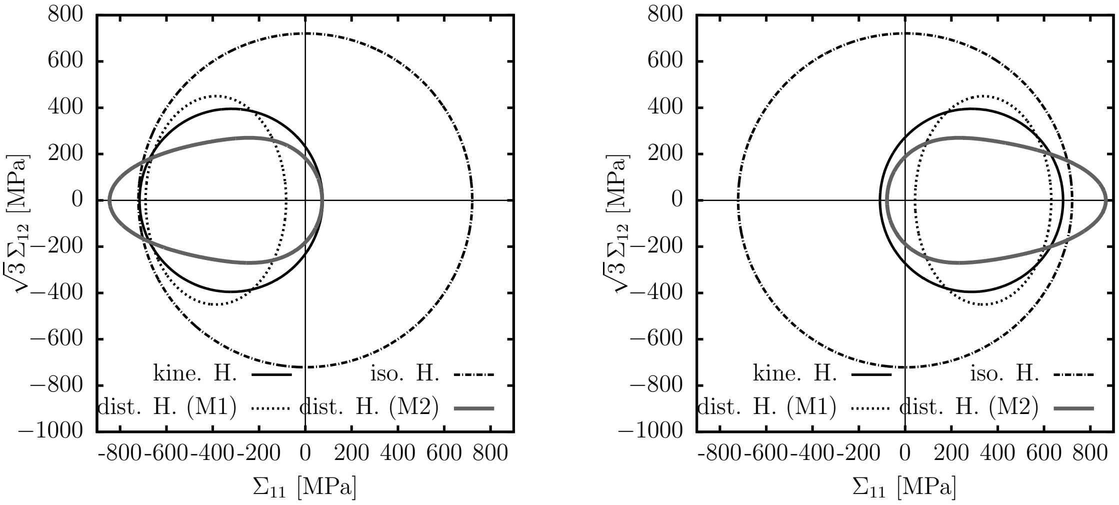

e) Unloading: $F_{11} - 1 = -0.4$ f) Loading: $F_{11} - 1 = 0$

Figure 4.6: Uniaxial tensile test of the aluminium alloy Al 2024-T3: Yield surface evolution for the different hardening models at different loading stages

4.4.2.3 Thermal response

So far, thermal effects have not been considered in the model parameter identification process. Such effects will be included next. For that purpose, the measurements as reported in Hodowany et al. [54] will be considered. Since the thermomechanical coupling is bi-directional in nature, the consideration of thermal effects influences the mechanical response as well. In order to weaken this coupling, thermal softening is still ignored ($\omega_0 = 0$). In this case, the thermal problem influences the mechanical problem only through structural heating. However, this effect is not very pronounced for the material parameters characterising the aluminium alloy Al 2024-T3.

Following Stainier and Ortiz [123], the experiment performed in Hodowany et al. [54] is approximated by means of adiabatic heat conditions and no additional heat sources are considered. A straightforward and naive thermomechanical coupling ($\beta^{\mathcal{D}} = 1$, see Eq. (4.45)) of the purely mechanical models discussed in the previous subsection leads to the temperature evolution as shown in Fig. 4.7. Accordingly, all hardening models significantly over-predict the temperature increase due to dissipation. As pointed out in Subsection 4.2.1, the over-prediction of the temperature increase is a direct consequence of the over-prediction of the mechanical dissipation implicitly controlled by model parameter $\beta^{\mathcal{D}} = 1$. For this reason, a reduction of parameter $\beta^{\mathcal{D}}$ which also reduces the mechanical dissipation is expected to yield a more realistic temperature evolution. For instance, by setting $\beta^{\mathcal{D}} = 0.5$ only 50% of the initial yield stress enters the mechanical dissipation, while the remaining 50% of the initial stress corresponds to previous energetic hardening. The temperature evolution for $\beta^{\mathcal{D}} = 0.5$ is depicted in Fig. 4.8. As can be seen, the temperature increase predicted by the different models is now in better agreement with the experimental observations reported in Hodowany et al. [54].

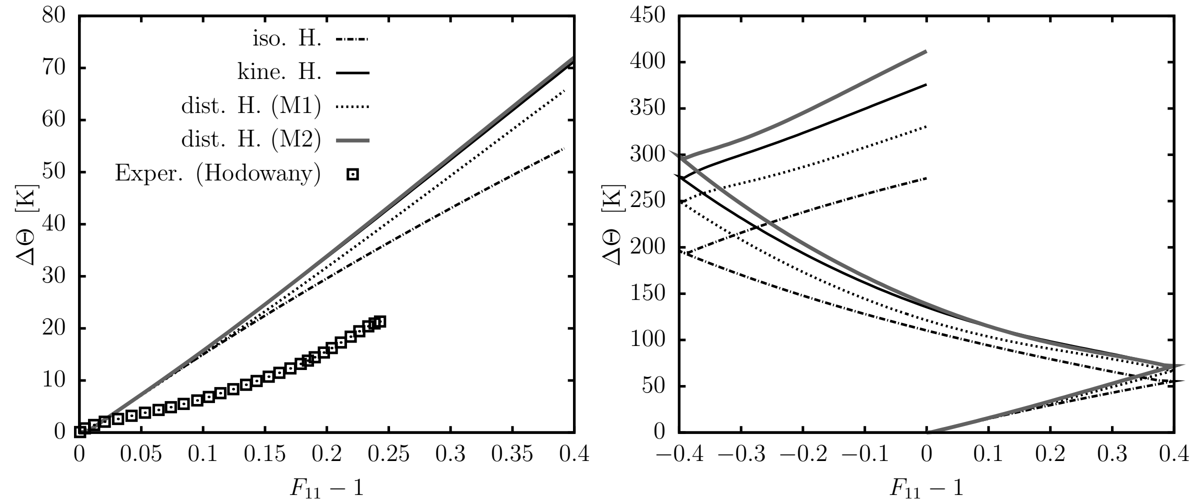

Figure 4.7: Uniaxial tensile test of the aluminium alloy Al 2024-T3: Temperature evolution $\Delta\Theta = \Theta - \Theta_0$ for $\beta_{\mathcal{D}} = 1$: a) (left) loading regime. b) (right) loading-unloading-loading

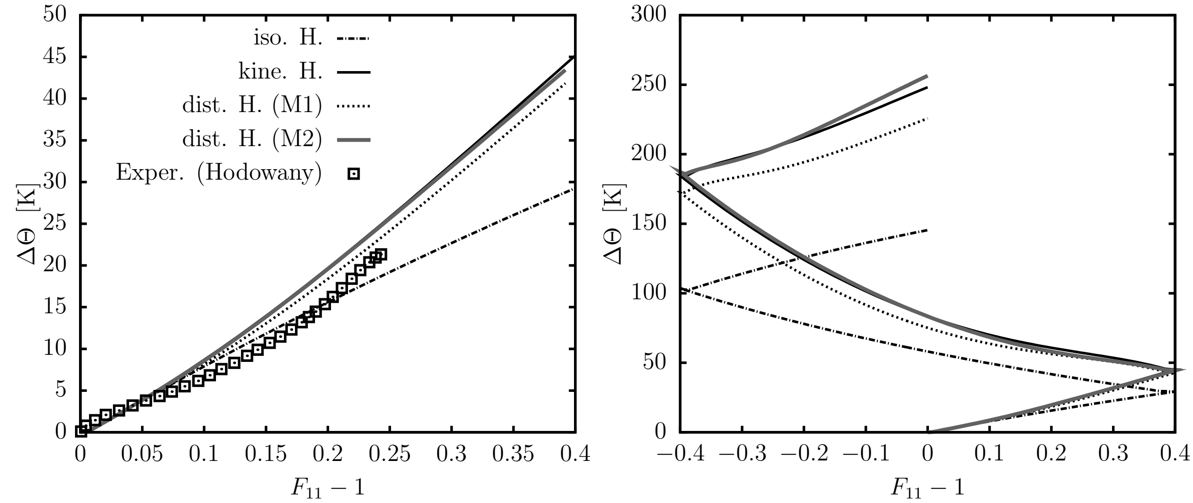

Figure 4.8: Uniaxial tensile test of the aluminium alloy Al 2024-T3: Temperature evolution $\Delta\Theta = \Theta - \Theta_0$ for $\beta_{\mathcal{D}} = 0.5$: a) (left) loading regime. b) (right) loading-unloading-loading

It bears emphasis that thermal softening has not yet been considered. In line with values reported in the literature (see, e.g. Simo and Miehe [121]), $\omega_0 = 0.003$ is chosen for the examples presented in the next subsections. As mentioned before, this parameter influences the mechanical as well as the thermal response of the considered material. For this reason, weighting factor $\beta^{\mathcal{D}}$ has to be adapted. A good agreement between experiment and model was obtained for $\beta^{\mathcal{D}} = 0.7$. Consequently, this value will be chosen in the following.

4.4.3 Contact bending test – distortional hardening model

Having discussed the basic features of the novel class of thermomechanically coupled distortional hardening models, more complex structural analyses will be analysed next. The first example is cyclic bending of a plate, see Fig. 4.9. A similar test setup can be found in Simo and Miehe [121]. The system consists of two rigid cylinders each with

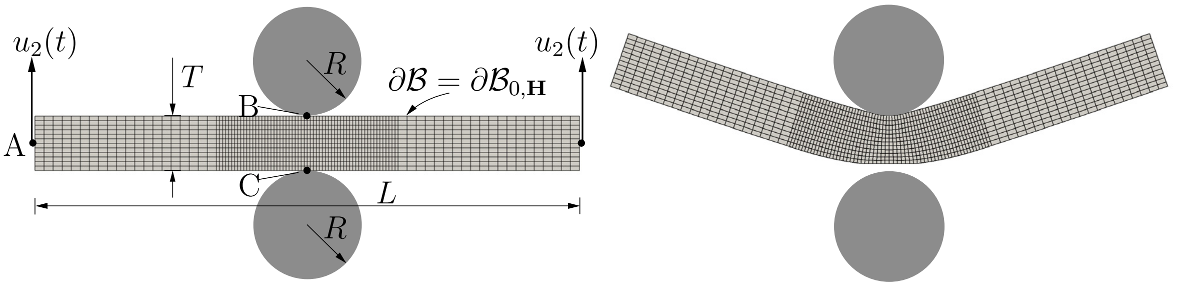

Figure 4.9: Contact bending test: Dimensions: L = 100 mm, T = 10 mm, R = 10 mm; Prescribed loading: $u_2(t) = u_0 \sin(\pi/0.4\,t)$, u_0 = 15 mm; material parameters are given in Tab. 4.3 and Tab. 4.4

a radius of $R = 10$ mm. The distance between the cylinders is 30 mm. A plate made of the aluminium alloy Al 2024-T3 is centred between the cylinders and is cyclically loaded by prescribing the vertical displacement $u_2(t) = u_0 \sin(\pi/0.4\,t)$ at both ends of the plate. The dimensions of the plate are 100×10 mm^2 and the material parameters corresponding to the aluminium plate are given in Tab. 4.3 and Tab. 4.4.

The plate is discretised by means of 100×12 9-noded quadrilateral elements with bi-quadratic shape function. The mesh is refined in the contact area. Plain strain conditions are assumed. Furthermore, it is assumed that the outer surface of the plate has a convective boundary $\partial\mathcal{B}_{0,\mathbf{H}}$ described by Eq. (4.95). For the contact between the cylinders and the plate, no friction is considered. This contact is modelled by the respective built-in algorithm of FEAP. It is based on an augmented Lagrangian method and an Uzawa algorithm. The simulation is divided into 1600 time steps with a constant time step of $\Delta t = 0.002$ s resulting in 4 bending cycles.

The contact bending test is numerically analysed by means of the distortional hardening model M1. For the sake of comparison, an additional computation based on kinematic hardening is also carried out.

The distributions of different plasticity-related internal variables are shown after four loading cycles in Fig. 4.10. The plots on the left hand side are associated with the distortional hardening model M1, whereas the plots on the right hand side are related with the kinematic hardening model. The top row depicts the distribution of the negative integrated plastic multiplier $\alpha^{\mathrm{i}} = -\int \lambda \,\mathrm{d}t$ and the bottom row shows the norm of the back strain tensor $\boldsymbol{\alpha}^{\mathrm{k}}$. According to Fig. 4.10, both hardening models seem to predict a similar elastoplastic response at first glance. However, a more detailed comparison leads to the conclusion that necking, i.e., strain localisation, is more pronounced for the purely kinematic hardening model.

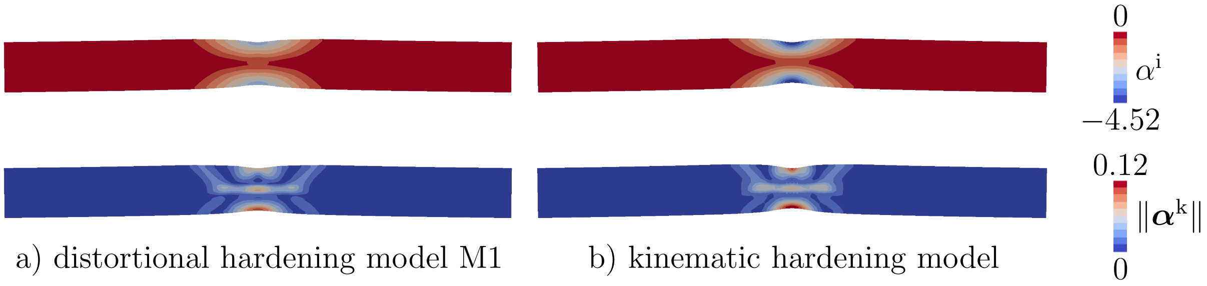

a) distortional hardening model M1 b) kinematic hardening model

Figure 4.10: Contact bending test: Distribution of plasticity-related internal variables (deformed configuration) after four loading cycles ($t = 3.2$ s). Top row: negative integrated plastic multiplier $\alpha^{\mathrm{i}} = -\int \lambda \,\mathrm{d}t$; bottom row: norm of the back strain tensor $\boldsymbol{\alpha}^{\mathrm{k}}$

As a consequence of the dissipation accompanying plastic deformations, the temperature increases in the plate, see Fig. 4.11. Due to coupling (2.78), the spatial temperature evolution is expected to be similar to the spatial distribution of the plasticity-related internal variables. This can indeed be verified by comparing Fig. 4.11 to Fig. 4.10. Again, necking is more pronounced for the kinematic hardening model, see Fig. 4.11.

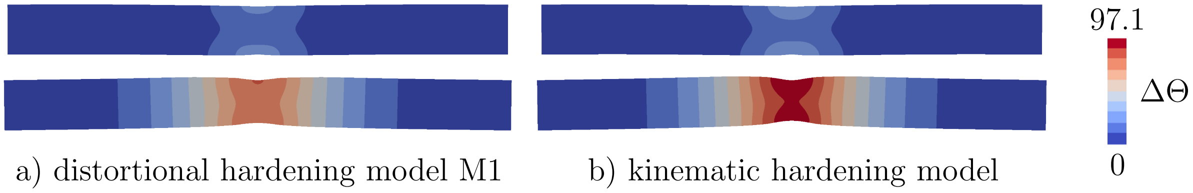
97.1
ΔΘ
0
a) distortional hardening model M1
b) kinematic hardening model

Figure 4.11: Contact bending test: Distribution of temperature increase $\Delta\Theta = \Theta - \Theta_0$ at two different time steps; top row: time $t = 0.8$ s; bottom row: after four loading cycles ($t = 3.2$ s)

Necking is the result of plastic strains which are localised in a narrow band. As can be seen in the right diagram in Fig. 4.12, this effect increases from a (plastic) loading cycle to a (plastic) loading cycle. Furthermore, necking is more pronounced in the case of the purely kinematic hardening model. Since necking in the middle of the bar is directly related to plastic deformations which, in turn, are linked to the temperature increase, the purely kinematic hardening model predicts higher temperatures in the middle of the bar (see right diagram in Fig. 4.12).

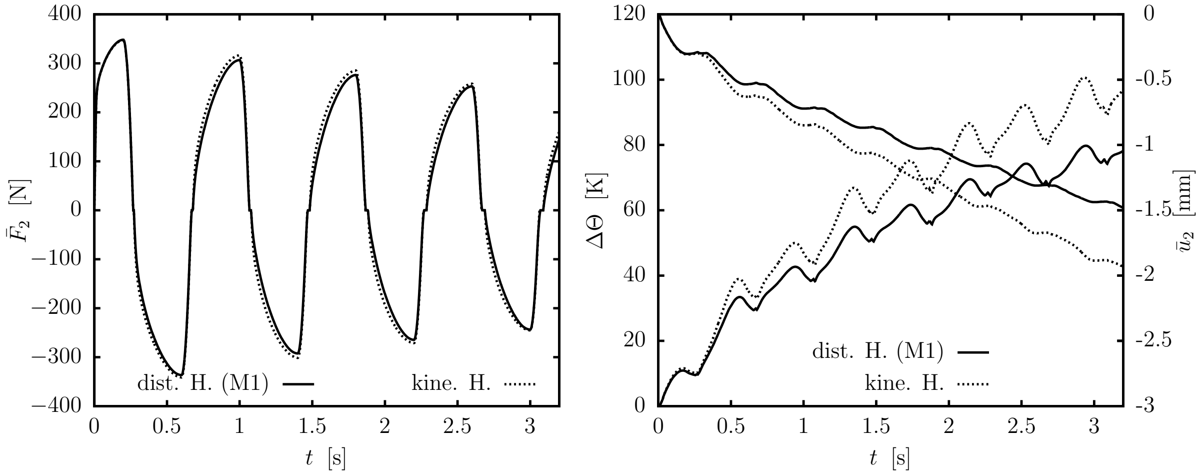

Figure 4.12: Contact bending test: Temporal evolution of different variables. Left: time vs. reaction force acting in point A (see Fig. 4.9); right: change in thickness ($\bar{u}_2 = x_{2,\mathrm{C}} - x_{2,\mathrm{B}}$) in the middle of the plate between points B and C (see Fig. 4.9) and temperature change at point B vs. time

From a structural mechanical point of view, necking leads to geometrically induced softening. This effect is superposed by thermal softening. As a result, the maximum loading (reaction force) decreases from loading cycle to loading cycle (see Fig. 4.12 - left diagram).

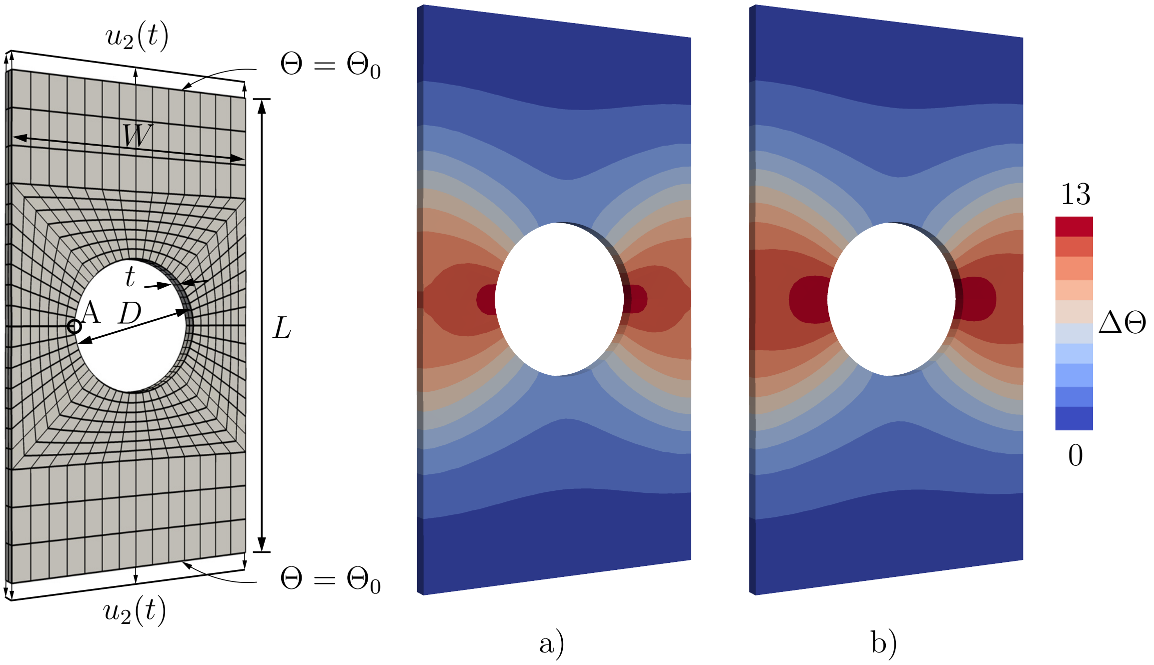

Figure 4.13: Numerical setup of the 3D test (left) with dimensions $L = 36$ mm, $D = 10$ mm, $W = 20$ mm, $t = 1$ mm. Temperature evolution (right) at time $t = 1$ s. Temperature evolution: a) distortional hardening model M2; b) kinematic hardening

4.4.4 Inhomogeneous tension test - distortional hardening model with higher curvature of the yield function in loading direction

This test deals with an uniaxial deformation of a plate with a cylindrical hole. The corresponding specimen has the dimensions $[L \times W \times t] = [36 \times 20 \times 1]$ mm^3, and the hole has the diameter $D = 10$ mm at the centre of the plate. At the top and the bottom surface, the plate is subjected to prescribed displacements $u_2(t) = u_0/2 \sin(\pi\, t)$ with $u_0 = 1.26$ mm. The test time takes $t \in [0, 1]$ s. Correspondingly, u_2 considers loading and unloading. Moreover, at the top and bottom surface the temperature is fixed to the reference temperature Θ_0. The setup of the test is illustrated in Fig. 4.13. Material parameters for the aluminium plate are taken from Tab. 4.3 and Tab. 4.4.

As depicted in Fig. 4.13, the specimen is discretised with 952 20-noded serendipity elements with quadratic ansatz functions. The test is performed in 100 time steps with the constant time step of $\Delta t = 0.01$ s.

The test is numerically analysed by means of distortional hardening model M2, which captures a higher curvature of the yield function in loading directions (see the example in Subsection 4.4.1). In order to compare the results, a second test based on kinematic hardening is also carried out.

The distribution of the temperature increase is shown in Fig. 4.13 for the distortinal hardening model M2 (a) and for the kinematic hardening model (b). The applied dis-

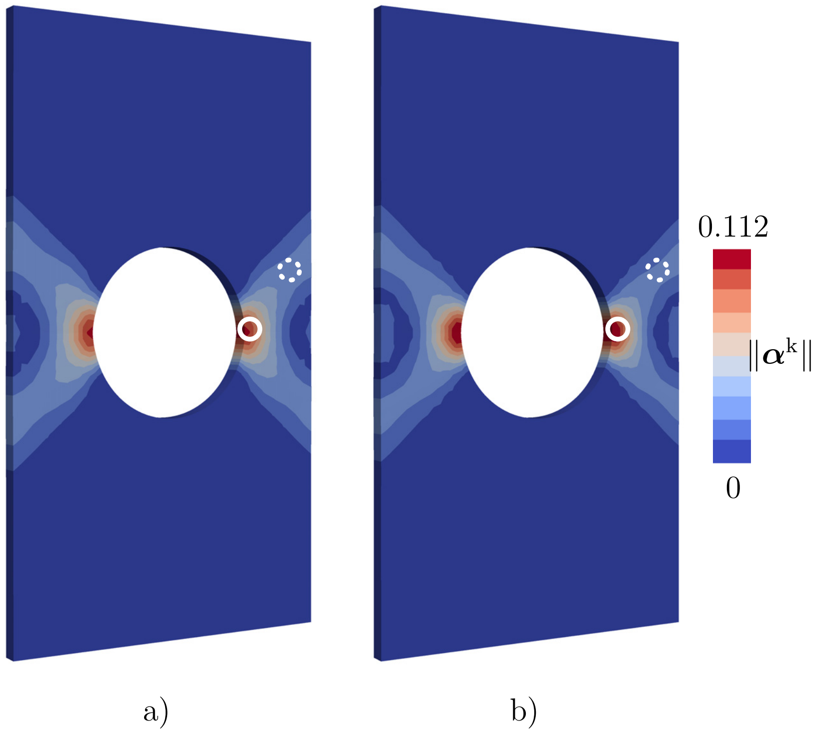

Figure 4.14: Inhomogeneous tension test: loading and unloading. Distortional hardening model M2 a) and purely kinematic hardening b) at $t = 1$ s. The marked area (solid line and dotted line) are associated with the yield surface evolutions in Fig. 4.15.

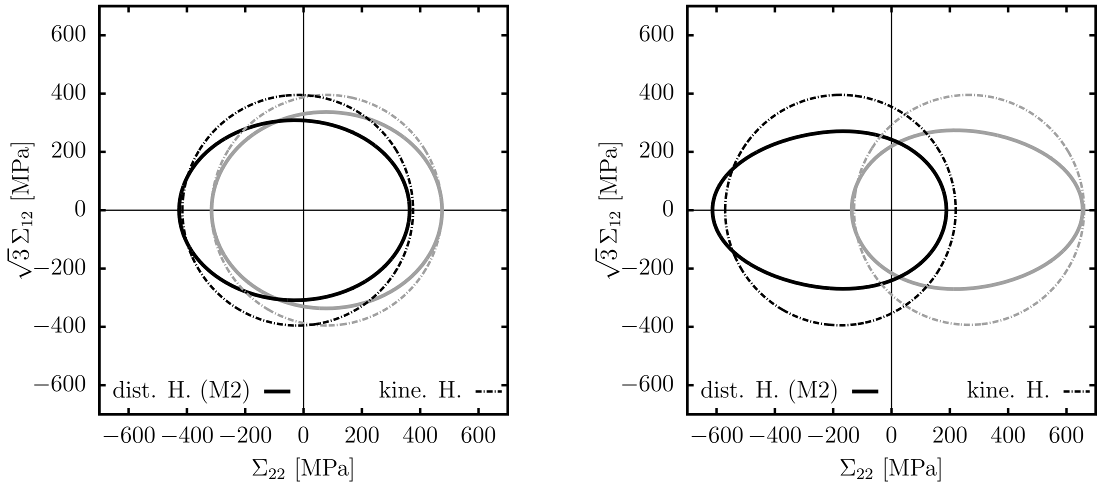

a) Yield surfaces for dotted line area

b) Yield surfaces for solid line area

Figure 4.15: Yield surface evolution of two marked points: a) yield surfaces correspond to the dotted white line in Fig. 4.14; b) yield surfaces correspond to the solid white line in Fig. 4.14. Yield surfaces in grey colour are associated with loading point $u_2 = u_0/2$ at $t = 0.5$ s and yield surfaces in black colour are associated with unloading point $u_2 = 0$ at $t = 1$ s.

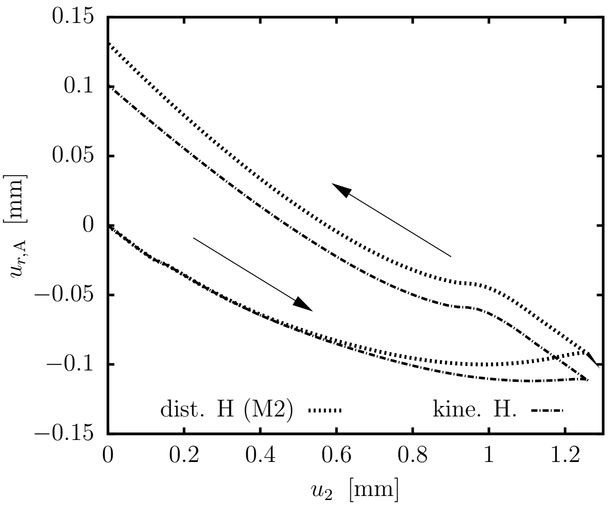

Figure 4.16: Radial displacement $u_{r,A}$ at the inner cycle point A as a function of the vertically applied displacement $u_2(t)$ (see setup in Fig. 4.13). Results are shown for distortional hardening model M2 and kinematic hardening. Arrows indicate loading and unloading.

placements lead to maximal temperature increase of $\Delta\Theta = 13$ K at the hole. Hence, thermal softening plays only a minor role. The temperatures are slightly higher for the kinematic hardening model. The distribution of the norm of the back strain tensor $\boldsymbol{\alpha}^{\mathrm{k}}$ is illustrated in Fig. 4.15. As one can observe, plastic strains localise for both models in a narrow band. Both models seem to predict a similar distribution. However, an analysis of the yield surface evolution in the plastic zone shows the differences between both models. Due to the anisotropic distortion of the yield surface the radial displacements at node point A (given in setup 4.13) evolves softer for the distortional hardening model M2. The results are illustrated as a function of the vertically applied displacement u_2 in Fig. 4.16.

4.4.5 Necking of an axisymmetric bar - distortional hardening model

Necking of a cylindrical tensile bar is analysed next, cf. Lehmann and Blix [71], Simo and Armero [117], Simo and Miehe [121], Wriggers et al. [137] and references cited therein. Two different conditions for the heat conduction between the specimen and the environment are considered in the cited works: on the hand hand adiabatic heat conduction at the external surface where no heat is exchanged with the surrounding medium or on the other hand non-adiabatic heat conduction at the external surface where heat can flow inside or outside of the bar. The non-adiabatic case is analysed in the following.

The considered cylindrical bar made of the aluminium alloy Al2024-T3 has a radius of $R = 6.413$ mm and a length of $L = 53.334$ mm. Due to axisymmetry, the problem size can be reduced to one quarter, see Fig. 4.17. Convection between the surface

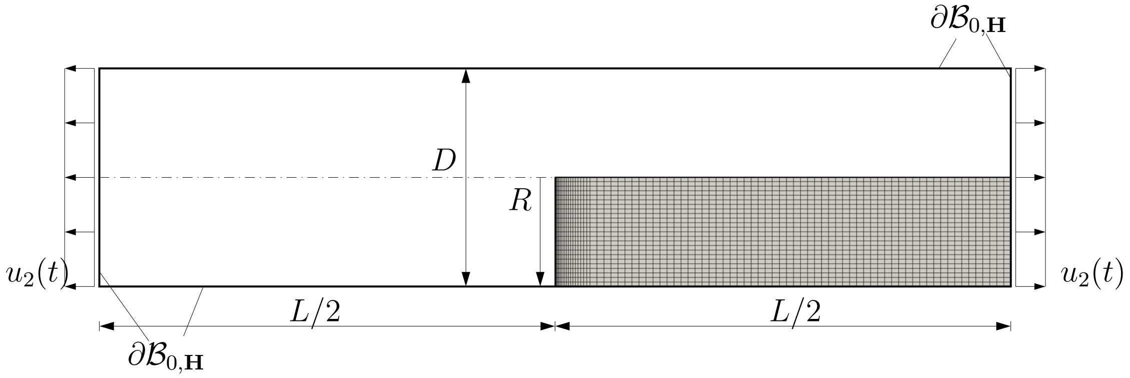
$\partial\mathcal{B}_{0,\mathbf{H}}$
D
R
$u_2(t)$
$u_2(t)$
$L/2$
$L/2$
$\partial\mathcal{B}_{0,\mathbf{H}}$

Figure 4.17: Necking of an axisymmetric bar: Numerical setup and finite element mesh of the axisymmetrical problem (one quarter). Dimensions are $L = 53.334$ mm, $D = 2\,R$, $R = 6.413$ mm and prescribed displacement is $u_2(t) \in [0, u_{2,\max}]$ with $u_{2,\max} = 10$ mm.

of the bar and the environment (surrounding air) is again described by means of the linear model according to Eq. (4.95). The top surface of the bar is subjected to the prescribed displacement $u_2(t)$ which is linearly increased in time up to an amplitude of $u_{2,\max} = 10$ mm. The velocity of the top surface is $\dot{u}_2 = 10$ mm/s.

The bar is again numerically analysed by means of the distortional hardening model M1 and the purely kinematical hardening model. The respective model parameters are still the same as the ones summarised in Tab. 4.3 and Tab. 4.4. In contrast to the isothermal or the adiabatic case [117, 136], no material imperfection is necessary in order to trigger necking. To be more explicit, convection at the bar's surface breaks the symmetry of the problem, i.e., the highest temperature leading to thermal softening occurs in the middle of the bar. The circular bar is discretised by means of 1920 axisymmetrical quadratic elements with 9 nodes and quadratic shape functions. A refined mesh is used in the expected necking area. All simulations were performed with a constant time step of $\Delta t = 0.001$ s.

The resulting temperature increase $\Delta\Theta = \Theta - \Theta_0$, the shear stress σ_{RZ} (Cauchy stress in the axisymmetric coordinate system; R corresponds to the radial direction, while Z denotes the respective orthogonal direction) and the norm of the kinematic hardening back-strain tensor $||\boldsymbol{\alpha}^{\mathrm{k}}||$ are displayed in the upper row in Fig. 4.18 for the distortional hardening model M1 and in Fig. 4.19 for the kinematic hardening model. Additionally, Fig. 4.18 and Fig. 4.19 show the evolved yield surfaces for three different material points at two different loading steps.

According to Fig. 4.18 and as expected, the distortional hardening model M1 predicts necking in the centre of the bar. Consequently, the highest plastic deformation (signalled by the norm of the equivalent plastic back-strain tensor; see top right picture in Fig. 4.18) is found in precisely this area. Through the coupling by means of the first law of thermodynamics (see Eq. (2.78)), the temperature increase looks qualitatively similar to the spatial distribution of $||\boldsymbol{\alpha}^{\mathrm{k}}||$. By way of contrast, the Cauchy shear stress plotted in the top middle picture in Fig. 4.18 looks slightly different: In line with thermal

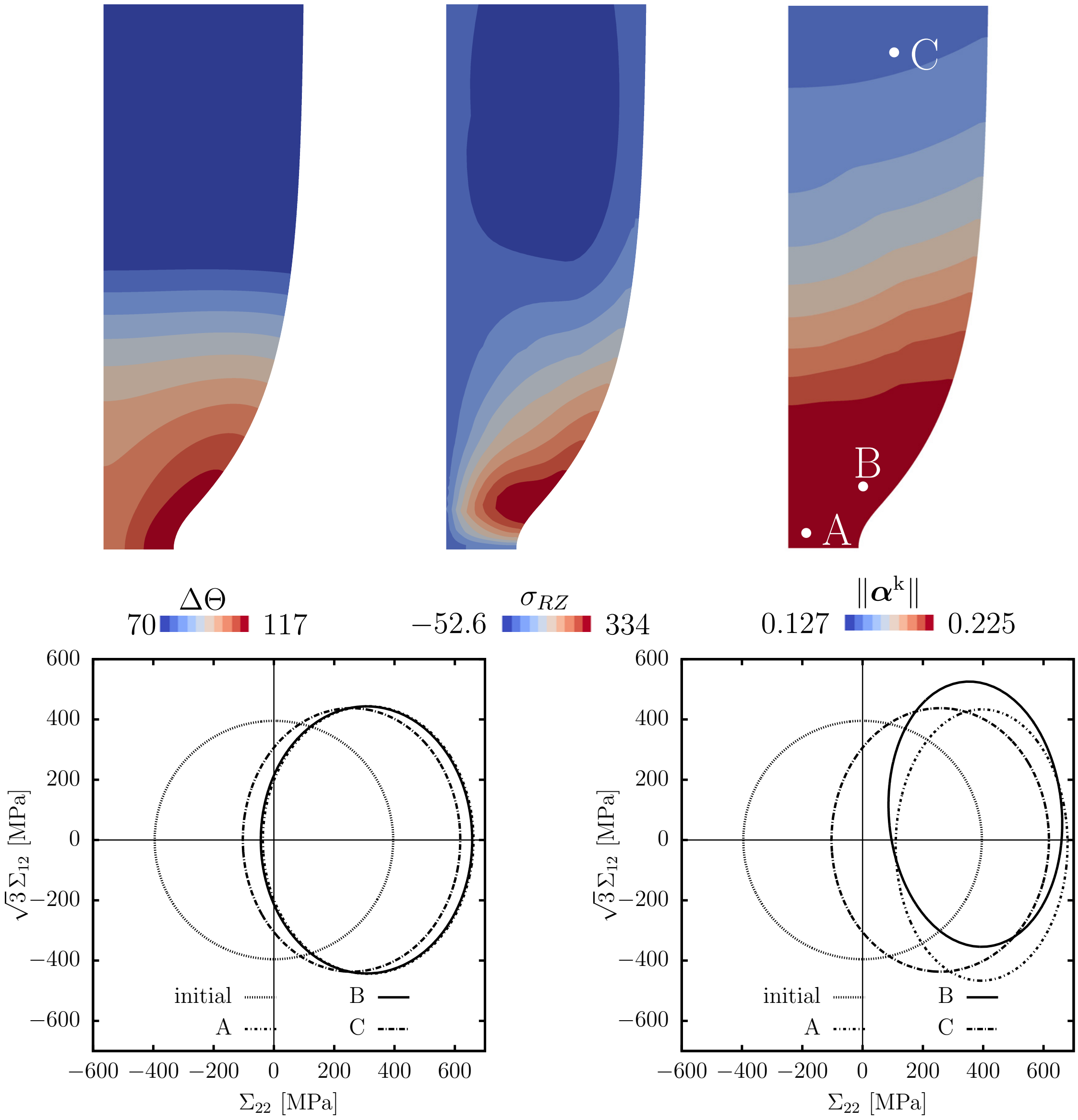

$u_2/u_{\max} = 0.600$ $u_2/u_{\max} = 0.925$

Figure 4.18: Necking of an axisymmetric bar – results obtained from the distortional hardening model M1: (top row; from left to right): temperature increase, shear stress (Cauchy stress in the axisymmetric coordinate system) and norm of the back strain tensor. The plots correspond to time step $u_2/u_{\max} = 0.925$; (bottom row): evolution of the yield surface for the three different points A, B and C (see top left plot) at two different time steps

softening, the maximum shear stress moves away from the necked cross section. Similar distributions of the increase in temperature due to plastic deformation, the shear stress and the norm of the back strain tensor are also observed for the model based on purely kinematic hardening, see Fig. 4.19. However, and agreeing with the computations for the uniaxial tensile test presented in the previous subsection, necking is more pronounced in the case of purely kinematic hardening.

A comparison between the yield surfaces predicted by the distortional hardening model M1 (bottom diagrams in Fig. 4.18) and those associated with the purely kinematic hardening model (bottom diagrams in Fig. 4.19) highlights the differences in the anisotropic hardening evolution. While for material point C this effect is less pronounced, a high distortion of the initially circular yield surface can indeed be seen for points A and B.

In order to obtain further insight into the physics of the problem, the evolution of the temperature for two characteristic points (P_1 and P_2) is depicted in Fig. 4.20. The diagrams correspond to the distortional hardening model M1, to the purely kinematic hardening model and to two different weighting factors for the dissipation $\beta^{\mathcal{D}} \in \{0.5, 0.7\}$. In addition, diagrams associated with adiabatic heat conduction are also presented for the sake of comparison (only for $\beta^{\mathcal{D}} = 0.7$). In line with Wriggers et al. [137], the less interesting adiabatic case leads to a (bi-)linear temperature increase for points P_1 and P_2. Furthermore, the thermal response of both points is almost identical. In Wriggers and Simo [136], the adiabatic case was analysed in detail and was found to be unstable. This problem can only be solved by carrying out a bifurcation analysis. By way of contrast, the more interesting and more realistic non-adiabatic case does not show this problem. Equally important and as a result of the different boundary conditions, the evolution of the temperature for point P_1 and P_2 are now different. In the necking domain at point P_1, a large temperature increase can be seen (up to to 120 K). This is related to the large plastic deformations in this domain. Clearly, this effect is more pronounced for a larger weighting factor $\beta^{\mathcal{D}}$. The temperature difference between the different hardening models is comparably small.

Regarding the non-adiabatic case, the evolutions corresponding to point P_1 and P_2 start to deviate at a loading amplitude of $u_2 \approx 5.7$ mm. According to Fig. 4.21, this amplitude is associated with the maximum loading and after $u_2 \approx 5.7$ mm softening occurs. However, softening is characterised by (plastic) loading in narrow bands, while the remaining part of the structure unloads elastically. Since point P_2 belongs to the "remaining part" and since elastic unloading has only a negligible effect on the temperature change, an almost constant temperature is predicted after $u_2 \approx 5.7$ mm for point P_2 in the non-adiabatic case. For adiabatic heat conduction this effect cannot be seen, since heat conduction leads to a smearing of the spatial temperature field.

The structural mechanical response is given in Fig. 4.21 by means of a load-displacement diagram (Fig. 4.21a) and by means of the evolution of the cross sectional diameter in the necking domain (Fig. 4.21b). The curves correspond to the different hardening models and different weighting factors for the dissipation $\beta^{\mathcal{D}} \in \{0.5, 0.7\}$.

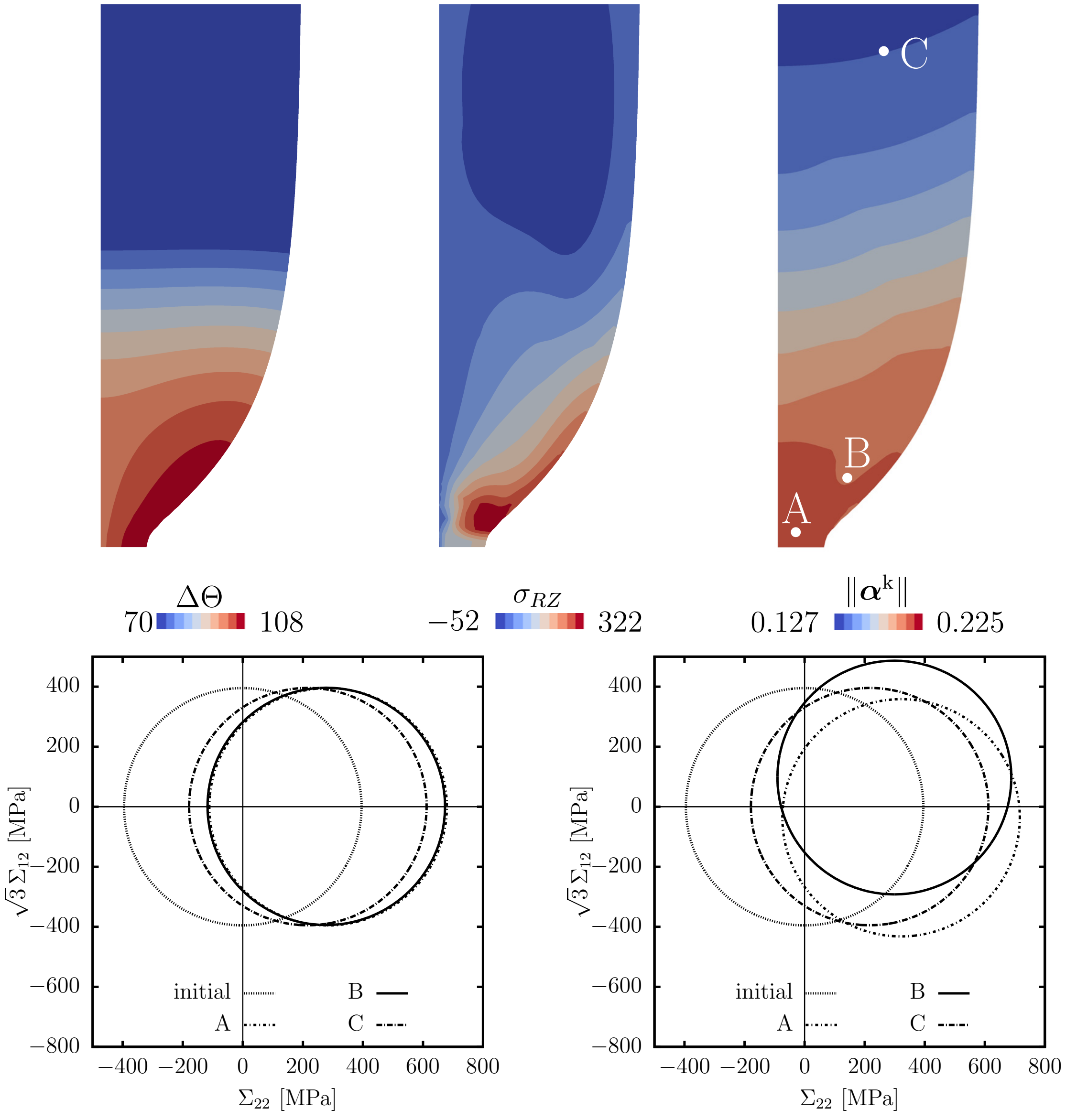

$u_2/u_{\max} = 0.600$ $u_2/u_{\max} = 0.925$

Figure 4.19: Necking of an axisymmetric bar – results obtained from the purely kinematic hardening model: (top row; from left to right): temperature increase, shear stress (Cauchy stress in the axisymmetric coordinate system) and norm of the back strain tensor. The plots correspond to time step $u_2/u_{\max} = 0.925$; (bottom row): evolution of the yield surface for the three different points A, B and C (see top left plot) at two different time steps

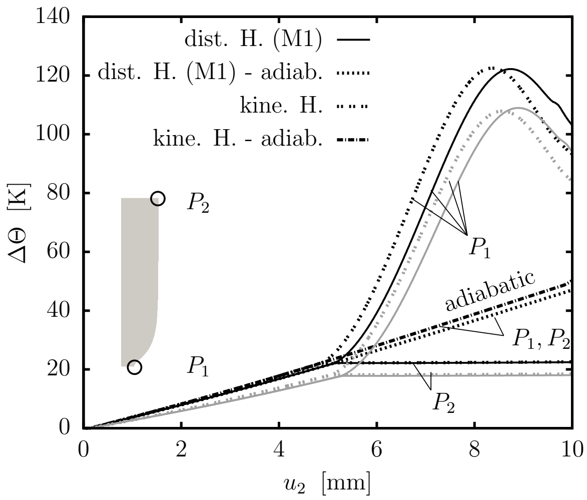

Figure 4.20: Necking of an axisymmetric bar – temperature evolution for the two different points P_1 and P_2. The results are obtained from distortional hardening model and the purely kinematic hardening model. Two different dissipative weighting factor are considered ($\beta^{\mathcal{D}} = 0.7$ in black colour and $\beta^{\mathcal{D}} = 0.5$ in grey colour). For the sake of comparison, results corresponding to adiabatic heat conduction are also shown (only for $\beta^{\mathcal{D}} = 0.7$).

Furthermore, in addition to the standard finite element formulation based on isoparametric quadratic shape functions (Q2), the EAS formulation advocated in Glaser and Armero [49], Simo and Armero [117] was also implemented. According to Fig. 4.21 all constitutive models and all numerical formulations lead to a similar mechanical response. Physically and numerically meaningful results are obtained up to a loading amplitude of $u_2 = 0.925\, u_{2,\max}$. After this state, the finite element meshes become too distorted. Interestingly, the four-noded enhanced assumed strain elements show already numerical problems at an amplitude of $u_2 = 0.825\, u_{2,\max}$. Further loading results in hourglassing as becomes evident in Fig. 4.22. However, both finite element formulations lead to almost identical results up to this point.

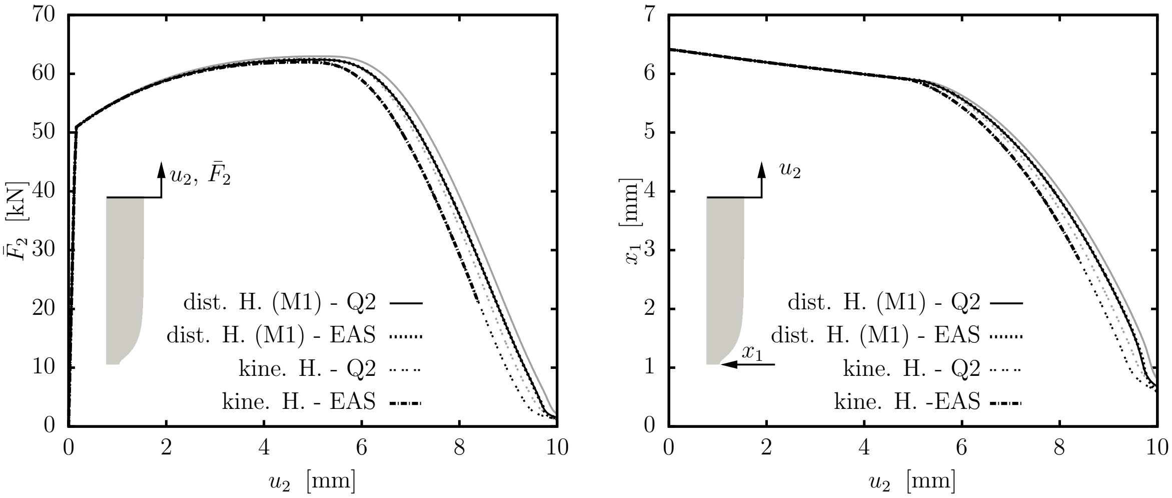

Figure 4.21: Necking of an axisymmetric bar – structural mechanical response: (left) Load-deflection curve and (right) radius-deflection curve. Two different dissipative weighting factor ($\beta^{\mathcal{D}} = 0.7$ in black colour and $\beta^{\mathcal{D}} = 0.5$ in grey colour) and two different finite element formulations (standard finite element with quadratic shape functions (Q2) and four-noded enhanced assumed strain elements according to Glaser and Armero [49], Simo and Armero [117] (EAS)) are considered.

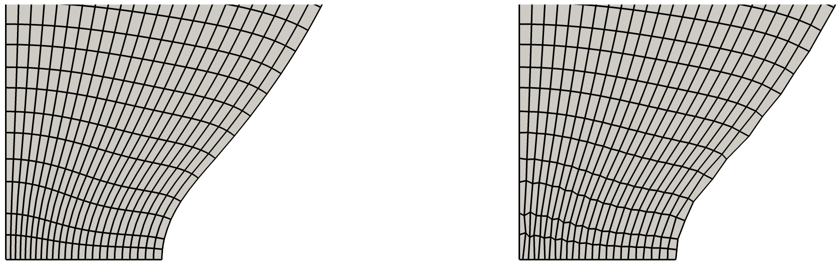

a) deformed mesh at $u_2/u_{2,\max} = 0.925$ for quadratic elements (Q2)

b) deformed mesh at $u_2/u_{2,\max} = 0.925$ for enhanced assumed strain elements (EAS)

Figure 4.22: Necking of an axisymmetric bar – deformed finite element meshes obtained from different finite element formulations; (left): standard finite elements with quadratic shape functions (Q2) and (right): enhanced assumed strain elements according to Glaser and Armero [49], Simo and Armero [117] (EAS)

5 Allen-Cahn-type phase field theory coupled to continuum mechanics: Computation of effective material properties based on variational constitutive updates

So far the developed material model for capturing the evolving microstructures was associated with the technological relevant macroscale. In order to get a more detailed insight into the evolution of microstructures, more precisely the transformation of phases, the more relevant microscale is analysed. For this purpose, phase field theories of Allen-Cahn-type can be applied for the description of phase transformations.

This chapter deals with efficient variational constitutive updates for an Allen-Cahn-type phase field theory coupled to a geometrically exact description of continuum mechanics. The starting point of the implementation is a unified variational principle: A time-continuous potential is introduced, the minimisers of which describe every aspect of the aforementioned coupled model – including the homogenisation assumptions defining the mechanical response of the bulk material in the diffuse interface region. With regard to these assumptions, classic models such as the one by Taylor/Voigt or the one by Reuss/Sachs are included. Additionally, more sound homogenisation approaches falling into the range of rank-1 convexification are also incorporated in the unified framework.

These homogenisation schemes include the recently proposed work of Mosler et al. [92], where the properties in the interface are determined by the Cauchy-Hadamard condition. In contrast to a classic rank-1 convexification given in Aubry and Ortiz [6], Ortiz and Repetto [98], Carstensen et al. [27], Bartel and Hackl [10], the normal vector in the Cauchy-Hadamard condition and the phase fraction are globally defined. Since in Mosler et al. [92] the normal vector is coupled to the phase front direction, the respective homogenisation is termed partial rank-1. In addition to this homogenisation assumption, a generalised version of Mosler et al. [92] is presented in this chapter. The underlying assumption is referred to as full rank-1 homogenisation and is based on the idea of a locally relaxed normal vector in the Cauchy-Hadamard condition – similar to classic rank-1 convexification.

Based on a direct discretisation of the underlying time-continuous potential in time and space, an efficient numerical finite element implementation is proposed. In order to guarantee admissible order parameters of the phase field, the unconstrained optimisation problem is supplemented by respective constraints. They are implemented by means of Lagrange parameters combined with the Fischer-Burmeister NCP functions, cf. Fischer [45]. This results in an exact fulfillment of the aforementioned constraints without considering any inequality. Several numerical examples show the predictive capabilities as well as the robustness and efficiency of the final algorithmic formulation. Furthermore, the influence of the homogenisation assumption is analysed in detail. It is shown that the choice of the homogenisation assumption does indeed influence the predicted microstructure in general. However, all models converge to the same solution in the limiting case.

This chapter is structured as follows: Section 5.1 gives a concise overview of the sharp interface regularisation. Moreover, a unified variational format is introduced in Section 5.2 for a phase field model coupled to mechanics. The homogenisation of the bulk energy in the diffuse interface is addressed in Section 5.3. Based on a unified framework proposed in Subsection 5.3.1, different homogenisation assumptions are derived and compared to each other in Subsection 5.3.2. These are: a) Reuss/Sachs, b) full rank-1, c) partial rank-1 and d) Taylor/Voigt. Section 5.4 deals with the numerical implementation. First, the underlying time-continuous coupled phase field model is discretised in time (Subsection 5.4.1). Subsequently, Fischer-Burmeisters NCP functions are applied to the coupled phase field model in Section 5.4.2, and the obtained algebraic system of equations is discretised in space and linearised within a finite element scheme in Section 5.4.3. The numerical framework and the modelling capabilities of the proposed homogenisation assumptions are presented in Section 5.5. Finally, the influence of varying interface thicknesses, in the sense of a sharp interface approximation, is analysed.

5.1 Diffuse approximation of interfaces

A body $\mathcal{B}_0$ consisting of N_V different phases is considered in the following. Their sets can be identified by the respective indicator functions. While such functions are discontinuous (either 0 or 1), if the interfaces between the different phases are understood as sharp interfaces, they are approximated by means of continuous functions in the case of a phase field description. In the phase field setting, these functions are often denoted as *order parameters* ξ_i. In line with the indicator function, they show the partition of unity property $\sum_{i=1}^{N_V} \xi_i = 1 \,\forall\, \mathbf{X} \in \mathcal{B}_0$. For the sake of simplicity, only dual-phase materials are considered in the following. The order parameters of the two phases are $\xi_1 \in [0, 1]$

and $\xi_2 \in [0,1]$. However, due to the partition of unity property, only one of these order parameters is independent, i.e.,

$$\xi_1 = 1 - \xi_2. \tag{5.1}$$

ξ_2 is chosen as the independent function and, in line with other publications on phase field theory, it is denoted as p, i.e., $p = \xi_2$. Based on the field,

$$p : \begin{cases} \mathcal{B}_0 \times \tau \to [0,1] \\ (\mathbf{X}, t) \mapsto p(\mathbf{X}, t) \end{cases} \tag{5.2}$$

the interface between two phases can be approximated.

The approximation of the interface is illustrated in Fig. 5.1. A classic smooth approximation for a dual-phase system was proposed in Modica and Mortola [87]. Without going into too much detail, it can be shown that the minimiser of the functional (under suitable boundary conditions)

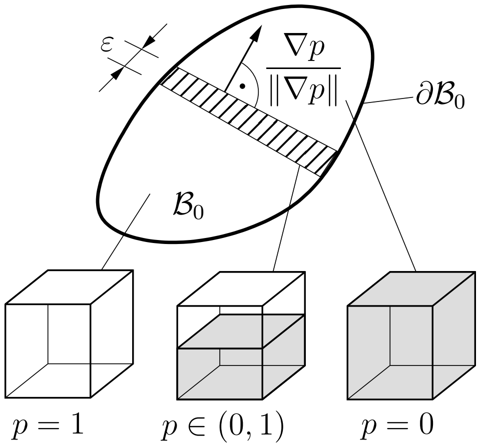

Figure 5.1: Illustration of a body $\mathcal{B}_0$ consisting of two phases (phase 1: $p = 0$ and phase 2: $p = 1$) and the interface ($p \in (0,1)$ with interface thickness ε). The normal of the interface is specified by $\mathbf{N} = \nabla p \|\nabla p\|$.

$$f^\varepsilon(p, \nabla p) = \int\limits_{\mathcal{B}_0} \left\{ \frac{6}{\varepsilon} p^2 \left[1 - p\right]^2 + \frac{3}{2} \varepsilon \|\nabla p\|^2 \right\} \mathrm{d}V \tag{5.3}$$

converges to the area of the sharp interface Γ. To be more precise,

$$\inf_{p \in [0,1]} f^\varepsilon(p) \quad \longrightarrow \quad \Gamma^\varepsilon \tag{5.4}$$

and Γ^{ε} converges to Γ in the sense of Γ-convergence. The thickness of the approximated interface is given by the value of ε. Here and in what follows the gradient ∇p is referred to the reference configuration, i.e.,

$$\mathrm{GRAD}p = \nabla_{\mathbf{X}} p = \nabla p. \tag{5.5}$$

Based on approximation (5.3) the energy related to the interfaces can be approximated by

$$\Psi_{\Gamma} = \psi_0^{\Gamma} \left\{ \frac{6}{\varepsilon} p^2 \left[1 - p\right]^2 + \frac{3}{2} \varepsilon \|\nabla p\|^2 \right\} \tag{5.6}$$

where ψ_0^{Γ} is the area specific interface energy. Accordingly, the interface energy within a body reads

$$\mathcal{I}_{\Gamma} = \int\limits_{\mathcal{B}_0} \Psi_{\Gamma} \, \mathrm{d}V \, . \tag{5.7}$$

5.2 A coupled phase field approach

5.2.1 Balance equations for a deformation driven phase field model

Next, the mechanical model and the interface model are coupled. The underlying boundary value problem is described by the deformation field $\boldsymbol{\varphi}$ and by the order parameter field p as introduced in the previous section (Eq. (5.2)). These two fields are restricted to the dissipation inequality and respective balance equations. The balance of linear momentum is the governing equation for the mechanical problem. In the referential configuration, the balance reads

$$\mathrm{DIV}\mathbf{P} + \rho_0 \, \mathbf{B} = \mathbf{0} \quad \text{on} \quad \mathcal{B}_0 \, , \tag{5.8}$$

as discussed in detail in Eq. (2.16). Without further discussion and derivation, angular momentum and mass conservation are assumed to be fulfilled, see Remark 2.3.1. For the phase field parameter, the balance of micro forces is applied. Following Gurtin [50] the internal micro forces π and the external micro forces γ of a cell equal the micro stresses $\boldsymbol{\xi} \cdot \mathbf{N}$ acting across the boundary of a unit cell. In the integral form the micro force balance reads

$$\int\limits_{\partial\Omega_0} \boldsymbol{\xi} \cdot \mathbf{N} \, \mathrm{d}A + \int\limits_{\Omega_0} \left[\pi + \gamma\right] \mathrm{d}V = 0 \, . \tag{5.9}$$

In this context, the word "micro" is associated with the order parameter p capturing the evolution of the underlying micro-structure. From a physics point of view, the internal micro force π describes forces associated with changing the configuration of atoms within the unit cell (similar to the explicit derivative within the framework of configurational/material forces). The external micro force γ is related to changes of atom configurations of external sources. However, the external sources are not considered in this work, i.e. $\gamma = 0$. Moreover, the first term in Eq. (5.9) corresponds to a flux across neighbouring cells in which $\boldsymbol{\xi}$ denotes the micro stress vector and in which $\mathbf{N}$ denotes the normal on the surface $\partial\Omega_0$, cf. Gurtin [50] p.180. By applying the Gauss theorem to the first term, the local form of the micro balance

$$\mathrm{DIV}\boldsymbol{\xi} + \pi = 0 \quad \text{on} \quad \mathcal{B}_0 \tag{5.10}$$

is derived. The consideration of micro forces causes the additive enhancement of the balance of energy (2.17), i.e.

$$\frac{\mathrm{d}}{\mathrm{d}t} \int\limits_{\Omega_0} \{K + E\} \,\mathrm{d}V = \mathcal{P}_{\mathbf{F}} + \mathcal{P}_{\Theta} + \mathcal{P}_p \,. \tag{5.11}$$

In the following, inertia effects are not considered, i.e. $K = 0$. The external power associated with the micro forces is determined by the flux of micro stresses acting on the surface $\bar{\xi} = \boldsymbol{\xi} \cdot \mathbf{N}$, i.e.

$$\mathcal{P}_p = \int\limits_{\partial\Omega_0} \bar{\xi}\, \dot{p} \,\mathrm{d}A \,. \tag{5.12}$$

The external mechanical power $\mathcal{P}_{\mathbf{F}}$ and the external thermal power $\mathcal{P}_{\Theta}$ are taken from Eq. (2.18) and Eq. (2.19). After transformation of the surface integrals into volume integrals and after insertion of micro force balance (5.10) into Eq. (5.11), the local energy balance

$$\dot{E} = \mathbf{P} : \dot{\mathbf{F}} - \mathrm{DIV}\boldsymbol{\mathcal{Q}} + R_{\Theta} - \pi\, \dot{p} + \boldsymbol{\xi} \cdot \nabla\dot{p} \tag{5.13}$$

is derived. While the stress power $\mathbf{P} : \dot{\mathbf{F}}$ is associated with the mechanical response and $-\mathrm{DIV}\boldsymbol{\mathcal{Q}} + R_{\Theta}$ is associated with the thermal response, the last two terms refer to the power generated by the micro field p. For the sake of simplicity, the isothermal case with $\boldsymbol{\mathcal{Q}} = \mathbf{0}, R_{\Theta} = 0, \dot{\Theta} = 0$ is discussed in the following. In this case, the internal energy (5.13) reduces to

$$\dot{\Psi} + \Theta\, \dot{N} = \mathbf{P} : \dot{\mathbf{F}} - \pi\, \dot{p} + \boldsymbol{\xi} \cdot \nabla\dot{p} \,, \tag{5.14}$$

where use is made of Legendre relation (2.42). For the derivation of the dissipation inequality, the term $\mathrm{DIV}\boldsymbol{\mathcal{Q}} - R_\Theta$ in Eq. (2.26) is replaced by Eq. (5.13) leading to the dissipation inequality

$$\mathcal{D} = \mathbf{P} : \dot{\mathbf{F}} + \Theta\, \dot{N} + \boldsymbol{\mathcal{Q}} \cdot \mathbf{G} - \pi\, \dot{p} + \boldsymbol{\xi} \cdot \nabla\dot{p} - \dot{E} \geq 0\,. \tag{5.15}$$

Focussing on isothermal conditions the dissipation inequality reduces therefore to

$$\mathcal{D} = \mathbf{P} : \dot{\mathbf{F}} - \pi\, \dot{p} + \boldsymbol{\xi} \cdot \nabla\dot{p} - \dot{\Psi} \geq 0\,. \tag{5.16}$$

Remark 5.2.1: *Following the work of Gurtin [50] the rate of the free energy cannot exceed the power of external forces, i.e.*

$$\frac{\mathrm{d}}{\mathrm{d}t} \int\limits_{\Omega_0} \Psi \,\mathrm{d}V \leq \mathcal{P}_{\mathbf{F}} + \mathcal{P}_p\,, \tag{5.17}$$

which is equivalent to the derived dissipation inequality in Eq. (5.16)*. Another important observation in this context is that if the homogeneous Neumann boundary* $\boldsymbol{\xi} \cdot \mathbf{N} = 0$ *on* $\partial\mathcal{B}_{0,\boldsymbol{\xi}}$ *holds, the Lyapunov relation*

$$\int\limits_{\mathcal{B}_0} \mathcal{D} \,\mathrm{d}V = -\frac{\mathrm{d}}{\mathrm{d}t} \int\limits_{\mathcal{B}_0} \Psi \,\mathrm{d}V \geq 0 \tag{5.18}$$

is fulfilled.

Boundary conditions: In order to solve the coupled system of equations (the linear momentum balance (5.8) and the micro force balance (5.10)), boundary and initial conditions need to be defined. For this purpose, the boundary of the referential body $\partial\mathcal{B}_0$ is decomposed for the mechanical and the phase field problem into their Dirichlet and Neumann boundaries

$$\partial\mathcal{B}_0 = \partial\mathcal{B}_{0,\boldsymbol{\varphi}} \cup \partial\mathcal{B}_{0,\mathbf{T}} \qquad \partial\mathcal{B}_0 = \partial\mathcal{B}_{0,p} \cup \partial\mathcal{B}_{0,\boldsymbol{\xi}}\,. \tag{5.19}$$

This boundary decomposition is disjunct in the sense $\mathcal{B}_{0,\boldsymbol{\varphi}} \cap \partial\mathcal{B}_{0,\mathbf{T}} = \emptyset$ for the mechanical problem and by $\partial\mathcal{B}_{0,p} \cap \partial\mathcal{B}_{0,\boldsymbol{\xi}} = \emptyset$ for the phase field problem. While for the mechanical boundaries the classic conditions

$$\boldsymbol{\varphi} = \bar{\boldsymbol{\varphi}} \text{ on } \mathcal{B}_{0,\boldsymbol{\varphi}} \quad \text{and} \quad \mathbf{P} \cdot \mathbf{N} = \bar{\mathbf{T}} \text{ on } \partial\mathcal{B}_{0,\mathbf{T}} \tag{5.20}$$

are applied, the Dirichlet and Neumann conditions for the phase parameter and the micro tractions are defined as

$$p = \bar{p} \text{ on } \mathcal{B}_{0,p} \quad \text{and} \quad \boldsymbol{\xi} \cdot \mathbf{N} = \bar{\xi} \text{ on } \partial\mathcal{B}_{0,\boldsymbol{\xi}}\,, \tag{5.21}$$

in which $\bar{p}$ and $\bar{\xi}$ denote the prescribed phase parameter and the prescribed micro tractions. Frequently, homogeneous micro tractions are assumed, i.e.

$$\bar{\xi} = 0 \quad \text{on} \quad \partial\mathcal{B}_{0,\boldsymbol{\xi}} \, . \tag{5.22}$$

This initial distribution of the order parameter p at time t_0 is denoted as

$$p(\mathbf{X}, t_0) = p_0(\mathbf{X}) \quad \text{in} \quad \mathcal{B}_0 \, . \tag{5.23}$$

5.2.2 Variationally consistent phase field modelling

In this section, suitable constitutive assumptions are included into the framework presented before. Here, hyperelasticity is assumed. Hence, the mechanical response is defined through a Helmholtz energy Ψ_{B} depending only on $\mathbf{F}$. Accounting for eigenstrains $\mathbf{F}^{\mathrm{B}}$ (Bain strains) in the material, the Helmholtz energy is of the type

$$\Psi_{\mathrm{B}} = \Psi_{\mathrm{B}}(\mathbf{F}^{\mathrm{e}}) \quad \text{with} \quad \mathbf{F}^{\mathrm{e}} = \mathbf{F} \cdot \mathbf{F}^{\mathrm{B}^{-1}} , \tag{5.24}$$

where frame indifference is postulated for Ψ_{B}. In this context the Bain strains $\mathbf{F}^{\mathrm{B}}$ are material specific constants which describe the transformation strain of an individual unit cell. The volume-specific Helmholtz energy of the bulk energy (5.24) combined with interface energy (5.6) is thus of the type

$$\Psi(\mathbf{F}, p, \nabla p) = \Psi_{\mathrm{B}}(\mathbf{F}, p, \nabla p) + \Psi_{\Gamma}(p, \nabla p) \, . \tag{5.25}$$

Accordingly, a deformation-independent interface energy is chosen, i.e., Ψ_{Γ} only depends on the phase field parameter (and its gradient), cf. Eq. (5.6). Furthermore and in contrast to a single phase material, the Helmholtz energy representing the bulk material also depends on p. This extension is necessary, since the bulk material response of points within the diffuse interface ($p \in (0, 1)$) is based on a suitable averaging or homogenisation of the constitutive models of the individual phases. Further details with regard to this homogenisation are discussed in detail in Section 5.3.

The constitutive model implied by Helmholtz energy (5.25) is supplemented by the dissipation inequality (5.16). By inserting the free energy (5.25) into the dissipation inequality (5.16), one obtains

$$\mathcal{D} = \left[\mathbf{P} - \frac{\partial \Psi}{\partial \mathbf{F}}\right] : \dot{\mathbf{F}} + \left[\boldsymbol{\xi} - \frac{\partial \Psi}{\partial \nabla p}\right] \cdot \dot{\overline{\nabla p}} - \left[\pi + \frac{\partial \Psi}{\partial p}\right] \dot{p} \geq 0 \tag{5.26}$$

and thus, application of the classic *Coleman & Noll* procedure yields the first Piola-Kirchhoff stress tensor $\mathbf{P}$ and the constitutive relation for the micro stresses $\boldsymbol{\xi}$

$$\mathbf{P} = \frac{\partial \Psi_{\mathrm{B}}}{\partial \mathbf{F}} \qquad \text{and} \qquad \boldsymbol{\xi} = \frac{\partial \Psi}{\partial \nabla p} \, . \tag{5.27}$$

By way of contrast, π is not chosen to be an energetical variable ($\pi \neq \partial\Psi/\partial p$). It can be interpreted as a generalized dissipative force which is associated with the phase motion. Therefore, an additional constitutive assumption is required. By inserting the state functions (5.27) into the dissipation inequality (5.26) the reduced dissipation inequality reads

$$\mathcal{D}_{\text{int}} = \mathcal{F}\,\dot{p} \qquad \text{with} \qquad \mathcal{F} = -\left[\pi + \frac{\partial\Psi}{\partial p}\right]. \tag{5.28}$$

By assuming that the dissipative driving force $\mathcal{F}$ is proportional to the phase motion i.e. $\mathcal{F} = \eta\,\dot{p}$, the dissipation inequality becomes $\mathcal{D}_{\text{int}} = \eta\,\dot{p}^2$. Hence, under the constraint that the mobility of the phase front η is $\eta \geq 0$, the dissipation inequality is always fulfilled. The constitutive model $\mathcal{F} = \eta\,\dot{p}$ is equivalent to choosing a convex dissipation functional of the form $\phi(\mathcal{F}) = 1/2\,\mathcal{F}^2/\eta$. Alternatively, its dual – in the sense of a Legendre-Fenchel transformation of the type $\phi^*(\dot{p}) = \mathcal{F}\,\dot{p} - \phi(\mathcal{F})$ –

$$\phi^*(\dot{p}) = \frac{1}{2}\,\eta\dot{p}^2 \tag{5.29}$$

can be applied. This dual dissipation functional is also referred to as *Ginzburg-Landau-type* dissipation functional.

Next, a variational structure – similar to the one characterised by Eq. (2.84) – is derived. For that purpose, the rate potential

$$\dot{\mathcal{E}}(\mathbf{F}, p, \nabla p) = \dot{\Psi}_{\text{B}}(\mathbf{F}, p, \nabla p) + \dot{\Psi}_{\Gamma}(p, \nabla p) + \phi^*(\dot{p}) \tag{5.30}$$

is introduced. For rate-independent materials, i.e., those depending on a dissipation functional which is positively homogeneous of degree one, this rate potential equals the stress power. For such materials, the total power of the total body is given by

$$\dot{\mathcal{I}} = \int\limits_{\mathcal{B}_0} \dot{\mathcal{E}}(\boldsymbol{\varphi}, p)\,\mathrm{d}V - \mathcal{P}_{\mathbf{F}}(\boldsymbol{\varphi})\,. \tag{5.31}$$

Although this interpretation is lost for rate-dependent materials such as those discussed in this chapter, rate potential (5.31) will nevertheless be considered in the following. As will be shown, the minimiser of the time-discrete potential corresponding to Eq. (5.31) is the solution of the coupled boundary value problem, i.e.,

$$(\boldsymbol{\varphi}, p) = \arg \inf_{\boldsymbol{\varphi}, p} \Delta\mathcal{I}\,. \tag{5.32}$$

In order to show this, stationarity conditions of Eq. (5.31) are elaborated next. A variation with respect to the deformation mapping yields

$$\delta_{\dot{\varphi}}\dot{\mathcal{I}} = -\int\limits_{\mathcal{B}_0} \{\mathrm{DIV}(\partial_{\mathbf{F}}\Psi_{\mathrm{B}}) + \rho_0\,\mathbf{B}\} \cdot \delta\dot{\boldsymbol{\varphi}}\,\mathrm{d}V + \int\limits_{\partial\mathcal{B}_0} \left\{\partial_{\mathbf{F}}\Psi_{\mathrm{B}} \cdot \mathbf{N} - \bar{\mathbf{T}}\right\} \cdot \delta\dot{\boldsymbol{\varphi}}\,\mathrm{d}A = 0. \quad (5.33)$$

By inserting the stresses $\mathbf{P} = \partial_{\mathbf{F}}\Psi$ into this equation it can be seen that this stationary condition is equivalent to the balance of linear momentum and to the Neumann boundary conditions. To be more explicit, Eq. (5.33) is equivalent to

$$\begin{aligned} \mathrm{DIV}\mathbf{P} + \rho_0\,\mathbf{B} = \mathbf{0} \quad &\text{on} \quad \mathcal{B}_0\,, \\ \mathbf{P}\cdot\mathbf{N} = \bar{\mathbf{T}} \quad &\text{on} \quad \partial\mathcal{B}_{0,\mathbf{T}}\,, \end{aligned} \quad (5.34)$$

where $\mathbf{N}$ is the normal at the surface $\partial\mathcal{B}$ and where $\bar{\mathbf{T}}$ denotes the prescribed traction vector. Analogously, the stationary condition with respect to the phase field parameter gives

$$\begin{aligned} \delta_{\dot{p}}\dot{\mathcal{I}} = &\int\limits_{\mathcal{B}_0} \{\partial_p[\Psi_{\mathrm{B}} + \Psi_\Gamma] + \partial_{\dot{p}}\phi^* - \mathrm{DIV}\left(\partial_{\nabla p}[\Psi_{\mathrm{B}} + \Psi_\Gamma]\right)\}\;\delta\dot{p}\,\mathrm{d}V \\ &+ \int\limits_{\partial\mathcal{B}_0} \{\partial_{\nabla p}[\Psi_{\mathrm{B}} + \Psi_\Gamma]\cdot\mathbf{N}\}\;\delta\dot{p}\,\mathrm{d}A = 0\,. \end{aligned} \quad (5.35)$$

Since $\boldsymbol{\xi} = \partial_{\nabla p}[\Psi_{\mathrm{B}} + \Psi_\Gamma]$, Eq. (5.35) is equivalent to

$$\begin{aligned} \partial_p[\Psi_{\mathrm{B}} + \Psi_\Gamma] + \partial_{\dot{p}}\phi^* - \mathrm{DIV}\boldsymbol{\xi} = 0 \quad &\text{on} \quad \mathcal{B}_0\,, \\ \boldsymbol{\xi}\cdot\mathbf{N} = 0 \quad &\text{on} \quad \partial\mathcal{B}_{0,\boldsymbol{\xi}}\,, \end{aligned} \quad (5.36)$$

which shows the same structure as Eq. (5.34). According to Eq. (5.36), homogeneous Neumann boundary conditions are applied within the phase field problem. By inserting the dual dissipation functional (5.29) into Eq. (5.36) the micro force balance can be rewritten as

$$\partial_p[\Psi_{\mathrm{B}} + \Psi_\Gamma] - \mathrm{DIV}\,(\boldsymbol{\xi}) = -\eta\,\dot{p}\,. \quad (5.37)$$

This type of equation is known as a *Ginzburg-Landau*-type evolution equation characterising an Allen-Cahn-type phase field model. Note, that it does not imply conservation of volume (phase contents) within domain $\mathcal{B}_0$. This is in sharp contrast to *Cahn-Hilliard*-type phase field models as discussed in Chapter 6.

5.3 Bulk response within the diffuse interface

Once the Helmholtz energies are chosen, the mechanical properties of the two different bulk phases and those of the sharp interface are uniquely defined. However, the bulk properties within the diffuse interface region, where $p \in (0, 1)$, are not uniquely defined. According to Eq. (5.25), it has been assumed that the energy within the diffuse interface shows the form

$$\Psi_{\mathrm{B}} = \Psi_{\mathrm{B}}(\mathbf{F}, p, \nabla p). \tag{5.38}$$

Essentially, two different approaches for defining Eq. (5.38) can be found in the literature. Within the first class of approaches, a certain interpolation is postulated in an ad-hoc manner, cf. Khachaturyan [61]. Alternatively, and as proposed e.g. in Ammar et al. [3], de Rancourt et al. [36], Mosler et al. [92], Steinbach and Apel [124], this energy can be computed by applying homogenisation theories. For that purpose, an RVE with two different phases is analysed. Clearly, all models based on the homogenisation theory also fall into the first class of approaches. The opposite is not true. For instance, models based on a pure interpolation usually do not show the important localisation property inherent to the homogenisation theory. That is, the effective mechanical response of the bulk phase within the diffuse interface does not define the mechanical response of the individual phases. In the following only models based on homogenisation theory are considered. Further details can be found in Ammar et al. [3], Mosler et al. [92].

5.3.1 Fundamentals of the homogenisation theory

The fundamentals of the homogenisation theory are concisely summarised in this section. A comprehensive overview on classical homogenisation theories such as those by Taylor/Voigt and Reuss/Sachs or the self-consistent schemes is given in Nemat-Nasser and Hori [93]. For novel computational homogenisation schemes the interested reader is referred to Miehe et al. [86], Smit et al. [122], Svenning et al. [129] – among many others. For the sake of simplicity, focus shall lie on hyperelastic materials in the following. For dissipative materials, the reader is referred to Mosler et al. [92].

An RVE with two different phases is considered. This RVE is associated with a material point at the macroscale belonging to the diffuse interface region ($p \in (0, 1)$). The material response of the two hyperelastic phases in the RVE is defined by means of Helmholtz energies $\Psi_{\mathrm{B}_1}(\mathbf{F}_1^{\mathrm{e}})$ and $\Psi_{\mathrm{B}_2}(\mathbf{F}_2^{\mathrm{e}})$. They are of the type (5.24). Thus, the effect of Bain strains is accounted for. In phase field theory, the deformation within the two different phases belonging to the same macroscopic material point is approximated as piece-wise constant. The respective deformation gradients are denoted as $\mathbf{F}_1$ and $\mathbf{F}_2$. Accordingly, the macroscopic bulk energy of the RVE is computed as

$$\Psi_\mathrm{B} = \frac{1}{V(\mathcal{B}_0)} \int\limits_{\mathcal{B}_0} \Psi_{\mathrm{B_i}} \,\mathrm{d}V = [1-p]\,\Psi_{\mathrm{B}_1}\left(\mathbf{F}_1 \cdot \mathbf{F}_1^{\mathrm{B}^{-1}}\right) + p\,\Psi_{\mathrm{B}_2}\left(\mathbf{F}_2 \cdot \mathbf{F}_2^{\mathrm{B}^{-1}}\right). \tag{5.39}$$

Thus, the order parameter (related to the second phase) represents the volume ratio, i.e., $p = V(\mathcal{B}_{0,2})/V(\mathcal{B}_0)$. Likewise, the macroscopic deformation gradient $\mathbf{F}$ can be written as

$$\mathbf{F} = \frac{1}{V(\mathcal{B}_0)} \int\limits_{\mathcal{B}_0} \mathbf{F}_i \,\mathrm{d}V = [1-p]\,\mathbf{F}_1 + p\,\mathbf{F}_2\,. \tag{5.40}$$

By introducing the jump $[\![\mathbf{F}]\!] = \mathbf{F}_2 - \mathbf{F}_1$ of the deformation gradient from phase one to phase two, Eq. (5.40) yields

$$\mathbf{F}_1 = \mathbf{F} - p\,[\![\mathbf{F}]\!] \quad \text{and} \quad \mathbf{F}_2 = \mathbf{F} + [1-p]\,[\![\mathbf{F}]\!]\,. \tag{5.41}$$

In Fig. 5.2 possible configurations of the deformation gradient jump are depicted.

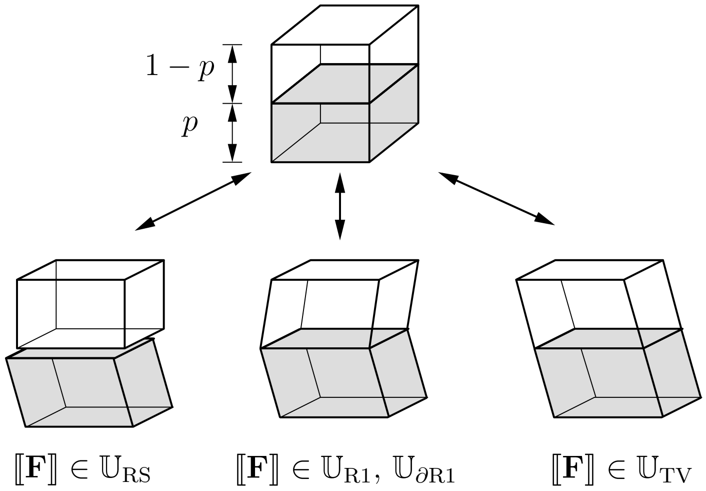
$1-p$
p
$[\![\mathbf{F}]\!] \in \mathbb{U}_\mathrm{RS}$
$[\![\mathbf{F}]\!] \in \mathbb{U}_\mathrm{R1}$, $\mathbb{U}_{\partial\mathrm{R1}}$
$[\![\mathbf{F}]\!] \in \mathbb{U}_\mathrm{TV}$

Figure 5.2: Illustration of the continuity of deformation in a dual phase material point. The jump of the deformation gradient $[\![\mathbf{F}]\!]$ depends on the admissible space $\mathbb{U}$ (the Taylor/Voigt space $\mathbb{U}_\mathrm{TV}$ and the spaces based on a rank-1 connection $\mathbb{U}_\mathrm{R1}$ and $\mathbb{U}_{\partial\mathrm{R1}}$ are kinematically compatible, the Reuss/Sachs space $\mathbb{U}_\mathrm{RS}$ is kinematically incompatible). A detailed discussion follows in Subsection 5.3.2.

Consequently, the macroscopic bulk energy (5.39) within the diffuse interface region can be rewritten into the alternative format

$$\begin{aligned}\Psi_\mathrm{B}(\mathbf{F}, p, [\![\mathbf{F}]\!]) = {} & [1-p]\,\Psi_{\mathrm{B}_1}\left([\mathbf{F} - p\,[\![\mathbf{F}]\!]] \cdot \mathbf{F}_1^{\mathrm{B}^{-1}}\right) \\ & + p\,\Psi_{\mathrm{B}_2}\left([\mathbf{F} + [1-p]\,[\![\mathbf{F}]\!]] \cdot \mathbf{F}_2^{\mathrm{B}^{-1}}\right)\,.\end{aligned} \tag{5.42}$$

Since hyperelasticity is based on the natural variational principle of energy minimisation, the jump $[\![\mathbf{F}]\!]$ is also computed by relaxing the energy (5.42) with respect to the jump. This relaxation depends on the space of admissible jumps and will be discussed in detail in the next subsections. Independent of the space of admissible jumps, this relaxation leads to the reduced (relaxed) bulk energy

$$\Psi_{\mathrm{B}}^{\mathrm{red}} = \inf_{[\![\mathbf{F}]\!] \in \mathbb{U}} \Psi_{\mathrm{B}}(\mathbf{F}, p, [\![\mathbf{F}]\!]) \,, \tag{5.43}$$

which serves as an effective hyperelastic potential defining the effective mechanical response. To be more precise, the effective first Piola-Kirchhoff stress tensor reads

$$\mathbf{P} = \frac{\partial \Psi_{\mathrm{B}}^{\mathrm{red}}}{\partial \mathbf{F}} = [1-p]\mathbf{P}_1 + p\mathbf{P}_2 \,, \tag{5.44}$$

where

$$\mathbf{P}_i = \frac{\partial \Psi_{\mathrm{B}_i}}{\partial \mathbf{F}_i} = \frac{\partial \Psi_{\mathrm{B}_i}}{\partial \mathbf{F}_i^{\mathrm{e}}} \cdot \mathbf{F}_i^{\mathrm{B}-\mathrm{T}} \tag{5.45}$$

are the first Piola-Kirchoff stress tensors within the two phases.

It becomes apparent that models relying on such homogenisation theories show the localisation property, i.e. the individual stresses in the interface follow directly from the homogenisation assumption. In contrast, models based on pure interpolation schemes do not inherit this property (Remark 5.3.1).

Remark 5.3.1: *An effective bulk energy of Khachaturyan-type is represented by*

$$\Psi_{\mathrm{B}} = \widehat{\Psi}_{\mathrm{B}}\left(\bar{\mathbf{F}}(\mathbf{F}, p), \bar{\mathbf{F}}^{\mathrm{B}}(p, \mathbf{F}_1^{\mathrm{B}}, \mathbf{F}_2^{\mathrm{B}}), \bar{\mathcal{X}}(p, \mathcal{X}_1, \mathcal{X}_2)\right) \,, \tag{5.46}$$

which depends on homogenised Bain strains $\bar{\mathbf{F}}^{\mathrm{B}}$ and homogenised material parameters $\bar{\mathcal{X}}$. Therein, an explicit interpolation for the Bain strains and the material parameters is assumed, e.g. Levitas et al. [77].

5.3.2 Space of admissible jumps in the deformation gradient – different homogenisation assumptions

As mentioned before, the effective bulk behaviour (5.43) depends on the space of admissible jumps in the deformation gradient. According to Eq. (5.36), the effective bulk energy, in turn, affects the driving force governing the evolution of the interfaces. It will be shown in this section that by choosing proper spaces $\mathbb{U}$ of the jump of the deformation gradient, some of the classic homogenisation assumptions can be obtained.

5.3.2.1 Reuss/Sachs-type homogenisation

The classic Reuss/Sachs assumption states that the stresses in both phases are identical, i.e., $\mathbf{P}_1 = \mathbf{P}_2$. Consequently, the traction vectors fulfil $[\![\mathbf{T}]\!] = [\mathbf{P}_2 - \mathbf{P}_2] \cdot \mathbf{N} = \mathbf{0}$. Ignoring interfacial effects such as surface tension, the Reuss/Sachs-type homogenisation assumption thus enforces equilibrium. However, kinematical compatibility/admissibility is completely ignored.

As shown in Mosler et al. [92], the Reuss/Sachs-type homogenisation is equivalent to the relaxed energy

$$\Psi_{\mathrm{B}}^{\mathrm{red}} = \inf_{[\![\mathbf{F}]\!] \in \mathbb{R}^{3\times 3}} \Psi_{\mathrm{B}}(\mathbf{F}, p, [\![\mathbf{F}]\!]) . \tag{5.47}$$

Hence, the space of admissible jumps in the deformation gradient is defined by 3 × 3 matrices, i.e., $[\![\mathbf{F}]\!] \in \mathbb{R}^{3\times 3}$. The equivalence between the variational problem (5.47) and the classic Reuss/Sachs assumption can be seen by computing the stationary condition corresponding to Eq. (5.47). To be more explicit, a variation with respect to $[\![\mathbf{F}]\!]$ yields

$$\begin{aligned} \delta_{[\![\mathbf{F}]\!]} \Psi_{\mathrm{B}} =& \frac{\partial \Psi_{\mathrm{B}}}{\partial [\![\mathbf{F}]\!]} : \delta [\![\mathbf{F}]\!] = 0 \quad \text{with} \\ & \frac{\partial \Psi_{\mathrm{B}}}{\partial [\![\mathbf{F}]\!]} = p\,[1-p]\,[-\mathbf{P}_1 + \mathbf{P}_2] = \mathbf{0} \\ & \quad \Leftrightarrow \qquad \mathbf{P}_2 - \mathbf{P}_1 = [\![\mathbf{P}]\!] = \mathbf{0} , \end{aligned} \tag{5.48}$$

and therefore the respective driving force acting at the interface is computed as

$$\begin{aligned} \delta_p \Psi_{\mathrm{B}} =& \frac{\partial \Psi_{\mathrm{B}}}{\partial p} \delta p \quad \text{with} \\ & \frac{\partial \Psi_{\mathrm{B}}}{\partial p} = [\![\Psi_{\mathrm{B}}]\!] - \mathbf{P} : [\![\mathbf{F}]\!] , \end{aligned} \tag{5.49}$$

where the macroscopic stress tensor $\mathbf{P}$ shows the form (5.44) and $[\![\Psi_{\mathrm{B}}]\!] = \Psi_{\mathrm{B}_2} - \Psi_{\mathrm{B}_1}$ denotes the energy jump of the two bulk energies.

5.3.2.2 Full rank-1 homogenisation

The Reuss/Sachs-type homogenisation assumption is statically compatible, i.e., it fulfils equilibrium at the interface. However, it is not kinematically compatible. The condition guaranteeing kinematical compatibility is the *Cauchy & Hadamard* condition. For an interface with normal vector $\tilde{\mathbf{N}}$ this condition reads

$$[\![\mathbf{F}]\!] = \mathbf{a} \otimes \tilde{\mathbf{N}} . \tag{5.50}$$

Here, vector $\mathbf{a}$ characterises the jump of the deformation gradient. Accordingly, the deformation gradients in the two phases are rank-1 connected. Inserting condition (5.50) into Eq. (5.42) leads to the macroscopic energy

$$\begin{aligned}\Psi_\mathrm{B}(\mathbf{F},p,\mathbf{a},\tilde{\mathbf{N}}) = [1-p]\,\Psi_{\mathrm{B}_1}\left(\left[\mathbf{F}-p\,[\mathbf{a}\otimes\tilde{\mathbf{N}}]\right]\cdot\mathbf{F}_1^{\mathrm{B}^{-1}}\right)\\ +p\,\Psi_{\mathrm{B}_2}\left(\left[\mathbf{F}+[1-p]\,[\mathbf{a}\otimes\tilde{\mathbf{N}}]\right]\cdot\mathbf{F}_2^{\mathrm{B}^{-1}}\right)\,.\end{aligned} \tag{5.51}$$

In line with the Reuss/Sachs-type homogenisation assumption, a relaxation of this potential with respect to the jump in the deformation gradient yields the relaxed macroscopic energy. Since the jump is now of type (5.50), this relaxation reads

$$\Psi_\mathrm{B}^\mathrm{red} = \inf_{\substack{\mathbf{a}\in\mathbb{R}^3\\ \tilde{\mathbf{N}}\in S^2}}\ \Psi_\mathrm{B}(\mathbf{F},p,\mathbf{a},\tilde{\mathbf{N}})\,, \tag{5.52}$$

where S^2 is the three-dimensional unit sphere. Evidently, the full rank-1-type homogenisation fulfils kinematic compatibility at the interface. In order to check static compatibility, the stationary conditions related to the relaxed energy (5.52) are analysed. The first of those is obtained as

$$\begin{aligned}\delta_\mathbf{a}\Psi_\mathrm{B} =&\frac{\partial\Psi_\mathrm{B}}{\partial\mathbf{a}}\cdot\delta\mathbf{a}=0\quad\text{with}\\ &\frac{\partial\Psi_\mathrm{B}}{\partial\mathbf{a}} = p\,[1-p]\,\left[-\mathbf{P}_1\cdot\tilde{\mathbf{N}}+\mathbf{P}_2\cdot\tilde{\mathbf{N}}\right]=\mathbf{0}\\ &\quad\Leftrightarrow\qquad [\mathbf{P}_2-\mathbf{P}_1]\cdot\tilde{\mathbf{N}} = [\![\mathbf{P}]\!]\cdot\tilde{\mathbf{N}}=\mathbf{0}\,.\end{aligned} \tag{5.53}$$

Thus, static equilibrium is indeed fulfilled at an interface with the normal vector $\tilde{\mathbf{N}}$ (if interfacial effects such as surface tension are neglected). The second stationary condition reads

$$\delta_{\tilde{\mathbf{N}}}\Psi_\mathrm{B} =\frac{\partial\Psi_\mathrm{B}}{\partial\tilde{\mathbf{N}}}\cdot\delta\tilde{\mathbf{N}}=0\quad\text{with}\qquad\frac{\partial\Psi_\mathrm{B}}{\partial\tilde{\mathbf{N}}}=\mathbf{0}\,. \tag{5.54}$$

The constraint $\tilde{\mathbf{N}}\in S^2$ is enforced by setting $\tilde{\mathbf{N}}=\mathbf{N}/||\mathbf{N}||\ \ \forall\,\mathbf{N}\in\mathbb{R}^3$. By doing so, Eq. $(5.54)_2$ can be re-written as

$$\begin{aligned}\frac{\partial\Psi_\mathrm{B}}{\partial\mathbf{N}} &= p\,[1-p]\,\mathbf{a}\cdot[\mathbf{P}_2-\mathbf{P}_1]\cdot\frac{\partial\tilde{\mathbf{N}}}{\partial\mathbf{N}}\\ &= p\,[1-p]\,\mathbf{a}\cdot[\![\mathbf{P}]\!]\cdot\frac{1}{||\mathbf{N}||}\left[\mathbf{I}-\tilde{\mathbf{N}}\otimes\tilde{\mathbf{N}}\right]=\mathbf{0}\\ &\Leftrightarrow\qquad \mathbf{a}\cdot[\![\mathbf{P}]\!]\cdot\frac{1}{||\mathbf{N}||}\left[\mathbf{I}-\tilde{\mathbf{N}}\otimes\tilde{\mathbf{N}}\right]=\mathbf{0}.\end{aligned} \tag{5.55}$$

For $\mathbf{a} \cdot [\![\mathbf{P}]\!] \neq \mathbf{0}$, this equation vanishes only for $\mathbf{a} \cdot [\![\mathbf{P}]\!]$ being parallel to $\tilde{\mathbf{N}}$, since $\tilde{\mathbf{N}} \cdot \left[\mathbf{I} - \tilde{\mathbf{N}} \otimes \tilde{\mathbf{N}}\right] = \mathbf{0}$. Condition (5.55) is equivalent to torque equilibrium across the interface (cf. Aubry and Ortiz [6]), i.e.,

$$\mathbf{a} \cdot [-\mathbf{P}_1 + \mathbf{P}_2] \times \tilde{\mathbf{N}} = \mathbf{a} \cdot [\![\mathbf{P}]\!] \times \tilde{\mathbf{N}} = \mathbf{0}\,. \tag{5.56}$$

As shown in Levitas and Ozsoy [74, 75] Eq. (5.56), together with linear momentum (5.55) implies $\mathbf{a} \cdot [\![\mathbf{P}]\!] = \mathbf{0}$. Finally, the driving force related to the bulk energy is computed. It yields

$$\begin{aligned} \delta_p \Psi_{\mathrm{B}} =& \frac{\partial \Psi_{\mathrm{B}}}{\partial p} \delta p \quad \text{with} \\ & \frac{\partial \Psi_{\mathrm{B}}}{\partial p} = [\![\Psi_{\mathrm{B}}]\!] - \mathbf{P} : [\mathbf{a} \otimes \tilde{\mathbf{N}}]\,. \end{aligned} \tag{5.57}$$

Denoting the space of admissible jumps in the deformation gradient as $\mathbb{U}_{\mathrm{RS}}$ for the Reuss/Sachs-type homogenisation assumption and the one related to the approach based on the rank-1 connection as $\mathbb{U}_{\mathrm{R1}}$, the obvious ordering $\mathbb{U}_{\mathrm{R1}} \subset \mathbb{U}_{\mathrm{RS}}$ holds. Therefore, the effective energy corresponding to the Reuss/Sachs method represents a lower bound.

5.3.2.3 Partial rank-1 homogenisation

Although full rank-1 homogenisation is certainly not a new relaxation, it is novel within the phase field framework. The first publication in which a similar relaxation is incorporated into phase field theory is the one by Mosler et al. [92]. However, and in contrast to the classic rank-1 homogenisation discussed in the previous paragraph, the normal vector $\tilde{\mathbf{N}}$ is not considered to be an independent variable in Mosler et al. [92]. Instead, this normal is related to the phase field by enforcing $\tilde{\mathbf{N}} = \mathbf{N} = \nabla p / \|\nabla p\|$. As a consequence, the macroscopic bulk energy then reads

$$\begin{aligned} \Psi_{\mathrm{B}}(\mathbf{F}, p, \nabla p, \mathbf{a}) = [1-p]\, \Psi_{\mathrm{B}_1} & \left([\mathbf{F} - p\, [\mathbf{a} \otimes \mathbf{N}]] \cdot \mathbf{F}_1^{\mathrm{B}^{-1}} \right) \\ + p\, \Psi_{\mathrm{B}_2} & \left([\mathbf{F} + [1-p]\, [\mathbf{a} \otimes \mathbf{N}]] \cdot \mathbf{F}_2^{\mathrm{B}^{-1}} \right)\,. \end{aligned} \tag{5.58}$$

Since the normal vector $\mathbf{N}$ depends on the (non-local) gradient of the phase field, it cannot be computed from a local relaxation. For this reason, the relaxed energy is given by

$$\Psi_{\mathrm{B}}^{\mathrm{red}} = \inf_{\mathbf{a} \in \mathbb{R}^3} \Psi_{\mathrm{B}}(\mathbf{F}, p, \nabla p, \mathbf{a})\,. \tag{5.59}$$

The respective stationary condition – in line with Eq. (5.53) – is obtained as

$$\begin{aligned}\delta_{\mathbf{a}}\Psi_{\mathrm{B}} =& \frac{\partial \Psi_{\mathrm{B}}}{\partial \mathbf{a}} \cdot \delta \mathbf{a} = 0 \quad \text{with} \\ & \frac{\partial \Psi_{\mathrm{B}}}{\partial \mathbf{a}} = p\,[1-p]\;[-\mathbf{P}_1 \cdot \mathbf{N} + \mathbf{P}_2 \cdot \mathbf{N}] = \mathbf{0} \\ & \qquad \Leftrightarrow \qquad [\mathbf{P}_2 - \mathbf{P}_1] \cdot \mathbf{N} = [\![\mathbf{P}]\!] \cdot \mathbf{N} = \mathbf{0}\,.\end{aligned} \tag{5.60}$$

Hence, static equilibrium at the interface is again fulfilled. Finally, the driving force of the interface due to the bulk energy is given by

$$\begin{aligned}\delta_p\Psi_{\mathrm{B}} =& \frac{\partial \Psi_{\mathrm{B}}}{\partial p}\delta p + \frac{\partial \Psi_{\mathrm{B}}}{\partial \nabla p} \cdot \delta \nabla p \quad \text{with} \\ & \frac{\partial \Psi_{\mathrm{B}}}{\partial p} = [\![\Psi_{\mathrm{B}}]\!] - \mathbf{P} : [\mathbf{a} \otimes \mathbf{N}]\,, \\ & \frac{\partial \Psi_{\mathrm{B}}}{\partial \nabla p} = p\,[1-p]\,\mathbf{a} \cdot [-\mathbf{P}_1 + \mathbf{P}_2] \cdot \partial_{\nabla p}\mathbf{N}\,.\end{aligned} \tag{5.61}$$

Accordingly, since the energy also depends on the gradient of the order parameter, an additional term arises.

By comparing the equations characterising the full rank-1 homogenisation presented in the previous paragraph to those related to the partial rank-1 homogenisation, one can see that the only difference between such approaches is constraint $\tilde{\mathbf{N}} = \mathbf{N} = \nabla p / \|\nabla p\|$. Thus, both approaches are statically as well as kinematically compatible. While the full rank-1 homogenisation guarantees equilibrium and kinematic compatibility at an interface with normal $\tilde{\mathbf{N}}$ which is independent of the phase field, the partial rank-1 homogenisation guarantees the same properties at an interface defined by the phase field, i.e., $\tilde{\mathbf{N}} = \mathbf{N} = \nabla p / \|\nabla p\|$.

Remark 5.3.2: *The normal vector* $\mathbf{N} = \nabla p / \|\nabla p\|$ *is only well defined if gradient* ∇p *does not vanish. However, this cannot be guaranteed in general. For instance, within each of the phases, i.e., where either* $p = 0$ *or* $p = 1$*, this condition is evidently not fulfilled. Speaking of the physics, the normal vector is not constrained in such cases. For this reason, partial rank-1 homogenisation is then identical to a full rank-1 homogenisation. Further details are omitted here, but will be discussed in Section 5.4.*

Remark 5.3.3: *While partial rank-1 homogenisation has already been successfully applied in phase field theory, cf. Mosler et al. [92], this is not the case for the full rank-1 homogenisation. However, the full rank-1 homogenisation is indeed mathematically sound, cf. Aubry and Ortiz [6] and Carstensen et al. [27]. Furthermore, due to the order relation* $\mathbb{U}_{\partial \mathrm{R1}} \subset \mathbb{U}_{\mathrm{R1}} \subset \mathbb{U}_{\mathrm{RS}}$ *of the spaces of admissible jumps in the deformation gradient, full rank-1 homogenisation fills the gap between Reuss-/Sachs-type homogenisation and homogenisation based on partial rank-1 homogenisation.*

Remark 5.3.4: *Within the previous subsection, the partial rank-1 homogenisation was presented for two phases. If real materials are to be modelled, the presented framework certainly has to be extended to multiple phases ($n > 2$). For that purpose, the presented rank-1 laminate approximation has to be extended to a rank-n laminate approximation – similar to the works Ortiz and Repetto [98],Bartel and Hackl [10],Bartels et al. [14].*

5.3.2.4 Taylor/Voigt-type homogenisation

The simplest choice for the space of the admissible jumps in the deformation gradient is the empty set, i.e., $\mathbf{F} = \mathbf{F}_1 = \mathbf{F}_2$. In this case the resulting bulk energy reads

$$\Psi_\mathrm{B}(\mathbf{F}, p) = [1-p]\,\Psi_{\mathrm{B}_1}\left(\mathbf{F}\cdot\mathbf{F}_1^{\mathrm{B}^{-1}}\right) + p\,\Psi_{\mathrm{B}_2}\left(\mathbf{F}\cdot\mathbf{F}_2^{\mathrm{B}^{-1}}\right)\,. \tag{5.62}$$

The choice $\mathbf{F} = \mathbf{F}_1 = \mathbf{F}_2$ is kinematically compatible. However, static equilibrium is ignored. Therefore, $\mathbf{P}_1\cdot\mathbf{N} \neq -\mathbf{P}_2\cdot\mathbf{N}$ where $\mathbf{N}$ is the normal vector implied by the phase field. Since no jump is considered in the Taylor/Voigt-type homogenisation, the driving force at the interface due to the bulk energy simplifies to

$$\begin{aligned} \delta_p\Psi_\mathrm{B} =& \frac{\partial\Psi_\mathrm{B}}{\partial p}\delta p \quad \text{with} \\ \frac{\partial\Psi_\mathrm{B}}{\partial p} =& [\![\Psi_\mathrm{B}]\!]\,. \end{aligned} \tag{5.63}$$

5.3.2.5 Summary

The four different presented homogenisation assumptions can be defined by their spaces of admissible jumps in the deformation gradient. Such spaces are

$$[\![\mathbf{F}]\!] \in \begin{cases} \mathbb{R}^{3\times3} & = \mathbb{U}_\mathrm{RS} \\ \left\{\mathbf{a}\otimes\tilde{\mathbf{N}}\,|\,\mathbf{a}\in\mathbb{R}^3;\ \tilde{\mathbf{N}}\in S^2\right\} & = \mathbb{U}_\mathrm{R1} \\ \{\mathbf{a}\otimes\mathbf{N}\,|\,\mathbf{a}\in\mathbb{R}^3;\ \mathbf{N}=\nabla p/\|\nabla p\|\} & = \mathbb{U}_{\partial\mathrm{R1}} \\ \emptyset & = \mathbb{U}_\mathrm{TV}\,. \end{cases} \tag{5.64}$$

A graphic illustration of the different spaces is shown in Fig. 5.2. Accordingly, they show the order relation $\mathbb{U}_\mathrm{RS} \supset \mathbb{U}_\mathrm{R1} \supset \mathbb{U}_{\partial\mathrm{R1}} \supset \mathbb{U}_\mathrm{TV}$. This, in turn, implies the order of relaxed energies

$$\inf_{[\![\mathbf{F}]\!]\in\mathbb{U}_\mathrm{RS}} \Psi_\mathrm{B} \leq \inf_{[\![\mathbf{F}]\!]\in\mathbb{U}_\mathrm{R1}} \Psi_\mathrm{B} \leq \inf_{[\![\mathbf{F}]\!]\in\mathbb{U}_{\partial\mathrm{R1}}} \Psi_\mathrm{B} \leq \inf_{[\![\mathbf{F}]\!]\in\mathbb{U}_\mathrm{TV}} \Psi_\mathrm{B}\,. \tag{5.65}$$

From a physics point of view, only the approaches based on rank-1 homogenisation are sound, since they fulfil static as well as kinematic compatibility. Interestingly, a mathematical point of view leads to the same conclusion: The Taylor/Voigt-assumption usually leads to energies which are not rank-1 convex implying that they are not quasi-convex.

For this reason, numerical solutions based on such models are not objective. Similarly, the Reuss/Sachs-type approach is not mathematically sound either. To be more precise, convexity combined with material frame indifference leads to unphysical models, cf. Ball [8]. Nevertheless, despite such deficiencies, the Taylor/Voigt-homogenisation as well as the Reuss/Sachs-homogenisation will be considered in the following. The reasons for this are two-fold. First, they serve as upper and lower bounds for the two other approaches. Furthermore, the diffuse interface region, i.e., the only region which is affected by the homogenisation assumption is supposed to be sufficiently small in phase field theories (the sharp interface model is recovered in the limiting case for which the thickness of the interface converges to zero).

Although the aforementioned homogenisation assumptions are indeed different, they can be written in a unified variational principle. In order to derive this principle, the jump in the deformation gradient is inserted into the rate potential (5.30)), i.e.,

$$\dot{\mathcal{E}} = \dot{\Psi}_{\mathrm{B}}(\mathbf{F}, p, [\![\mathbf{F}]\!]) + \dot{\Psi}_{\Gamma}(p, \nabla p) + \phi^*(\dot{p}) \tag{5.66}$$

and hence, Eq. (5.31) changes to

$$\dot{\mathcal{I}} = \int\limits_{\mathcal{B}_0} \dot{\mathcal{E}}(\boldsymbol{\varphi}, p, [\![\mathbf{F}]\!])\,\mathrm{d}V - \mathcal{P}_{\mathbf{F}}(\dot{\boldsymbol{\varphi}}). \tag{5.67}$$

In summary, the only difference between the four different homogenisation assumptions is the space of admissible jumps in the deformation gradient.

Remark 5.3.5: *Independent of the homogenisation assumption, by enforcing* $\partial_p \Psi_{\mathrm{B}}|_{[\![\mathbf{F}]\!]\in\mathbb{U}} = [\![\Psi_{\mathrm{B}}]\!] - \mathbf{P} : [\![\mathbf{F}]\!] = 0$ *and neglecting interfacial effects, an immobile phase front is enforced. This expression is known as the normal of the Eshelby's momentum tensor. It is related to the evolution of material defects.*

5.4 Numerical implementation

5.4.1 Incremental variational updates

This section elaborates on an efficient numerical implementation falling within the range of *variational constitutive updates* as introduced in Section 2.6. The underlying idea of such updates is the direct time discretisation of the variational time-continuous problem (5.67). Considering, time interval $\tau = [t_n, t_{n+1}]$, the integration of Eq. (5.67) reads

$$\begin{aligned} \Delta\mathcal{I} = \int\limits_{\tau} \dot{\mathcal{I}}\,\mathrm{d}t = \int\limits_{t_n}^{t_{n+1}} \dot{\mathcal{I}}\,\mathrm{d}t = \int\limits_{\mathcal{B}_0} \Delta\mathcal{E}(\boldsymbol{\varphi}_{n+1}, p_{n+1}, \boldsymbol{\beta}_{n+1}, \boldsymbol{\varphi}_n, p_n, \boldsymbol{\beta}_n)\,\mathrm{d}V \\ - \mathcal{P}_{\mathbf{F}}(\boldsymbol{\varphi}_{n+1}) + \mathcal{P}_{\mathbf{F}}(\boldsymbol{\varphi}_n) \end{aligned} \tag{5.68}$$

with

$$\begin{aligned}\Delta\mathcal{E} = {} & \Psi_{\mathrm{B}}\left(\mathbf{F}_{n+1}, p_{n+1}, \nabla p_{n+1}, \boldsymbol{\beta}_{n+1}\right) - \Psi_{\mathrm{B}}\left(\mathbf{F}_{n}, p_{n}, \nabla p_{n}, \boldsymbol{\beta}_{n}\right) \\ & + \Psi_{\Gamma}(p_{n+1}, \nabla p_{n+1}) - \Psi_{\Gamma}(p_n, \nabla p_n) + \Delta t\, \phi^{*}\left((p_{n+1} - p_n)/\Delta t\right) \ ,\end{aligned} \tag{5.69}$$

where $\Delta t = t_{n+1} - t_n$ denotes the time increment. If the external loads are conservative, the only approximation in Eq. (5.69) is the integration of the dissipation functional ϕ^*. Clearly, other consistent approximations of the rate potential (5.67) are also possible. In this respect, the choice of the time-discrete potential is not unique but relies on the time discretisation. Assuming the variables at time t_n to be known, the unknowns in Eq. (5.68) are $\{\mathbf{F}_{n+1}, p_{n+1}, \nabla p_{n+1}, \boldsymbol{\beta}_{n+1}\}$. Here and in what follows, $\boldsymbol{\beta}$ contains all unknowns defining the jump of the deformation gradient across the interface. For instance, in the case of the homogenisation scheme based on partial rank-1 homogenisation, $\boldsymbol{\beta} = \mathbf{a}$, while $\boldsymbol{\beta}$ contains all nine coordinates of $[\![\mathbf{F}]\!]$ for the Reuss/Sachs-type homogenisation approach. The update of $\boldsymbol{\beta}$ in the case of a partial rank-1 homogenisation is explicitly derived in Appendix C.1. An overview of the definition of $\boldsymbol{\beta}$ is given in Table 5.1. While the parametrisation a) corresponding to the Reuss/Sachs assumption is obvious, constraint $\|\tilde{\mathbf{N}}\| = 1$ associated with the full rank-1 method (b)) is enforced through spherical coordinates, i.e.,

Homogenisation	a) Reuss/Sachs	b) full rank-1	c) partial rank-1	d) Taylor/Voigt
Structure of $[\![\mathbf{F}]\!]$	$[\![\mathbf{F}]\!]$	$\mathbf{a} \otimes \tilde{\mathbf{N}}$	$\mathbf{a} \otimes \nabla p / \lVert\nabla p\rVert$	$\mathbf{0}$
Parametrisation of $\boldsymbol{\beta}$	$[\![\mathbf{F}]\!]$	$\mathbf{a}, \tilde{\mathbf{N}}$	$\mathbf{a}$ if $\lVert\nabla p\rVert > 0$ $\mathbf{a}, \tilde{\mathbf{N}}$ if $\lVert\nabla p\rVert = 0$	$\mathbf{0}$
dim($\boldsymbol{\beta}$)	9	5	3(5)	0

Table 5.1: Definition of the variable $\boldsymbol{\beta}$ for the different homogenisation assumptions. $\boldsymbol{\beta}$ represents a parametrisation of the jump of the deformation gradient $[\![\mathbf{F}]\!]$

$$\tilde{\mathbf{N}} = \begin{bmatrix} \sin\alpha\,\cos\gamma \\ \sin\alpha\,\sin\gamma \\ \cos\alpha \end{bmatrix} . \tag{5.70}$$

For the partial rank-1 homogenisation, $\boldsymbol{\beta} = \mathbf{a}$ as long as $\mathbf{N} = \nabla p / \|\nabla p\|$ is well defined, see Remark 5.3.2. Speaking in the sense of physics, nucleations of new phases in such domains are not biased by pre-existing interfaces – as in the method based on full rank-1 homogenisation. Accordingly, the function is extended as

$$\mathbf{N} \in \begin{cases} \dfrac{\nabla p}{\|\nabla p\|} & \text{if} \quad \|\nabla\, p\| > 0 \\ \text{Eq. (5.70)} & \text{otherwise} \ . \end{cases} \tag{5.71}$$

As a consequence, vector $\boldsymbol{\beta}$ shows the dimension 3 (dim($\mathbf{a}$)) or 5 (dim($\mathbf{a}$)+dim($\mathbf{N}(\alpha,\gamma)$)) for the homogenisation method based on partial rank-1 homogenisation.

In order to improve the readability, the time index $(\bullet)_{n+1}$ associated with the current time step is removed in the following. Hence, the time-discrete optimisation problem of the time-continuous potential (5.67) reads

$$(\boldsymbol{\varphi}, p, \boldsymbol{\beta}) = \arg \inf_{\boldsymbol{\varphi},p} \inf_{\boldsymbol{\beta}} \; \Delta\mathcal{I} \tag{5.72}$$

Since the variable $\boldsymbol{\beta}$ is a local quantity, the minimisation problem (5.72) can be conveniently decomposed into a local problem (depending on $\boldsymbol{\beta}$) and a reduced global problem (depending only on $\boldsymbol{\varphi}$ and p). To be more explicit, the local problem is given by

$$\begin{aligned}\Delta\mathcal{E}^{\mathrm{red}} = {} & \inf_{\boldsymbol{\beta}} \left\{\Psi_{\mathrm{B}}\left(\mathbf{F}, p, \nabla p, \boldsymbol{\beta}\right)\right\} - \Psi_{\mathrm{B}}\left(\mathbf{F}_n, p_n, \nabla p_n, \boldsymbol{\beta}_n\right) \\ & + \Psi_{\Gamma}(p, \nabla p) - \Psi_{\Gamma}(p_n, \nabla p_n) \\ & + \Delta t\, \phi^{*}\left((p - p_n)/\Delta t\right)\end{aligned} \tag{5.73}$$

and its solution defines the global problem

$$\inf_{\boldsymbol{\varphi},p} \Delta\mathcal{I}^{\mathrm{red}} = \int\limits_{\mathcal{B}_0} \Delta\mathcal{E}^{\mathrm{red}}(\boldsymbol{\varphi}, p, \boldsymbol{\varphi}_n, p_n)\, \mathrm{d}V - \mathcal{P}_{\mathbf{F}}(\boldsymbol{\varphi}) + \mathcal{P}_{\mathbf{F}}(\boldsymbol{\varphi}_n)\,. \tag{5.74}$$

Interestingly, the reduced functional $\Delta\mathcal{E}^{\mathrm{red}}$ acts like a hyperelastic potential, i.e., its partial derivative yields the first Piola-Kirchhoff stress tensor

$$\mathbf{P} = \frac{\partial \Delta\mathcal{E}^{\mathrm{red}}}{\partial \mathbf{F}}\,. \tag{5.75}$$

For this reason, stationarity of potential $\Delta\mathcal{I}^{\mathrm{red}}$ implies

$$\delta_{\boldsymbol{\varphi}}\, \Delta\mathcal{I}^{\mathrm{red}} = \int\limits_{\mathcal{B}_0} \mathbf{P} : \delta\mathbf{F}\, \mathrm{d}V - \int\limits_{\mathcal{B}_0} \rho_0 \mathbf{B} \cdot \delta\boldsymbol{\varphi}\, \mathrm{d}V - \int\limits_{\partial\mathcal{B}_0} \bar{\mathbf{T}} \cdot \delta\boldsymbol{\varphi}\, \mathrm{d}A = 0\,, \tag{5.76}$$

which is the weak form of equilibrium. For the sake of completeness, stationarity of potential $\Delta\mathcal{I}^{\mathrm{red}}$ with respect to the phase field is also given. It can be written as

$$\delta_p\, \Delta\mathcal{I}^{\mathrm{red}} = \int\limits_{\mathcal{B}_0} \left\{\frac{\partial\, \Delta\mathcal{E}^{\mathrm{red}}}{\partial p}\, \delta p + \frac{\partial\, \Delta\mathcal{E}^{\mathrm{red}}}{\partial \nabla p} \cdot \nabla\delta p\right\} \mathrm{d}V = 0\,. \tag{5.77}$$

Eq. (5.77) is the weak form of Eq. (5.36).

Remark 5.4.1: *In the model based on partial rank-1 homogenisation, the interface normal* $\mathbf{N} = \nabla p / \|\nabla p\|$ *depends on the phase field variable* p. *Numerical experiments showed that an explicit approximation of this normal vector affects the results only marginally by simultaneously increasing the efficiency significantly. As a consequence, the approximation*

$$\mathbf{N} = \left.\frac{\nabla p}{\|\nabla p\|}\right|_{t_{n+1}} \approx \left.\frac{\nabla p}{\|\nabla p\|}\right|_{t_n} \tag{5.78}$$

is applied.

5.4.2 Constrained optimisation

The variational principle $\inf \Delta \mathcal{I}^{\mathrm{red}}(\boldsymbol{\varphi}, p)$ does not naturally enforce the constraint $p \in [0,1]$ in general. This is due to the mechanical driving forces. For this reason, the constrained optimisation problem

$$\begin{aligned} \inf \Delta \mathcal{I}^{\mathrm{red}}(\boldsymbol{\varphi}, p) \quad \text{subject to} \quad r_1 &= \;\; p - 1 \leq 0 \\ r_2 &= \quad\; -p \leq 0 \end{aligned} \tag{5.79}$$

has to be considered. Lagrange multipliers represent a natural way to enforce such constraints. Therefore, the extended Lagrangian functional

$$\Delta \tilde{\mathcal{I}}^{\mathrm{red}}(\boldsymbol{\varphi}, p, \lambda_1, \lambda_2) = \Delta \mathcal{I}^{\mathrm{red}}(\boldsymbol{\varphi}, p) + \lambda_1 \, r_1 + \lambda_2 \, r_2 \tag{5.80}$$

is introduced. The Lagrange multipliers $\lambda_i \geq 0$ are dual to the variables to r_i. It bears emphasis that only one of such multipliers can be active, i.e., either p reaches the bound $p = 0$ (λ_2) or $p = 1$ (λ_1). The classical Karush-Kuhn-Tucker (KKT) conditions associated with Eq. (5.80) are (cf. Geiger and Kanzow [48])

$$\begin{aligned} \delta_p \Delta \mathcal{I}^{\mathrm{red}}(\boldsymbol{\varphi}, p) + \lambda_1 \, \partial_p r_1 + \lambda_1 \, \partial_p r_1 &= 0 \, , \\ \lambda_i &\geq 0 \, , \\ r_i &\leq 0 \, , \\ \lambda_i \, r_i &= 0 \quad \text{for} \quad i = \{1, 2\} \end{aligned} \tag{5.81}$$

and evidently enforce the aforementioned constraints. However, the numerical treatment of the inequalities in Eq. (5.81) is not straightforward. An efficient way of solving (5.81) – in the sense of a Newton-based solution scheme – is given in Fischer [45] (see also Bartel and Hackl [10]), in which the inequalities and equalities $(5.81)_2$ – $(5.81)_4$ are replaced by the equivalent NCP functions

$$g_i = \sqrt{r_i^2 + \lambda_i^2} + r_i - \lambda_i = 0 \qquad i = \{1, 2\} \, . \tag{5.82}$$

To be more explicit, $g_i = 0$ is equivalent to $\{\lambda_i \geq 0;\ r_i \leq 0;\ \lambda_i\, r_i = 0\}$. Consequently, no inequalities have to be considered in the numerical implementation and problem (5.81) can be re-written in residual form as

$$\mathbf{R_{FB}}(p, \lambda_1, \lambda_2) = \begin{bmatrix} \delta_p \Delta\tilde{\mathcal{I}}^{\text{red}}(\boldsymbol{\varphi}, p, \lambda_1, \lambda_2) \\ g_1(p, \lambda_1) \\ g_2(p, \lambda_2) \end{bmatrix} = \begin{bmatrix} \delta_p \Delta\mathcal{I}^{\text{red}}(\boldsymbol{\varphi}, p) + \lambda_1\, \delta p - \lambda_2\, \delta p \\ \sqrt{[p-1]^2 + \lambda_1^2} + [p-1] - \lambda_1 \\ \sqrt{[-p]^2 + \lambda_2^2} - p - \lambda_2 \end{bmatrix} = \mathbf{0}\,. \tag{5.83}$$

By combining Eq. (5.83) with the weak form of equilibrium, the fully coupled problems yields

$$\begin{bmatrix} \delta_{\boldsymbol{\varphi}} \Delta\mathcal{I}^{\text{red}}\,(\boldsymbol{\varphi}, p) \\ \mathbf{R_{FB}}(p, \lambda_1, \lambda_2) \end{bmatrix} = \begin{bmatrix} \delta_{\boldsymbol{\varphi}} \Delta\mathcal{I}^{\text{red}}\,(\boldsymbol{\varphi}, p) \\ \delta_p \Delta\mathcal{I}^{\text{red}}\,(\boldsymbol{\varphi}, p) + \lambda_1\, \delta p - \lambda_2\, \delta p \\ g_1(p, \lambda_1) \\ g_2(p, \lambda_2) \end{bmatrix} = \mathbf{0} \quad \text{on} \quad \mathcal{B}_0\,. \tag{5.84}$$

This problem is completed by the boundary conditions

$$\begin{aligned} \boldsymbol{\varphi} &= \bar{\boldsymbol{\varphi}} \quad \text{on} \quad \partial\mathcal{B}_{0,\boldsymbol{\varphi}}\,, \\ \mathbf{P}\cdot\mathbf{N} &= \mathbf{T} \quad \text{on} \quad \partial\mathcal{B}_{0,\mathbf{T}}\,, \\ p &= \bar{p} \quad \text{on} \quad \partial\mathcal{B}_{0,p}\,, \\ \boldsymbol{\xi}\cdot\mathbf{N} &= 0 \quad \text{on} \quad \partial\mathcal{B}_{0,\boldsymbol{\xi}}\,. \end{aligned} \tag{5.85}$$

Herein, the deformation map $\boldsymbol{\varphi}$, the phase parameter p and the additional Lagrange parameters λ_1 and λ_2 are the primary field variables of the coupled four-field problem.

Remark 5.4.2: *In the numerical implementation, the slightly adjusted NCP functions*

$$\begin{aligned} g_1(p, \lambda_1) &= \sqrt{[p - 1 + \varepsilon_0]^2 + \lambda_1^2 + \varepsilon_{\text{tol}}^2} + [p - 1 + \varepsilon_0] - \lambda_1 \\ g_2(p, \lambda_2) &= \sqrt{[-p + \varepsilon_0]^2 + \lambda_2^2 + \varepsilon_{\text{tol}}^2} + [-p + \varepsilon_0] - \lambda_2 \end{aligned} \tag{5.86}$$

are applied (see Eq. (5.82)). By introducing the perturbations ε_0 and ε_{tol} a numerically more stable version of the original FB functions is obtained. While ε_{tol} enforces the solution to be real-valued, the perturbation ε_0 moves points at the boundaries $p = 0$ and $p = 1$ slightly to the interior of the interval. Numerical experiments have shown that the latter perturbation improves the performance of the algorithm without significantly changing the results.

Remark 5.4.3: *The extension of the algorithm to more than two phases is straightforward: For each phase the two constraints ${}^j r_1 = {}^j p - 1 \leq 0$ and ${}^j r_2 = -{}^j p \leq 0$ are defined.*

Remark 5.4.4: *Although the presented algorithm for enforcing the constraint* $p \in [0,1]$ *is indeed promising – this will also be confirmed by numerical examples – a negative side effect should also be mentioned: the symmetry intrinsic to the underlying variational problem is lost. Hence, the matrices resulting from a finite element discretisation are not symmetric anymore.*

Remark 5.4.5: *As mentioned before, the natural constraint* $p \in [0,1]$ *is generally not fulfilled due to the additional mechanical driving forces. One way of avoiding this problem – not discussed in this thesis in detail – is therefore the modification of the mechanical driving force* $\partial_p \Psi_\mathrm{B}$*. Since this driving force is the variational derivative of the effective bulk energy within the diffuse interface, one could directly modify the underlying bulk energy, i.e.* $\Psi_\mathrm{B} = [1 - h(p)]\, \Psi_{\mathrm{B}_1} + h(p)\, \Psi_{\mathrm{B}_2}$ *such that the driving force reads*

$$\frac{\partial \Psi_\mathrm{B}}{\partial p} = \frac{\partial \Psi_\mathrm{B}}{\partial h} \frac{\partial h}{\partial p} \,. \tag{5.87}$$

For instance by choosing the interpolation function $h(p) = p^2\,[3 - 2\,p]$*, the properties* $h(p=1) = 1$ *and* $h(p=0) = 0$ *are naturally fulfilled and the driving force vanishes in the limiting cases* $\partial_p h(p=1)$ *and* $\partial_p h(p=0)$*. Clearly, the order parameter does not represent the relative volume ratio for this interpolation scheme.*

5.4.3 Finite element implementation

5.4.3.1 Discretisation of the weak form

The starting point of the finite element formulation to be elaborated is the partition of the reference body

$$\mathcal{B}_0 \approx \mathcal{B}_0^\mathrm{h} = \bigcup_{e=1}^{n_\mathrm{el}} \mathcal{B}_0^e \tag{5.88}$$

into n_el finite elements. In each element $\mathcal{B}_0^e$ the reference configuration $\mathbf{X}$ and the field variables $\boldsymbol{\varphi}$ and p are approximated by

$$\mathbf{X}|_{\mathcal{B}_0^e} \approx \mathbf{X}^\mathrm{h} = \sum_{a=1}^{n_\mathrm{en}^\mathbf{X}} N_\mathbf{X}^a\, \mathbf{X}^a \,, \quad \boldsymbol{\varphi}|_{\mathcal{B}_0^e} \approx \boldsymbol{\varphi}^\mathrm{h} = \sum_{a=1}^{n_\mathrm{en}^{\boldsymbol{\varphi}}} N_{\boldsymbol{\varphi}}^a\, \boldsymbol{\varphi}^a \,, \quad p|_{\mathcal{B}_0^e} \approx p^h = \sum_{a=1}^{n_\mathrm{en}^p} N_p^a\, p^a \,. \tag{5.89}$$

Here, $N_{(\bullet)}^{(\bullet)}$ are shape functions and $\mathbf{X}^a$, $\boldsymbol{\varphi}^a$ and p^a are the referential coordinates, the deformation mapping and the phase field parameter at node a. In what follows, isoparametric elements are considered and the unknown fields are interpolated by means of the same shape functions, i.e., $N^a = N_\mathbf{X}^a = N_{\boldsymbol{\varphi}}^a = N_p^a$ and $n_\mathrm{en} = n_\mathrm{en}^\mathbf{X} = n_\mathrm{en}^{\boldsymbol{\varphi}} = n_\mathrm{en}^p$. In sharp contrast to the field variables $\boldsymbol{\varphi}$ and p, the Lagrange multipliers λ_1 and λ_2 are not interpolated, since the NCP functions are applied at the nodes and gradients of the Lagrange parameters are not required (see Remark 5.4.6).

Based on the interpolations (5.89), the approximations of the gradients are obtained as

$$\mathbf{F}^h = \nabla\boldsymbol{\varphi}^{\mathrm{h}} = \sum_{a=1}^{n_{\mathrm{en}}} \boldsymbol{\varphi}^a \otimes \nabla N^a\,, \quad \nabla p^h = \sum_{a=1}^{n_{\mathrm{en}}} p^a\, \nabla N^a\,, \tag{5.90}$$

where ∇N^a denotes the gradient of N^a with respect to the reference configuration $\mathbf{X}$. In line with a Bubnov-Galerkin discretisation, the test functions are defined by means of the same functions spanning the primary variables. Consequently, the test functions and their gradients read

$$\begin{aligned} \delta\boldsymbol{\varphi}^{\mathrm{h}} &= \sum_{a=1}^{n_{\mathrm{en}}} N^a\,\delta\boldsymbol{\varphi}^a\,, \quad \delta p^h = \sum_{a=1}^{n_{\mathrm{en}}} N^a\,\delta p^a\,, \\ \delta\mathbf{F}^h = \nabla\delta\boldsymbol{\varphi}^{\mathrm{h}} &= \sum_{a=1}^{n_{\mathrm{en}}} \delta\boldsymbol{\varphi}^a \otimes \nabla N^a\,, \quad \nabla\delta p^h = \sum_{a=1}^{n_{\mathrm{en}}} \delta p^a\, \nabla N^a. \end{aligned} \tag{5.91}$$

Based on the previous interpolations, the variational derivatives $(5.84)_1$ (linear momentum) and $(5.84)_2$ (integrated evolution equation of the phase field) are computed. Focussing on one finite element, such variational derivatives yield

$$\begin{aligned} \delta_{\boldsymbol{\varphi}}\Delta\tilde{\mathcal{I}}^{\mathrm{red}}|_{\mathcal{B}_0^e} &= \sum_{a=1}^{n_{\mathrm{en}}} \delta\boldsymbol{\varphi}^a \cdot \left[\mathbf{f}^a_{\boldsymbol{\varphi},\mathrm{int}} - \mathbf{f}^a_{\boldsymbol{\varphi},\mathrm{vol}} - \mathbf{f}^a_{\boldsymbol{\varphi},\mathrm{sur}}\right]\,, \\ \delta_p\Delta\tilde{\mathcal{I}}^{\mathrm{red}}|_{\mathcal{B}_0^e} &= \sum_{a=1}^{n_{\mathrm{en}}} \delta p^a\,\left[f^a_{p,\mathrm{int}} + \lambda_1^a - \lambda_2^a\right]\,. \end{aligned} \tag{5.92}$$

Here, $\delta\boldsymbol{\varphi}^a$ and δp^a denote the virtual placement and the virtual phase field parameter at node a. The nodal element forces entering Eq. (5.92) are

$$\begin{aligned} \mathbf{f}^a_{\boldsymbol{\varphi},\mathrm{int}} &= \int_{\mathcal{B}_0^e} \mathbf{P}\cdot\nabla N^a\,\mathrm{d}V\,, \quad \mathbf{f}^a_{\boldsymbol{\varphi},\mathrm{vol}} = \int_{\mathcal{B}_0^e} N^a\,\rho_0\,\mathbf{B}\,\mathrm{d}V\,, \quad \mathbf{f}^a_{\boldsymbol{\varphi},\mathrm{sur}} = \int_{\partial\mathcal{B}_0^e} N^a\,\bar{\mathbf{T}}\,\mathrm{d}A\,, \\ f^a_{p,\mathrm{int}} &= \int_{\mathcal{B}_0^e} \left\{N^a\,\partial_p\,\Delta\mathcal{E}^{\mathrm{red}} + \nabla N^a\cdot\boldsymbol{\xi}\right\}\,\mathrm{d}V\,. \end{aligned} \tag{5.93}$$

In Eq. (5.93), $\mathbf{f}^a_{\boldsymbol{\varphi},\mathrm{vol}}$ and $\mathbf{f}^a_{\boldsymbol{\varphi},\mathrm{sur}}$ are the external volume and the external surface force vectors of the mechanical problem. Finally, by assembling the nodal contributions of all finite elements and considering that the weak forms have to be fulfilled for any admissible test function, the global residuum at node point A associated with the underlying boundary value problem can be written in the form

$$\mathbf{r}^A = \mathop{\mathsf{A}}_{e=1}^{n_\text{el}} \begin{bmatrix} \mathbf{r}^a_{\boldsymbol{\varphi}} \\ r^a_p \\ r^a_{\lambda_1} \\ r^a_{\lambda_2} \end{bmatrix} = \mathbf{0} \quad \text{with} \quad \begin{bmatrix} \mathbf{r}^a_{\boldsymbol{\varphi}} \\ r^a_p \\ r^a_{\lambda_1} \\ r^a_{\lambda_2} \end{bmatrix} = \begin{bmatrix} \mathbf{f}^a_{\boldsymbol{\varphi},\text{int}} - \mathbf{f}^a_{\boldsymbol{\varphi},\text{vol}} - \mathbf{f}^a_{\boldsymbol{\varphi},\text{sur}} \\ f^a_{p,\text{int}} + \lambda^a_1 - \lambda^a_2 \\ g_1(p^a, \lambda^a_1) \\ g_2(p^a, \lambda^a_2) \end{bmatrix} . \tag{5.94}$$

Here, A represents the assembly over all elements $e = 1, \ldots, n_\text{el}$.

Remark 5.4.6: *Within the numerical implementation, bi-linear and tri-linear shape functions are used for the 2D and 3D simulations. By using linear shape functions, the extrema of* p *are always at the nodes and thus, enforcing* $p \in [0, 1]$ *at such nodes implies that* $p \in [0, 1]$ *everywhere.*

5.4.3.2 Linearisation of the discretised weak form

The non-linear algebraic system of equations (5.94) is solved by means of a Newton-type iteration. For that purpose, the linearisation of the global residuum (5.94) is required. In line with the computation of the residuum, this linearisation is computed by assembling the element contributions. Considering discretisations $(5.89)_2$ and $(5.89)_3$ the generic format of such linearisations with respect to the variables at node b is given by

$$\begin{aligned} \Delta\mathbf{r}^a_{\boldsymbol{\varphi}} &= \sum_{b=1}^{n_\text{en}} \left[\frac{\mathrm{d}\mathbf{r}^a_{\boldsymbol{\varphi}}}{\mathrm{d}\boldsymbol{\varphi}^b} \cdot \Delta\boldsymbol{\varphi}^b + \frac{\mathrm{d}\mathbf{r}^a_{\boldsymbol{\varphi}}}{\mathrm{d}p^b} \Delta p^b \right] , \\ \Delta r^a_p &= \sum_{b=1}^{n_\text{en}} \left[\frac{\mathrm{d}r^a_p}{\mathrm{d}\boldsymbol{\varphi}^b} \cdot \Delta\boldsymbol{\varphi}^b + \frac{\mathrm{d}r^a_p}{\mathrm{d}p^b} \Delta p^b + \frac{\mathrm{d}r^a_p}{\mathrm{d}\lambda^b_1} \Delta\lambda^b_1 + \frac{\mathrm{d}r^a_p}{\mathrm{d}\lambda^b_2} \Delta\lambda^b_2 \right] , \\ \Delta r^a_{\lambda_1} &= \frac{\mathrm{d}r^a_{\lambda_1}}{\mathrm{d}p^b} \Delta p^b + \frac{\mathrm{d}r^a_{\lambda_1}}{\mathrm{d}\lambda^b_1} \Delta\lambda^b_1 , \\ \Delta r^a_{\lambda_2} &= \frac{\mathrm{d}r^a_{\lambda_2}}{\mathrm{d}p^b} \Delta p^b + \frac{\mathrm{d}r^a_{\lambda_2}}{\mathrm{d}\lambda^b_2} \Delta\lambda^b_2 . \end{aligned} \tag{5.95}$$

Here, $\Delta(x)$ denotes the linearisation of the variable (x) – or in a numerical setting, the increments of the variable (x). These increments are collected in the vector $\Delta\mathbf{d}^b = [\Delta\boldsymbol{\varphi}^b, \Delta p^b, \Delta\lambda^b_1, \Delta\lambda^b_2]^\text{T}$ corresponding to node b of the respective finite element. Since the residuals $r^a_{\lambda_1}$ and $r^a_{\lambda_2}$ depend only on the nodal values of the same node, their linearisation yields a diagonal matrix. For this reason, it is convenient to decompose the linearisation into two parts. While the first part is related to the incremental potential (5.80), the second part precisely corresponds to the constraints enforced by $r^a_{\lambda_1}$ and $r^a_{\lambda_2}$. Concerning the incremental potential (5.80) reflected in the residuals $\mathbf{r}^a_{\boldsymbol{\varphi}}$ and $\mathbf{r}^a_{\boldsymbol{\varphi}}$ the stiffness matrices are computed as

$$
\begin{aligned}
\mathbf{K}^{ab}_{\boldsymbol{\varphi}\boldsymbol{\varphi}} &= \frac{\mathrm{d}\mathbf{r}^a_{\boldsymbol{\varphi}}}{\mathrm{d}\boldsymbol{\varphi}^b} = \int\limits_{\mathcal{B}^e_0} \nabla N^a \bullet \frac{\mathrm{d}\mathbf{P}}{\mathrm{d}\mathbf{F}} \cdot \nabla N^b \,\mathrm{d}V\,,\\
\mathbf{K}^{ab}_{\boldsymbol{\varphi}p} &= \frac{\mathrm{d}\mathbf{r}^a_{\boldsymbol{\varphi}}}{\mathrm{d}p^b} = \int\limits_{\mathcal{B}^e_0} \left\{ N^b \,\frac{\mathrm{d}\mathbf{P}}{\mathrm{d}p} \cdot \nabla N^a + \left[\frac{\mathrm{d}\mathbf{P}}{\mathrm{d}\nabla p} \cdot \nabla N^b\right] \cdot \nabla N^a \right\} \mathrm{d}V\,,\\
\mathbf{K}^{ab}_{p\boldsymbol{\varphi}} &= \frac{\mathrm{d}r^a_p}{\mathrm{d}\boldsymbol{\varphi}^b} = \mathbf{K}^{ab\;\mathrm{T}}_{\boldsymbol{\varphi}p}\,,\\
K^{ab}_{pp} &= \frac{\mathrm{d}r^a_p}{\mathrm{d}p^b} = \int\limits_{\mathcal{B}^e_0} \left\{ N^a \,\frac{\mathrm{d}\left[\partial_p\, \Delta\mathcal{E}^{\mathrm{red}}\right]}{\mathrm{d}p}\, N^b + 2\,\nabla N^a \cdot \frac{\mathrm{d}\boldsymbol{\xi}}{\mathrm{d}p}\, N^b + \nabla N^a \cdot \frac{\mathrm{d}\boldsymbol{\xi}}{\mathrm{d}\nabla p} \cdot \nabla N^b \right\} \mathrm{d}V\,,
\end{aligned}
\tag{5.96}
$$

where dead-loads have been assumed for the sake of simplicity. The tangents $\mathrm{d}\mathbf{P}/\mathrm{d}\mathbf{F}$, $\mathrm{d}\mathbf{P}/\mathrm{d}p$, $\mathrm{d}\mathbf{P}/\mathrm{d}\nabla p$, $\mathrm{d}\left[\partial_p\, \Delta\mathcal{E}^{\mathrm{red}}\right]/\mathrm{d}p$, $\mathrm{d}\boldsymbol{\xi}/\mathrm{d}p$ and $\mathrm{d}\boldsymbol{\xi}/\mathrm{d}\nabla p$ entering the stiffness matrix are derived in Appendix C.2. It bears emphasis that such tangents depend on the reduced potential (5.73), which in turn depends on the vector $\boldsymbol{\beta}$. For this reason – and in line with the sensitivities in plasticity theory – the tangents require the linearisation of the local minimisation problem (5.73) as well. For instance,

$$
\mathrm{d}\mathbf{P} = \mathrm{d}\left[\frac{\partial\Delta\mathcal{E}^{\mathrm{red}}}{\partial\mathbf{F}}\right] = \frac{\partial^2\Delta\mathcal{E}^{\mathrm{red}}}{\partial\mathbf{F}^2} : \mathrm{d}\mathbf{F} + \frac{\partial^2\Delta\mathcal{E}^{\mathrm{red}}}{\partial\mathbf{F}\partial p}\,\mathrm{d}p + \frac{\partial^2\Delta\mathcal{E}^{\mathrm{red}}}{\partial\mathbf{F}\partial\boldsymbol{\beta}} \circ \mathrm{d}\boldsymbol{\beta}\,. \tag{5.97}
$$

The mixed derivative $\partial^2\Delta\mathcal{E}^{\mathrm{red}}/\partial\mathbf{F}\partial\lambda_i$ vanishes to zero. Most terms in Eq. (5.97) are standard – except for the last one. Since $\boldsymbol{\beta}$ does not enter the global problem explicitly, its sensitivities with respect to the primary variables have to be considered, i.e.,

$$
\mathrm{d}\boldsymbol{\beta} = \frac{\partial\boldsymbol{\beta}}{\partial\mathbf{F}} : \mathrm{d}\mathbf{F} + \frac{\partial\boldsymbol{\beta}}{\partial p}\,\mathrm{d}p\,, \tag{5.98}
$$

in which the derivative with respect to the Lagrangian parameter $\partial\boldsymbol{\beta}/\partial\lambda_i$ vanishes to zero. They follow from the linearisation of the local minimisation problem (5.73). Further details are omitted here, but are given in Appendix C.2.

Finally, by taking the Fischer-Burmeister restrictions into account, the additional contributions to the tangent matrices are given by

$$
\begin{aligned}
K^{ab}_{p\lambda_1} &= \frac{\mathrm{d}r^a_p}{\mathrm{d}\lambda^b_1} = 1, & K^{ab}_{p\lambda_2} &= \frac{\mathrm{d}r^a_p}{\mathrm{d}\lambda^b_2} = -1, \\
K^{ab}_{\lambda_1 p} &= \frac{\mathrm{d}r^a_{\lambda_1}}{\mathrm{d}p^b} = \frac{\partial g^a_1}{\partial p^b}, & K^{ab}_{\lambda_1\lambda_1} &= \frac{\mathrm{d}r^a_{\lambda_1}}{\mathrm{d}\lambda^b_1} = \frac{\partial g^a_1}{\partial \lambda^b_1}, \\
K^{ab}_{\lambda_2 p} &= \frac{\mathrm{d}r^a_{\lambda_2}}{\mathrm{d}p^b} = \frac{\partial g^a_2}{\partial p^b}, & K^{ab}_{\lambda_2\lambda_2} &= \frac{\mathrm{d}r^a_{\lambda_1}}{\mathrm{d}\lambda^b_2} = \frac{\partial g^a_2}{\partial \lambda^b_2}.
\end{aligned}
\tag{5.99}
$$

As mentioned before, they show a diagonal structure. A more detailed and explicit derivation of these additional stiffness matrices is summarised in Appendix C.3.

5.5 Numerical examples

In this section, several numerical examples are presented. In order to allow for a good analysis and interpretation of the results, relatively simple, but nevertheless meaningful benchmarks have been chosen. They are academic in nature and were not supposed to represent a certain material in a realistic manner. The specific constitutive assumptions and the numerical setup are described in Subsection 5.5.1. The 2D and 3D computations are investigated in Subsections 5.5.2 and 5.5.3.

5.5.1 Prototype phase field model

The numerical examples presented in the following subsections are based on the bulk energies

$$
\begin{aligned}
\Psi_{\mathrm{B}_1}(\mathbf{F}^{\mathrm{e}}_1) &= \frac{\mu_1}{2}\left[J_1^{\mathrm{e}-2/3}\,\mathbf{F}^{\mathrm{e}}_1 : \mathbf{F}^{\mathrm{e}}_1 - 3\right] + \frac{\kappa_1}{2}\left[\frac{J_1^{\mathrm{e}2}}{2} - \frac{1}{2} - \log J^{\mathrm{e}}_1\right] + \Psi^0_{\mathrm{B}_1}\,, \\
\Psi_{\mathrm{B}_2}(\mathbf{F}^{\mathrm{e}}_2) &= \frac{\mu_2}{2}\left[J_2^{\mathrm{e}-2/3}\,\mathbf{F}^{\mathrm{e}}_2 : \mathbf{F}^{\mathrm{e}}_2 - 3\right] + \frac{\kappa_2}{2}\left[\frac{J_2^{\mathrm{e}2}}{2} - \frac{1}{2} - \log J^{\mathrm{e}}_2\right] + \Psi^0_{\mathrm{B}_2}\,,
\end{aligned}
\tag{5.100}
$$

for the two phases. The model parameters of these isotropic neo-Hooke energies are the shear modulus $\mu_i = 1/2\,\mathrm{E}_i/[1+\nu_i]$ and the bulk modulus $\kappa_i = 1/3\,\mathrm{E}_i/[1-2\,\nu_i]$, where E_i and ν_i are the Young's modulus and the Poisson's ratio, and where $\Psi^0_{\mathrm{B}_i}$ are chemical energies being independent of the deformation.

The effective elastic deformation gradients $\mathbf{F}^{\mathrm{e}}_i$ in Eq. (5.100) associated with the two phases follow from the multiplicative decomposition of total deformations gradients $\mathbf{F}_i$ into elastic and Bain-strain related parts $\mathbf{F}^{\mathrm{B}}_i$, i.e.,

$$
\mathbf{F}^{\mathrm{e}}_1 = \mathbf{F}_1 \cdot \mathbf{F}^{\mathrm{B}^{-1}}_1\,, \qquad \mathbf{F}^{\mathrm{e}}_2 = \mathbf{F}_2 \cdot \mathbf{F}^{\mathrm{B}^{-1}}_2\,,
\tag{5.101}
$$

cf. Eq. (5.24). Based on such deformation gradients, their Jacobians are defined as $J_i^{\mathrm{e}} = \det \mathbf{F}_i^{\mathrm{e}}$.

With regard to the Bain strains $\mathbf{F}_i^{\mathrm{B}}$, the polar decompositions

$$\mathbf{F}_1^{\mathrm{B}} = \mathbf{Q} \cdot \mathbf{U}_1^{\mathrm{B}}\,, \qquad \mathbf{F}_2^{\mathrm{B}} = \mathbf{U}_2^{\mathrm{B}}\,, \tag{5.102}$$

are considered and the right stretch tensors are chosen to be

$$\mathbf{U}_1^{\mathrm{B}} = \begin{bmatrix} \dfrac{\alpha+\gamma}{2} & \dfrac{\alpha-\gamma}{2} & 0 \\ \dfrac{\alpha-\gamma}{2} & \dfrac{\alpha+\gamma}{2} & 0 \\ 0 & 0 & \beta \end{bmatrix}, \qquad \mathbf{U}_2^{\mathrm{B}} = \begin{bmatrix} \dfrac{\alpha+\gamma}{2} & -\dfrac{\alpha-\gamma}{2} & 0 \\ -\dfrac{\alpha-\gamma}{2} & \dfrac{\alpha+\gamma}{2} & 0 \\ 0 & 0 & \beta \end{bmatrix}. \tag{5.103}$$

Furthermore, the rotation tensor $\mathbf{Q}$ is defined by

$$\mathbf{Q} = \begin{bmatrix} \dfrac{2\alpha\gamma}{\alpha^2+\gamma^2} & -\dfrac{\alpha^2-\gamma^2}{\alpha^2+\gamma^2} & 0 \\ \dfrac{\alpha^2-\gamma^2}{\alpha^2+\gamma^2} & \dfrac{2\alpha\gamma}{\alpha^2+\gamma^2} & 0 \\ 0 & 0 & 1 \end{bmatrix}. \tag{5.104}$$

The resulting Bain strains (deformation gradients) fulfil the twinning equation $\mathbf{F}_1^{\mathrm{B}} - \mathbf{F}_2^{\mathrm{B}} = [\![\mathbf{F}^{\mathrm{B}}]\!] = \mathbf{a} \otimes \tilde{\mathbf{N}}$ for the two normal vectors $\tilde{\mathbf{N}} = \pm \mathbf{e}_1$ and $\tilde{\mathbf{N}} = \pm \mathbf{e}_2$, where $\mathbf{e}_i$ are the cartesian basis vectors. Hence, $\mathbf{F}_1^{\mathrm{B}}$ and $\mathbf{F}_2^{\mathrm{B}}$ are rank-1 connected and the corresponding interface is referred to as coherent interface. The parameters α, β, γ can be interpreted as edge lengths of the underlying unit cells (see also Hildebrand and Miehe [53] and references cited therein). They are chosen as $\alpha = 1.0619$, $\beta = 0.9178$ and $\gamma = 1.0231$, cf. Hildebrand and Miehe [53].

The constitutive model is completed by means of an interface energy and a dissipation functional related to the propagation of such interfaces. In line with Eq. (5.6), a constant interface energy is adopted and the dissipation is described by the *Ginzburg-Landau* dissipation functional (5.29), in which the phase mobility is denoted as η.

With regard to the numerical implementation, each node of the finite element discretisation shows six degrees of freedom in the three dimensional case (see Section 5.4.2) – three coordinates associated with the deformation mapping, the order parameter p as well as two Lagrange multipliers necessary in order to enforce the constraint $p \in [0, 1]$. Certainly, both Lagrange multipliers cannot be simultaneously active reducing the number of degrees of freedom per node to five. Following the same line of thought, each node shows 5, respectively 4, degrees of freedom in 2D. Furthermore, the 3D constitutive model is also considered in the 2D case supplemented by plane strain conditions. The resulting finite element formulation is implemented into the parallel version of FEAP, see Taylor [131]. The global system of equations is solved in a monolithic manner. To this end, the

Newton updates are computed iteratively with a Jacobian-type preconditioner and the Krylov-subspace biconjugate gradient stabilised method (BCGS).

5.5.1.1 Setup for numerical tests

All numerical analyses presented in this section are related to relaxation tests. The considered body $\mathcal{B}_0$ is initialised by a random phase distribution $p_0(\mathbf{X}) \in [0,1] \;\; \forall\, \mathbf{X} \in \mathcal{B}_0$ with an initial volume ratio of $\bar{p}_0 = 0.5$, i.e., 50% of phase 1 and 50% of phase 2 (in terms of volume). In the notation $\bar{p}_0$, subscript 0 denotes the time and the superposed bar denotes averaged or homogenised variables (in line with homogenisation theory). Accordingly,

$$\bar{p}_0 = \frac{1}{V(\mathcal{B}_0)} \int\limits_{\mathcal{B}_0} p^h_{\mathcal{B}_0}(t=0)\,\mathrm{d}V\,. \tag{5.105}$$

In order to trigger the formation of a certain microstructure, the deformation at the boundary $\partial\mathcal{B}_0$ of the body $\mathcal{B}_0$ is prescribed by

$$\hat{\boldsymbol{\varphi}} = \bar{\mathbf{F}} \cdot \mathbf{X} \quad \forall \mathbf{X} \in \partial\mathcal{B}_0\,. \tag{5.106}$$

Here, $\bar{\mathbf{F}}$ can be interpreted as the macroscopic deformation gradient. It is a linear combination of the Bain strains $\mathbf{F}^{\mathrm{B}}_1$ and $\mathbf{F}^{\mathrm{B}}_2$ such that the relaxed microstructure will also show both phases. In order to interpret the numerical results more easily, the same material parameters are chosen for both phases (Young's moduli, Poisson's ratios and the chemical energies). It bears emphasis that even in this case the different homogenisation assumptions indeed lead to different results, since the Bain strains are different.

5.5.2 Comparison of the homogenisation assumptions – 3D computations

The four proposed homogenisation assumptions presented in Section 5.3 are analysed here by means of fully 3D finite element simulations. For that purpose, the body $\mathcal{B}_0$ is defined by a cube with the dimensions $1 \times 1 \times 1$ [mm^3]. It is discretised by 64^3 finite elements. An equidistant grid with a constant element length $h = 1/64$ [mm] is chosen. The macroscopic deformation gradient $\bar{\mathbf{F}}$ prescribing the motion at the boundary is $\hat{\mathbf{F}} = 2\,\left[[1-\bar{p}_0]\,\mathbf{F}^{\mathrm{B}}_1 + \bar{p}_0\,\mathbf{F}^{\mathrm{B}}_2\right]$ with $\bar{p}_0 = 0.5$ (initial volume ratio of the two different phases). The respective macroscopic deformation gradient has been chosen in order to activate and to check the geometrically exact description (finite deformations). Thus, the analysed 2D and 3D examples are academic in nature and were not supposed to represent a certain material in a realistic manner. The material constants are summarised in Tab. 5.2. For all simulations, constant time steps with $\Delta t = 0.00005$ s are used and the total number of time steps is 2000. This number was chosen such that a steady state was observed for all computations within the final time step.

Phase	Name	Symbol	Value	Unit
Phase 1	Youngs modulus	E_1	40	[GPa]
	Poisson ratio	ν_1	0.3	[-]
	Chemical energy	$\Psi^0_{\mathrm{B}_1}$	0	[MPa]
Phase 2	Youngs modulus	E_2	40	[GPa]
	Poisson ratio	ν_2	0.3	[-]
	Chemical energy	$\Psi^0_{\mathrm{B}_2}$	0	[MPa]
Interface	Area specific surface energy	ψ^Γ_0	0.5	[N/mm]
	Interface thickness	ε	$1/[8\,\pi]$	[mm]
	Mobility	η	0.1	[N s/mm^2]

Table 5.2: Material parameters for 3D finite element computations of a cube; Material parameters of the bulk energy (see Eq. (5.100)), material parameters of the surface energy (see Eq. (5.6)) and material parameters of the dissipation functional (see Eq. (5.29))

During the first time steps, the stored energy significantly reduces in all computations. This is due to the fact that the highly heterogeneous initial random phase distribution is not energetically favourable for the applied loading conditions. Accordingly, a re-ordering towards domains with the same phases can be seen. The averaged stored energies corresponding to the steady state ($t = 0.1$ s), together with the converged volume ratios between the two phases are given in Tab. 5.3. It bears emphasis that the dissipation is zero for the steady state (no further propagation of interfaces) and thus, the total stored energy is identical to the functional (5.68) defining the initial boundary value problem. To be more precise, in the steady state case (cf. Eq. (5.68) and (5.69); no external forces) this functional reads

Homogenisation	a) Reuss/Sachs	b) full rank-1	c) partial rank-1	d) Taylor/Voigt
$\bar{\Psi}$ [MPa]	184.569	184.742	185.952	188.528
$\bar{p}$ [–]	0.503322	0.503455	0.483585	0.484384

Table 5.3: Averaged stored energy and averaged phase distribution after 2000 time steps for the 3D computations

$$\Delta\mathcal{I} = \int_{\mathcal{B}_0} \left\{ [\Psi_{\mathrm{B}}(t_{n+1}) + \Psi_\Gamma(t_{n+1})] - [\Psi_{\mathrm{B}}(t_n) + \Psi_\Gamma(t_n)] \right\} \,\mathrm{d}V. \tag{5.107}$$

Since the terms depending on the previous time step t_n are constant and just shift the minimum of the functional, they are not relevant for the variational problem. For this reason, functional (5.107) can indeed be replaced by the stored energy of the body

$$\bar{\Psi} = \int\limits_{\mathcal{B}_0} \left[\Psi_{\mathrm{B}}(t_{n+1}) + \Psi_{\Gamma}(t_{n+1})\right]\ \mathrm{d}V. \tag{5.108}$$

Since the bulk energies corresponding to the different homogenisation assumptions fulfil the inequalities (5.65) and since the stored energy (5.108) defining the functional to be minimised precisely depends on the bulk energies, the stored energy associated with the steady state solution seems to inherit the ordering (5.65), see Tab. 5.3. Thus, the Reuss/Sachs homogenisation assumption leads to the lowest energy, while the Taylor/Voigt assumption defines the upper bound. However, it bears emphasis that strictly mathematically speaking, the aforementioned inheritance is not clear, since the final energies depend also on the path.

From analysing the converged volume fraction as shown in Tab. 5.3 one can see that the initial condition $\bar{p}_0 = 0.5$ is not exactly preserved – in line with the underlying Allen-Cahn framework, cf. Chapter 6. However, due to the considered boundary conditions, the converged volume ratios $\bar{p}$ are still close to $\bar{p}_0 = 0.5$. Furthermore, the deviations between the different homogenisation assumptions are relatively small.

Although the averaged volume ratio is almost identical for each of the different homogenisation assumptions, the spatial distributions of the phases do differ. This is illustrated in Fig. 5.3 for the steady states ($t = 0.1$ s). While the Reuss/Sachs homogenisation assumption and the full rank-1 homogenisation lead to an almost identical two-column-like microstructure, partial rank-1 homogenisation and the Taylor/Voigt homogenisation assumption predict an almost identical matrix-inclusion-like microstructure. Furthermore, a very sharp interphase is captured by the Taylor/Voigt assumption. By way of contrast, the Reuss/Sachs assumption yields a more diffuse interface representation. The degree of diffusion increases in the order Taylor/Voigt, partial rank-1 homogenisation, full rank-1 homogenisation and Reuss/Sachs – in line with the ordering of the stored energy, cf. Tab. 5.3.

At a first glance, the sharpness of the interface predicted by the Taylor/Voigt assumption seems to be in good agreement with the underlying sharp interface problem. However, it is well known that the Taylor/Voigt assumption generally predicts too sharp phase transitions. For instance, if the mixture of two convex energies (phases) is to be computed, the Taylor assumption will either lead to the energy of phase one or to that of phase 2. It will not predict a mixing of energies. However, this is neither realistic from a physics nor from a mathematical point of view (non-convexity). The sharpness of the diffuse interface is mostly related to the energy barrier separating the individual phases. If the length scale of the diffuse interface is chosen to be smaller, this energy barrier increases and thus, the separation of different phases is more pronounced. This leads to sharper approximation of the interfaces. In the limiting case – the length parameter converges to zero – all homogenisation assumptions predict the same results.

As shown before, the underlying homogenisation assumption clearly influences the numerical predictions in general. However, it also influences the numerical performance. The presented results are based on the parallel version of FEAP, see Taylor [131]. The numerical analyses were run on 12 cores (partition into 12 sub-domains). The fastest computation took roughly 50 CPU hours and corresponds to the Reuss/Sachs homogenisation, while the Taylor/Voigt model took roughly 125 CPU hours. This ordering is proportional to the activation of the NCP functions: They are not activated in Reuss/Sachs model, while they are indeed strongly active for the Taylor/Voigt model. The models based on rank-1 homogenisation are in between.

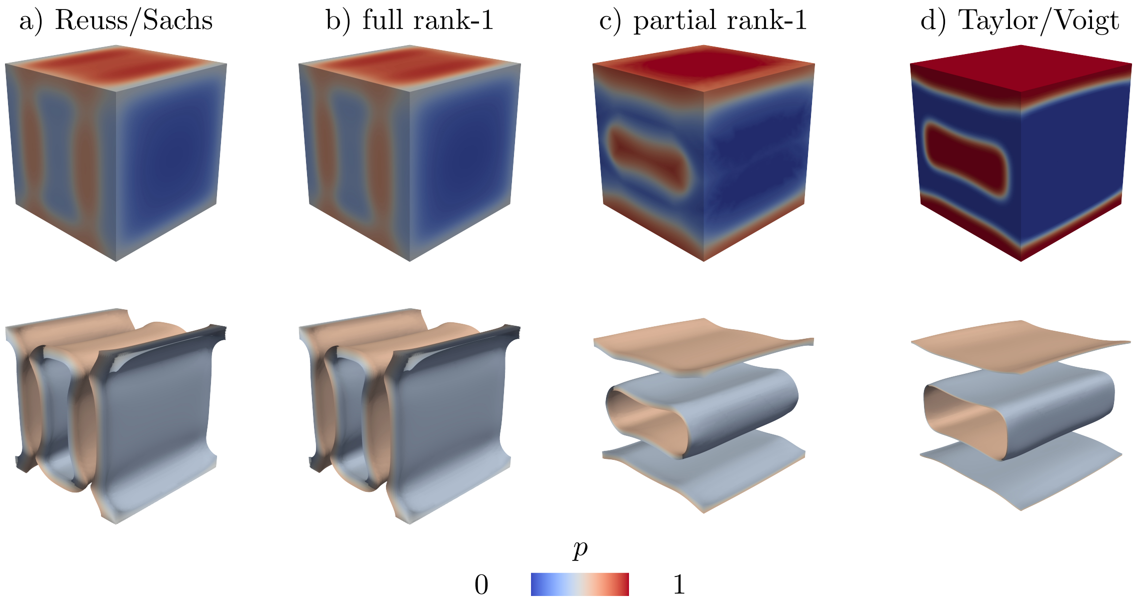

Figure 5.3: Microstructural evolution of phase parameter p for different homogenisation assumptions at $t = 0.1$ s; (top row) 3D plot of phase distribution p; (bottom row) 3D interface contour plot $p \in (0.4, 0.6)$ of the top row; a) Reuss/Sachs model; b) full rank-1 homogenisation; c) partial rank-1 homogenisation; d) Taylor/Voigt model

5.5.3 Further numerical analyses in 2D

While the influence of the homogenisation assumption on the numerically predicted response was analysed in the previous subsection, further numerical aspects are investigated here. To be more precise, two points are discussed separately. While Subsection 5.5.3.1 is associated with the effect of the proposed Lagrange multipliers, in combination with the NCP functions by Fischer-Burmeister, the convergence behaviour of the different phase field models methods for a vanishing interface thickness is dealt with in Subsection 5.5.3.2.

All tests are again related to the numerical setup illustrated in Subsection 5.5.1.1 – however, now in 2D. The dimensions of the square are $\mathcal{B}_0 = 50 \times 50$ [mm^2]. It is discretised by an equidistant finite element grid with an element length h. Again, an initial volume ratio of $\bar{p}_0 = 0.5$ of the two phases is assumed and the boundary $\partial\mathcal{B}_0$ is deformed by the macroscopic deformation gradient $\hat{\mathbf{F}}$. However, the slightly changed macroscopic deformation gradient $\hat{\mathbf{F}} = \left[[1 - 0.4]\,\mathbf{F}_1^{\mathrm{B}} + 0.4\,\mathbf{F}_2^{\mathrm{B}}\right]$ is now considered. The material parameters are selected according to Tab. 5.4. For all simulations, a time step of $\Delta t = 0.0001$ s was chosen and the simulations were stopped at $t = 3$ s.

Phase	Name	Symbol	Value	Unit
Phase 1	Youngs modulus	E_1	25000	[MPa]
	Poisson ratio	ν_1	0.3	[-]
	Chemical energy	$\Psi^0_{\mathrm{B}_1}$	0	[MPa]
Phase 2	Youngs modulus	E_2	25000	[MPa]
	Poisson ratio	ν_2	0.3	[-]
	Chemical energy	$\Psi^0_{\mathrm{B}_2}$	0	[MPa]
Interface	Mobility	η	1.0	[N s/mm^2]
	Area specific surf. energy	ψ^Γ_0	21.0	[N/mm]
	Interface thickness	ε	1.25 (Sec. 5.5.3.1) 2.5/1.25/0.625 (Sec. 5.5.3.2)	[mm]

Table 5.4: Material parameters for 2D finite element computations of a square; Material parameters of the bulk energy (see Eq. (5.100)), material parameters of the surface energy (see Eq. (5.6)) and material parameters of the dissipation functional (see Eq. (5.29))

5.5.3.1 Effect of constraint optimisation based on Lagrange multipliers in combination with the NCP functions by Fischer-Burmeister

The effect of the Lagrange multipliers necessary in order to enforce $p \in [0, 1]$ is analysed based on 2D computations. Since the 2D computations are numerically less extensive, a finer grid with 100×100 can be chosen.

Similar to the 3D computations, a re-ordering of the phases can be observed during the first stage of the relaxation process. This leads to clusters of phase 1 ($p = 0$) and clusters of phase 2 ($p = 1$). However, due to the mechanical driving force, some of the material points belonging to such clusters tend towards states which are not admissible ($p \notin [0, 1]$). In this case, the driving forces associated with the Lagrange multipliers λ_1 and λ_2 become active and prevent such inadmissible states. The spatial distributions of the plastic multipliers for the time $t = 0.255$ s are shown in Fig. 5.4. According to Fig. 5.4 – and in line with the results discussed in the previous subsection – the spatial distribution of the two different phases does indeed depend on the underlying homogenisation assumption. The same also holds for the activity of the aforementioned Lagrange multipliers. It can be seen that the most frequently applied assumption, the

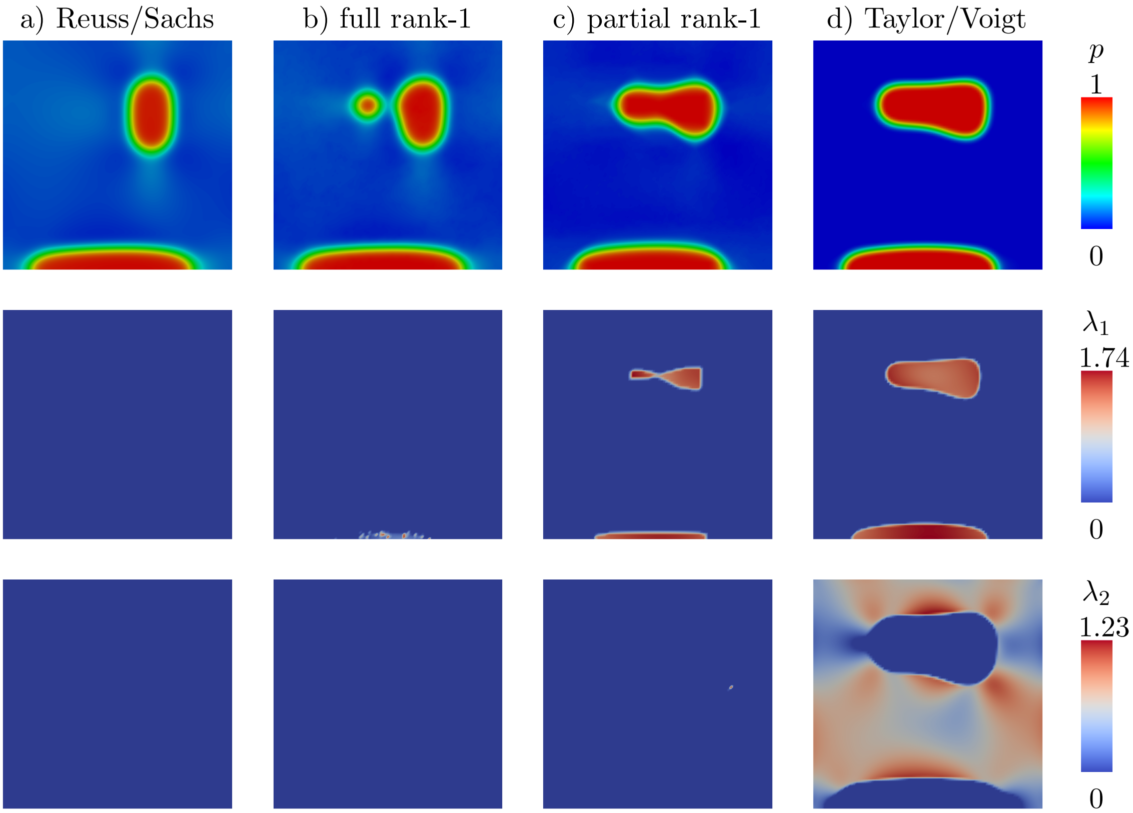

Figure 5.4: 2D numerical analyses showing the influence of the Lagrange multipliers λ_1 and λ_2 for the different homogenisation assumption (at time $t = 0.255$ s): (top row) distribution of the phases, (middle row) distribution of Lagrangian multiplier λ_1, (bottom row) distribution of Lagrangian multiplier λ_2

Taylor/Voigt assumption, leads to the strongest activity, while the Reuss/Sachs-type homogenisation approach seems to naturally enforce the constraint $p \in [0, 1]$. In summary, the degree of activity (Reuss/Sachs → Taylor/Voigt) is inversely proportional to the degree of relaxation (Taylor/Voigt → Reuss/Sachs) for the analysed example.

Since a monolithic Newton-type algorithm is employed to solve the set of nonlinear equations resulting from a temporal and spatial discretisation, the activity of the Lagrange multipliers also has an effect on the Newton iteration. To be more explicit, while only three global iterations are required, if λ_1 and λ_2 are not active, $4 - 8$ iterations are required, if λ_1 or λ_2 are active (for the relative convergence criteria $|\Delta\mathbf{d}^{\mathrm{T}} \cdot \mathbf{r}| \leq 10^{-22}\, |\Delta\mathbf{d}^{\mathrm{T}} \cdot \mathbf{r}|_{\mathrm{initial}}$ and $\|\mathbf{r}\| \leq 10^{-9}\, \|\mathbf{r}\|_{\mathrm{initial}}$ depending on the nodal residuum $\mathbf{r}$ according to Eq. (5.94) and the increment of the nodal unknowns $\Delta\mathbf{d}$; the subscript $(\bullet)_{\mathrm{initial}}$ signals the initial values, i.e., at iteration number zero).

The number of Newton iterations certainly also depends on the choice of the initial values. Whereas, for the displacement field and the order parameter p the choice is obvious (last converged step), two different strategies are investigated for the Lagrange multipliers. In the first implementation strategy, both multipliers are set to zero (as initial value). By way of contrast and following the assumptions for the displacement field and the order parameter p, λ_1 and λ_2 are initialised according to their converged counterparts of the previous loading step within the second implementation. The results of this investigation are summarised in Tab. 5.5. According to Tab. 5.5, the second method is significantly more efficient.

Lagrangian	updated $(\lambda_1;\lambda_2)\big\vert_{t_{n+1}}^{k=0} = (\lambda_1;\lambda_2)\big\vert_{t_n}$	re-initialised $(\lambda_1;\lambda_2)\big\vert_{t_{n+1}}^{k=0} = (0;0)$
$\sum$ Iterations till $t = 0.255$ s	12928	24967

Table 5.5: Results of 2D numerical analyses showing the influence of the chosen initial values of the Lagrange parameters on the total number of Newton iterations for the Taylor/Voigt homogenisation. $(\lambda_1;\lambda_2)\big\vert_{t_{n+1}}^{k=0} = (\lambda_1;\lambda_2)\big\vert_{t_n}$ corresponds to an initialisation according to the converged previous loading step.

5.5.3.2 Convergence behaviour of the different homogenisation assumptions

The influence of the homogenisation assumption on the numerically predicted response has already been analysed in the previous sections: In general, the homogenisation assumption indeed affects the results. However, all phase field models were derived by means of an underlying sharp interface model. For this reason, all models should converge to this underlying sharp interface model, if the diffuse interface thickness converges to zero. The numerical analyses presented in this subsection follow this line of thought, i.e, the influence of the parameter ε defining the thickness of the diffuse interface is investigated. To be more precise, the three different length scales $\varepsilon = 2.5$ mm (50 × 50 discretisation), $\varepsilon = 1.25$ mm (100 × 100 discretisation) and $\varepsilon = 0.625$ mm (200 × 200 discretisation) are considered in the following. In order to guarantee a minimum resolution of the interface topology, the diffuse interface is discretised by means of 2.5 finite elements ($\varepsilon = 2.5\,h$, cf. Hildebrand and Miehe [53]). The numerical convergence tests are evaluated by means of three different criteria: (1) spatial distribution of the phase field parameter, (2) evolution of the stored energy (motivated by the steady state; see also previous subsection) and (3) volume ratio between the two phases.

The spatial distributions of the phase field parameter corresponding to the steady state solution are summarised in Fig. 5.5. While the finer discretisations with the smaller diffuse interface thickness ($\varepsilon = 1.25$ mm and $\varepsilon = 0.625$ mm) do show a non-trivial microstructure, this is not the case for the thicker diffuse interface ($\varepsilon = 2.5$ mm). The discretisations with $\varepsilon = 2.5$ mm are too coarse in order to capture the considered random initial microstructure, i.e., these discretisations act like filters and lead to a smearing of the phases. Furthermore, the energy barrier induced by the interface energy increases with decreasing length scale parameter ε. Since the coarsest discretisation shows the largest ε, it leads to the lowest energy barrier. Accordingly, mixing of the phases is energetically more favourable than phase separation for the coarsest discretisation.

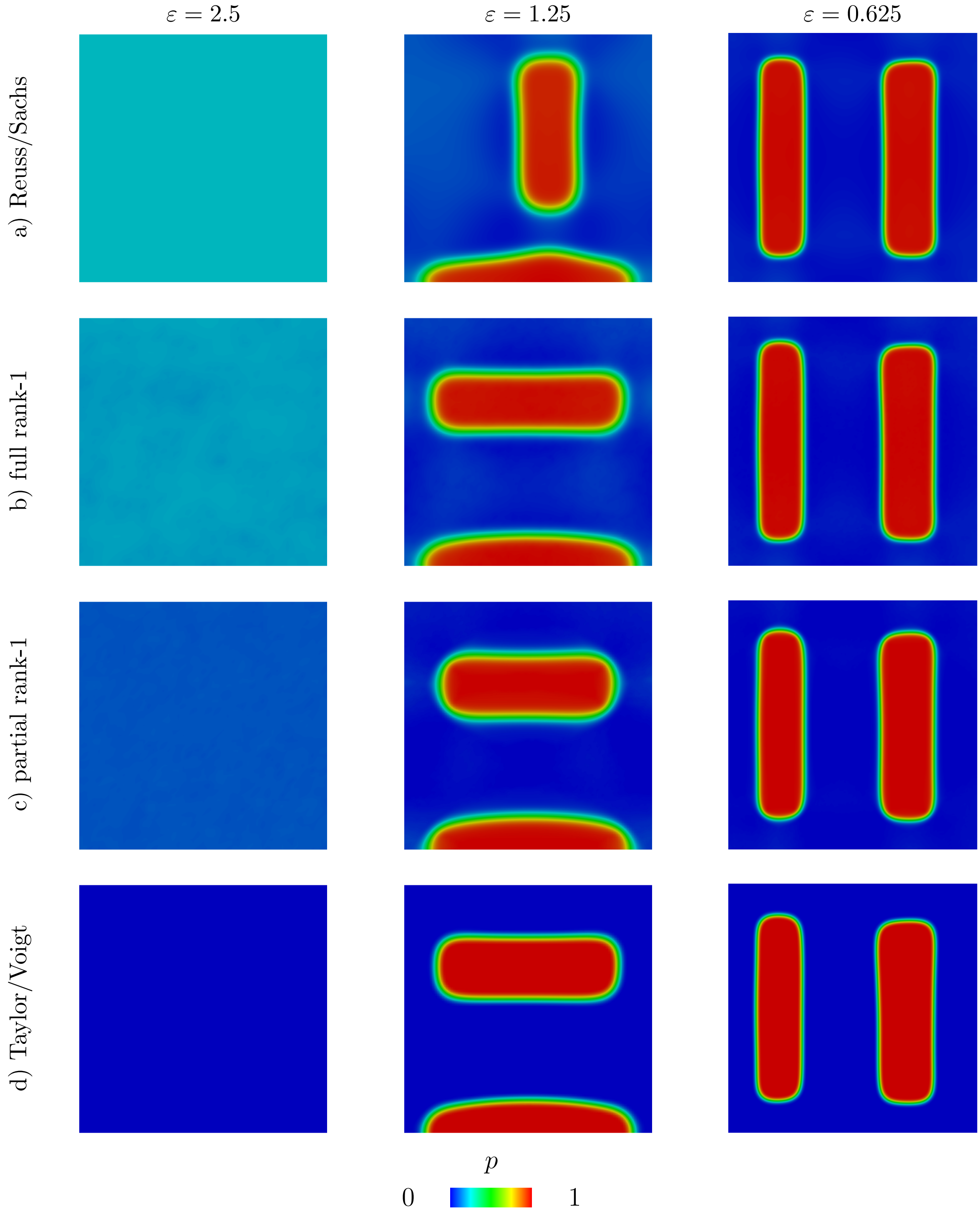

Figure 5.5: Influence of the interface thickness ε on the prediction of the microstructure $p(\mathbf{X})$ for the different homogenisation assumption; Horizontal: variation of the interface thickness $\varepsilon = 2.5/1.25/0.625$ mm. Vertical: different homogenisation assumptions; Material parameters according to Tab. 5.4

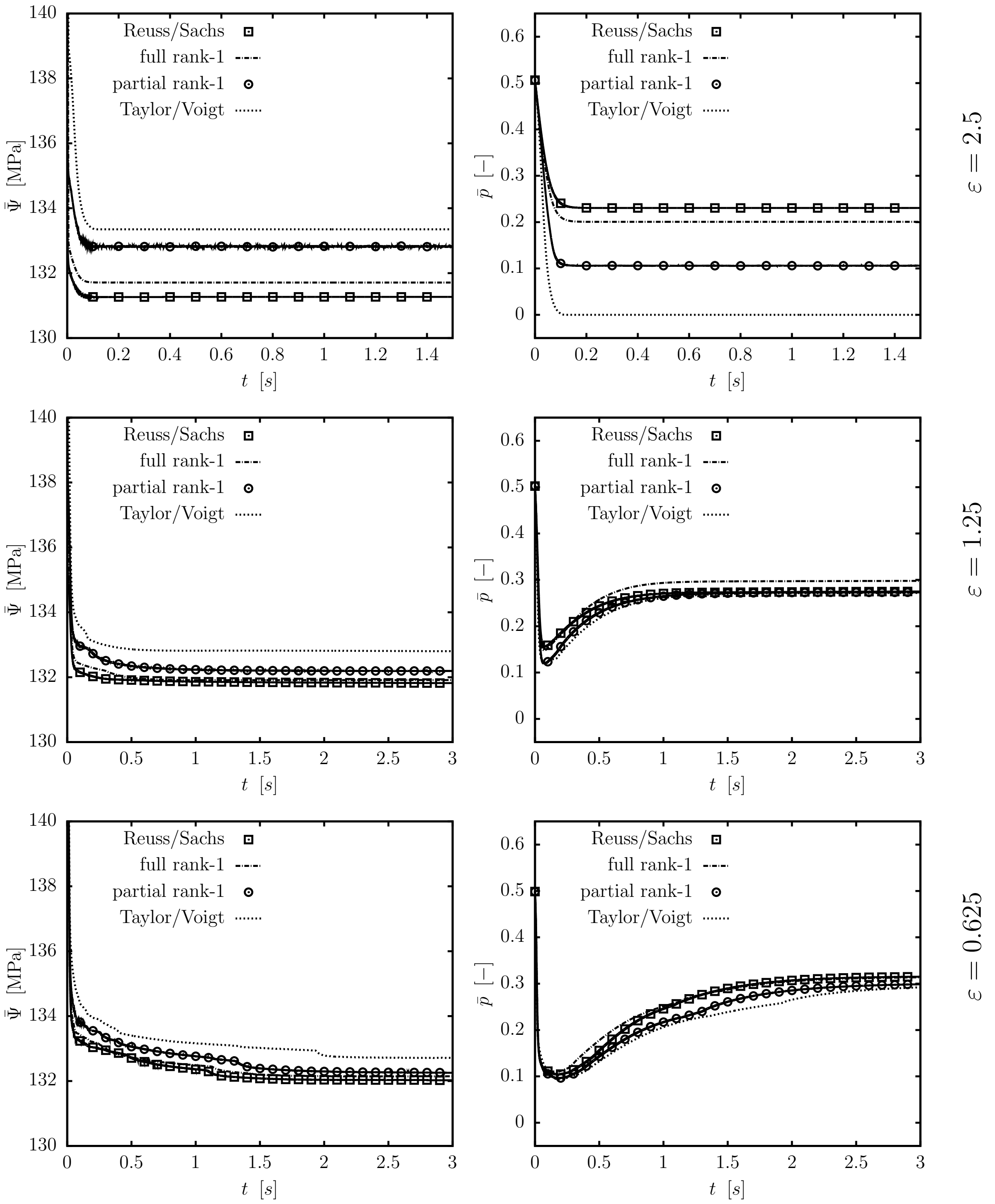

Figure 5.6: Influence of the interface thickness ε on the prediction of the stored energy $\bar{\Psi}$ and the volume ratio $\bar{p}$ depending on the time t

By way of contrast, the two finer discretisations with smaller length scale parameters ($\varepsilon = 1.25$ mm and $\varepsilon = 0.625$ mm) result in a phase separation. While for a parameter $\varepsilon = 0.625$ mm the phase distribution seems to be independent of the underlying homogenisation assumption, a deviation is observed for $\varepsilon = 1.25$ mm. Particularly the microstructure associated with the Reuss/Sachs assumption is different from the other presented homogenisation approaches for $\varepsilon = 1.25$ mm. In summary, the discretisations are not allowed to be too coarse, even relatively fine discretisations show an influence of the considered homogenisation schemes (a 100 × 100 × 100 discretisation shows already more than 5 million degrees of freedom in 3D), and for sufficiently fine discretisations (and length scale parameters ε) all homogenisation assumptions seem to converge to the same solution.

This is also confirmed by the predicted average stored energy $\bar{\Psi}$ and the volume ratio between the two phases, see Fig. 5.6. While for the coarse discretisation and the large length scale parameter ε the results strongly depend on the homogenisation assumption (first row in Fig. 5.6), a convergence for the finer meshes with smaller length scale parameters can be seen (bottom row in Fig. 5.6). Only the stored energy $\bar{\Psi}$ corresponding to the Taylor/Voigt assumption shows a larger deviation. Furthermore, the averaged energies $\bar{\Psi}$ follow the same order as the bulk energies do (see Eq. 5.65), i.e.,

$$\bar{\Psi}^{\mathrm{RS}} \leq \bar{\Psi}^{\mathrm{R1}} \leq \bar{\Psi}^{\partial\mathrm{R1}} \leq \bar{\Psi}^{\mathrm{TV}}. \tag{5.109}$$

However, it bears emphasis that Ineq. (5.65) does not imply Ineq. (5.109) in general, since the final energies $\bar{\Psi}$ are indeed path-dependent.

6 Cahn-Hilliard-type phase field models coupled to continuum mechanics

This chapter presents mechanically driven phase field models, which describe diffusive phase segregation in solids. The theory originates from *Cahn-Hilliard* [24] for phase segregation in the context of spinodal decomposition. In contrast to phase field theories based on Allen and Cahn [2] as discussed in the previous chapter, Cahn-Hilliard-type phase field models describe long term phase transformation processes. Modelling of diffusion based phase transformations is relevant in many technological applications like drug delivery, bio and chemical technology. In the following sections the mechanically induced diffusive phase transformation is analysed in the context of the evolution of microstructures and topology optimisation.

The main difference between the Allen-Cahn-type and the Cahn-Hilliard-type phase field theory is exemplified by different kinds of phase motions in the unit cell. To be more specific, the re-arrangement of phases within Cahn-Hilliard-type models is driven by the difference in the *chemical potential.* Following the framework of Gurtin [50], the chemical potential is governed by the (chemical) micro force balances which describe the transport of phases within and across unit cells. Based on this theory, a Cahn-Hilliard-type evolution equation is derived which enforces the conservation of volume.

As mentioned before, the focus of this chapter lies on the modelling of a deformation-diffusion driven phase field model. The coupling of Cahn-Hilliard phase field models to continuum mechanics (elasticity) was developed by Larché and Cahn [69] and Onuki [97]. However, the elastic properties in the interface are not derived by homogenisation theories as discussed in Section 5.3. In line with Section 5.3 the material behaviour of each phase is determined in the current chapter by its individual bulk energy. By assuming a deformation jump across the interface, effective elastic properties in the interface follow naturally from homogenisation theory. For the present chapter a homogenisation based on the Taylor/Voigt assumption is elaborated. With respect to the modelling of a deformation-diffusion driven phase field theory, a mixed three-field theory depending of the deformation, the phase parameter and the chemical potential is chosen. This approach provides the use of low order ansatz functions for the underlying finite element scheme, and higher order ansatz functions for the resolution of the underlying fourth-order differential equation are not required, cf. Dedè et al. [38], Rajagopal et al. [106], Stogner et al. [128].

A problem which arises in deformation-diffusion induced phase field modelling is the fulfilment of the natural phase parameter constraint $p \in [0,1]$. Due to the coupling to mechanics, admissible states for the phase parameter cannot be guaranteed a priori, which results in a constrained optimisation problem. In line with Section 5.4, the constrained system of equations is transformed into an equivalent system of equations, which fulfils the aforementioned constraints naturally. For this purpose, a robust implementation by means of Fischer-Burmeister NCP-functions is again applied.

The exact fulfilment of the phase parameter constraint and the conservation property of Cahn-Hilliard-type models are very important for two deformation-diffusion driven models which are considered in the following. In Section 6.1 a deformation driven Cahn-Hilliard model is derived based on incremental energy minimisation. The second model in Section 6.2 deals with topology optimisation.

6.1 Microstructural evolution based on a Cahn-Hilliard-type phase field model

In this section a deformation driven Cahn-Hilliard-type phase field theory is developed by means of variational constitutive updates. The starting point is a time-continuous potential at finite strains. The minimiser of this potential follow jointly from the optimisation (minimisation) principle, cf. Miehe et al. [84, 85]. With regard to the numerical implementation, the time-continuous potential is discretised in time and space. The aforementioned NCP-functions by Bartel and Hackl [10], Fischer [45] are applied for a robust algorithmic formulation.

As mentioned before, the focus lies on the volume conservation property of the diffusion driven Cahn-Hilliard theory. In order to demonstrate this feature, phase transformations based on different transformation (Bain) strains are analysed.

The following subsections are structured as follows: In Subsection 6.1.1 the underlying balance equations are derived. In Subsection 6.1.2 the balance equations and constitutive assumptions are transferred into a variationally consistent framework. Subsequently, the numerical implementation is addressed in Subsection 6.1.3.1 (variational updates), Subsection 6.1.3.2 (constrained optimisation) and Subsection 6.1.3.3 (finite element implementation). The capability of the framework is demonstrated in Subsection 6.1.4 by means of the analysis of evolving microstructures.

6.1.1 Balance equations for a coupled deformation-diffusion driven phase field model

A dual-phase system is considered in the following. In line with the phase field modelling of Allen-Cahn-type in Section 5.1, the interface of this dual-phase system is assumed to occupy a certain volume of the material. The respective fields for the phase parameter and the deformation field are identical to the definitions in Eq. (5.2) and Eq. (2.1). For the diffusion process, the additional *chemical potential*

$$\mu : \begin{cases} \mathcal{B}_0 \times \tau \rightarrow \mathbb{R} \\ (\mathbf{X}, t) \mapsto \mu(\mathbf{X}, t) \end{cases} \tag{6.1}$$

is introduced as the third field variable. The gradient of the chemical potential is referred to the reference configuration

$$\mathrm{GRAD}\mu = \nabla_{\mathbf{X}}\mu = \nabla\mu\,. \tag{6.2}$$

The deformation, phase parameter and chemical potential are restricted to their respective balance equations and boundary conditions. For the deformation field the governing equation is the balance of linear momentum (cf. Eq. (2.16))

$$\mathrm{DIV}\mathbf{P} + \rho_0\,\mathbf{B} = \mathbf{0} \quad \text{on} \quad \mathcal{B}_0\,, \tag{6.3}$$

where inertia effects are not taken into account. For the micro force balance, external micro forces are not considered (cf. Eq. (5.9)) which leads to the reduced balance equation

$$\mathrm{DIV}\boldsymbol{\xi} + \pi = 0 \quad \text{on} \quad \mathcal{B}_0\,. \tag{6.4}$$

Moreover, the evolution of the phase parameter within the unit cell fulfils the volume constraint of the total amount of material. Thus, the phase field parameter p is identified as a diffusing quantity, which can also be denoted as *concentration* (cf. Miehe et al. [85]). The transport of phases is described by the balance of *chemical micro forces* (see Gurtin [50])

$$\frac{\mathrm{d}}{\mathrm{d}t}\int\limits_{\Omega_0} p\,\mathrm{d}V = -\int\limits_{\partial\Omega_0} \mathbf{H}\cdot\mathbf{N}\,\mathrm{d}A + \int\limits_{\Omega_0} M\,\mathrm{d}V\,. \tag{6.5}$$

It states that the rate of phases equals the transport which is prescribed by the flux $\mathbf{H}$ over the unit boundary $\partial\Omega_0$ and by the external supply M, cf. Eq. (2.10). The minus sign accounts for the flux direction of the phase transport. In the following a system without external supply is assumed. After transformation of the surface integral in Eq. (6.5) into a volume integral, the local form of the chemical micro force balance

$$\dot{p} = -\mathrm{DIV}\mathbf{H} \;\text{ on } \mathcal{B}_0 \tag{6.6}$$

is derived. The consideration of chemical forces leads to an adjustment of the balance of energy. In the integral form, the balance of energy reads now

$$\frac{\mathrm{d}}{\mathrm{d}t}\int_{\Omega_0} \{K + E\}\,\mathrm{d}V = \mathcal{P}_{\mathbf{F}} + \mathcal{P}_{\Theta} + \mathcal{P}_p + \mathcal{P}_\mu\,, \tag{6.7}$$

in which the chemical power

$$\mathcal{P}_\mu = -\int_{\partial\Omega_0} \bar{H}\,\mu\,\mathrm{d}A \tag{6.8}$$

is taken into account together with the external forces given in Eq. (2.18) ($\mathcal{P}_{\mathbf{F}}$), Eq. (2.19) ($\mathcal{P}_\Theta$) and Eq. (5.12) ($\mathcal{P}_\mu$). The prescribed mass flux on the boundary is denoted by $\bar{H} = \mathbf{H}\cdot\mathbf{N}$. After applying the Gauss divergence theorem and after insertion of balance equations (6.3), (6.4) and (6.6), the local energy balance

$$\dot{E} = \mathbf{P} : \dot{\mathbf{F}} - \mathrm{DIV}\boldsymbol{\mathcal{Q}} + R_\Theta - (\pi - \mu)\,\dot{p} + \boldsymbol{\xi}\cdot\dot{\nabla p} - \mathbf{H}\cdot\nabla\mu\,, \tag{6.9}$$

is obtained. Kinetic energy is again omitted here. An important observation with respect to Eq. (6.9) is that phase parameter and chemical potential are dual conjugated to one another. This duality motivates a mixed variational principal as will be shown in the following. For isothermal conditions ($\boldsymbol{\mathcal{Q}} = \mathbf{0}, R_\Theta = 0, \dot{\Theta} = 0$), which are considered here, and by means of the Legendre transformation (2.42) the internal energy results in

$$\dot{\Psi} + \Theta\,\dot{N} = \mathbf{P} : \dot{\mathbf{F}} - (\pi - \mu)\,\dot{p} + \boldsymbol{\xi}\cdot\dot{\nabla p} - \mathbf{H}\cdot\nabla\mu\,. \tag{6.10}$$

For the derivation of the second law of thermodynamics, the term $\mathrm{DIV}\boldsymbol{\mathcal{Q}} - R_\Theta$ in Eq. (6.9) is used within the dissipation inequality (2.26). The resulting dissipation inequality reads

$$\mathcal{D} = \mathbf{P} : \dot{\mathbf{F}} + \Theta\,\dot{N} + \boldsymbol{\mathcal{Q}}\cdot\mathbf{G} - (\pi - \mu)\,\dot{p} + \boldsymbol{\xi}\cdot\dot{\nabla p} - \mathbf{H}\cdot\nabla\mu - \dot{E} \geq 0\,. \tag{6.11}$$

As mentioned before, the focus is on isothermal processes so that, inequality (6.11) reduces to

$$\mathcal{D} = \mathbf{P} : \dot{\mathbf{F}} - (\pi - \mu)\,\dot{p} + \boldsymbol{\xi}\cdot\dot{\nabla p} - \mathbf{H}\cdot\nabla\mu - \dot{\Psi} \geq 0\,. \tag{6.12}$$

It should be emphasised that the dissipation inequality (6.12) could also be derived by use of relation (5.17) (see Remark 5.2.1).

Boundary conditions: The coupled system of equations can only be solved by considering initial and boundary conditions. Therefore, the underlying boundary, here in its reference configuration $\partial\mathcal{B}_0$, is decomposed into Dirichlet and Neumann boundaries. Since the mechanical-diffuse driven phase field problem is determined by three field quantities, the deformation field, the chemical potential and the phase parameter, the boundaries of these fields are specified by

$$\partial\mathcal{B}_0 = \partial\mathcal{B}_{0,\boldsymbol{\varphi}} \cup \partial\mathcal{B}_{0,\mathbf{T}} \qquad \partial\mathcal{B}_0 = \partial\mathcal{B}_{0,p} \cup \partial\mathcal{B}_{0,\boldsymbol{\xi}} \qquad \partial\mathcal{B}_0 = \partial\mathcal{B}_{0,\mu} \cup \partial\mathcal{B}_{0,\mathbf{H}}\,. \tag{6.13}$$

These boundaries are disjunct in the sense $\partial\mathcal{B}_{0,\boldsymbol{\varphi}} \cap \partial\mathcal{B}_{0,\mathbf{T}} = \emptyset$, $\partial\mathcal{B}_{0,p} \cap \partial\mathcal{B}_{0,\boldsymbol{\xi}} = \emptyset$ and $\partial\mathcal{B}_{0,\mu} \cap \partial\mathcal{B}_{0,\mathbf{H}} = \emptyset$. For the sake of completeness, the boundary conditions of the mechanical (cf. Eq. (2.32)) and those of the phase field boundary value problem (cf. Eq. (5.21)) are given again, i.e.

$$\boldsymbol{\varphi} = \bar{\boldsymbol{\varphi}} \text{ on } \partial\mathcal{B}_{0,\boldsymbol{\varphi}}\,, \qquad \mathbf{P}\cdot\mathbf{N} = \bar{\mathbf{T}} \text{ on } \partial\mathcal{B}_{0,\mathbf{T}} \tag{6.14}$$

and

$$p = \bar{p} \text{ on } \partial\mathcal{B}_{0,p}\,, \qquad \boldsymbol{\xi}\cdot\mathbf{N} = 0 \text{ on } \partial\mathcal{B}_{0,\boldsymbol{\xi}}\,. \tag{6.15}$$

On the boundary, the chemical potential reads

$$\mu = \bar{\mu} \text{ on } \partial\mathcal{B}_{0,\mu}\,, \qquad \mathbf{H}\cdot\mathbf{N} = \bar{H} \text{ on } \partial\mathcal{B}_{0,\mathbf{H}}\,. \tag{6.16}$$

While $\bar{\mu}$ is the prescribed chemical potential on the Dirichlet boundary $\partial\mathcal{B}_{0,\mu}$, flux $\bar{H}$ is the prescribed quantity on the Neumann boundary $\partial\mathcal{B}_{0,\mathbf{H}}$. Note, that for a homogeneous Neumann boundary

$$\bar{H} = 0 \text{ on } \partial\mathcal{B}_0 \tag{6.17}$$

no mass can flow inside or outside the body and conversation of the integrated phase parameter is fulfilled (if no source terms are considered), see also Remark 6.1.3. The initial conditions for the phase parameter are defined by the distribution in $\mathcal{B}_0$ at the initial time t_0

$$p(\mathbf{X}, t_0) = p_0(\mathbf{X}) \text{ in } \mathcal{B}_0\,. \tag{6.18}$$

6.1.2 A variationally consistent phase field model coupled to elasticity and diffusion

The starting point of the constitutive modelling is the energy of the deformation driven phase field model given in Subsection 5.2.2. Again, the free energy (5.25), more precise,

$$\Psi(\mathbf{F}, p, \nabla p) = \Psi_{\mathrm{B}}(\mathbf{F}, p) + \Psi_{\Gamma}(p, \nabla p) \tag{6.19}$$

is additively decomposed into a bulk energy part Ψ_{B} which is a function of the deformation gradient and the phase parameter, and into a surface energy part Ψ_Γ which is independent of the mechanical deformation. Postulating that the Helmholtz energy Ψ is consistent with the dissipation inequality (6.12), Ψ cannot be a function of the chemical potential μ or gradient $\nabla\mu$, since p and μ are dual variables. Inserting Eq. (6.19) into dissipation inequality (6.12) yields

$$\mathcal{D} = \left[\mathbf{P} - \frac{\partial\Psi}{\partial\mathbf{F}}\right] : \dot{\mathbf{F}} - \left[\pi + \frac{\partial\Psi}{\partial p} - \mu\right] \dot{p} + \left[\boldsymbol{\xi} - \frac{\partial\Psi}{\partial\nabla p}\right] \cdot \dot{\nabla p} - \mathbf{H}\cdot\nabla\mu \geq 0\,. \tag{6.20}$$

For arbitrary $\dot{\mathbf{F}}$, $\dot{p}$ and $\dot{\nabla p}$ the application of the classic *Coleman & Noll* procedure leads to the requirement that the terms in the brackets vanish. Thus, the constitutive relations for the Piola-Kirchhoff stress tensor $\mathbf{P}$, the internal micro force π and the micro stress vector $\boldsymbol{\xi}$ are obtained as

$$\mathbf{P} = \frac{\partial\Psi_{\mathrm{B}}}{\partial\mathbf{F}}\,, \qquad \pi = \mu - \frac{\partial\Psi_{\mathrm{B}}}{\partial p} - \frac{\partial\Psi_\Gamma}{\partial p}\,, \qquad \boldsymbol{\xi} = \frac{\partial\Psi_{\mathrm{B}}}{\partial\nabla p} + \frac{\partial\Psi_\Gamma}{\partial\nabla p}\,. \tag{6.21}$$

In contrast to Allen-Cahn-type phase field models, the motion of the phases is controlled by a diffusion process. Therefore, π is a constitutive quantity. Re-inserting the relations given in Eq. (6.21) into inequality (6.20) leads to the requirement

$$\mathcal{D}_{\mathrm{dif}} = -\mathbf{H}\cdot\nabla\mu \geq 0\,, \tag{6.22}$$

where $\mathcal{D}_{\mathrm{dif}}$ denotes the dissipation due to diffusion. Similarly to thermal conductivity (cf. Eq. (2.55)), the diffusion process is described by a potential of the type

$$\widehat{\phi} = \frac{1}{2}\kappa|\nabla\mu|^2\,. \tag{6.23}$$

Clearly, the constitutive flux

$$\mathbf{H} = -\frac{\partial\widehat{\phi}}{\partial\nabla\mu} \tag{6.24}$$

fulfils the necessary dissipation inequality (6.22), which results in $\kappa\,|\nabla\mu|^2 \geq 0$ for all $\kappa > 0$. In this regard κ specifies the mobility of the diffusion process. More complex and more realistic diffusion relations may be obtained by the use of an anisotropic mobility tensor which also depends on the phase parameter.

Following the work of Gurtin [50], Miehe et al. [84, 85], the deformation-diffusion coupled phase field theory shows a variational structure. This means all balance equations follow naturally as Euler/Lagrange equations from the minimisation of a functional. Similar to the previous chapter, the functional consists of a stored energy rate, a dissipation functional and power terms as a consequence of external forces. The time-continuous potential reads

$$\dot{\mathcal{I}} = \int\limits_{\partial\mathcal{B}_0} \dot{\Psi}(\boldsymbol{\varphi}, p)\,\mathrm{d}V + \Phi(\dot{p}) - \mathcal{P}_{\mathbf{F}}(\dot{\boldsymbol{\varphi}})\,. \tag{6.25}$$

Note, that in the current potential (6.25) external power is not generated by micro tractions on the boundary, since Eq. (6.15) is assumed. The dissipation functional Φ follows from the maximisation

$$\Phi(\dot{p}) = \sup_{\mu} \left\{ \int\limits_{\mathcal{B}_0} \{-\mu\,\dot{p} - \widehat{\phi}(\nabla\mu)\}\,\mathrm{d}V - \mathcal{P}_{\mu}(\mu) \right\}\,, \tag{6.26}$$

where the external power $\mathcal{P}_{\mu}$ is taken from Eq. (6.8). As pointed out in Miehe et al. [85], this maximisation can be seen as *generalised Legendre transformation* in which $\dot{p}$ and μ are dual to each other similar to the variational formulation in thermoelasticity, cf. Subsection 2.6.2. The maximisation of dissipation functional (6.26) with respect to the chemical potential is equivalent to the balance of chemical micro forces (6.6), which will be proven later, and the solution

$$\mu = \arg \sup_{\mu} \left\{ \int\limits_{\mathcal{B}_0} \{-\mu\,\dot{p} - \widehat{\phi}(\nabla\mu)\}\,\mathrm{d}V - \mathcal{P}_{\mu}(\mu) \right\} \tag{6.27}$$

is the maximiser of the dissipation functional (6.26).

In the following, a mixed variational potential is presented based on a three-field description depending on the deformations, the phase field and the chemical potential. The time-continuous potential thus reads

$$\dot{\mathcal{I}} = \int\limits_{\mathcal{B}_0} \dot{\mathcal{E}}(\boldsymbol{\varphi}, p, \mu,)\,\mathrm{d}V - \mathcal{P}_{\mathbf{F}}(\dot{\boldsymbol{\varphi}}) - \mathcal{P}_{\mu}(\mu)\,, \tag{6.28}$$

in which the potential

$$\dot{\mathcal{E}} = \dot{\Psi}_{\mathrm{B}}(\mathbf{F}, p, \nabla p) + \dot{\Psi}_{\Gamma}(p, \nabla p) - \mu\,\dot{p} - \widehat{\phi}(\nabla\mu) \tag{6.29}$$

consists of stored energy contributions ($\dot{\Psi}_{\mathrm{B}}$ and $\dot{\Psi}_{\Gamma}$) and dissipative contributions ($-\mu\,\dot{p} - \widehat{\phi}$). In this context, the power related external forces are assumed to be linearly dependent on the field variables. In contrast to the 2-field potential (6.25), the diffusion potential $\widehat{\phi}$ is directly embedded in the rate potential (6.29). Thus, the resulting potential represents a saddle-point problem with μ and p being dual to one another.

Applying the framework of variationally consistent updates, the unknowns follow naturally from the optimisation of the time-discretised potential $\Delta\mathcal{I}$, i.e.

$$(\boldsymbol{\varphi}, p, \mu) = \arg \inf_{\boldsymbol{\varphi},p} \sup_{\mu} \; \Delta\mathcal{I}\,. \tag{6.30}$$

While the evolutions of the deformation field and the phase field are determined by minimisation, the chemical potential is determined by maximisation. Further details regarding the time-discretisation are discussed in Subsection 6.1.3.1.

In order to prove the consistency with respect to the balance equations presented in Subsection 6.1.1, the stationary conditions of potential (6.28) are analysed. The variation with respect to the deformation mapping yields by means of relation Eq. $(6.21)_1$ the balance of linear momentum (6.3) and the Neumann condition $(6.14)_2$, cf. Eq (5.33). The variation with respect to the phase parameter yields

$$\begin{aligned} \delta_{\dot{p}}\dot{\mathcal{I}} = &\int\limits_{\mathcal{B}_0} \left\{\partial_p[\Psi_{\mathrm{B}} + \Psi_{\Gamma}] - \mu - \mathrm{DIV}\left(\partial_{\nabla p}[\Psi_{\mathrm{B}} + \Psi_{\Gamma}]\right)\right\} \delta\dot{p}\,\mathrm{d}V \\ &+ \int\limits_{\partial\mathcal{B}_0} \left\{\partial_{\nabla p}[\Psi_{\mathrm{B}} + \Psi_{\Gamma}] \cdot \mathbf{N}\right\} \delta\dot{p}\,\mathrm{d}A = 0\,. \end{aligned} \tag{6.31}$$

For admissible virtual phase parameter $\delta\dot{p}$, the equivalent balance of micro forces and the associated Neumann conditions are thus obtained, i.e.

$$\begin{aligned} -\mathrm{DIV}\boldsymbol{\xi} - \pi = 0 \quad &\text{on} \quad \mathcal{B}_0\,, \\ \boldsymbol{\xi} \cdot \mathbf{N} = 0 \quad &\text{on} \quad \partial\mathcal{B}_{0,\boldsymbol{\xi}}\,, \end{aligned} \tag{6.32}$$

in which the constitutive micro force $(6.21)_2$ and the constitutive micro stress $(6.21)_3$ are substituted. Similarly, the equivalent chemical balance equation and the associated Neumann condition are obtained from the necessary stationarity condition

$$\begin{aligned} \delta_{\mu}\dot{\mathcal{I}} = &\int\limits_{\mathcal{B}_0} \left\{-\dot{p} + \mathrm{DIV}\left(\partial_{\nabla\mu}\widehat{\phi}\right)\right\} \delta\mu\,\mathrm{d}V \\ &- \int\limits_{\partial\mathcal{B}_0} \left\{\partial_{\nabla\mu}\widehat{\phi} \cdot \mathbf{N} + \bar{H}\right\} \delta\mu\,\mathrm{d}A = 0\,. \end{aligned} \tag{6.33}$$

Together with the mass flux (6.24) this condition is equivalent to

$$\begin{aligned} -\dot{p} - \mathrm{DIV}\mathbf{H} = 0 \quad &\text{on} \quad \mathcal{B}_0\,, \\ \mathbf{H} \cdot \mathbf{N} = \bar{H} \quad &\text{on} \quad \partial\mathcal{B}_{0,\mathbf{H}}\,, \end{aligned} \tag{6.34}$$

being the balance equation (6.6) and the Neumann condition $(6.16)_2$.

Remark 6.1.1: *A classic Cahn-Hilliard-type evolution equation is obtained by combining balance equations* $(6.34)_1$ *and* $(6.32)_1$ *and the constitutive relations* $(6.21)_2$, $(6.21)_3$ *and* (6.23)*. The resulting fourth order differential equation*

$$\begin{aligned} \dot{p} &= -\mathrm{DIV}\mathbf{H} \\ &= \kappa\,\mathrm{DIV}\left(\nabla\mu\right) \\ &= \kappa\,\mathrm{DIV}\left(\nabla\left\{\partial_p\Psi_\mathrm{B} + \partial_p\Psi_\Gamma - \mathrm{DIV}\left(\partial_{\nabla p}\Psi_\Gamma\right)\right\}\right) \end{aligned} \tag{6.35}$$

describes the phase parameter evolution for deformation-diffusion phase field problems. At equilibrium, for $p = \text{const.}$, *the chemical potential* μ *is uniformly distributed.*

Remark 6.1.2: *In contrast to the Cahn-Hilliard-type evolution equation, the well-known Fickian diffusion law is driven by the gradient of the phase parameter* ∇p*, i.e.*

$$\dot{p} = \kappa\,\mathrm{DIV}(\nabla p)\,. \tag{6.36}$$

At equilibrium, for $p = \text{const.}$, *the phases are uniformly distributed.*

Remark 6.1.3: *For flux condition* $\bar{H} = \mathbf{H}\cdot\mathbf{N} = 0$ *on* $\partial\mathcal{B}_0$ *the integrated chemical balance equation* $(6.34)_1$ *reduces to*

$$\int\limits_{\mathcal{B}_0} \dot{p}\,\mathrm{d}V = \int\limits_{\mathcal{B}_0} -\mathrm{DIV}\mathbf{H}\,\mathrm{d}V = \int\limits_{\partial\mathcal{B}_0} -\mathbf{H}\cdot\mathbf{N}\,\mathrm{d}A = \int\limits_{\partial\mathcal{B}_0} -\bar{H}\,\mathrm{d}A = 0\,. \tag{6.37}$$

Consequently, the total volume of the material is conserved within the body $\mathcal{B}_0$*.*

6.1.2.1 Homogenisation of elastic properties in the interface

The hyperelastic material response in the individual phases are of the type

$$\Psi_{\mathrm{B}_i} = \Psi_{\mathrm{B}_i}\left(\mathbf{F}^\mathrm{e}_i, p\right) \qquad \text{with} \qquad \mathbf{F}^\mathrm{e}_i = \mathbf{F}_i\cdot\mathbf{F}_i^{\mathrm{B}^{-1}}\,, \tag{6.38}$$

where $\mathbf{F}^\mathrm{B}_i$ describes the eigenstrain (Bain strain) of each individual phase $i = \{1,2\}$. For the definition of mechanical properties in the interface a homogenisation theory in line with Section 5.3 is elaborated. For the sake of simplicity, the Taylor/Voigt assumption $[\![\mathbf{F}]\!] = 0$ is taken, fulfilling kinematic compatibility but lacking statical compatibility. In order to fulfil statical as well as kinematical compatibility, homogenisation theories based on rank-1 connections in the interface (see Subsection 5.3) can also be applied. Considering a Taylor/Voigt homogenisation assumption, the resulting total bulk energy reads

$$\Psi_\mathrm{B}(\mathbf{F},p) = [1-p]\,\Psi_{\mathrm{B}_1}\left(\mathbf{F}\cdot\mathbf{F}_1^{\mathrm{B}^{-1}}\right) + p\,\Psi_{\mathrm{B}_2}\left(\mathbf{F}\cdot\mathbf{F}_2^{\mathrm{B}^{-1}}\right)\,. \tag{6.39}$$

Note, that the homogenised energy is independent of the phase gradient. Based on energy (6.39) equations $(6.21)_1$-$(6.21)_3$ result in

$$\mathbf{P} = [1-p]\mathbf{P}_1 + p\mathbf{P}_2\,, \qquad \pi = \mu - [\![\Psi_\mathrm{B}]\!] - \frac{\partial \Psi_\Gamma}{\partial p}\,, \qquad \boldsymbol{\xi} = \frac{\partial \Psi_\Gamma}{\partial \nabla p}\,, \tag{6.40}$$

in which $[\![\Psi_\mathrm{B}]\!] = \Psi_{\mathrm{B}_2} - \Psi_{\mathrm{B}_1}$ is the jump in energy between the two phases. The individual stresses are defined as

$$\mathbf{P}_i = \frac{\partial \Psi_{\mathrm{B}_i}}{\partial \mathbf{F}_i^\mathrm{e}} \cdot \mathbf{F}_i^{\mathrm{B}-\mathrm{T}}\,. \tag{6.41}$$

6.1.3 Numerical implementation

The following section deals with the numerical implementation of the proposed mixed three-field variational formulation.

6.1.3.1 Incremental variational updates

By applying the framework of incremental variational updates as introduced in Subsection 2.6.1, the time-continuous rate potential is discretised. To this end, time interval $\tau = [t_n, t_{n+1}]$ is considered. The underlying incremental potential reads after time integration of Eq. (6.28)

$$\begin{aligned} \Delta\mathcal{I} = \int_{t_n}^{t_{n+1}} \dot{\mathcal{I}}\,\mathrm{d}t = \int_{\mathcal{B}_0} \Delta\mathcal{E}(\boldsymbol{\varphi}_{n+1}, p_{n+1}, \mu_{n+1}, \boldsymbol{\varphi}_n, p_n, \mu_n)\,\mathrm{d}V \\ - \mathcal{P}_\mathbf{F}(\boldsymbol{\varphi}_{n+1}) + \mathcal{P}_\mathbf{F}(\boldsymbol{\varphi}_n) - \Delta t\,\mathcal{P}_\mu(\mu_{n+1})\,, \end{aligned} \tag{6.42}$$

with $\Delta t = t_{n+1} - t_n$ being the time increment. For the sake of simplicity, conservative external loads are assumed. Furthermore, the time-continuous potential (6.29) is approximated by

$$\begin{aligned} \Delta\mathcal{E} = {} & \Psi_\mathrm{B}\left(\mathbf{F}_{n+1}, p_{n+1}\right) - \Psi_\mathrm{B}\left(\mathbf{F}_n, p_n\right) \\ & + \Psi_\Gamma(p_{n+1}, \nabla p_{n+1}) - \Psi_\Gamma(p_n, \nabla p_n) \\ & - \mu_{n+1}\left[p_{n+1} - p_n\right] - \Delta t\,\widehat{\phi}\left(\nabla \mu_{n+1}\right)\,. \end{aligned} \tag{6.43}$$

For readability reasons, the time index $n+1$ at the current time t_{n+1} is neglected in the following. The deformation, phase parameter and the chemical potential at current time are now obtained by means of the variational principle

$$(\boldsymbol{\varphi}, p, \mu) = \arg \inf_{\boldsymbol{\varphi}, p} \sup_{\mu}\ \Delta\mathcal{I}\,. \tag{6.44}$$

In order to see this more explicitly, the respective stationarity conditions

$$
\begin{aligned}
\delta_{\varphi}\, \Delta\mathcal{I} &= \int\limits_{\mathcal{B}_0} \mathbf{P} : \delta\mathbf{F}\, \mathrm{d}V - \int\limits_{\mathcal{B}_0} \rho_0 \mathbf{B} \cdot \delta\boldsymbol{\varphi}\, \mathrm{d}V - \int\limits_{\partial\mathcal{B}_0} \bar{\mathbf{T}} \cdot \delta\boldsymbol{\varphi}\, \mathrm{d}A = 0\,, \\
\delta_{p}\, \Delta\mathcal{I} &= \int\limits_{\mathcal{B}_0} \{-\pi\, \delta p + \boldsymbol{\xi} \cdot \nabla\delta p\}\; \mathrm{d}V = 0\,, \\
\delta_{\mu}\, \Delta\mathcal{I} &= \int\limits_{\mathcal{B}_0} \{-[p - p_n]\, \delta\mu + \Delta\mathbf{H} \cdot \nabla\delta\mu\}\; \mathrm{d}V - \Delta t \int\limits_{\partial\mathcal{B}_0} \bar{H}\, \delta\mu\, \mathrm{d}A = 0\,,
\end{aligned}
\tag{6.45}
$$

are computed. Note, that Eq. $(6.45)_1$-$(6.45)_3$ are equivalent to respective weak formulations. An interesting point regarding these variations is that the constitutives $\mathbf{P}$, π, $\boldsymbol{\xi}$ and $\Delta\mathbf{H}$ follow naturally as partial derivatives from the incremental potential $\Delta\mathcal{E}$, i.e.

$$
\begin{aligned}
\mathbf{P} &= \frac{\partial\Delta\mathcal{E}}{\partial\mathbf{F}} = \frac{\partial\Psi_{\mathrm{B}}}{\partial\mathbf{F}} = [1-p]\,\mathbf{P}_1 + p\,\mathbf{P}_2\,, \qquad & \boldsymbol{\xi} &= \frac{\partial\Delta\mathcal{E}}{\partial\nabla p} = \frac{\partial\Psi_{\Gamma}}{\partial\nabla p}\,, \\
\pi &= -\frac{\partial\Delta\mathcal{E}}{\partial p} = \mu - [\![\Psi_{\mathrm{B}}]\!] - \frac{\partial\Psi_{\Gamma}}{\partial p}\,, & \Delta\mathbf{H} &= \frac{\partial\Delta\mathcal{E}}{\partial\nabla\mu} = -\Delta t\, \frac{\partial\widehat{\phi}}{\partial\nabla\mu}\,.
\end{aligned}
\tag{6.46}
$$

6.1.3.2 Constrained optimisation

As discussed in Subsection 5.4.2, the constraint $p \in [0,1]$ is a priori not guaranteed for the saddle point problem (6.44). In order to enforce this constraint, the extended Lagrangian potential

$$
\Delta\tilde{\mathcal{I}}(\boldsymbol{\varphi}, p, \mu, \lambda_1, \lambda_2) = \Delta\mathcal{I}(\boldsymbol{\varphi}, p, \mu) + \lambda_1\, r_1 + \lambda_2\, r_2 \tag{6.47}
$$

is introduced. Again, $\lambda_1 \geq 0$ is the Lagrange parameter of the constraint $r_1 = p - 1 \leq 0$ and $\lambda_2 \geq 0$ is the Lagrange parameter of the constraint $r_2 = -p \leq 0$. Following the proposed solution method in Subsection 5.4.2, the nonlinear complementary conditions are solved by introducing equivalent *Fischer-Burmeister* NCP functions $g_i(p, \lambda_i) = 0$ for $i = \{1, 2\}$, see Eq. (5.82). For further details, the interested reader is referred to Subsection 5.4.2 and to Bartel and Hackl [10], Fischer [45]. Finally, the overall system of linear equations can be written into the residual form

$$
\begin{bmatrix}
\delta_{\varphi}\Delta\tilde{\mathcal{I}}(\boldsymbol{\varphi}, p, \mu, \lambda_1, \lambda_2) \\
\delta_{\mu}\Delta\tilde{\mathcal{I}}(\boldsymbol{\varphi}, p, \mu, \lambda_1, \lambda_2) \\
\delta_{p}\Delta\tilde{\mathcal{I}}(\boldsymbol{\varphi}, p, \mu, \lambda_1, \lambda_2) \\
g_1(p, \lambda_1) \\
g_2(p, \lambda_2)
\end{bmatrix}
=
\begin{bmatrix}
\delta_{\varphi}\Delta\mathcal{I}(\boldsymbol{\varphi}, p, \mu) \\
\delta_{\mu}\Delta\mathcal{I}(\boldsymbol{\varphi}, p, \mu) \\
\delta_{p}\Delta\mathcal{I}(\boldsymbol{\varphi}, p, \mu) + \lambda_1\, \delta p - \lambda_2\, \delta p \\
\sqrt{[p-1]^2 + \lambda_1^2} + [p-1] - \lambda_1 \\
\sqrt{[-p]^2 + \lambda_2^2} - p - \lambda_2
\end{bmatrix}
= \mathbf{0} \quad \text{on} \quad \mathcal{B}_0. \tag{6.48}
$$

Standard Newton based solution schemes can be applied to solve the nonlinear system of equations together with the associated boundary conditions in Eq. (6.14), (6.16), (6.15) and appropriate initial conditions (6.16). As mentioned before, the introduction of 2 additional field variables λ_1 and λ_2 increases the system of nonlinear equations to 5 field variables. However, since only one Lagrange parameter can be active, either r_1 or r_2 is not satisfied, the system of equations could be reduced to only one constraint. In the present work both NCP functions are taken into account. Apart from the constrained optimisation, the consideration of the NCP functions leads to the loss of the variational structure, see Remark 5.4.4.

6.1.3.3 Finite element implementation

Next, the presented incremental potential for the coupled problem is spatially discretised by finite elements. To this end, the referential body is approximated by the partition

$$\mathcal{B}_0 \approx \mathcal{B}_0^{\mathrm{h}} = \bigcup_{e=1}^{n_{\mathrm{el}}} \mathcal{B}_0^e \,, \tag{6.49}$$

into n_{el} elements. Focussing on one element $\mathcal{B}_0^{\mathrm{e}}$, the referential coordinates $\mathbf{X}$, the deformation map $\boldsymbol{\varphi}$, the phase parameter p and the chemical potential μ, are approximated by

$$\begin{aligned} \mathbf{X}|_{\mathcal{B}_0^{\mathrm{e}}} \approx \mathbf{X}^{\mathrm{h}} = \sum_{a=1}^{n_{\mathrm{en}}} N^a \, \mathbf{X}^a \,, \quad \boldsymbol{\varphi}|_{\mathcal{B}_0^{\mathrm{e}}} \approx \boldsymbol{\varphi}^{\mathrm{h}} = \sum_{a=1}^{n_{\mathrm{en}}} N^a \, \boldsymbol{\varphi}^a \,, \\ p|_{\mathcal{B}_0^{\mathrm{e}}} \approx p^h = \sum_{a=1}^{n_{\mathrm{en}}} N^a \, p^a \,, \quad \mu|_{\mathcal{B}_0^{\mathrm{e}}} \approx \mu^h = \sum_{a=1}^{n_{\mathrm{en}}} N^a \, \mu^a \,. \end{aligned} \tag{6.50}$$

The nodal values at element node a are denoted as $\mathbf{X}^a$, $\boldsymbol{\varphi}^a$, p^a and μ^a. Following the isoparametric concept, all presented field variables are interpolated by the same shape functions N^a. As already emphasised in Subsection 5.4.3, the Lagrange parameters λ_1 and λ_2 are not interpolated since they constrain the phase parameter at node point a. Furthermore, within all presented numerical examples linear shape functions are utilised, due to the constraint $p \in [0, 1]$ (see Remark 5.4.6). Based on the approximations (6.50), the gradients with respect to the reference configuration

$$\mathbf{F}^h = \nabla \boldsymbol{\varphi}^{\mathrm{h}} = \sum_{a=1}^{n_{\mathrm{en}}} \boldsymbol{\varphi}^a \otimes \nabla N^a \,, \quad \nabla p^h = \sum_{a=1}^{n_{\mathrm{en}}} p^a \, \nabla N^a \,, \quad \nabla \mu^h = \sum_{a=1}^{n_{\mathrm{en}}} \mu^a \, \nabla N^a \tag{6.51}$$

are obtained, where the gradient of the shape function with respect to the referential configuration is denoted by ∇N^a. Following a standard Bubnov-Galerkin discretisation, the virtual displacement $\delta \boldsymbol{\varphi}$, the virtual phase parameter δp and the virtual chemical potential $\delta \mu$ are interpolated with the same ansatz functions. Subsequently, these relations are inserted into the residual form (6.48). For one element, the discretised weak formulations read

$$
\begin{aligned}
\delta_{\boldsymbol{\varphi}} \Delta\tilde{\mathcal{I}}|_{\mathcal{B}_0^e} &= \sum_{a=1}^{n_{\text{en}}} \delta\boldsymbol{\varphi}^a \cdot \left[\mathbf{f}^a_{\boldsymbol{\varphi},\text{int}} - \mathbf{f}^a_{\boldsymbol{\varphi},\text{vol}} - \mathbf{f}^a_{\boldsymbol{\varphi},\text{sur}}\right] \,, \\
\delta_{\mu} \Delta\tilde{\mathcal{I}}|_{\mathcal{B}_0^e} &= \sum_{a=1}^{n_{\text{en}}} \delta\mu^a \,\left[f^a_{\mu,\text{int}} - f^a_{\mu,\text{sur}}\right] \,, \\
\delta_{p} \Delta\tilde{\mathcal{I}}|_{\mathcal{B}_0^e} &= \sum_{a=1}^{n_{\text{en}}} \delta p^a \,\left[f^a_{p,\text{int}} + \lambda_1^a - \lambda_2^a\right] \,,
\end{aligned}
\tag{6.52}
$$

in which $\delta\boldsymbol{\varphi}^a$, $\delta\mu^a$ and δp^a denote the virtual placement, virtual phase parameter and virtual chemical potential at node point a. The nodal forces in Eq. (6.52) are defined as

$$
\begin{aligned}
\mathbf{f}^a_{\boldsymbol{\varphi},\text{int}} &= \int_{\mathcal{B}_0^e} \mathbf{P}\cdot\nabla N^a \,\mathrm{d}V\,, \quad \mathbf{f}^a_{\boldsymbol{\varphi},\text{vol}} = \int_{\mathcal{B}_0^e} N^a \rho_0\, \mathbf{B}\,\mathrm{d}V\,, \quad \mathbf{f}^a_{\boldsymbol{\varphi},\text{sur}} = \int_{\partial\mathcal{B}_0^e} N^a\, \bar{\mathbf{T}}\,\mathrm{d}A\,, \\
f^a_{\mu,\text{int}} &= \int_{\mathcal{B}_0^e} \left\{-N^a\,[p-p_n] + \nabla N^a \cdot \Delta\mathbf{H}\right\} \mathrm{d}V\,, \quad f^a_{\mu,\text{sur}} = \int_{\partial\mathcal{B}_0^e} N^a\, \Delta t\, \bar{H}\,\mathrm{d}A\,, \\
f^a_{p,\text{int}} &= \int_{\mathcal{B}_0^e} \left\{-N^a\,\pi + \nabla N^a \cdot \boldsymbol{\xi}\right\} \mathrm{d}V\,.
\end{aligned}
\tag{6.53}
$$

The external forces are related to the body forces $\mathbf{f}^a_{\boldsymbol{\varphi},\text{vol}}$, the traction forces $\mathbf{f}^a_{\boldsymbol{\varphi},\text{sur}}$ and the forces related to the external mass flux $f^a_{\mu,\text{sur}}$. For the finite element solution the forces in Eq. (6.53) are assembled in the residual form

$$
\mathbf{r}^A = \mathop{\mathbf{A}}_{e=1}^{n_{\text{el}}} \begin{bmatrix} \mathbf{r}^a_{\boldsymbol{\varphi}} \\ r^a_{\mu} \\ r^a_{p} \\ r^a_{\lambda_1} \\ r^a_{\lambda_2} \end{bmatrix} = \mathbf{0} \quad \text{with} \quad \begin{bmatrix} \mathbf{r}^a_{\boldsymbol{\varphi}} \\ r^a_{\mu} \\ r^a_{p} \\ r^a_{\lambda_1} \\ r^a_{\lambda_2} \end{bmatrix} = \begin{bmatrix} \mathbf{f}^a_{\boldsymbol{\varphi},\text{int}} - \mathbf{f}^a_{\boldsymbol{\varphi},\text{vol}} - \mathbf{f}^a_{\boldsymbol{\varphi},\text{sur}} \\ f^a_{\mu,\text{int}} - f^a_{\mu,\text{sur}} \\ f^a_{p,\text{int}} + \lambda_1^a - \lambda_2^a \\ g_1(p^a, \lambda_1^a) \\ g_2(p^a, \lambda_2^a) \end{bmatrix} . \tag{6.54}
$$

A solution for the global node point A is found if the global residual $\mathbf{r}^A$ vanishes.

The nonlinear coupled system of equations (6.54) can be solved numerically by various solution schemes (see e.g. Geiger and Kanzow [47]). Coupled systems of equations are solved either monolithically or in a staggered scheme, e.g. Simo and Miehe [121]. For the present model a monolithic solution scheme based on Newton-type iteration is applied. For this purpose, the nodal residuals on the element level $\mathbf{r}^a = [\mathbf{r}^a_{\boldsymbol{\varphi}}, r^a_\mu, r^a_p, r^a_{\lambda_1}, r^a_{\lambda_2}]^{\mathrm{T}}$ are linearised with respect to the nodal solution vector $\mathbf{d}^b = [\boldsymbol{\varphi}^b, \mu^b, p^b, \lambda^b_1, \lambda^b_2]^{\mathrm{T}}$ of node point b. The resulting nodal stiffness components can be written as

$$\mathbf{K}^{ab} = \frac{\mathrm{d}\mathbf{r}^a}{\mathrm{d}\mathbf{d}^b} = \begin{bmatrix} \mathbf{K}^{ab}_{\boldsymbol{\varphi}\boldsymbol{\varphi}} & \mathbf{K}^{ab}_{\boldsymbol{\varphi}\mu} & \mathbf{K}^{ab}_{\boldsymbol{\varphi}p} & 0 & 0 \\ \mathbf{K}^{ab}_{\mu\boldsymbol{\varphi}} & K^{ab}_{\mu\mu} & K^{ab}_{\mu p} & 0 & 0 \\ \mathbf{K}^{ab}_{p\boldsymbol{\varphi}} & K^{ab}_{p\mu} & K^{ab}_{pp} & K^{ab}_{p\lambda_1} & K^{ab}_{p\lambda_2} \\ 0 & 0 & K^{ab}_{\lambda_1 p} & K^{ab}_{\lambda_1\lambda_1} & 0 \\ 0 & 0 & K^{ab}_{\lambda_2 p} & 0 & K^{ab}_{\lambda_2\lambda_2} \end{bmatrix} . \tag{6.55}$$

As mentioned in Subsection 6.1.3.2, the consideration of the additional NCP functions yields an unsymmetrical stiffness matrix. Although the upper matrix, referring to the variables $[\boldsymbol{\varphi}^b, \mu^b, p^b]$, is based on a variational principle and is therefore symmetric in nature, the lower matrix shows an unsymmetrical, however, diagonal structure. Here, the interested reader is referred to Subsection 5.4.3, where the stiffness components are derived in Eq. (5.99).

The symmetrical part of the stiffness components are computed in the following. Based on the incremental variational structure and the constitutive relations in Eq. (6.46), the nodal stiffness components are obtained by

$$\begin{aligned}
\mathbf{K}^{ab}_{\boldsymbol{\varphi}\boldsymbol{\varphi}} &= \frac{\mathrm{d}\mathbf{r}^a_{\boldsymbol{\varphi}}}{\mathrm{d}\boldsymbol{\varphi}^b} = \int_{\mathcal{B}^e_0} \nabla N^a \bullet \left[[1-p]\,\frac{\partial^2 \Psi_{\mathrm{B}_1}}{\partial \mathbf{F}_1^2} + p\,\frac{\partial^2 \Psi_{\mathrm{B}_2}}{\partial \mathbf{F}_2^2} \right] \cdot \nabla N^b \,\mathrm{d}V \,, \\
\mathbf{K}^{ab}_{\boldsymbol{\varphi}p} &= \frac{\mathrm{d}\mathbf{r}^a_{\boldsymbol{\varphi}}}{\mathrm{d}p^b} = \int_{\mathcal{B}^e_0} N^b\,[\mathbf{P}_2 - \mathbf{P}_1] \cdot \nabla N^a \,\mathrm{d}V \,, \\
K^{ab}_{\mu\mu} &= \frac{\mathrm{d}r^a_\mu}{\mathrm{d}\mu^b} = \int_{\mathcal{B}^e_0} -\nabla N^a \cdot \frac{\partial^2 \widehat{\phi}}{\partial \nabla\mu^2} \cdot \nabla N^b \,\mathrm{d}V \,, \\
K^{ab}_{\mu p} &= \frac{\mathrm{d}r^a_\mu}{\mathrm{d}p^b} = \int_{\mathcal{B}^e_0} -N^a\,N^b \,\mathrm{d}V \,, \\
K^{ab}_{pp} &= \frac{\mathrm{d}r^a_p}{\mathrm{d}p^b} = \int_{\mathcal{B}^e_0} \left\{ N^a\,\frac{\partial^2 \Psi_\Gamma}{\partial p^2}\,N^b + \nabla N^a \cdot \frac{\partial^2 \Psi_\Gamma}{\partial \nabla p^2} \cdot \nabla N^b \right\} \mathrm{d}V \,,
\end{aligned} \tag{6.56}$$

in which, as noted before, dead-loads are assumed for the present model. The trivial stiffness components are identified as $\mathbf{K}^{ab}_{\boldsymbol{\varphi}\mu} = \mathbf{K}^{ab\,\mathrm{T}}_{\mu\boldsymbol{\varphi}} = \mathbf{0}$. The remaining stiffness components are symmetric and are not presented here.

6.1.4 Numerical example

In this section a numerical test is presented which demonstrates the capabilities of the underlying deformation-diffusion driven phase field model. For this purpose, the evolution of microstructure in a dual-phase material is analysed.

6.1.4.1 Phase field prototype model

The following prototype model is defined by the hyperelastic energies

$$\begin{aligned}\Psi_{\mathrm{B}_1}(\mathbf{F}_1^{\mathrm{e}}) &= \frac{\mu_1}{2}\left[J_1^{\mathrm{e}\,-2/3}\,\mathbf{F}_1^{\mathrm{e}} : \mathbf{F}_1^{\mathrm{e}} - 3\right] + \frac{\kappa_1}{2}\left[\frac{J_1^{\mathrm{e}2}}{2} - \frac{1}{2} - \log J_1^{\mathrm{e}}\right] + \Psi_{\mathrm{B}_1}^0\,,\\ \Psi_{\mathrm{B}_2}(\mathbf{F}_2^{\mathrm{e}}) &= \frac{\mu_2}{2}\left[J_2^{\mathrm{e}\,-2/3}\,\mathbf{F}_2^{\mathrm{e}} : \mathbf{F}_2^{\mathrm{e}} - 3\right] + \frac{\kappa_2}{2}\left[\frac{J_2^{\mathrm{e}2}}{2} - \frac{1}{2} - \log J_2^{\mathrm{e}}\right] + \Psi_{\mathrm{B}_2}^0\,,\end{aligned} \tag{6.57}$$

where each energy term is determined by three material constants. These constants are the shear modulus $\mu_i = 1/2\,\mathrm{E}_i/[1+\nu_i]$ and the bulk modulus $\kappa_i = 1/3\,\mathrm{E}_i/[1-2\,\nu_i]$ which are functions of Youngs modulus E_i and Poisson ratio ν_i. The energy offsets $\Psi_{\mathrm{B}_i}^0$ take account of chemical contributions. However, they are assumed as constants here. The elastic energies in Eq. (6.57) only depend on the elastic deformation gradients $\mathbf{F}_i^{\mathrm{e}} = \mathbf{F}_i \cdot \mathbf{F}_i^{\mathrm{B}-1}$ (cf. Eq. (6.38)). As mentioned before, the elastic properties in the interface are derived by the Taylor/Voigt assumption $\mathbf{F}_1 = \mathbf{F}_2 = \mathbf{F}$. Accordingly, the elastic deformation gradients for phase one and two yield

$$\mathbf{F}_1^{\mathrm{e}} = \mathbf{F} \cdot \mathbf{F}_1^{\mathrm{B}-1} \qquad \mathbf{F}_2^{\mathrm{e}} = \mathbf{F} \cdot \mathbf{F}_2^{\mathrm{B}-1}\,. \tag{6.58}$$

In order to examine the influence of Bain strain pairs $\mathbf{F}_1^{\mathrm{B}}/\mathbf{F}_2^{\mathrm{B}}$ on the microstructure, three different Bain strain pairs are considered in the following. These Bain strain pairs are specified as

- Bain configuration 1: Pure shear connected

$$\mathbf{F}_1^{\mathrm{B}} = \begin{bmatrix}1&0&0\\0&1&0\\0&0&1\end{bmatrix}, \qquad \mathbf{F}_2^{\mathrm{B}} = \begin{bmatrix}1+\alpha&0&0\\0&1-\dfrac{\alpha}{2}&0\\0&0&1-\dfrac{\alpha}{2}\end{bmatrix}, \tag{6.59}$$

  with $\alpha = 0.1$;

- Bain configuration 2: Simple shear connected

$$\mathbf{F}_1^{\mathrm{B}} = \begin{bmatrix}1&0&0\\0&1&0\\0&0&1\end{bmatrix}, \qquad \mathbf{F}_2^{\mathrm{B}} = \begin{bmatrix}1&\alpha&0\\0&1&0\\0&0&1\end{bmatrix}, \tag{6.60}$$

with $\alpha = 0.1$;

- Bain configuration 3: Rank-1 connected

$$\mathbf{F}_1^{\mathrm{B}} = \begin{bmatrix} -\dfrac{[\alpha+\gamma]\,[\alpha^2-4\alpha\gamma+\gamma^2]}{2\,[\alpha^2+\gamma^2]} & -\dfrac{\alpha-\gamma}{2} & 0 \\ \dfrac{[\alpha-\gamma]\,[\alpha^2+4\alpha\gamma+\gamma^2]}{2\,[\alpha^2+\gamma^2]} & \dfrac{\alpha+\gamma}{2} & 0 \\ 0 & 0 & \beta \end{bmatrix}, \; \mathbf{F}_2^{\mathrm{B}} = \begin{bmatrix} \dfrac{\alpha+\gamma}{2} & -\dfrac{\alpha-\gamma}{2} & 0 \\ -\dfrac{\alpha-\gamma}{2} & \dfrac{\alpha+\gamma}{2} & 0 \\ 0 & 0 & \beta \end{bmatrix}. \tag{6.61}$$

with $\alpha = 1.0619$, $\beta = 0.9178$ and $\gamma = 1.0231$ (taken from Hildebrand and Miehe [53]);

It should be emphasised, that Bain configuration 3 satisfies the twinning equation $\mathbf{F}_1^{\mathrm{B}} - \mathbf{F}_2^{\mathrm{B}} = \mathbf{a} \otimes \tilde{\mathbf{N}}$ for the normalised vector $\tilde{\mathbf{N}} = \pm\mathbf{e}_1$, where $\mathbf{e}_1$ is the Cartesian basis vector. Thus, the deformations within the different phases are rank-1 connected and the corresponding interface is denoted as mechanically coherent interface. Further details are given in Hildebrand and Miehe [53].

Next, the interface energy Ψ_Γ and the diffusion potential $\widehat{\phi}$ are specified. As already given in Eq. (5.6) and Eq. (6.23), these are

$$\begin{aligned} \Psi_\Gamma &= \psi_0^\Gamma \left\{ \frac{6}{\varepsilon} p^2 \,[1-p]^2 + \frac{3}{2}\varepsilon \|\nabla p\|^2 \right\}, \\ \widehat{\phi} &= \frac{1}{2}\kappa |\nabla\mu|^2 . \end{aligned} \tag{6.62}$$

The interface energy is determined by the area specific interface energy ψ_0^Γ and the length scale parameter ε which describes the interface thickness. The mobility of the diffusive interface is defined by κ.

The nonlinear system of equations (Eq. (6.54) and Eq. (6.55)) was implemented in a straightforward manner into the parallel version of FEAP Taylor [131]. In addition to a fully three-dimensional model, plane strain conditions were also implemented. The number of unknowns per node is in the general 3D case seven and in the 2D case six. The system of equations is solved monolithically within a Newton-type solution scheme. Based on the unsymmetrical stiffness matrix in Eq. (6.55) a solver for unsymmetric matrices is required. To this end, the direct SuperLU solver of the PETSc library Balay et al. [7] is applied.

6.1.4.2 Influence of Bain strains on the evolution of the microstructure

The following example is related to the evolution of microstructures driven by deformation and diffusion. For this purpose, a 2D quadratic plate with an edge length of

Phase	Name	Symbol	Value	Unit
Phase 1	Youngs modulus	E_1	74000	[MPa]
	Poisson ratio	ν_1	0.34	[-]
	Chemical energy	$\Psi^0_{\mathrm{B}_1}$	0	[MPa]
Phase 2	Youngs modulus	E_2	74000	[MPa]
	Poisson ratio	ν_2	0.34	[-]
	Chemical energy	$\Psi^0_{\mathrm{B}_2}$	0	[MPa]
Interface	Area specific surface energy	ψ^{I}_0	20.0	[N/mm]
	Interface thickness	ε	3.0	[mm]
	Diffusion mobility	κ	10.0	[mm^4/N s]

Table 6.1: Material parameters for the evolution of microstructure based on different Bain strains

$L = 100$ mm and a circular void in its centre with a diameter of $L/3$ is considered. The outer boundary of the body has fixed displacements, i.e. $\bar{\boldsymbol{\varphi}} = \mathbf{0}$ on $\partial\mathcal{B}_{0,\varphi}$. The setup of the test is illustrated in Fig. 6.1. The phase parameter is initialized by

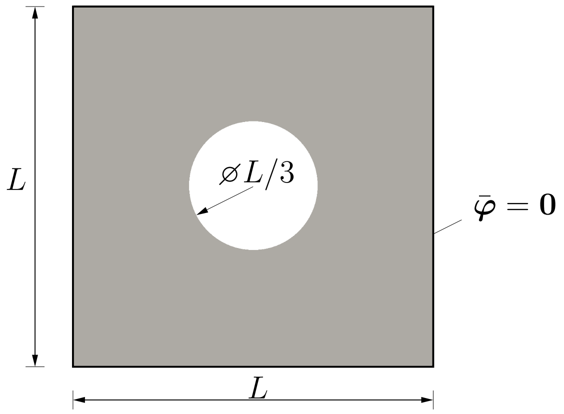

Figure 6.1: Boundary value problem for the analysis of different Bain strains; Edge length $L = 100$ mm

$$\bar{p}_0(\mathbf{X}) = 0.5 \ \ \forall \mathbf{X} \in \mathcal{B}_0 \, . \tag{6.63}$$

Accordingly, 50% of the volume fraction refer to phase one and the other 50% of the volume fraction refer to phase two. Conservation is enforced through the boundary condition (see Eq. (6.37))

$$\bar{H} = 0 \quad \text{on} \quad \partial\mathcal{B}_0 \, . \tag{6.64}$$

The applied material parameters of the two phases are summarised in Tab. 6.1. The elastic constants are identical. However, the mechanical behaviour differs in phase one and two since Bain strain one and Bain strain two are different. In the following, three different Bain strain pairs, as defined in the previous section, are tested. The domain in Fig. 6.1 is discretised with ∼15000 linear 4-noded quadrilateral elements resulting in more than 90000 degrees of freedom. An adaptive time increment refinement is used, in which the time increment starts at $\Delta t = 10^{-6}$ s and increases to $\Delta t = 0.01$ s. The adaptive time update is identical for all simulations.

During the first steps it can be seen that the initial phase distribution is energetically not favourable. The structural inhomogeneity of the plate leads to an inhomogeneous deformation state. Driven by the mechanical deformation field, phase domains are nucleated at the circular hole. Consequently, the energetic relaxation causes the formation of fine microstructure. Subsequently, a re-ordering can be detected in which clusters of either phase one ($p = 0$) or phase two ($p = 1$) develop, leading to a reduction of the interface area.

With respect to the constrained optimisation, the NCP functions are activated in all simulations. The influence of NCP functions leads to the exact fulfilment of the phase constraint. Furthermore, the total amount of phase volume 1 and 2 is conserved during the simulations.

In Fig. 6.2 the evolution of phases and the material distribution, are shown for the three proposed Bain configurations. As expected, the formation of microstructure depends on the considered Bain pairs. Although the boundary value problem is symmetrical, the microstructure does not evolve symmetrically. This can be explained by numerical perturbations during the nucleation process. However, the steady state solutions corresponding to Bain configuration 1 & 2 at t_{end} seem to be symmetrical. Only Bain configuration 3 results in an unsymmetrical microstructure. Figure 6.2 displays also the mechanical transformation behaviour. While for Bain configurations 1 & 3 the deformation of the inner circle increases with time, the final form of the Bain configuration 2 relaxes from a sheared ellipse to the initial circle form. This is due to the fact that phase one (identity Bain strain) surrounds the inner circle.

The evolution of the chemical potential μ is displayed in Fig. 6.3 for the time steps t_1 and t_{end}. High gradients of the chemical potential are initially present for all configurations. Corresponding to the material distribution in Fig. 6.2, the high gradients govern the diffusion process. At time t_{end} the chemical potential is nearly constant throughout the domain for all distributions, which confirms the steady state solution. Only for Bain pair 3 a small gradient still exists.

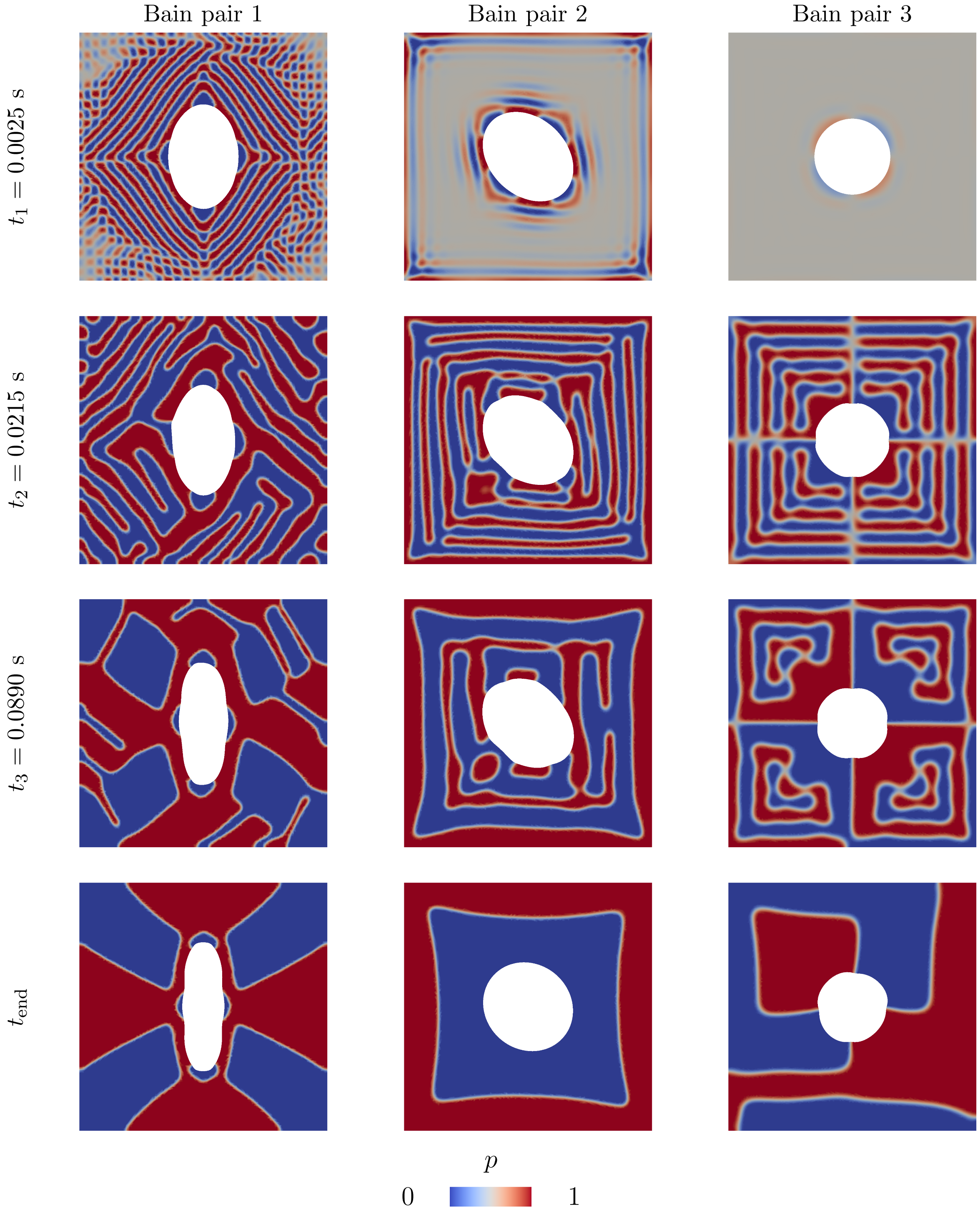

Figure 6.2: Evolution of phase field parameter p for three different Bain strain pairs at four time steps (top down evolution); Bain pair 1 (left column), Bain pair 2 (middle column) and Bain pair 3 (right column) are chosen according to page 151; Plots are shown in the deformed configuration (scale parameter 5×); Steady state solutions at t_{end}: Bain pair 1 $t_{\mathrm{end}} = 0.589$ s, Bain pair 2 $t_{\mathrm{end}} = 2.014$ s, Bain pair 3 $t_{\mathrm{end}} = 6.064$ s

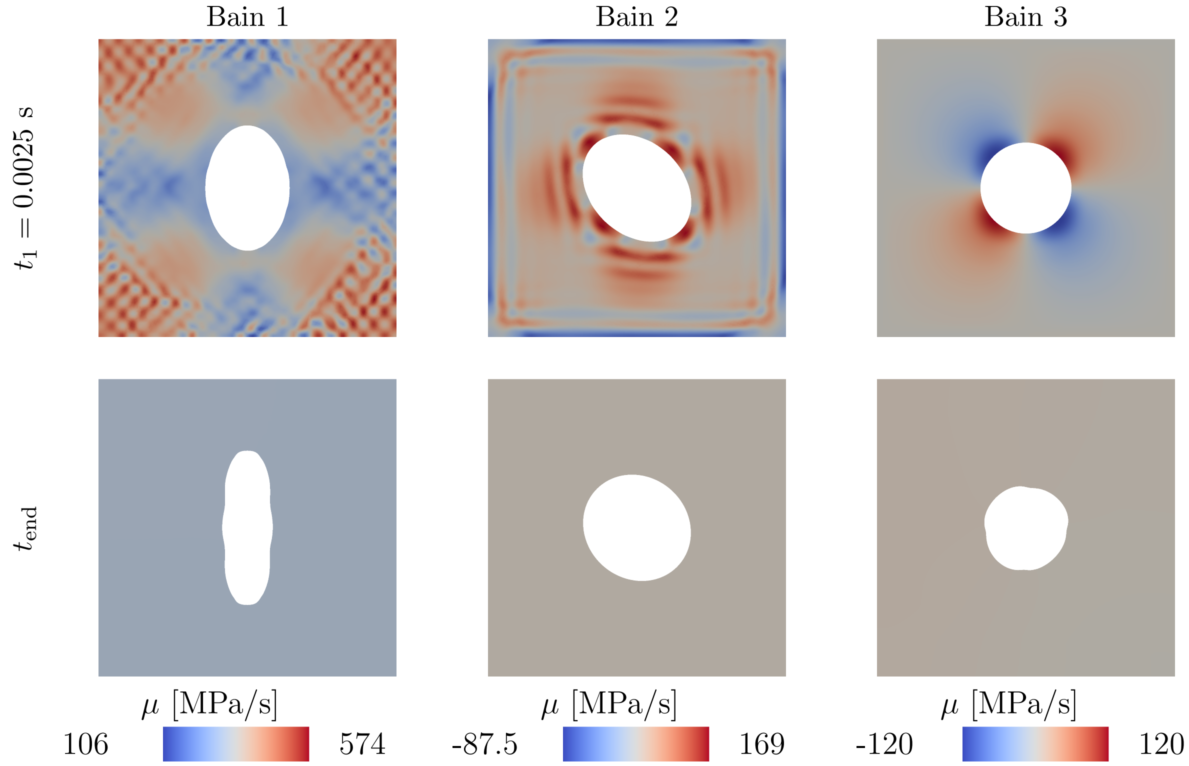

Figure 6.3: Distribution of chemical potential μ for three different Bain strain pairs at two time steps; Bain pair 1 (left column), Bain pair 2 (middle column) and Bain pair 3 (right column) are chosen according to page 151; Plots are shown in the deformed configuration (scale parameter 5×); Steady state solutions at t_{end}: Bain pair 1 $t_{\mathrm{end}} = 0.589$ s, Bain pair 2 $t_{\mathrm{end}} = 2.014$ s, Bain pair 3 $t_{\mathrm{end}} = 6.064$ s

6.2 A Cahn-Hilliard based phase field model for topology optimisation

The Cahn-Hilliard model presented before naturally account for a redistribution of material by simultaneously conserving the total volume. Thus, the framework is also promising for topology optimisation.

In line with Blank et al. [19], Bourdin and Chambolle [22], Dedè et al. [38], Wallin et al. [134] the phase parameter $p \in [0, 1]$ represents the material distribution (topology) of the problem. The phase $p = 1$ characterises the material phase and $p = 0$ denotes the void phase. Intermediate phases $p \in (0, 1)$ are penalized due to the underlying interface energy of Modica and Mortola [87]. In contrast to the classic *solid isotropic material penalisation* ansatz (SIMP), cf. Bendsøe and Sigmund [16], Kotucha [67], a gradient of the phase parameter is included in a natural fashion. As a result of this gradient regularisation mesh-dependencies in finite element schemes are avoided.

The re-arrangement of material is driven by the gradient of the chemical potential. However, the underlying balance of chemical micro forces is coupled to the balance of linear momentum. Therefore, the material distribution is also driven by the elastic material behaviour. Following the publication of Wallin et al. [134], the optimization procedure is governed by an objective functional. This objective functional consists of bulk energy, interface energy and mass diffusion potential. The optimisation of this objective functional is subjected to the balance of linear momentum and traction continuity. For this purpose, all constraints are incorporated by using Lagrangian multipliers. Hence, all governing equations follow jointly from the stationary conditions. As mentioned before, the conservation of volume is naturally embedded in the underlying Cahn-Hilliard-type phase field theory.

Furthermore, the resulting system of equations is subjected to the admissible phase range $p \in [0, 1]$. Different strategies for guaranteeing this constraint can be found in the literature, see e.g. Kotucha [67], Wallin and Ristinmaa [133], Wallin et al. [134]. In the present section, the robust NCP functions of Fischer-Burmeister are applied again for the exact fulfilment of this constraint. Surprisingly, the final system of governing equations shows a strong similarity to the derived equations of the previous section.

This section is structured as follows: After an introduction to structural topology optimisation within a geometrically linearised theory in Subsection 6.2.1, a model for topology optimisation is derived in Subsection 6.2.2 based on a Cahn-Hilliard-type phase field theory. The capability and robustness of the governing formulation is demonstrated in Subsection 6.2.3.

6.2.1 Structural topology optimisation

The problem which is addressed in topology optimisation is associated with the distribution of material in the design space $\mathcal{B}_0$. For the distribution of material, the design parameter $p \in [0,1]$ is introduced, where $p = 0$ determines void and $p = 1$ determines full material. In order to compare the optimal design, an objective functional is defined and subjected to certain constraints. In the following, the stored energy

$$\int_{\mathcal{B}_0} \Psi_{\mathrm{B}}(\boldsymbol{\varepsilon}, p)\,\mathrm{d}V \tag{6.65}$$

is chosen as the objective function. According to Kotucha [67] the minimisation of Eq. (6.65) is equivalent to the maximisation of structure stiffness for linearised elasticity theory. Here, $\boldsymbol{\varepsilon}$ denotes the linearised Green-Lagrange strain tensor $\mathbf{E} = 1/2\,[\mathbf{C} - \mathbf{I}]$. Similar to the homogenisation of bulk energies in dual-phases, the bulk energy of a material point is assumed as

$$\Psi_{\mathrm{B}} = [1-p]\,\Psi_{\mathrm{B}_1} + p\,\Psi_{\mathrm{B}_2}\,, \tag{6.66}$$

in which every phase energy is defined as $\Psi_{\mathrm{B}_i} = 1/2\,\boldsymbol{\varepsilon}_i : \mathbb{C}_i : \boldsymbol{\varepsilon}_i$. Here, the fourth-order tensor $\mathbb{C}_i$ denotes the elastic stiffness. Assuming a homogenisation of Taylor/Voigt, i.e. $\boldsymbol{\varepsilon} = \nabla\mathbf{u} = \boldsymbol{\varepsilon}_1 = \boldsymbol{\varepsilon}_2$, the averaged strain tensor is identical in every phase. Since phase one is associated with the void phase $\Psi_{\mathrm{B}_1} = 0$. Thus, the bulk energy reduces to

$$\Psi_{\mathrm{B}} = p\,\Psi_{\mathrm{B}_2} = p\,\frac{1}{2}\,\boldsymbol{\varepsilon} : \mathbb{C} : \boldsymbol{\varepsilon}\,. \tag{6.67}$$

Accordingly, the local Cauchy stress yields $\boldsymbol{\sigma} = p\,\mathbb{C} : \boldsymbol{\varepsilon}$. The determination of the design parameter is subjected to the balance of linear momentum, stress continuity and the preservation of material volume. Therefore, the summarised constrained optimisation problem reads

$$\inf_{p} \int_{\mathcal{B}_0} \Psi_{\mathrm{B}}(\boldsymbol{\varepsilon}, p)\,\mathrm{d}V \qquad \text{subject to:} \qquad \begin{aligned} \mathrm{div}\boldsymbol{\sigma} + \rho_0\,\mathbf{b} = \mathbf{0} \quad &\text{on} \quad \mathcal{B}_0\,, \\ \boldsymbol{\sigma}\cdot\mathbf{n} = \bar{\mathbf{t}} \quad &\text{on} \quad \partial\mathcal{B}_0\,, \\ \int_{\mathcal{B}_0} p(\mathbf{x})\,\mathrm{d}V = V_0\,. & \end{aligned} \tag{6.68}$$

Here, V_0 represents the total volume of material phase. The solution of problem (6.68) provides the distribution of the material phase, i.e. the topology. However, the numerical optimisation of this problem becomes challenging if only the integer values $p = 0$ or $p = 1$ are allowed. To overcome this, intermediate values, i.e. $p \in [0, 1]$, are permitted. However, this leads to an undesired smearing of phases. For this purpose, different regularisation approaches have been developed in the past. A frequently applied approach is based on the SIMP ansatz (solid isotropic material penalisation), see Bendsøe and Sigmund [16], Kotucha [67] for further details. However, models based on the SIMP ansatz are not uniquely defined which leads to mesh dependencies in finite element schemes (see also Kotucha [67]). By introducing a gradient of the design parameter, this mesh dependency can be avoided, cf Sigmund and Petersson [115]. An alternative approach for the regularisation of intermediate phases is addressed in Wallin et al. [134]. It is based on the extension of the objective functional with an additional interface energy. This interface energy is related to the phase field theory as advocated in Section 5.1. The proposed model in Wallin et al. [134] is also applied in the rest of this section.

6.2.2 Regularised topology optimisation based on Cahn-Hilliard-type phase field modelling

The objective functional (6.68) is now extended by the classic sharp interface approximation of Modica and Mortola [87] as introduced in Section 5.1. Based on this interface energy, the minima of the material distribution corresponds to the void phase ($p = 0$) and the material phase ($p = 1$). Intermediate phases $p \in (0, 1)$ are penalised. Moreover, the total amount of material conservation as required in Eq. $(6.68)_3$ is directly incorporated into the objective functional by using the Cahn-Hilliard-type potential (6.29). Following the approach in Eq. (6.29) together with the boundary condition $\nabla\mu \cdot \mathbf{n} = 0$, the rate form of the objective potential reads

$$\dot{\widehat{\Phi}} = \int\limits_{\mathcal{B}_0} \Big\{ \dot{\Psi}_{\mathrm{B}}(\boldsymbol{\varepsilon}, p) + \dot{\Psi}_{\Gamma}(p, \nabla p) - \mu\, \dot{p} - \widehat{\phi}(\nabla\mu) \Big\} \,\mathrm{d}V\,, \tag{6.69}$$

where Ψ_Γ again represents the interface energy of Modica and Mortola [87] and where $\widehat{\phi}$ again denotes the mass-diffusion potential. Focussing on the numerical implementation, the time-continuous potential is transferred into a time-discrete potential. Integration of Eq. (6.69) over time interval $\tau \in [t_n, t_{n+1}]$ leads to

$$\Delta\widehat{\Phi} = \int\limits_{t_n}^{t_{n+1}} \dot{\widehat{\Phi}}\,\mathrm{d}t = \int\limits_{\mathcal{B}_0} \Big\{ \Psi_{\mathrm{B}} - \Psi_{\mathrm{B}}|_n + \Psi_\Gamma - \Psi_\Gamma|_n - \mu\,[p - p_n] - \Delta t\, \widehat{\phi}(\nabla\mu) \Big\} \,\mathrm{d}V\,. \tag{6.70}$$

For the sake of simplicity, the time index $(\bullet)_{n+1}$ denoting the values and functions at current time t_{n+1} is omitted here. Values and functions corresponding to the previous time t_n are indicated by the index $(\bullet)_n$. The time increment is denoted by $\Delta t = t_{n+1} - t_n$.

By using the incremental functional (6.70) the optimisation problem in Eq. (6.68) reduces to

$$\inf_p \sup_\mu \Delta\widehat{\Phi} \qquad \text{subject to:} \qquad \begin{aligned} \operatorname{div}\boldsymbol{\sigma} + \rho_0\,\mathbf{b} = \mathbf{0} \quad &\text{on} \quad \mathcal{B}_0\,, \\ \boldsymbol{\sigma}\cdot\mathbf{n} = \bar{\mathbf{t}} \quad &\text{on} \quad \partial\mathcal{B}_0\,, \end{aligned} \tag{6.71}$$

where the objective potential is still subjected to balance of linear momentum and stress continuity. In order to take account of these constraints, the Lagrangian multipliers $\boldsymbol{\lambda}^{\mathrm{e}}$ and $\boldsymbol{\lambda}^{\mathrm{t}}$ are introduced. The extended functional for the underlying design space yields

$$\Delta\widehat{\Phi}^{\mathrm{ext}} = \Delta\widehat{\Phi} + \int\limits_{\mathcal{B}_0} \boldsymbol{\lambda}^{\mathrm{e}}\cdot[\operatorname{div}\boldsymbol{\sigma} + \rho_0\,\mathbf{b}]\;\mathrm{d}V + \int\limits_{\partial\mathcal{B}_0} \boldsymbol{\lambda}^{\mathrm{t}}\cdot[\boldsymbol{\sigma}\cdot\mathbf{n} - \bar{\mathbf{t}}]\;\mathrm{d}A\,. \tag{6.72}$$

Consequently, the objective functional in Eq. (6.72) depends on the displacement field $\mathbf{u}$, phase parameter p, the chemical potential μ and the Lagrangian parameters $\boldsymbol{\lambda}^{\mathrm{e}}$ and $\boldsymbol{\lambda}^{\mathrm{t}}$. To solve optimisation problem (6.72) the stationarity condition

$$\delta\,\Delta\widehat{\Phi}^{\mathrm{ext}} = 0 \tag{6.73}$$

is derived with respect to all unknowns. According to Eq. (6.73) the necessary conditions

$$\begin{aligned}
\delta_{\mathbf{u}}\Delta\widehat{\Phi}^{\mathrm{ext}} &= \int\limits_{\mathcal{B}_0} \left[\frac{\partial\Psi_{\mathrm{B}}}{\partial\boldsymbol{\varepsilon}} - \nabla\boldsymbol{\lambda}^{\mathrm{e}} : \frac{\partial\boldsymbol{\sigma}}{\partial\boldsymbol{\varepsilon}}\right] : \delta\boldsymbol{\varepsilon}\,\mathrm{d}V \\
&\quad + \int\limits_{\partial\mathcal{B}_0} \left[\boldsymbol{\lambda}^{\mathrm{e}} + \boldsymbol{\lambda}^{\mathrm{t}}\right]\cdot\left[\mathbf{n}\cdot\frac{\partial\boldsymbol{\sigma}}{\partial\boldsymbol{\varepsilon}}\right] : \delta\boldsymbol{\varepsilon}\,\mathrm{d}A = 0\,, \\
\delta_p\Delta\widehat{\Phi}^{\mathrm{ext}} &= \int\limits_{\mathcal{B}_0} \left\{\left[\frac{\partial\Psi_{\mathrm{B}}}{\partial p} + \frac{\partial\Psi_\Gamma}{\partial p} - \mu - \nabla\boldsymbol{\lambda}^{\mathrm{e}} : \frac{\partial\boldsymbol{\sigma}}{\partial p}\right]\delta p + \frac{\partial\Psi_\Gamma}{\partial\nabla p}\cdot\nabla\delta p\right\}\,\mathrm{d}V \\
&\quad + \int\limits_{\partial\mathcal{B}_0} \left[\boldsymbol{\lambda}^{\mathrm{e}} + \boldsymbol{\lambda}^{\mathrm{t}}\right]\cdot\left[\mathbf{n}\cdot\frac{\partial\boldsymbol{\sigma}}{\partial p}\right]\,\delta p\,\mathrm{d}A = 0\,, \qquad (6.74) \\
\delta_\mu\Delta\widehat{\Phi}^{\mathrm{ext}} &= \int\limits_{\mathcal{B}_0} \left\{-[p - p_n]\,\delta\mu - \Delta t\,\frac{\partial\widehat{\phi}}{\partial\nabla\mu}\cdot\nabla\delta\mu\right\}\,\mathrm{d}V = 0\,, \\
\delta_{\boldsymbol{\lambda}^{\mathrm{e}}}\Delta\widehat{\Phi}^{\mathrm{ext}} &= \int\limits_{\mathcal{B}_0} [\operatorname{div}\boldsymbol{\sigma} + \rho_0\,\mathbf{b}]\cdot\delta\boldsymbol{\lambda}^{\mathrm{e}}\,\mathrm{d}V = 0\,,
\end{aligned}$$

$$\delta_{\boldsymbol{\lambda}^{\mathrm{t}}}\Delta\widehat{\Phi}^{\mathrm{ext}} = \int\limits_{\partial\mathcal{B}_0} [\boldsymbol{\sigma}\cdot\mathbf{n} - \bar{\mathbf{t}}]\cdot\delta\boldsymbol{\lambda}^{\mathrm{t}}\,\mathrm{d}A = 0$$

are required. From Eq. $(6.74)_1$ it can be concluded that the bracket expressions for arbitrary $\delta\boldsymbol{\varepsilon}$ need to vanish, i.e.

$$\begin{aligned} \frac{\partial\Psi_{\mathrm{B}}}{\partial\boldsymbol{\varepsilon}} - \nabla\boldsymbol{\lambda}^{\mathrm{e}} : \frac{\partial\boldsymbol{\sigma}}{\partial\boldsymbol{\varepsilon}} = \mathbf{0} \quad &\text{on} \quad \mathcal{B}_0\,, \\ \boldsymbol{\lambda}^{\mathrm{e}} + \boldsymbol{\lambda}^{\mathrm{t}} = \mathbf{0} \quad &\text{on} \quad \partial\mathcal{B}_0\,. \end{aligned} \tag{6.75}$$

By using Eq. (6.67) and $\boldsymbol{\sigma} = p\,\mathbb{C} : \boldsymbol{\varepsilon}$, Eq. $(6.75)_1$ leads to the requirement

$$\nabla\boldsymbol{\lambda}^{\mathrm{e}} = \boldsymbol{\varepsilon}\,. \tag{6.76}$$

Based on this relation and definition $\nabla\boldsymbol{\lambda}^{\mathrm{e}} : \partial_p\boldsymbol{\sigma} = 2\,\Psi_{\mathrm{B}_2}$, the governing equation for the phase parameter is derived from Eq. $(6.74)_2$. Considering Gauss theorem and the homogeneous Neumann boundary $\boldsymbol{\xi}\cdot\mathbf{n} = \partial_{\nabla p}\Psi_\Gamma\cdot\mathbf{n} = 0$, leads to

$$\begin{aligned} \frac{\partial\Psi_{\mathrm{B}}}{\partial p} + \frac{\partial\Psi_\Gamma}{\partial p} - \mu - \nabla\boldsymbol{\lambda}^{\mathrm{e}} : \frac{\partial\boldsymbol{\sigma}}{\partial p} - \operatorname{div}\left(\frac{\partial\Psi_\Gamma}{\partial\nabla p}\right) &= \\ -\Psi_{\mathrm{B}_2} + \frac{\partial\Psi_\Gamma}{\partial p} - \mu - \operatorname{div}\left(\frac{\partial\Psi_\Gamma}{\partial\nabla p}\right) &= \\ -\pi - \operatorname{div}\boldsymbol{\xi} = 0 \quad \text{on} \quad \mathcal{B}_0\,,& \end{aligned} \tag{6.77}$$

in which the constitutive relations $\pi = \mu + \Psi_{\mathrm{B}_2} - \partial_p\Psi_\Gamma$ and $\boldsymbol{\xi} = \partial_{\nabla p}\Psi_\Gamma$ are substituted. Thus, Eq. $(6.74)_2$ is equivalent to the weak form of micro force balance as derived in Eq. (6.4). The second term in Eq. $(6.74)_2$ vanishes due to the condition $(6.75)_2$. Furthermore, variation $(6.74)_3$ corresponds to the time integrated weak form of the chemical force balance (6.5) under consideration of the boundary condition $\Delta\mathbf{h}\cdot\mathbf{n} = 0$. In order to prove this, Gauss theorem is applied to variation $(6.74)_3$ leading to the requirement

$$\begin{aligned} -[p - p_n] + \operatorname{div}\left(\Delta t\,\frac{\partial\widehat{\phi}}{\partial\nabla\mu}\right) &= \\ -[p - p_n] - \operatorname{div}\Delta\mathbf{h} = 0 \quad \text{on} \quad \mathcal{B}_0\,,& \end{aligned} \tag{6.78}$$

where the constitutive flux $\Delta\mathbf{h} = -\Delta t\,\partial_{\nabla\mu}\widehat{\phi}$ is inserted. Furthermore, the variations in Eq. $(6.74)_4$ and Eq. $(6.74)_5$ imply equilibrium and traction force continuity on the boundary, i.e.

$$\begin{aligned} \operatorname{div}\boldsymbol{\sigma} + \rho_0\,\mathbf{b} = \mathbf{0} \quad &\text{on} \quad \mathcal{B}_0\,, \\ \boldsymbol{\sigma}\cdot\mathbf{n} = \bar{\mathbf{t}} \quad &\text{on} \quad \partial\mathcal{B}_0\,. \end{aligned} \tag{6.79}$$

It should be emphasised that the objective functional in Eq. (6.72) does not represent a variational structure. Although the three governing equations, equilibrium, balance of micro forces and balance of chemical forces, result from the stationarity condition of Eq. (6.72), the Hessian of the coupled system (6.77)-(6.77) does not show a symmetric structure. However, exceptions may be constructed (see Remark 6.2.1).

Remark 6.2.1: *Phase field models for topology optimisation generally show no variational structure. However, for the presented model a rate potential of the form*

$$\dot{\mathcal{I}} = \int_{\mathcal{B}_0} \left\{ \dot{\Psi}_\Gamma - \dot{\Psi}_\mathrm{B} - \mu\, \dot{p} - \widehat{\phi} \right\} \mathrm{d}V + \mathcal{P}_\mathbf{F}(\dot{\mathbf{u}}) \tag{6.80}$$

can be constructed. Evidently, all presented Euler-Lagrange equations in Eq. (6.74) *are stationary conditions associated with Eq.* (6.80) *(see also Eq.* (6.82)*).*

With respect to the numerical implementation, the optimisation is subject to admissible phases $p \in [0,1]$. In order to remain in the interval, several techniques are known in the context of phase field theory. For instance, in Wallin et al. [134] a cut-off function for the phase separation and a residual interpolation function are suggested to guarantee the constraint $p \in [0,1]$. Although states outside this range are highly penalised, the authors in Wallin et al. [134] obtained non admissible values in their numerical examples. Thus, an alternative method is necessary for the aforementioned constraint. In the following, a robust and exact optimisation based on the proposed NCP-functions in Subsection 5.4.2 is elaborated. Similarly to Subsection 6.1.3.2, the incorporation of the inequality constraints $r_1 = p - 1 \leq 0$ and $r_2 = -p \leq 0$ leads to the Lagrangian functional

$$\Delta\overset{\sim}{\widehat{\Phi}}^{\mathrm{ext}} = \Delta\widehat{\Phi} + \int_{\mathcal{B}_0} \boldsymbol{\lambda}^\mathrm{e} \cdot [\mathrm{div}\boldsymbol{\sigma} + \rho_0\, \mathbf{b}]\ \mathrm{d}V + \int_{\partial\mathcal{B}_0} \boldsymbol{\lambda}^\mathrm{t} \cdot [\boldsymbol{\sigma} \cdot \mathbf{n} - \bar{\mathbf{t}}]\ \mathrm{d}A + r_1\,\lambda_1 + r_2\,\lambda_2\,. \tag{6.81}$$

The stationarity conditions corresponding to Eq. (6.81) are given by

$$\begin{bmatrix} \int_{\mathcal{B}_0} -\boldsymbol{\sigma} : \delta\boldsymbol{\varepsilon}\,\mathrm{d}V + \int_{\mathcal{B}_0} \rho_0\,\mathbf{b}\cdot\delta\mathbf{u}\,\mathrm{d}V + \int_{\partial\mathcal{B}_0} \bar{\mathbf{t}}\cdot\delta\mathbf{u}\,\mathrm{d}A \\ \int_{\mathcal{B}_0} \{-[p - p_n]\,\delta\mu + \Delta\mathbf{h}\cdot\nabla\delta\mu\}\ \mathrm{d}V \\ \int_{\mathcal{B}_0} \{[-\Psi_{\mathrm{B}_2} + \partial_p\Psi_\Gamma - \mu]\ \delta p + \boldsymbol{\xi}\cdot\nabla\delta p\}\ \mathrm{d}V + \lambda_1\,\delta p - \lambda_2\,\delta p \\ \sqrt{[p - 1 + \varepsilon_1]^2 + \lambda_1^2} + [p - 1 + \varepsilon_1] - \lambda_1 \\ \sqrt{[-p + \varepsilon_2]^2 + \lambda_2^2} + [-p + \varepsilon_2] - \lambda_2 \end{bmatrix} = \mathbf{0} \quad \text{on} \quad \mathcal{B}_0. \tag{6.82}$$

For numerical stability, the slightly adjusted NCP functions (see Remark 5.4.2) with $\varepsilon_\mathrm{tol} = 0$ are suggested. By choosing the perturbations $\varepsilon_1 = 0$ and $\varepsilon_2 = 10^{-3}$ the admissible interval $p \in [0,1]$ moves to interior points, so that a small residual stiffness remains in the void phase and no singularity occurs. The nonlinear system of equations is spatially discretised by means of finite elements and is solved by employing a monolithic Newton-type solution scheme. For the consistent finite element implementation the interested reader is referred to Subsection 6.1.3.3. The comparison of the residuals in Eq. (6.48) (for the Cahn-Hilliard-type phase field model) and in Eq. (6.82) shows a similar structure. Only the residual of the phase parameter differs.

Remark 6.2.2: *Within the presented formulation several model parameters are applied, which are purely related to the numerical stability within topology optimisation based on phase field. These parameter are the area specific interface energy* ψ_0^Γ *and the interface thickness* ε.

6.2.3 Numerical example

The capability of the presented topology optimisation is demonstrated in the following example.

As starting point the constitutive assumptions are defined. For that purpose, the elastic energy, the surface energy and the dissipation potential due to diffusion are chosen. Since the void phase requires no energy, only the material phase (phase two) is specified. It reads

$$\Psi_{\mathrm{B}_2} = \frac{1}{2}\boldsymbol{\varepsilon} : \mathbb{C}_2 : \boldsymbol{\varepsilon} \qquad \text{with} \qquad \mathbb{C}_2 = \mathbb{C} = \bar{\mu}\,[\mathbf{I}\overline{\otimes}\mathbf{I} + \mathbf{I}\underline{\otimes}\mathbf{I}] + \bar{\lambda}\,\mathbf{I}\otimes\mathbf{I}\,. \tag{6.83}$$

The Lamé constants $\bar{\mu} = 1/2\,E/[1+\nu]$ and $\bar{\lambda} = E\nu/[1+\nu]/[1-2\nu]$ are expressed by means of Youngs modulus E and Poissons ratio ν. As mentioned before, the interface energy Ψ_Γ and the dissipation potenial $\widehat{\phi}$ are taken from Eq. (5.6) and Eq. (6.23), i.e.

$$\begin{aligned} \Psi_\Gamma &= \psi_0^\Gamma \left\{ \frac{6}{\varepsilon} p^2\,[1-p]^2 + \frac{3}{2}\varepsilon \|\nabla p\|^2 \right\}\,, \\ \widehat{\phi} &= \frac{1}{2}\kappa |\nabla \mu|^2\,. \end{aligned} \tag{6.84}$$

The area specific interface energy ψ_0^Γ and the length parameter ε are interpreted as purely numerical parameters. The same interpretation also holds for the diffusive mobility of phases described by κ. All used model parameters are given in Tab. 6.2.

The optimal design of a 2D rectangular structure with the dimensions 6×1 mm^2 subjected to a point load is studied next. The setup of the boundary value problem is illustrated in Fig. 6.4. The structure is initialised by a constant phase distribution $p_0(\mathbf{x}) = 0.5\ \forall \mathbf{x}\ \in \mathcal{B}_0$. Accordingly, 50% of the volume belongs to material. In order to prevent the material to locate at the design space boundary $\partial R_p = \partial \mathcal{B}_0$, which can be observed in Blank et al. [19], Wallin and Ristinmaa [133], Wallin et al. [134], an

Phase	Name	Symbol	Value	Unit
Phase 1	Void	–	–	–
Phase 2	Youngs modulus	E_2	74000	[MPa]
	Poisson ratio	ν_2	0.33	[-]
Interface	Area specific surface energy	ψ_0^Γ	0.3	[N/mm]
	Interface thickness	ε	1/64	[mm]
	Diffusion mobility	κ	0.05	[mm^4/N s]

Table 6.2: Model parameters for topology optimisation based on phase field

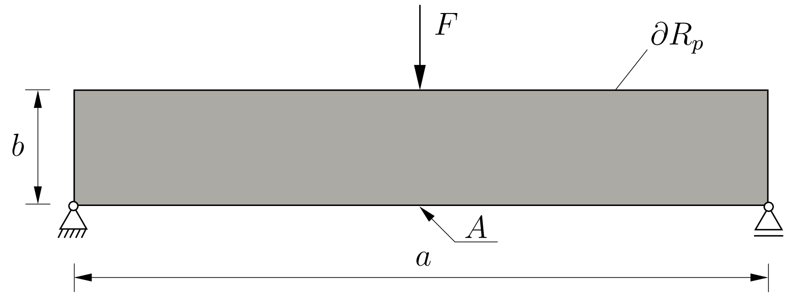

Figure 6.4: Setup of the boundary value problem applied to topology optimisation. Point load $F =$ 100 N; Dimension $a \times b = 6 \times 1$ mm^2

additional boundary integral as proposed in Wallin and Ristinmaa [133] is introduced. Based on the weak Robin-type boundary

$$\gamma \int\limits_{\partial R_p} p\,\delta p\,\mathrm{d}A\,, \tag{6.85}$$

an additional surface element is applied along the boundary ∂R_p. Based on this surface element, the phases $p \in (0, 1]$ are penalised along ∂R_p. As a result, only the void phase can be located along these boundaries. Parameter $\gamma = 10000$ N/mm^2 controls the penalisation of phases along ∂R_p.

With respect to the finite element discretisation, the structure is discretised into 384×64 quadrilateral 4 noded elements with bi-linear shape functions (cf. Subsection 6.1.4). Consequently, the characteristic element length is $h = 1/64$ mm. During the simulation, the mesh grid is not refined and all material parameters in Tab. 6.2 remain constant. In contrast, in Wallin and Ristinmaa [133], Wallin et al. [134] an adaptive mesh refinement strategy is applied and the length scale parameter ϵ is decreased during the simulation. In the present simulation, only the time increment is adaptively updated (cf. Blank et al. [19]). Beginning with time increment $\Delta t = 5 \cdot 10^{-6}$ s, the increment is increased during the simulation to $\Delta t = 2 \cdot 10^{-4}$ s. The simulation is stopped after 9800 time steps at $t = 1.275$ s.

The nonlinear system of equations has ~150000 degrees of freedom and is solved in the parallel version of FEAP, see Taylor [131]. In order to reduce the computation time, the domain is resolved into 8 parts. Due to the unsymmetrical stiffness matrix, the direct SuperLU solver of PETSc library (Balay et al. [7]) is utilised. The relative convergence criteria are $|\Delta \mathbf{d}^{\mathrm{T}} \cdot \mathbf{r}| \leq 10^{-20}\, |\Delta \mathbf{d}^{\mathrm{T}} \cdot \mathbf{r}|_{\mathrm{initial}}$ and $\|\mathbf{r}\| \leq 10^{-8}\, \|\mathbf{r}\|_{\mathrm{initial}}$ according to the description on page 132.

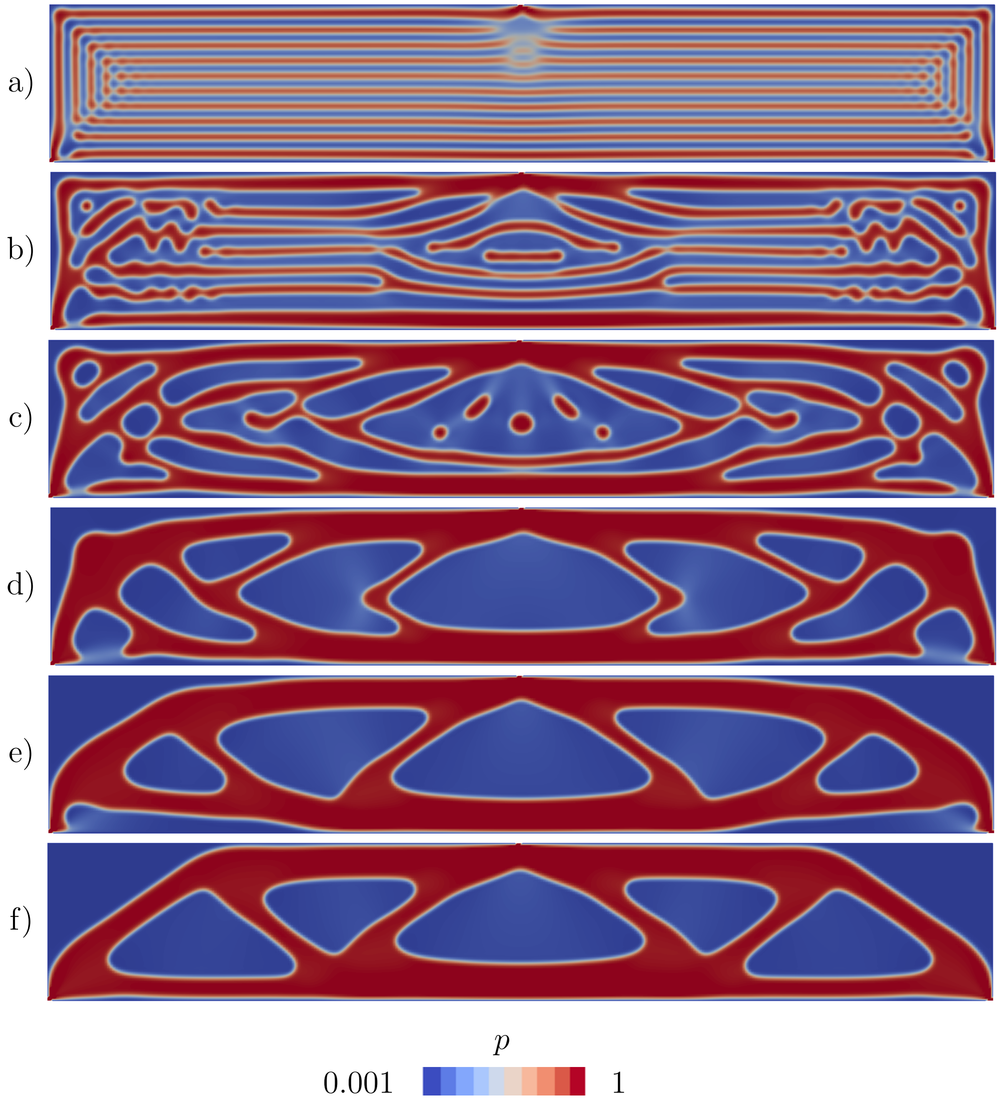

Figure 6.5: Re-distribution of design parameter p for different time steps. Colour range from void phase (blue) to material phase (red). Formation of structure starting from a) $t = 0.001$ s over b) $t = 0.005$ s, c) $t = 0.015$ s, d) $t = 0.060$ s, e) $t = 0.315$ s and finally to the truss-like structure in f) $t = 1.275$ s.

In Fig. 6.5a)-f) the evolution of the design parameter is shown. The colour scale is defined from blue to red, with the range $p \in [0.001, 1]$. The lower range bound is the result of the adjusted NCP functions, given in Eq. $(6.82)_5$. As a result of the

NCP functions, values beyond the range $p \in [0.001, 1]$ are not obtained. In Fig. 6.5a)-f) it can be seen that, within the first time steps, fine laminates are formed due to the Cahn-Hilliard based phase segregation, known as spinodal decomposition. Subsequently, a coarsening of laminates to larger domains is observed. At the final stage at time $t = 1.275$ s a classic truss-like structure is obtained.

A similar result was also obtained in Kotucha [67]. However, in Kotucha [67] the length scale parameter is adaptively reduced during the simulation, which results in a finer interface thickness. In contrast to the results in Kotucha [67] no material is located at the design boundary ∂R_p as can be seen in Fig. 6.5.

The total amount of material is conserved, such that the volume averaged phase parameter remains at $\bar{p} = 0.5$ during the complete simulation. It can be observed that the material phase is distributed according to the maximum principle stresses of the original problem dedicated in Fig. 6.4. This leads to an increase of the stiffness or equivalently to the reduction of structural compliance. As a result of the increased stiffness, the bending of the structure in Fig. 6.6 is reduced during the optimisation. Regarding the distribution of the chemical potential, at time $t = 1.275$ s a nearly constant distribution μ is observed in the design space similar to the example in Subsection 6.1.4.2. Hence, a steady state solution can be assumed for this state, cf. Remark 6.1.1.

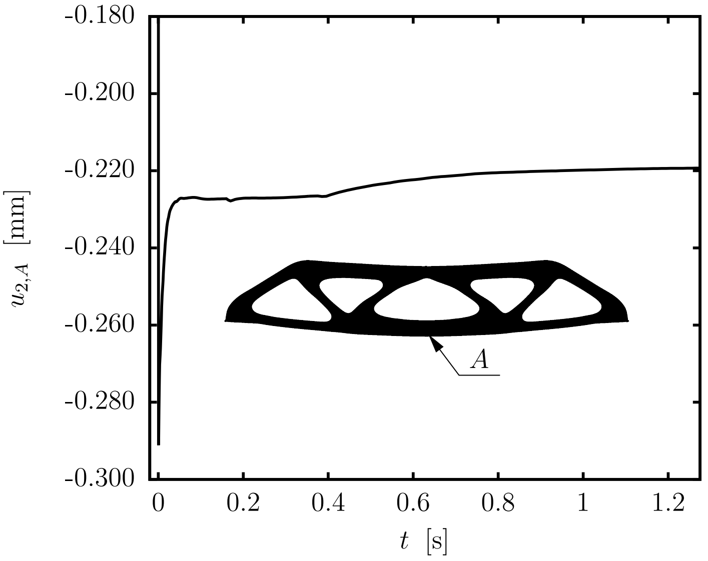

Figure 6.6: Vertical displacement $u_2(t)$ of node A plotted over the time.

7 Conclusion and outlook

7.1 Concluding remarks

7.1.1 Macroscopic models accounting for the evolution of microstructures

The modelling of anisotropic/distortional hardening within a thermomechanically coupled setting was the focus of Chapter 3 and Chapter 4. The presented model is one of the two main contributions within this thesis. A straightforward thermodynamically consistent implementation usually leads to an over-prediction of the temperatures, and a thermomechanical coupling based on a Taylor-Quinney approach can lead to thermodynamical inconsistencies. Consequently, a novel model has been developed in Chapter 3 which is thermodynamically consistent and predicts the temperatures realistically. It has been shown that this realistic temperature prediction is equivalent to a correct definition of stored and dissipative energy parts of the Helmholtz energy. Alternatively, the temperature prediction can be improved by consideration of a pre-loaded history of the continuum. The description of anisotropic texture evolution by means of yield surface distortion was discussed in Chapter 4. The advocated model was based on a generalised distortional hardening model and accounted for dynamic and latent hardening. The novel model also featured a higher curvature of the yield surface in loading direction compared to the reverse direction. Furthermore, the model was thermodynamically consistent and was embedded into the aforementioned novel thermomechanically coupled framework. In order to resolve complex boundary value problems efficiently, a fully implicit return-mapping scheme has been applied for the fourth-order evolution equations driving dynamic and latent hardening. By elaborating a suitable representation of the exponential time integration, the complexity of the updating scheme has significantly been reduced, and the final plasticity model incorporating isotropic, kinematic and distortional hardening has the same number of algebraic equations as a plasticity model for purely isotropic hardening. The resulting system of equations was solved fully implicitly in a thermomechanically coupled finite element scheme. Several examples demonstrated the good predictive capabilities which are necessary to simulate the macroscale, most relevant for technological applications.

7.1.2 Explicit modelling of evolving microstructures by means of phase field theories

The second main part of this thesis was presented in Chapter 5 and Chapter 6. Both chapters dealt with the modelling of evolving microstructures by means of novel phase field theories. First, an Allen-Cahn-type phase field theory coupled to continuum mechanics at finite strain was derived in Chapter 5. It has been shown that the bulk material response in the diffuse interface can be computed by different homogenisation assumptions. The presented homogenisation theories were the state-of-the-art approaches: Taylor/Voigt and Reuss/Sachs as well as novel homogenisation assumptions based on a rank-1 connection in the interface. The novel homogenisation approaches include the partial rank-1 homogenisation advocated in Mosler et al. [92] as well as a novel full rank-1 homogenisation. In order to compare the different approaches, the framework of incremental energy minimisation was adopted where the different homogenisation assumptions were shown to be minimisers of an underlying potential. By using a suitable time discretisation of the aforementioned (rate) potential, an efficient numerical implementation was derived. However, the resulting algebraic system of equations could not be solved by means of an unconstrained algorithm, since the phase parameter did not naturally fulfil constraint $p \in [0, 1]$. In order to fulfil the respective constraint, Fischer-Burmeister NCP equations were applied. Several numerical experiments demonstrated the efficiency and the robustness of the proposed numerical framework. In addition, the performance of the proposed homogenisation assumptions was analysed. It has been shown that the evolution of microstructures does indeed depend on the homogenisation assumption. However, in the limiting case, for an infinitesimal small interface, all models converged to the same solution. Due to the statical and kinematical compatibility and the numerical performance (computational time) homogenisation assumptions based on rank-1 outperformed the other schemes. The Allen-Cahn-type phase field model presented in Chapter 5 was associated with displacive phase transformations. Phase transformations based on diffusion were the focus of Chapter 6. To be more precise, deformation and diffusion based phase transformations were investigated by means of Cahn-Hilliard-type phase field models in Chapter 6. Two subjects were discussed in detail in this chapter. In the first part, the continuum mechanically coupled Allen-Cahn-type model presented in the previous chapter was extended to a Cahn-Hilliard-type model. It was shown that all unknowns (deformation map, chemical potential and phase parameter) followed jointly as minimisers from the underlying incremental potential. With respect to the numerical implementation, the aforementioned potential was discretised in spaces by means of finite elements and the constrained problem was transformed into an equivalent unconstrained problem by employing the Fischer-Burmeister NCP functions – in line with the previous chapter. In order to demonstrate the diffusion based volume conservation, the evolution of microstructure was analysed for different transformation strains. In the second part, the volume conserving property of the mechanically coupled Cahn-Hilliard-type phase field model has been used for topology optimisation. The resulting stationary conditions showed a strong analogy to the system of equations characterising the classic Cahn-Hilliard-type phase field theory. Finally, the optimal topology computed by means of the novel algorithm led to a classic truss-like structure.

7.2 Outlook

This thesis dealt with different aspects regarding the evolution of microstructures. Clearly, there is always room for improvement of material models which can account for more complex phenomena or more efficient numerical implementations. Some of these improvements are discussed below.

Although the presented model in Chapter 4 captures the most relevant effects at the macroscale and is therefore suitable for a wide range of metallic materials, some aspects could be considered in future works in order to strengthen the proposed theory. The anisotropic texture evolution leads to a distortion of the yield surface as highlighted in Barthel et al. [15], Feigenbaum and Dafalias [43], Haddidi et al. [52], Shi and Mosler [113]. However, a direct connection to the slip planes of plastic slip systems as discussed in frameworks associated with crystal plasticity (df. Homayonifar and Mosler [56], Miehe et al. [86], Ortiz and Repetto [98]) is not given. Especially the cross-hardening effect, which is observed in many alloys (see Ishikawa [58], Khan et al. [62]), is responsible for the distortion of the yield surface. A verification by using crystal plasticity could motivate a further decomposition of the latent hardening, such that the introduced curvature change factor in Section 4.1.4 can be replaced by a more micromechanically motivated ansatz. Furthermore, the thermomechnical coupling and anisotropic yield surface evolution need to be validated simultaneously. Since experiments are limited to either monitoring temperatures in uniaxial plastic loading tests (cf. Hodowany et al. [54], Oliferuk et al. [96]) or to measuring the distortion of yield surfaces under isothermal conditions, a combination of both tests could provide more information for the parameter identification.

Regarding the constitutive model at the microscale as presented in Chapter 5, the proposed phase field framework based on efficient rank-1 homogenisation schemes should be extended to multi-phase materials. An extension to multiple phases can be found in Steinbach and Apel [124], Steinbach and Pezzolla [126]. However, a multi-phase description based on rank-1 connections at the interface cannot be implemented in a straightforward manner. Ideas relevant for such an extension can be found in the context of convexification, cf. Bartel and Hackl [10], Bartels et al. [14], Ortiz and Repetto [98]. However, an adaptation for diffuse interfaces is still required. Furthermore, the current phase field models were only applied to hyperelastic material. As noted in Mosler et al.

[92] the proposed framework can also be applied to dissipative materials. However, the history dependent internal variables require special attention, cf. Ammar et al. [3], de Rancourt et al. [36]. Furthermore, thermal effects should also be included in the phase field model, cf. Liu and Dunne [78].

Finally, the model at the microscale should be linked to the model at the macroscale, e.g. by using multiscale finite element methods, see Miehe et al. [86], Nemat-Nasser and Hori [93].

A Computation of internal energy

A.1 Computation of internal energy by means of Legendre transformation

According to Eq. (2.42), the internal energy can be computed by means of the Legendre transformation

$$E(\mathbf{F}, N, \boldsymbol{\alpha}) = E^{\mathrm{el}}(\mathbf{F}, N) + E^{\mathrm{pl}}(\boldsymbol{\alpha}) = \Psi^{\mathrm{el}}(\mathbf{F}, \Theta) + \Psi^{\mathrm{pl}}(\boldsymbol{\alpha}) + \Theta\, N\,, \tag{A.1}$$

where the specific thermoelastic energy (3.62) and an arbitrary plastic energy Ψ^{pl} are assumed. The internal variable $\boldsymbol{\alpha}$ denotes a generalised set of hardening related variables. Since Ψ^{pl} is assumed to be independent on the temperature, the counterpart, E^{pl} is independent of the entropy. This can be derived by computing

$$E = \inf_{\Theta} \left\{ \Psi + \Theta\, N \right\}\,. \tag{A.2}$$

Consequently, $E^{\mathrm{pl}} = \Psi^{\mathrm{pl}}$ and the Legendre transformation (A.1) can be reduced to the thermoelastic response (3.63)-(3.66), such that

$$E^{\mathrm{el}}(\bar{\mathbf{C}}^{\mathrm{e}}, J, N) = W(\bar{\mathbf{C}}^{\mathrm{e}}, J) + U(J) + M(J, \Theta) + T(\Theta) + \Theta\, N\,. \tag{A.3}$$

In order to substitute Θ by N, the necessary condition imposed by Eq. (A.2) requires

$$\frac{\partial E^{\mathrm{el}}}{\partial \Theta} = -3\, \alpha_0\, \frac{\kappa}{2} \left[J - \frac{1}{J} \right] - c_0 \ln \left(\frac{\Theta}{\Theta_0} \right) + N = 0\,. \tag{A.4}$$

The solution of this equation yields the constitutive relation

$$\Theta = \Theta_0 \exp \left(\frac{N - 3/2\, \alpha_0\, \kappa\, [J - 1/J]}{c_0} \right)\,. \tag{A.5}$$

Re-inserting Θ into Eq. (A.3) leads to the internal energy expression

$$\begin{aligned} E^{\mathrm{el}}(\bar{\mathbf{C}}^{\mathrm{e}}, J, N) = W(\bar{\mathbf{C}}^{\mathrm{e}}, J) + U(J) + \Theta_0\ [3/2\,\alpha_0\,\kappa\ [J - 1/J] - c_0] \\ + \Theta_0\, c_0\ \exp\left(\frac{N - 3/2\,\alpha_0\,\kappa\ [J - 1/J]}{c_0}\right)\ . \end{aligned} \tag{A.6}$$

Hence, E is indeed independent of Θ.

B Implementation of thermomechanically coupled distortional hardening

---

Details of the implementation of the thermomechanically coupled distortional hardening model proposed in Chapter 4 can be found in the following sections.

B.1 Thermomechanically coupled algorithmic tangent

In the present work, the thermomechanically coupled system of non-linear equations is solved in a monolithic manner by means of Newton's scheme. Therefore, the algorithmic tangent of the thermomechanically coupled hardening model needs to be derived. According to linearisations (4.81) and (4.82), the sensitivities with respect to $\boldsymbol{\chi} = [\Delta\lambda, \boldsymbol{\Xi}]^{\mathrm{T}}$ are required for that purpose. The linearisation of the residual $\mathbf{r}_\chi$ leads to

$$\mathrm{d}\mathbf{r}_\chi = \frac{\partial \mathbf{r}_\chi}{\partial \mathbf{F}} : \mathrm{d}\mathbf{F} + \frac{\partial \mathbf{r}_\chi}{\partial \Theta}\,\mathrm{d}\Theta + \frac{\partial \mathbf{r}_\chi}{\partial \boldsymbol{\chi}} \cdot \mathrm{d}\boldsymbol{\chi} = \mathbf{0}\,, \tag{B.1}$$

such that the sensitivity $\mathrm{d}\boldsymbol{\chi}$ is obtained as

$$\mathrm{d}\boldsymbol{\chi} = -\left[\frac{\partial \mathbf{r}_\chi}{\partial \boldsymbol{\chi}}\right]^{-1} \cdot \left[\frac{\partial \mathbf{r}_\chi}{\partial \mathbf{F}} : \mathrm{d}\mathbf{F} + \frac{\partial \mathbf{r}_\chi}{\partial \Theta}\,\mathrm{d}\Theta\right]. \tag{B.2}$$

Next, this sensitivity is inserted into the linearisation of the stresses (4.81) and into the linearisation of the equation defining self-heating (see Eq. (4.82)). This yields the reduced linearisations

$$\mathrm{d}\mathbf{P} = \left[\frac{\partial \mathbf{P}}{\partial \mathbf{F}} - \frac{\partial \mathbf{P}}{\partial \boldsymbol{\chi}} \cdot \left[\frac{\partial \mathbf{r}_\chi}{\partial \boldsymbol{\chi}}\right]^{-1} \cdot \frac{\partial \mathbf{r}_\chi}{\partial \mathbf{F}}\right] : \mathrm{d}\mathbf{F} + \left[\frac{\partial \mathbf{P}}{\partial \Theta} - \frac{\partial \mathbf{P}}{\partial \boldsymbol{\chi}} \cdot \left[\frac{\partial \mathbf{r}_\chi}{\partial \boldsymbol{\chi}}\right]^{-1} \cdot \frac{\partial \mathbf{r}_\chi}{\partial \Theta}\right] \mathrm{d}\Theta \tag{B.3}$$

and

$$\begin{aligned} \mathrm{d}\Delta\mathcal{H}_\Theta = & \left[\frac{\partial\Delta\mathcal{H}_\Theta}{\partial\mathbf{F}} - \frac{\partial\Delta\mathcal{H}_\Theta}{\partial\boldsymbol{\chi}} \cdot \left[\frac{\partial\mathbf{r}_\chi}{\partial\boldsymbol{\chi}}\right]^{-1} \cdot \frac{\partial\mathbf{r}_\chi}{\partial\mathbf{F}}\right] : \mathrm{d}\mathbf{F} \\ & + \left[\frac{\partial\Delta\mathcal{H}_\Theta}{\partial\Theta} - \frac{\partial\Delta\mathcal{H}_\Theta}{\partial\boldsymbol{\chi}} \cdot \left[\frac{\partial\mathbf{r}_\chi}{\partial\boldsymbol{\chi}}\right]^{-1} \cdot \frac{\partial\mathbf{r}_\chi}{\partial\Theta}\right] , \mathrm{d}\Theta \end{aligned} \tag{B.4}$$

which only depend on the global fields $\boldsymbol{\varphi}$ (through $\mathbf{F}$) and Θ. The partial derivatives of the type $\partial\mathbf{P}/\partial(\bullet)$ and $\partial\Delta\mathcal{H}_\Theta/\partial(\bullet)$ entering the tangents (B.3) and (B.4) can be computed in a straightforward manner. For the sake of completeness, the variables $\mathbf{P}$ and $\Delta\mathcal{H}_\Theta$ associated with the prototype model used in the numerical examples are given here. They can be written as

$$\begin{aligned} \mathbf{P} &= \frac{\partial\Psi}{\partial\mathbf{F}^\mathrm{e}} \cdot \mathbf{F}^{\mathrm{p}^{-\mathrm{T}}} \\ &= \mu\, J^{-2/3} \left[\mathbf{F}^\mathrm{e} \cdot \mathbf{F}^{\mathrm{p}^{-\mathrm{T}}} - \frac{1}{3}\, \|\mathbf{F}^\mathrm{e}\|^2\, \mathbf{F}^{-\mathrm{T}}\right] + \frac{\kappa}{2}\left[J^2 - 1\right]\, \mathbf{F}^{-\mathrm{T}} \\ &\quad + [\Theta - \Theta_0]\left[-3\,\alpha_0 \frac{\kappa}{2}\left[J + \frac{1}{J}\right]\right] \mathbf{F}^{-\mathrm{T}} , \\ \Delta\mathcal{H}_\Theta &= \Theta\left[-3\,\alpha_0\frac{\kappa}{2}\left[1 + \frac{1}{J^2}\right]\right] [J - J_n] \\ &\quad + \Delta\lambda\left\{\beta^\mathcal{D}\, y_0\left[1 - \omega_0\left[\frac{\Theta}{\beta^\mathcal{D}} - \Theta_0\right]\right] + \frac{b^\mathrm{k}}{c^\mathrm{k}}\, \|\partial_{\boldsymbol{\Sigma}}\phi\|\, \mathbf{Q}^\mathrm{k} : \mathbf{Q}^\mathrm{k} + 2\, g^\mathrm{dis}\right\} . \end{aligned} \tag{B.5}$$

B.2 Enhanced assumed strain finite elements

The implementation of (nearly) incompressible material is especially for the modelling of elastoplastic material of utmost importance, since in the plastic regime isochoric material behaviour is commonly assumed. For this purpose, special finite element formulations are necessary since a standard linear interpolation leads to spurious locking phenomena, which are the reason for unnatural stiffness, for instance, in bending dominated states. One method to avoid such problems is to increase the interpolation order of the shape functions as proposed in Subsection 4.3.2. Alternatively, the enhanced assumed strain (EAS) formulation can be employed, which goes back to the works of Simo and Rifai [118] and Simo and Armero [117]. In these works, incompatible deformation modes are covered by an enhanced deformation gradient. The advantages within this method are the prevention of spurious locking and the use of low order element formulations which are more efficient from a computational point of view.

The starting point of the EAS formulation is the additive split of the deformation gradient into a conforming part GRAD$\boldsymbol{\varphi}$ and an enhanced part $\widetilde{\mathbf{F}}$, i.e.

$$\mathbf{F} = \mathrm{GRAD}\boldsymbol{\varphi} + \widetilde{\mathbf{F}} \,. \tag{B.6}$$

The associated spaces, to be more precise, the space of the displacement gradient, denoted as GRAD($\mathfrak{U}$), and the space of the enhanced gradient, denoted as $\mathfrak{F}$, are disjunct, i.e. $\mathrm{GRAD}(\mathfrak{U}) \cap \mathfrak{F} = \emptyset$. Originally, this enhancement was introduced in a mixed Hu-Washizu-type formulation where displacements $\boldsymbol{\varphi}$, enhanced deformation gradient $\widetilde{\mathbf{F}}$ and stresses $\mathbf{P}$ are independent from one another. The variations with respect to these fields lead to an additional balance equation which requires L_2-orthogonality of stresses and enhanced deformation gradient. The weak form of this condition is defined as

$$\delta W_{\widetilde{\mathbf{F}}} = \int\limits_{\mathcal{B}_0} \mathbf{P} : \delta\widetilde{\mathbf{F}} \,\mathrm{d}V = 0 \qquad \forall\, \delta\widetilde{\mathbf{F}} \in L_2(\mathcal{B}_0) \,. \tag{B.7}$$

The associated fields of a thermomechanically coupled EAS element formulation, i.e. the geometry, the displacements and the temperature, are interpolated according to Subsection 4.3.2. Again, a Bubnow-Galerkin approach is applied. According to Eq. (B.6) the approximation of the deformation gradient implies an enhanced deformation gradient. Therefore, the discretisation of $\mathbf{F}$ is determined by

$$\mathbf{F}^h = \mathrm{GRAD}\boldsymbol{\varphi}^h + \widetilde{\mathbf{F}}^h \,. \tag{B.8}$$

While the conforming part GRAD$\boldsymbol{\varphi}^h$ is defined by Eq. $(4.73)_1$, the enhanced deformation gradient $\widetilde{\mathbf{F}}^h$ is approximated by a special interpolation scheme.

Remark B.2.1: *Geometry, displacements and temperature are linearly interpolated in this work. Since the EAS element is applied to an axisymmetric quadrilateral element formulation, a 4-noded element ($n_{\mathrm{en}} = 4$) with bi-linear shape functions is taken.*

In line with Glaser and Armero [49] the enhanced deformation gradient $\widetilde{\mathbf{F}}^h$ is multiplicatively decomposed into

$$\widetilde{\mathbf{F}}^h = \mathbf{F}_0 \cdot \widetilde{\mathbb{F}} \qquad \text{with} \qquad \mathbf{F}_0 = \mathrm{GRAD}\boldsymbol{\varphi}\big|_{\boldsymbol{\xi}=\mathbf{0}} \,. \tag{B.9}$$

The conforming deformation gradient $\mathbf{F}_0$ evaluated at the centroid of the element guarantees a frame indifferent formulation as noted in Simo and Armero [117]. The enhanced interpolation $\widetilde{\mathbb{F}}$ is defined as

$$\widetilde{\mathbb{F}} = \frac{j_0}{j}\, \mathbf{J}_0^{-\mathrm{T}} \cdot \mathbb{F} \cdot \mathbf{J}_0^{-1} \tag{B.10}$$

and is referred to the reference configuration. In this context, $\mathbf{J}_0$ denotes the Jacobian of the isoparametric map $\mathbf{J} = \partial_{\boldsymbol{\xi}}\mathbf{X}^h$ which is evaluated at the centroid of the master element, i.e. $\mathbf{J}_0 = \mathbf{J}\big|_{\boldsymbol{\xi}=\mathbf{0}}$. The determinant of the Jacobian is given as $j = \det\mathbf{J}$. Accordingly, $j_0 = j\big|_{\boldsymbol{\xi}=\mathbf{0}}$ denotes the determinant evaluated at the centroid of the master element. As can be seen the enhanced deformation gradient field (B.10) is a function of the natural coordinate $\boldsymbol{\xi}$. Consequently, the operation given in Eq. (B.10) describes an invariant transformation of the enhanced field $\mathbb{F}$ into the reference configuration. More precisely, the enhanced field

$$\mathbb{F} = \sum_{c=1}^{n_{\text{enh}}} \beta^c \, \mathbb{F}^c \tag{B.11}$$

is interpolated by n_{enh} local enhanced parameter β^c and interpolation matrices $\mathbb{F}^c$ (cf. [49, 66]). An interpolation scheme for the axisymmetric element formulation used in this work is given in Appendix B.3.

Based on the discretised field variables and test functions, the weak balance equations for the mechanical and thermal problem are derived (cf. Eq. (4.76)). Due to the enhanced formulation, weak form (B.7) is also considered. More explicitly, the spatially and temporally discretised forms of the three-field formulation read for one element

$$\begin{aligned}
\delta W_{\boldsymbol{\varphi}}\big|_{\mathcal{B}_0^e} &= \sum_{a=1}^{n_{\text{en}}} \delta\boldsymbol{\varphi}^a \cdot \left[\mathbf{f}^a_{\boldsymbol{\varphi},\text{int}} - \mathbf{f}^a_{\boldsymbol{\varphi},\text{sur}} - \mathbf{f}^a_{\boldsymbol{\varphi},\text{vol}}\right] \, , \\
\delta W_{\Theta}\big|_{\mathcal{B}_0^e} &= \sum_{a=1}^{n_{\text{en}}} \delta\Theta^a \, \left[f^a_{\Theta,\text{int}} + f^a_{\Theta,\text{sur}} - f^a_{\Theta,\text{vol}}\right] \, , \\
\delta W_{\beta}\big|_{\mathcal{B}_0^e} &= \sum_{c=1}^{n_{\text{enh}}} \delta\beta^c \, f^c_{\beta,\text{int}}
\end{aligned} \tag{B.12}$$

and depend on the unknowns $\{\boldsymbol{\varphi}, \Theta, \beta\}$. The virtual enhanced parameter $\delta\beta^c$ refers to interpolation c of the enhancement. The corresponding nodal forces are defined for the mechanical problem as

$$\begin{aligned}
\mathbf{f}^a_{\boldsymbol{\varphi},\text{int}} &= \int_{\mathcal{B}_0^e} \mathbf{P} \cdot \left[\nabla N^a + \nabla N^a\big|_{\boldsymbol{\xi}=\mathbf{0}} \cdot \widetilde{\mathbb{F}}\right] \, \mathrm{d}V \, , \\
\mathbf{f}^a_{\boldsymbol{\varphi},\text{sur}} &= \int_{\partial\mathcal{B}_0^e} N^a \, \bar{\mathbf{T}} \, \mathrm{d}A \, , \quad \mathbf{f}^a_{\boldsymbol{\varphi},\text{vol}} = \int_{\mathcal{B}_0^e} N^a \, \rho_0 \, \mathbf{B} \, \mathrm{d}V \, ,
\end{aligned} \tag{B.13}$$

for the thermal problem as

$$\begin{aligned} f^a_{\Theta,\mathrm{int}} &= \int\limits_{\mathcal{B}^e_0} \left\{ N^a \, \frac{1}{\Delta t} \left\{ c \, [\Theta - \Theta_n] - \Delta \mathcal{H}_\Theta \right\} - \nabla N^a \cdot \mathbf{H} \right\} \mathrm{d}V \,, \\ f^a_{\Theta,\mathrm{sur}} &= \int\limits_{\partial\mathcal{B}^e_0} N^a \, \bar{H} \, \mathrm{d}A \,, \quad f^a_{\Theta,\mathrm{vol}} = \int\limits_{\mathcal{B}^e_0} N^a \, \rho_0 \, R_\Theta \, \mathrm{d}V \end{aligned} \tag{B.14}$$

and for the enhanced problem as

$$f^c_{\beta,\mathrm{int}} = \int\limits_{\mathcal{B}^e_0} \mathbf{P} : \left[\mathbf{F}_0 \cdot \frac{j_0}{j} \, \mathbf{J}_0^{-\mathrm{T}} \cdot \mathbb{F}^c \cdot \mathbf{J}_0^{-1} \right] \mathrm{d}V \,. \tag{B.15}$$

Note, that $\mathbf{P}$ and $\Delta\mathcal{H}_\Theta$ are functions of the discretised deformation gradient $\mathbf{F}^h$ in Eq. (B.8) and are therefore dependent on the enhanced parameter β. For the subsequent numerical implementation, the assembled nodal representation of the global residual forces (cf. Eq. (4.78)) is reformulated into an element wise representation. Due to the special structure of the system of equations, two element residua

$$\begin{aligned} \mathop{\mathbf{A}}_{e=1}^{n_\mathrm{el}} \mathbf{r}^e_m &= \mathbf{0} \,, \\ \mathbf{r}^e_\beta &= \mathbf{0} \quad (e = 1, \cdots, n_\mathrm{el}) \end{aligned} \tag{B.16}$$

are defined, which are specified as

$$\mathbf{r}^e_m = \begin{bmatrix} \mathbf{f}^1_{\boldsymbol{\varphi},\mathrm{int}} - \mathbf{f}^1_{\boldsymbol{\varphi},\mathrm{sur}} - \mathbf{f}^1_{\boldsymbol{\varphi},\mathrm{vol}} \\ f^1_{\Theta,\mathrm{int}} + f^1_{\Theta,\mathrm{sur}} - f^1_{\Theta,\mathrm{vol}} \\ \vdots \\ \mathbf{f}^{n_\mathrm{en}}_{\boldsymbol{\varphi},\mathrm{int}} - \mathbf{f}^{n_\mathrm{en}}_{\boldsymbol{\varphi},\mathrm{sur}} - \mathbf{f}^{n_\mathrm{en}}_{\boldsymbol{\varphi},\mathrm{vol}} \\ f^{n_\mathrm{en}}_{\Theta,\mathrm{int}} + f^{n_\mathrm{en}}_{\Theta,\mathrm{sur}} - f^{n_\mathrm{en}}_{\Theta,\mathrm{vol}} \end{bmatrix} \,, \qquad \mathbf{r}^e_\beta = \begin{bmatrix} f^1_{\beta,\mathrm{int}} \\ \vdots \\ f^{n_\mathrm{enh}}_{\beta,\mathrm{int}} \end{bmatrix} \,. \tag{B.17}$$

Forces with respect to the displacement field $\boldsymbol{\varphi}$ and the temperature field Θ are assembled over all elements. In contrast to this global assembling, forces with respect to the enhanced field are treated element wise. According to Eq. (B.7) residuum $\mathbf{r}^e_\beta$ requires L_2-continuity. More precisely, since $\widetilde{\mathbf{F}}$ and $\mathbf{P}$ are discontinuous across the element boundaries, enhanced parameter β needs only to be continuous within the element $\mathcal{B}^e_0$. Thus, the enhanced parameter can be condensed out by means of static condensation.

For this purpose, the non-linear system of equations (B.16) is linearised with respect to the vectors $\mathbf{d}^e = [\boldsymbol{\varphi}^1, \Theta^1, \cdots, \boldsymbol{\varphi}^{n_\text{en}}, \Theta^{n_\text{en}}]$ and $\boldsymbol{\beta}^e = [\beta^1, \cdots, \beta^{n_\text{enh}}]$, i.e.

$$
\begin{aligned}
\mathop{\mathsf{\mathbf{A}}}_{e=1}^{n_\text{el}} \mathbf{r}^e_\mathbf{d} + \mathbf{K}^e_\mathbf{dd} \cdot \Delta\mathbf{d}^e + \mathbf{K}^e_{\mathbf{d}\beta} \cdot \Delta\boldsymbol{\beta}^e &= \mathbf{0} \\
\mathbf{r}^e_\beta + \mathbf{K}^e_{\beta\mathbf{d}} \cdot \Delta\mathbf{d}^e + \mathbf{K}^e_{\beta\beta} \cdot \Delta\boldsymbol{\beta}^e &= \mathbf{0} \quad (e = 1, \cdots, n_\text{el})\,.
\end{aligned}
\tag{B.18}
$$

The corresponding element stiffnesses are

$$
\begin{aligned}
&\mathbf{K}^e_\mathbf{dd} = \frac{\mathrm{d}\mathbf{r}^e_\mathbf{d}}{\mathrm{d}\mathbf{d}^e} = \begin{bmatrix}
\mathbf{K}^{11}_{\boldsymbol{\varphi}\boldsymbol{\varphi}} & \mathbf{K}^{11}_{\boldsymbol{\varphi}\Theta} & \cdots & \cdots & \cdots \\
\mathbf{K}^{11}_{\Theta\boldsymbol{\varphi}} & K^{11}_{\Theta\Theta} & \cdots & \cdots & \cdots \\
\vdots & \vdots & \ddots & \vdots & \vdots \\
\cdots & \cdots & \cdots & \mathbf{K}^{n_\text{en}n_\text{en}}_{\boldsymbol{\varphi}\boldsymbol{\varphi}} & \mathbf{K}^{n_\text{en}n_\text{en}}_{\boldsymbol{\varphi}\Theta} \\
\cdots & \cdots & \cdots & \mathbf{K}^{n_\text{en}n_\text{en}}_{\Theta\boldsymbol{\varphi}} & K^{n_\text{en}n_\text{en}}_{\Theta\Theta}
\end{bmatrix}, \\
&\mathbf{K}^e_{\mathbf{d}\beta} = \frac{\mathrm{d}\mathbf{r}^e_m}{\mathrm{d}\boldsymbol{\beta}^e} = \begin{bmatrix}
\mathbf{K}^{11}_{\boldsymbol{\varphi}\beta} & \cdots & \cdots \\
K^{11}_{\Theta\beta} & \cdots & \cdots \\
\vdots & \ddots & \vdots \\
\cdots & \cdots & \mathbf{K}^{n_\text{en}n_\text{enh}}_{\boldsymbol{\varphi}\beta} \\
\cdots & \cdots & K^{n_\text{en}n_\text{enh}}_{\Theta\beta}
\end{bmatrix}, \quad
\mathbf{K}^e_{\beta\mathbf{d}} = \frac{\mathrm{d}\mathbf{r}^e_\beta}{\mathrm{d}\mathbf{d}^e} = \begin{bmatrix}
\mathbf{K}^{11}_{\beta\boldsymbol{\varphi}} & \cdots & \cdots \\
K^{11}_{\beta\Theta} & \cdots & \cdots \\
\vdots & \ddots & \vdots \\
\cdots & \cdots & \mathbf{K}^{n_\text{en}n_\text{enh}}_{\beta\boldsymbol{\varphi}} \\
\cdots & \cdots & K^{n_\text{en}n_\text{enh}}_{\beta\Theta}
\end{bmatrix}, \\
&\mathbf{K}^e_{\beta\beta} = \frac{\mathrm{d}\mathbf{r}^e_\beta}{\mathrm{d}\boldsymbol{\beta}^e} = \begin{bmatrix}
K^{11}_{\beta\beta} & \cdots & \cdots \\
\vdots & \ddots & \vdots \\
\cdots & \cdots & K^{n_\text{enh}n_\text{enh}}_{\beta\beta}
\end{bmatrix},
\end{aligned}
\tag{B.19}
$$

in which the associated nodal stiffness components are defined as

$$
\begin{aligned}
\mathbf{K}^{ab}_{\boldsymbol{\varphi}\boldsymbol{\varphi}} &= \frac{\mathrm{d}\mathbf{r}^a_{\boldsymbol{\varphi}}}{\mathrm{d}\boldsymbol{\varphi}^b} = \int\limits_{\mathcal{B}^e_0} \left[\nabla N^a + \nabla N^a\big|_{\boldsymbol{\xi}=\mathbf{0}} \cdot \widetilde{\mathbb{F}}\right] \bullet \frac{\mathrm{d}\mathbf{P}}{\mathrm{d}\mathbf{F}} \cdot \left[\nabla N^b + \nabla N^b\big|_{\boldsymbol{\xi}=\mathbf{0}} \cdot \widetilde{\mathbb{F}}\right] \mathrm{d}V\,, \\
\mathbf{K}^{ab}_{\boldsymbol{\varphi}\Theta} &= \frac{\mathrm{d}\mathbf{r}^a_{\boldsymbol{\varphi}}}{\mathrm{d}\Theta^b} = \int\limits_{\mathcal{B}^e_0} N^b \, \frac{\mathrm{d}\mathbf{P}}{\mathrm{d}\Theta} \cdot \left[\nabla N^a + \nabla N^a\big|_{\boldsymbol{\xi}=\mathbf{0}} \cdot \widetilde{\mathbb{F}}\right] \mathrm{d}V\,, \\
\mathbf{K}^{ab}_{\Theta\boldsymbol{\varphi}} &= \frac{\mathrm{d}r^a_\Theta}{\mathrm{d}\boldsymbol{\varphi}^b} = \int\limits_{\mathcal{B}^e_0} N^a \, \frac{\mathrm{d}\Delta\mathcal{H}_\Theta}{\mathrm{d}\mathbf{F}} \cdot \left[\nabla N^b + \nabla N^b\big|_{\boldsymbol{\xi}=\mathbf{0}} \cdot \widetilde{\mathbb{F}}\right] \mathrm{d}V\,, \\
K^{ab}_{\Theta\Theta} &= \frac{\mathrm{d}r^a_\Theta}{\mathrm{d}\Theta^b} = \int\limits_{\mathcal{B}^e_0} N^a \, \frac{1}{\Delta t} \left\{c - \frac{\mathrm{d}\Delta\mathcal{H}_\Theta}{\mathrm{d}\Theta}\right\} N^b + k_0 \, \nabla N^a \cdot \nabla N^b \, \mathrm{d}V \\
&\qquad + \int\limits_{\mathcal{B}^e_0} N^a \frac{\partial \bar{H}}{\partial \Theta} N^b \, \mathrm{d}V
\end{aligned}
\tag{B.20}
$$

and

$$
\begin{aligned}
\mathbf{K}^{ad}_{\boldsymbol{\varphi}\beta} &= \frac{\mathrm{d}\mathbf{r}^a_{\boldsymbol{\varphi}}}{\mathrm{d}\beta^d} = \int\limits_{\mathcal{B}^e_0} \left[\nabla N^a + \nabla N^a\big|_{\boldsymbol{\xi}=\mathbf{0}} \cdot \widetilde{\mathbb{F}}\right] \bullet \frac{\mathrm{d}\mathbf{P}}{\mathrm{d}\mathbf{F}} : \left[\mathbf{F}_0 \cdot \frac{j_0}{j}\,\mathbf{J}_0^{-\mathrm{T}} \cdot \mathbb{F}^d \cdot \mathbf{J}_0^{-1}\right] \\
&\qquad\qquad\qquad + \mathbf{P} \cdot \left[\nabla N^a\big|_{\boldsymbol{\xi}=\mathbf{0}} \cdot \frac{j_0}{j}\,\mathbf{J}_0^{-\mathrm{T}} \cdot \mathbb{F}^d \cdot \mathbf{J}_0^{-1}\right] \mathrm{d}V\,, \\
K^{ad}_{\Theta\beta} &= \frac{\mathrm{d}r^a_{\Theta}}{\mathrm{d}\beta^d} = \int\limits_{\mathcal{B}^e_0} N^a\,\frac{\mathrm{d}\Delta\mathcal{H}_\Theta}{\mathrm{d}\mathbf{F}} : \left[\mathbf{F}_0 \cdot \frac{j_0}{j}\,\mathbf{J}_0^{-\mathrm{T}} \cdot \mathbb{F}^d \cdot \mathbf{J}_0^{-1}\right] \mathrm{d}V\,, \\
\mathbf{K}^{cb}_{\beta\boldsymbol{\varphi}} &= \frac{\mathrm{d}r^c_{\beta}}{\mathrm{d}\boldsymbol{\varphi}^b} = {\mathbf{K}^{bc}_{\boldsymbol{\varphi}\beta}}^{\mathrm{T}}\,, \\
K^{cb}_{\beta\Theta} &= \frac{\mathrm{d}r^c_{\beta}}{\mathrm{d}\Theta^b} = \int\limits_{\mathcal{B}^e_0} \left[\mathbf{F}_0 \cdot \frac{j_0}{j}\,\mathbf{J}_0^{-\mathrm{T}} \cdot \mathbb{F}^c \cdot \mathbf{J}_0^{-1}\right] : \frac{\mathrm{d}\mathbf{P}}{\mathrm{d}\Theta}\,N^b\,\mathrm{d}V\,, \\
K^{cd}_{\beta\Theta} &= \frac{\mathrm{d}r^c_{\beta}}{\mathrm{d}\beta^d} = \int\limits_{\mathcal{B}^e_0} \left[\mathbf{F}_0 \cdot \frac{j_0}{j}\,\mathbf{J}_0^{-\mathrm{T}} \cdot \mathbb{F}^c \cdot \mathbf{J}_0^{-1}\right] : \frac{\mathrm{d}\mathbf{P}}{\mathrm{d}\mathbf{F}} : \left[\mathbf{F}_0 \cdot \frac{j_0}{j}\,\mathbf{J}_0^{-\mathrm{T}} \cdot \mathbb{F}^d \cdot \mathbf{J}_0^{-1}\right] \mathrm{d}V\,.
\end{aligned}
\tag{B.21}
$$

Details of the derivatives $\mathrm{d}\mathbf{P}/\mathrm{d}\mathbf{F}, \mathrm{d}\mathbf{P}/\mathrm{d}\Theta, \mathrm{d}\Delta\mathcal{H}_\Theta/\mathrm{d}\mathbf{F}$ and $\mathrm{d}\Delta\mathcal{H}_\Theta/\mathrm{d}\Theta$ can be found in Appendix B.1.

Now, the focus is on the static condensation of the enhanced part. By transforming $(\mathrm{B.18})_2$ the increment

$$
\Delta\boldsymbol{\beta}^e = -{\mathbf{K}^e_{\beta\beta}}^{-1} \cdot \left[\mathbf{K}^e_{\beta\mathbf{d}} \cdot \Delta\mathbf{d}^e + \mathbf{r}^e_{\beta}\right] \tag{B.22}
$$

is obtained. Re-inserted into $(\mathrm{B.18})_1$ yields the condensed system of equations

$$
\mathop{\mathsf{A}}_{e=1}^{n_{\mathrm{el}}} \left[\mathbf{r}^e_{\mathbf{d}} - \mathbf{K}^e_{\mathbf{d}\beta} \cdot {\mathbf{K}^e_{\beta\beta}}^{-1} \cdot \mathbf{r}^e_{\beta}\right] + \left[\mathbf{K}^e_{\mathbf{dd}} - \mathbf{K}^e_{\mathbf{d}\beta} \cdot {\mathbf{K}^e_{\beta\beta}}^{-1} \cdot \mathbf{K}^e_{\beta\mathbf{d}}\right] \cdot \Delta\mathbf{d}^e = \mathbf{0}\,. \tag{B.23}
$$

It should be noted, that the resulting element stiffness shows no symmetry since the underlying coupled material model does not follow from a variational principle. Thus, the solution scheme is non-symmetric and requires non-symmetric solvers. The implementation of static condensation is based on a correct updating scheme of the enhanced interpolation parameter, cf. de Souza Neto et al. [37]. Such an updating scheme is presented in Fig. B.1.

```
1. Set Newton iteration $k+1$

2. Update $\mathbf{d}^e$ based on given $\Delta\mathbf{d}^e$:
   $\mathbf{d}^e \longleftarrow \mathbf{d}^e + \Delta\mathbf{d}^e$

3. Update $\boldsymbol{\beta}^e$:
   compute/load residuals and stiffnesses at $k$-th iteration: ${\mathbf{K}^e_{\beta\beta}}^{-1}$, $\mathbf{K}^e_{\beta\mathbf{d}}$, $\mathbf{r}^e_{\beta}$
   compute: $\Delta\boldsymbol{\beta}^e = -{\mathbf{K}^e_{\beta\beta}}^{-1} \cdot \left[\mathbf{K}^e_{\beta\mathbf{d}} \cdot \Delta\mathbf{d}^e + \mathbf{r}^e_{\beta}\right]$
   update: $\boldsymbol{\beta}^e \longleftarrow \boldsymbol{\beta}^e + \Delta\boldsymbol{\beta}^e$

4. Compute $\mathbf{F}^h$ and constitutive relations (see Fig. 4.2)

5. Compute element stiffness matrices $\mathbf{K}^e_{\mathbf{dd}}$, $\mathbf{K}^e_{\mathbf{d}\beta}$, $\mathbf{K}^e_{\beta\beta}$, $\mathbf{K}^e_{\beta\mathbf{d}}$ and element residual
   vectors $\mathbf{r}^e_{\mathbf{d}}$, $\mathbf{r}^e_{\beta}$. Then compute the modified element stiffness $\widetilde{\mathbf{K}}^e_{\mathbf{dd}}$ and the
   modified element residual $\widetilde{\mathbf{r}}^e_{\mathbf{d}}$:
   $\widetilde{\mathbf{K}}^e_{\mathbf{dd}} = \mathbf{K}^e_{\mathbf{dd}} - \mathbf{K}^e_{\mathbf{d}\beta} \cdot {\mathbf{K}^e_{\beta\beta}}^{-1} \cdot \mathbf{K}^e_{\beta\mathbf{d}}$
   $\widetilde{\mathbf{r}}^e_{\mathbf{d}} = \mathbf{r}^e_{\mathbf{d}} - \mathbf{K}^e_{\mathbf{d}\beta} \cdot {\mathbf{K}^e_{\beta\beta}}^{-1} \cdot \mathbf{r}^e_{\beta}$

6. Check global tolerance:
   IF $\left\| \mathop{\mathsf{A}}_{e=1}^{n_{\mathrm{el}}} \widetilde{\mathbf{r}}^e_{\mathbf{d}} \right\| \leq$ TOL THEN
         EXIT
   ELSE
         GO TO 7.
   ENDIF

7. Solve the global system of equations:
   $\mathop{\mathsf{A}}_{e=1}^{n_{\mathrm{el}}} \widetilde{\mathbf{K}}^e_{\mathbf{dd}} \cdot \Delta\mathbf{d} = -\widetilde{\mathbf{r}}^e_{\mathbf{d}}$
   GO TO 1.
```

Figure B.1: EAS implementation: algorithmic scheme for static condensation

B.3 Enhanced assumed strain formulation for axisymmetric elements

Although the axisymmetric case is solved in the two-dimensional $R-Z$ space, its deformation gradient and the respective stresses are three-dimensional. Hence, the enhanced assumed strain element formulation needs to be adjusted. Following Simo and Armero [117], Simo and Rifai [118], the enhanced interpolation is transformed to the reference configuration by the Jacobian

$$\mathbf{J}_0 = \begin{bmatrix} \left[\partial_{\boldsymbol{\xi}} \mathbf{X}^h\big|_{\boldsymbol{\xi}=\mathbf{0}}\right]^{2\times 2} & \mathbf{0} \\ \mathbf{0}^{\mathrm{T}} & 1 \end{bmatrix}, \tag{B.24}$$

in which only the $\{3,3\}$-entry is additionally taken into account. The interpolation functions of the enhanced field $\mathbb{F}$ are restricted to the orthogonality constraint $\int_\square \mathbb{F}\, R(\boldsymbol{\xi})\, \mathrm{d}\boldsymbol{\xi} = \mathbf{0}$ (see Simo and Rifai [118]). A consistent enhanced interpolation reads for $n_{\mathrm{enh}} = 5$

$$\begin{aligned} \mathbb{F}^1 &= \begin{bmatrix} \xi-\bar{\xi} & 0 & 0 \\ 0 & 0 & 0 \\ 0 & 0 & 0 \end{bmatrix}, \quad \mathbb{F}^2 = \begin{bmatrix} 0 & \xi-\bar{\xi} & 0 \\ 0 & 0 & 0 \\ 0 & 0 & 0 \end{bmatrix}, \quad \mathbb{F}^3 = \begin{bmatrix} 0 & 0 & 0 \\ \eta-\bar{\eta} & 0 & 0 \\ 0 & 0 & 0 \end{bmatrix}, \\ \mathbb{F}^4 &= \begin{bmatrix} 0 & 0 & 0 \\ 0 & \eta-\bar{\eta} & 0 \\ 0 & 0 & 0 \end{bmatrix}, \quad \mathbb{F}^5 = \begin{bmatrix} 0 & 0 & 0 \\ 0 & 0 & 0 \\ 0 & 0 & \xi\,\eta\, j/[j_0\, R] \end{bmatrix}, \end{aligned} \tag{B.25}$$

with

$$\bar{\xi} = \frac{1}{\displaystyle\int_\square R(\boldsymbol{\xi})\, \mathrm{d}\xi \mathrm{d}\eta} \int_\square \xi\, R(\boldsymbol{\xi})\, \mathrm{d}\xi \mathrm{d}\eta, \qquad \bar{\eta} = \frac{1}{\displaystyle\int_\square R(\boldsymbol{\xi})\, \mathrm{d}\xi \mathrm{d}\eta} \int_\square \eta\, R(\boldsymbol{\xi})\, \mathrm{d}\xi \mathrm{d}\eta\,. \tag{B.26}$$

This formulation is slightly different from the original presented by Simo and Rifai [118]. It considers a change of the off-diagonal terms $\mathbb{F}^2$ and $\mathbb{F}^3$ as proposed and analysed by Korelc and Wriggers [66].

C Phase field modelling – Computation of properties within the diffuse interface

---

The following sections are related to the effective computation of properties within the diffuse interface, which is characteristic for phase field approaches, as addressed in Chapter 5.

C.1 Computation of the relaxed energy and update of the stresses based on partial rank-1 homogenisation

Independent of the homogenisation assumption, the relaxed energy follows from minimizing the energy with respect to the variables $\boldsymbol{\beta}$, cf. Subsection 5.4.1. The respective necessary condition reads $\partial_{\boldsymbol{\beta}} \Psi_{\mathrm{B}} = \mathbf{0}$. In the case of a partial rank-1 homogenisation, $\boldsymbol{\beta}$ equals $\mathbf{a}$, i.e. $\boldsymbol{\beta} = \mathbf{a}$. Within each time step, a Newton based procedure is used for computing the solution of the non-linear equation $\partial_{\boldsymbol{\beta}} \Psi_{\mathrm{B}} = \mathbf{0}$. Due to numerical robustness, the interface normal $\mathbf{N} = \nabla p / \|\nabla p\|$ is held constant during the computation (mixed explicit/implicit update), i.e. $\mathbf{N} = \nabla p / \|\nabla p\| |_{t_n}$.

The update of the Newton algorithm is given by

$$\mathbf{a} \longleftarrow \mathbf{a} - \left[\mathbf{N} \bullet \frac{\partial^2 \Psi_{\mathrm{B}}}{\partial [\![\mathbf{F}]\!]^2} \cdot \mathbf{N} \right]^{-1} \cdot \left[\frac{\partial \Psi_{\mathrm{B}}}{\partial [\![\mathbf{F}]\!]} \cdot \mathbf{N} \right] \tag{C.1}$$

with the partial derivatives

$$\begin{aligned} \frac{\partial \Psi_{\mathrm{B}}}{\partial [\![\mathbf{F}]\!]} &= [1-p]\, p \, [-\mathbf{P}_1 + \mathbf{P}_2] \ , \\ \frac{\partial^2 \Psi_{\mathrm{B}}}{\partial [\![\mathbf{F}]\!]^2} &= [1-p]\, p \left[p \, \frac{\partial \mathbf{P}_1}{\partial \mathbf{F}_1} + [1-p] \, \frac{\partial \mathbf{P}_2}{\partial \mathbf{F}_2} \right] \end{aligned} \tag{C.2}$$

depending on the stresses ($\mathbf{P}_i$) and the tangents ($\partial \mathbf{P}_i / \partial \mathbf{F}_i$) in the two phases. Considering the Bain-type deformation gradients $\mathbf{F}_i^{\mathrm{B}}$ within the two different phases, the generic structures of $\mathbf{P}_i$ and $\partial \mathbf{P}_i / \partial \mathbf{F}_i$ reads

$$\begin{aligned} \mathbf{P}_i &= \frac{\partial \Psi_{\mathrm{B}_i}}{\partial \mathbf{F}_i^{\mathrm{e}}} \cdot \mathbf{F}_i^{\mathrm{B}-\mathrm{T}} , \\ \frac{\partial \mathbf{P}_i}{\partial \mathbf{F}_i} &= \mathbf{F}_i^{\mathrm{e}-1} \odot \frac{\partial^2 \Psi_{\mathrm{B}_i}}{\partial \mathbf{F}_i^{\mathrm{e}2}} \cdot \mathbf{F}_i^{\mathrm{e}-\mathrm{T}} . \end{aligned} \tag{C.3}$$

For the prototype model presented in Section 5.5 (the Helmholtz energies are defined by Eq. (5.100)), the constitutive model dependent derivatives are obtained as

$$\begin{aligned} \frac{\partial \Psi_{\mathrm{B}_i}}{\partial \mathbf{F}_i^{\mathrm{e}}} &= \mu_i \, J_i^{\mathrm{e}-2/3} \left[\mathbf{F}_i^{\mathrm{e}} - \frac{1}{3} \, \|\mathbf{F}_i^{\mathrm{e}}\|^2 \, \mathbf{F}_i^{\mathrm{e}-\mathrm{T}} \right] + \frac{\kappa_i}{2} \left[J_i^{\mathrm{e}2} - 1 \right] \, \mathbf{F}_i^{\mathrm{e}-\mathrm{T}} \\ \frac{\partial^2 \Psi_{\mathrm{B}_i}}{\partial \mathbf{F}_i^{\mathrm{e}2}} &= \frac{\mu_i}{3} \, J_i^{\mathrm{e}-2/3} \Bigg[\\ & \qquad 3 \, \mathbb{I} + \frac{2}{3} \, \|\mathbf{F}_i^{\mathrm{e}}\|^2 \, \mathbf{F}_i^{\mathrm{e}-\mathrm{T}} \otimes \mathbf{F}_i^{\mathrm{e}-\mathrm{T}} - 4 \, \mathbf{F}_i^{\mathrm{e}} \otimes \mathbf{F}_i^{\mathrm{e}-\mathrm{T}} - \|\mathbf{F}_i^{\mathrm{e}}\|^2 \, \frac{\partial \mathbf{F}_i^{\mathrm{e}-\mathrm{T}}}{\partial \mathbf{F}_i^{\mathrm{e}}} \Bigg] \\ & \qquad + \frac{\kappa_i}{2} \left[2 \, J_i^{\mathrm{e}2} \mathbf{F}_i^{\mathrm{e}-\mathrm{T}} \otimes \mathbf{F}_i^{\mathrm{e}-\mathrm{T}} + \left[J_i^{\mathrm{e}2} - 1 \right] \, \frac{\partial \mathbf{F}_i^{\mathrm{e}-\mathrm{T}}}{\partial \mathbf{F}_i^{\mathrm{e}}} \right] \end{aligned} \tag{C.4}$$

with

$$\frac{\partial \mathbf{F}_i^{\mathrm{e}-\mathrm{T}}}{\partial \mathbf{F}_i^{\mathrm{e}}} = -\mathbf{F}_i^{\mathrm{e}-\mathrm{T}} \underline{\otimes} \mathbf{F}_i^{\mathrm{e}-1} . \tag{C.5}$$

C.2 Computation of the algorithmic tangent

Within the presented work, the resulting discretised initial boundary value problems are solved by means of a monolithic Newton's method. Therefore, the algorithmic tangent, derived in Subsection 5.4.3, is required. According to Eq. ((5.96)), it depends on the derivatives $\mathrm{d}\mathbf{P}/\mathrm{d}\mathbf{F}$, $\mathrm{d}\mathbf{P}/\mathrm{d}p$, $\mathrm{d}\mathbf{P}/\mathrm{d}\nabla p$, $\mathrm{d}\left[\partial_p \, \Delta\mathcal{E}^{\mathrm{red}}\right]/\mathrm{d}p$, $\mathrm{d}\boldsymbol{\xi}/\mathrm{d}p$ and $\mathrm{d}\boldsymbol{\xi}/\mathrm{d}\nabla p$. In order to compute such derivatives, the linearisations

$$\begin{aligned} \mathrm{d}\mathbf{P} = \mathrm{d} \left[\frac{\partial \, \Delta\mathcal{E}}{\partial \mathbf{F}} \right] &= \frac{\partial^2 \, \Psi_{\mathrm{B}}}{\partial \mathbf{F}^2} : \mathrm{d}\mathbf{F} + \frac{\partial^2 \, \Psi_{\mathrm{B}}}{\partial \mathbf{F} \, \partial p} \, \mathrm{d}p + \frac{\partial^2 \, \Psi_{\mathrm{B}}}{\partial \mathbf{F} \, \partial \boldsymbol{\beta}} \circ \mathrm{d}\boldsymbol{\beta} , \\ \mathrm{d} \left[\frac{\partial \, \Delta\mathcal{E}}{\partial p} \right] &= \frac{\partial^2 \, \Psi_{\mathrm{B}}}{\partial p \, \partial \mathbf{F}} : \mathrm{d}\mathbf{F} + \frac{\partial^2 \, \Delta\mathcal{E}}{\partial p^2} \, \mathrm{d}p + \frac{\partial^2 \, \Psi_{\mathrm{B}}}{\partial p \, \partial \boldsymbol{\beta}} \circ \mathrm{d}\boldsymbol{\beta} , \\ \mathrm{d}\boldsymbol{\xi} = \mathrm{d} \left[\frac{\partial \, \Delta\mathcal{E}}{\partial \nabla p} \right] &= \frac{\partial^2 \, \Psi_{\Gamma}}{\partial \nabla p^2} \cdot \mathrm{d}\nabla p \end{aligned} \tag{C.6}$$

are considered. By inserting the linearisation of the stationary condition $\partial_{\boldsymbol{\beta}}\Psi_{\mathrm{B}}$ yielding

$$\mathrm{d}\left[\frac{\partial\Psi_{\mathrm{B}}}{\partial\boldsymbol{\beta}}\right] = \frac{\partial^2\,\Psi_{\mathrm{B}}}{\partial\boldsymbol{\beta}^2}\circ\mathrm{d}\boldsymbol{\beta} + \frac{\partial^2\,\Psi_{\mathrm{B}}}{\partial\boldsymbol{\beta}\,\partial\mathbf{F}} : \mathrm{d}\mathbf{F} + \frac{\partial^2\,\Psi_{\mathrm{B}}}{\partial\boldsymbol{\beta}\,\partial p}\,\mathrm{d}p = \mathbf{0} \tag{C.7}$$

into the linearisations (C.6), the non-trivial derivatives defining the stiffness matrices are finally obtained as

$$\begin{aligned}
\frac{\mathrm{d}\mathbf{P}}{\mathrm{d}\mathbf{F}} &= \frac{\partial^2\,\Psi_{\mathrm{B}}}{\partial\mathbf{F}^2} - \frac{\partial^2\,\Psi_{\mathrm{B}}}{\partial\mathbf{F}\,\partial\boldsymbol{\beta}}\circ\left[\frac{\partial^2\,\Psi_{\mathrm{B}}}{\partial\boldsymbol{\beta}^2}\right]^{-1}\circ\frac{\partial^2\,\Psi_{\mathrm{B}}}{\partial\boldsymbol{\beta}\,\partial\mathbf{F}}\,,\\
\frac{\mathrm{d}\mathbf{P}}{\mathrm{d}p} &= \frac{\mathrm{d}R_p}{\mathrm{d}\mathbf{F}} = \frac{\partial^2\,\Psi_{\mathrm{B}}}{\partial\mathbf{F}\,\partial p} - \frac{\partial^2\,\Psi_{\mathrm{B}}}{\partial\mathbf{F}\,\partial\boldsymbol{\beta}}\circ\left[\frac{\partial^2\,\Psi_{\mathrm{B}}}{\partial\boldsymbol{\beta}^2}\right]^{-1}\circ\frac{\partial^2\,\Psi_{\mathrm{B}}}{\partial\boldsymbol{\beta}\,\partial p}\,,\\
\frac{\mathrm{d}\partial_p\,\Delta\mathcal{E}}{\mathrm{d}p} &= \frac{\partial^2\,\Delta\mathcal{E}}{\partial p^2} - \frac{\partial^2\,\Psi_{\mathrm{B}}}{\partial p\,\partial\boldsymbol{\beta}}\circ\left[\frac{\partial^2\,\Psi_{\mathrm{B}}}{\partial\boldsymbol{\beta}^2}\right]^{-1}\circ\frac{\partial^2\,\Psi_{\mathrm{B}}}{\partial\boldsymbol{\beta}\,\partial p}\,,\\
\frac{\mathrm{d}\boldsymbol{\xi}}{\mathrm{d}\nabla p} &= \frac{\partial^2\,\Psi_{\Gamma}^{\varepsilon}}{\partial\nabla p^2}.
\end{aligned} \tag{C.8}$$

The trivial derivatives are $\mathrm{d}\mathbf{P}/\mathrm{d}\nabla p = \mathbf{0}$ and $\mathrm{d}\boldsymbol{\xi}/\mathrm{d}p = \mathbf{0}$ due to their independency of the respective variables, cf. Remark (5.4.1).

C.3 Components of algorithmic tangent due to NCP functions

According to Eq. (5.86), the implemented slightly adjusted Fischer-Burmeister NCP functions are defined as

$$\begin{aligned}
g_1(p,\lambda_1) &= \sqrt{[p-1+\varepsilon_0]^2+\lambda_1^2+\varepsilon_{\mathrm{tol}}^2} + [p-1+\varepsilon_0] - \lambda_1\,,\\
g_2(p,\lambda_2) &= \sqrt{[-p+\varepsilon_0]^2+\lambda_2^2+\varepsilon_{\mathrm{tol}}^2} + [-p+\varepsilon_0] - \lambda_2\,.
\end{aligned} \tag{C.9}$$

The derivatives of such functions entering the stiffness matrix read

$$\begin{aligned}
\frac{\partial g_1}{\partial p} &= \frac{[p-1+\varepsilon_0]}{\sqrt{[p-1+\varepsilon_0]^2+\lambda_1^2+\varepsilon_{\mathrm{tol}}^2}} + 1\,,\\
\frac{\partial g_1}{\partial \lambda_1} &= \frac{\lambda_1}{\sqrt{[p-1+\varepsilon_0]^2+\lambda_1^2+\varepsilon_{\mathrm{tol}}^2}} - 1\,,\\
\frac{\partial g_2}{\partial p} &= \frac{[p-\varepsilon_0]}{\sqrt{[-p+\varepsilon_0]^2+\lambda_2^2+\varepsilon_{\mathrm{tol}}^2}} - 1\,,\\
\frac{\partial g_2}{\partial \lambda_2} &= \frac{\lambda_1}{\sqrt{[-p+\varepsilon_0]^2+\lambda_2^2+\varepsilon_{\mathrm{tol}}^2}} - 1\,.
\end{aligned} \tag{C.10}$$

Bibliography

[1] S. R. Agnew and Ö. Duygulu. Plastic anisotropy and the role of non-basal slip in magnesium alloy AZ31B. *International Journal of Plasticity*, 21(6):1161–1193, 2005. doi:10.1016/j.ijplas.2004.05.018.

[2] S. M. Allen and J. W. Cahn. A microscopic theory for antiphase boundary motion and its application to antiphase domain coarsening. *Acta Metallurgica*, 27(6): 1085–1095, 1979. ISSN 0001-6160. doi:10.1016/0001-6160(79)90196-2.

[3] K. Ammar, B. Appolaire, G. Cailletaud, and S. Forest. Combining phase field approach and homogenization methods for modelling phase transformation in elastoplastic media. *European Journal of Computational Mechanics*, 18(5-6):485–523, 2009. doi:10.3166/ejcm.18.485-523.

[4] L. Anand. A Cahn–Hilliard-type theory for species diffusion coupled with large elastic–plastic deformations. *Journal of the Mechanics and Physics of Solids*, 60 (12):1983–2002, 2012. doi:10.1016/j.jmps.2012.08.001.

[5] P. Armstrong and C. Frederick. A mathematical representation of the multiaxial Bauschinger effect. *CEGB: Report RD/B/N 731*, 1966.

[6] S. Aubry and M. Ortiz. The mechanics of deformation–induced subgrain–dislocation structures in metallic crystals at large strains. *Proceedings of the Royal Society of London A: Mathematical, Physical and Engineering Sciences*, 459(2040):3131–3158, 2003. ISSN 1364-5021. doi:10.1098/rspa.2003.1179.

[7] S. Balay, S. Abhyankar, M. F. Adams, J. Brown, P. Brune, K. Buschelman, L. Dalcin, V. Eijkhout, W. D. Gropp, D. Kaushik, M. G. Knepley, L. C. McInnes, K. Rupp, B. F. Smith, S. Zampini, H. Zhang, and H. Zhang. PETSc users manual. Technical Report ANL-95/11 - Revision 3.7, Argonne National Laboratory, 2016.

[8] J. M. Ball. Convexity conditions and existence theorems in nonlinear elasticity. *Archive for Rational Mechanics and Analysis*, 63(4):337–403, 1976. ISSN 1432-0673. doi:10.1007/BF00279992.

[9] A. Baltov and A. Sawczuk. A rule of anisotropic hardening. *Acta Mechanica*, 1 (2):81–92, 1965. doi:10.1007/bf01174305.

[10] T. Bartel and K. Hackl. Multiscale modeling of martensitic phase transformations: on the numerical determination of heterogeneous mesostructures within shape-memory alloys induced by precipitates. *Techn. Mech*, 30:324–342, 2010.

[11] A. Bartels, T. Bartel, M. Canadija, and J. Mosler. On the thermomechanical coupling in dissipative materials: A variational approach for generalized standard materials. *Journal of the Mechanics and Physics of Solids*, 82:218–234, 2015. doi:10.1016/j.jmps.2015.04.011.

[12] A. Bartels and J. Mosler. Efficient variational constitutive updates for Allen–Cahn-type phase field theory coupled to continuum mechanics. *Computer Methods in Applied Mechanics and Engineering*, 317:55–83, 2017. doi:10.1016/j.cma.2016.11.024.

[13] S. Bartels, C. Carstensen, K. Hackl, and U. Hoppe. Effective relaxation for microstructure simulations: algorithms and applications . *Computer Methods in Applied Mechanics and Engineering*, 193(48–51):5143–5175, 2004. ISSN 0045-7825. doi:10.1016/j.cma.2003.12.065. Advances in Computational Plasticity.

[14] S. Bartels, C. Carstensen, S. Conti, K. Hackl, U. Hoppe, and A. Orlando. Relaxation and the Computation of Effective Energies and Microstructures in Solid Mechanics. In *Analysis, Modeling and Simulation of Multiscale Problems*, pages 197–224. Springer Nature, 2006. doi:10.1007/3-540-35657-6_8.

[15] C. Barthel, V. Levkovitch, and B. Svendsen. Modeling of sheet metal forming processes taking into account distortional hardening. *International Journal of Material Forming*, 1(S1):105–108, 2008. doi:10.1007/s12289-008-0035-y.

[16] M. P. Bendsøe and O. Sigmund. *Topology Optimization.* Springer Science + Business Media, 2004. doi:10.1007/978-3-662-05086-6.

[17] M. Bever, D. Holt, and A. Titchener. The stored energy of cold work. *Progress in Materials Science*, 17:5–177, 1973. doi:10.1016/0079-6425(73)90001-7.

[18] M. A. Biot. Thermoelasticity and Irreversible Thermodynamics. *Journal of Applied Physics*, 27(3):240–253, 1956. doi:10.1063/1.1722351.

[19] L. Blank, H. Garcke, L. Sarbu, T. Srisupattarawanit, V. Styles, and A. Voigt. Phase-field Approaches to Structural Topology Optimization. In *Constrained Optimization and Optimal Control for Partial Differential Equations*, pages 245–256. Springer Science + Business Media, 2011. doi:10.1007/978-3-0348-0133-1_13.

[20] N. Bleier and J. Mosler. Efficient variational constitutive updates by means of a novel parameterization of the flow rule. *International Journal for Numerical Methods in Engineering*, 89(9):1120–1143, 2011. doi:10.1002/nme.3280.

[21] B. Bourdin, G. Francfort, and J.-J. Marigo. Numerical experiments in revisited brittle fracture . *Journal of the Mechanics and Physics of Solids*, 48(4):797–826, 2000. ISSN 0022-5096. doi:10.1016/S0022-5096(99)00028-9.

[22] B. Bourdin and A. Chambolle. Design-dependent loads in topology optimization. *ESAIM: COCV*, 9:19–48, 2003. doi:10.1051/cocv:2002070.

[23] M. Bouville and R. Ahluwalia. Effect of lattice-mismatch-induced strains on coupled diffusive and displacive phase transformations. *Physical Review B*, 75(5),

2007. doi:10.1103/physrevb.75.054110.

[24] J. W. Cahn and J. E. Hilliard. Free Energy of a Nonuniform System. I. Interfacial Free Energy. *The Journal of Chemical Physics*, 28(2):258–267, 1958. doi:10.1063/1.1744102.

[25] M. Canadija and J. Mosler. On the thermomechanical coupling in finite strain plasticity theory with non-linear kinematic hardening by means of incremental energy minimization. *International Journal of Solids and Structures*, 48(7-8):1120–1129, 2011. doi:10.1016/j.ijsolstr.2010.12.018.

[26] M. Canadija and J. Mosler. A variational formulation for thermomechanically coupled low cycle fatigue at finite strains. *International Journal of Solids and Structures*, 100-101:388–398, 2016. doi:10.1016/j.ijsolstr.2016.09.009.

[27] C. Carstensen, K. Hackl, and A. Mielke. Non-convex potentials and microstructures in finite-strain plasticity. *Proceedings of the Royal Society A: Mathematical, Physical and Engineering Sciences*, 458(2018):299–317, 2002. doi:10.1098/rspa.2001.0864.

[28] J.-L. Chaboche. Cyclic Viscoplastic Constitutive Equations, Part I: A Thermodynamically Consistent Formulation. *Journal of Applied Mechanics*, 60(4):813, 1993. doi:10.1115/1.2900988.

[29] J.-L. Chaboche. Cyclic Viscoplastic Constitutive Equations, Part II: Stored Energy - Comparison Between Models and Experiments. *Journal of Applied Mechanics*, 60(4):822, 1993. doi:10.1115/1.2900990.

[30] L.-Q. Chen. Phase-Field Models for Microstructure Evolution. *Annual Review of Materials Research*, 32(1):113–140, 2002. doi:10.1146/annurev.matsci.32.112001.132041.

[31] T. Clausmeyer, A. Güner, A. Tekkaya, V. Levkovitch, and B. Svendsen. Modeling and finite element simulation of loading-path-dependent hardening in sheet metals during forming. *International Journal of Plasticity*, 63:64–93, 2014. doi:10.1016/j.ijplas.2014.01.011.

[32] J. D. Clayton and J. Knap. Phase field modeling of twinning in indentation of transparent crystals. *Modelling and Simulation in Materials Science and Engineering*, 19(8):085005, 2011. doi:10.1088/0965-0393/19/8/085005.

[33] B. D. Coleman. Thermodynamics of materials with memory. *Archive for Rational Mechanics and Analysis*, 17(1):1–45, 1964. doi:10.1007/bf00283864.

[34] B. D. Coleman and M. E. Gurtin. Thermodynamics with Internal State Variables. *The Journal of Chemical Physics*, 47(2):597–613, 1967. doi:10.1063/1.1711937.

[35] B. D. Coleman and W. Noll. The thermodynamics of elastic materials with heat conduction and viscosity. *Archive for Rational Mechanics and Analysis*, 13(1): 167–178, 1963. doi:10.1007/bf01262690.

[36] V. de Rancourt, K. Ammar, B. Appolaire, and S. Forest. Homogenization of viscoplastic constitutive laws within a phase field approach. *Journal of the Mechanics and Physics of Solids*, 88:291–319, 2016. ISSN 0022-5096. doi:10.1016/j.jmps.2015.12.026.

[37] E. A. de Souza Neto, D. Peri, and D. R. J. Owen. Finite Elements for Large-Strain Incompressibility. In *Computational Methods for Plasticity*, pages 647–689. John Wiley & Sons, Ltd, 2008. ISBN 9780470694626. doi:10.1002/9780470694626.ch15.

[38] L. Dedè, M. J. Borden, and T. J. R. Hughes. Isogeometric Analysis for Topology Optimization with a Phase Field Model. *Archives of Computational Methods in Engineering*, 19(3):427–465, 2012. doi:10.1007/s11831-012-9075-z.

[39] C. Denoual, A. M. Caucci, L. Soulard, and Y.-P. Pellegrini. Phase-Field Reaction-Pathway Kinetics of Martensitic Transformations in a Model Fe 3 Ni Alloy . *Phys. Rev. Lett.*, 105(3), 2010. doi:10.1103/physrevlett.105.035703.

[40] A. Durga, P. Wollants, and N. Moelans. Evaluation of interfacial excess contributions in different phase-field models for elastically inhomogeneous systems. *Modelling and Simulation in Materials Science and Engineering*, 21(5):055018, 2013. doi:10.1088/0965-0393/21/5/055018.

[41] A. Durga, P. Wollants, and N. Moelans. A quantitative phase-field model for two-phase elastically inhomogeneous systems . *Computational Materials Science*, 99: 81–95, 2015. ISSN 0927-0256. doi:10.1016/j.commatsci.2014.11.057.

[42] M. Epstein and G. A. Maugin. Thermomechanics of volumetric growth in uniform bodies. *International Journal of Plasticity*, 16(7-8):951–978, 2000. doi:10.1016/s0749-6419(99)00081-9.

[43] H. P. Feigenbaum and Y. F. Dafalias. Directional distortional hardening in metal plasticity within thermodynamics. *International Journal of Solids and Structures*, 44(22-23):7526–7542, 2007. doi:10.1016/j.ijsolstr.2007.04.025.

[44] H. P. Feigenbaum and Y. F. Dafalias. Simple Model for Directional Distortional Hardening in Metal Plasticity within Thermodynamics. *Journal of Engineering Mechanics*, 134(9):730–738, 2008. doi:10.1061/(asce)0733-9399(2008)134:9(730).

[45] A. Fischer. A special newton-type optimization method. *Optimization*, 24(3-4): 269–284, 1992. doi:10.1080/02331939208843795.

[46] G. Francfort and J.-J. Marigo. Revisiting brittle fracture as an energy minimization problem . *Journal of the Mechanics and Physics of Solids*, 46(8):1319–1342, 1998. ISSN 0022-5096. doi:10.1016/S0022-5096(98)00034-9.

[47] C. Geiger and C. Kanzow. *Numerische Verfahren zur Lösung unrestringierter Optimierungsaufgaben.* Springer Berlin Heidelberg, 1999. doi:10.1007/978-3-642-58582-1.

[48] C. Geiger and C. Kanzow. *Theorie und Numerik restringierter Optimierungsaufgaben.* Springer Science + Business Media, 2002. doi:10.1007/978-3-642-56004-0.

[49] S. Glaser and F. Armero. On the formulation of enhanced strain finite elements in finite deformations. *Engineering Computations*, 14(7):759–791, 1997. doi:10.1108/02644409710188664.

[50] M. E. Gurtin. Generalized Ginzburg-Landau and Cahn-Hilliard equations based on a microforce balance. *Physica D: Nonlinear Phenomena*, 92(3–4):178 – 192, 1996. ISSN 0167-2789. doi:10.1016/0167-2789(95)00173-5.

[51] K. Hackl. Generalized standard media and variational principles in classical and finite strain elastoplasticity. *Journal of the Mechanics and Physics of Solids*, 45 (5):667–688, 1997. doi:10.1016/s0022-5096(96)00110-x.

[52] H. Haddidi, S. Bouvier, M. Banu, C. Maier, and C. Teodosiu. Towards an accurate description of the anisotropic behaviour of sheet metals under large plastic deformations: Modelling, numerical analysis and identification. *International Journal of Plasticity*, 22(12):2226–2271, 2006. doi:10.1016/j.ijplas.2006.03.010.

[53] F. Hildebrand and C. Miehe. A phase field model for the formation and evolution of martensitic laminate microstructure at finite strains. *Philosophical Magazine*, 92(34):4250–4290, 2012. doi:10.1080/14786435.2012.705039.

[54] J. Hodowany, G. Ravichandran, A. J. Rosakis, and P. Rosakis. Partition of plastic work into heat and stored energy in metals. *Experimental Mechanics*, 40(2):113–123, 2000. doi:10.1007/bf02325036.

[55] G. A. Holzapfel. *Nonlinear Solid Mechanics: A Continuum Approach for Engineering.* Wiley & Sons, 2000.

[56] M. Homayonifar and J. Mosler. Efficient modeling of microstructure evolution in magnesium by energy minimization. *International Journal of Plasticity*, 28(1): 1–20, 2012. doi:10.1016/j.ijplas.2011.05.011.

[57] K. Hutter and K. Jöhnk. *Continuum Methods of Physical Modeling.* Springer Nature, 2004. doi:10.1007/978-3-662-06402-3.

[58] H. Ishikawa. Subsequent yield surface probed from its current center. *International Journal of Plasticity*, 13(6-7):533–549, 1997. doi:10.1016/s0749-6419(97)00024-7.

[59] L. Jiang, H. Wang, P. Liaw, C. Brooks, and D. Klarstrom. Temperature evolution during low-cycle fatigue of ULTIMET® alloy: experiment and modeling. *Mechanics of Materials*, 36(1-2):73–84, 2004. doi:10.1016/s0167-6636(03)00032-2.

[60] S. Kalidindi and L. Anand. An approximate procedure for predicting the evolution of crystallographic texture in bulk deformation processing of fcc metals. *International Journal of Mechanical Sciences*, 34(4):309–329, 1992. doi:10.1016/0020-7403(92)90038-i.

[61] A. G. Khachaturyan. *Theory of Structural Transformations in Solids.* Wiley & Sons, 1983.

[62] A. S. Khan, R. Kazmi, A. Pandey, and T. Stoughton. Evolution of subsequent yield surfaces and elastic constants with finite plastic deformation. Part-I: A very low work hardening aluminum alloy (Al6061-T6511). *International Journal of Plasticity*, 25(9):1611–1625, 2009. doi:10.1016/j.ijplas.2008.07.003.

[63] A. S. Khan, A. Pandey, and T. Stoughton. Evolution of subsequent yield surfaces and elastic constants with finite plastic deformation. Part II: A very high work hardening aluminum alloy (annealed 1100 Al). *International Journal of Plasticity*, 26(10):1421–1431, 2010. doi:10.1016/j.ijplas.2009.07.008.

[64] A. S. Khan, A. Pandey, and T. Stoughton. Evolution of subsequent yield surfaces and elastic constants with finite plastic deformation. Part III: Yield surface in tension–tension stress space (Al 6061–T 6511 and annealed 1100 Al). *International Journal of Plasticity*, 26(10):1432–1441, 2010. doi:10.1016/j.ijplas.2009.07.007.

[65] O. Kintzel and J. Mosler. An incremental minimization principle suitable for the analysis of low cycle fatigue in metals: A coupled ductile–brittle damage model. *Computer Methods in Applied Mechanics and Engineering*, 200(45–46):3127–3138, 2011. doi:10.1016/j.cma.2011.07.006.

[66] J. Korelc and P. Wriggers. Consistent gradient formulation for a stable enhanced strain method for large deformations. *Engineering Computations*, 13(1):103–123, 1996. doi:10.1108/02644409610111001.

[67] G. Kotucha. *Regularisierung von Problemen der Topologieoptimierung unter Einbeziehung von Dichtegradienten.* PhD thesis, Ruhr-Universität Bochum, 2005.

[68] E. Kuhl. *Theory and Numerics of Open System Continuum Thermodynamics – Spatial and Material Settings.* Habilitation thesis, Universität Kaiserslautern, 2004.

[69] F. Larché and J. Cahn. Overview no. 41. The interactions of composition and stress in crystalline solids. *Acta Metallurgica*, 33(3):331–357, 1985. doi:10.1016/0001-6160(85)90077-x.

[70] E. H. Lee. Elastic-Plastic Deformation at Finite Strains. *Journal of Applied Mechanics*, 36(1):1–6, 1969. doi:10.1115/1.3564580.

[71] T. Lehmann and U. Blix. On the coupled thermo-mechanical process in the necking problem. *International Journal of Plasticity*, 1(2):175–188, 1985. doi:10.1016/0749-6419(85)90028-2.

[72] J. Lemaitre. A Continuous Damage Mechanics Model for Ductile Fracture. *Journal of Engineering Materials and Technology*, 107(1):83–89, 1985. doi:10.1115/1.3225775.

[73] V. I. Levitas. Phase field approach to martensitic phase transformations with large strains and interface stresses. *Journal of the Mechanics and Physics of Solids*, 70: 154–189, 2014. doi:10.1016/j.jmps.2014.05.013.

[74] V. I. Levitas and I. B. Ozsoy. Micromechanical modeling of stress-induced phase transformations. Part 1. Thermodynamics and kinetics of coupled interface propagation and reorientation. *International Journal of Plasticity*, 25(2):239–280, 2009. doi:10.1016/j.ijplas.2008.02.004.

[75] V. I. Levitas and I. B. Ozsoy. Micromechanical modeling of stress-induced phase transformations. Part 2. Computational algorithms and examples. *International Journal of Plasticity*, 25(3):546–583, 2009. doi:10.1016/j.ijplas.2008.02.005.

[76] V. I. Levitas, V. A. Levin, K. M. Zingerman, and E. I. Freiman. Displacive Phase Transitions at Large Strains: Phase-Field Theory and Simulations. *Phys. Rev. Lett.*, 103(2), 2009. doi:10.1103/physrevlett.103.025702.

[77] V. I. Levitas, A. M. Roy, and D. L. Preston. Multiple twinning and variant-variant transformations in martensite: Phase-field approach. *Physical Review B*, 88(5), 2013. doi:10.1103/physrevb.88.054113.

[78] D. Liu and D. Dunne. Atomic force microscope study of the interface of twinned martensite in copper–aluminium–nickel. *Scripta Materialia*, 48(12):1611–1616, 2003. doi:10.1016/s1359-6462(03)00140-4.

[79] J. Lubliner. *Plasticity Theory.* Dover, New York, 2008.

[80] J. Mandel. Plasticite Classique et Viscoplasticite. In *Cours and Lectures au CISM No. 97.* International Center for Mechanical Sciences, Springer-Verlag, New York, 1972.

[81] M. Maraldi, G. N. Wells, and L. Molari. Phase field model for coupled displacive and diffusive microstructural processes under thermal loading. *Journal of the Mechanics and Physics of Solids*, 59(8):1596–1612, 2011. doi:10.1016/j.jmps.2011.04.017.

[82] M. N. Mekonen, D. Steglich, J. Bohlen, D. Letzig, and J. Mosler. Mechanical characterization and constitutive modeling of Mg alloy sheets. *Materials Science and Engineering: A*, 540:174–186, 2012. doi:10.1016/j.msea.2012.01.122.

[83] C. Miehe, J. Schotte, and M. Lambrecht. Homogenization of inelastic solid materials at finite strains based on incremental minimization principles. Application to the texture analysis of polycrystals . *Journal of the Mechanics and Physics of Solids*, 50(10):2123–2167, 2002. ISSN 0022-5096. doi:10.1016/S0022-5096(02)00016-9.

[84] C. Miehe, F. E. Hildebrand, and L. Boger. Mixed variational potentials and inherent symmetries of the cahn-hilliard theory of diffusive phase separation. *Proceedings of the Royal Society A: Mathematical, Physical and Engineering Sciences*, 470(2164):20130641–20130641, 2014. doi:10.1098/rspa.2013.0641.

[85] C. Miehe, S. Mauthe, and H. Ulmer. Formulation and numerical exploitation of mixed variational principles for coupled problems of Cahn-Hilliard-type and standard diffusion in elastic solids. *International Journal for Numerical Methods in Engineering*, 99(10):737–762, 2014. doi:10.1002/nme.4700.

[86] C. Miehe, J. Schotte, and J. Schröder. Computational micromacro transitions and overall moduli in the analysis of polycrystals at large strains. *Computational Materials Science*, 16(1–4):372–382, 1999. ISSN 0927-0256. doi:10.1016/S0927-0256(99)00080-4.

[87] L. Modica and S. Mortola. Un esempio di Γ-convergenza. *Boll. Un. Mat. Ital.*, 14B:285–299, 1977.

[88] N. Moelans, B. Blanpain, and P. Wollants. An introduction to phase-field modeling of microstructure evolution. *Calphad*, 32(2):268–294, 2008. doi:10.1016/j.calphad.2007.11.003.

[89] J. Mosler. Variationally consistent modeling of finite strain plasticity theory with non-linear kinematic hardening. *Computer Methods in Applied Mechanics and Engineering*, 199:2753–2764, 2010. doi:10.1016/j.cma.2010.03.025.

[90] J. Mosler and O. Bruhns. On the implementation of rate-independent standard dissipative solids at finite strain – Variational constitutive updates. *Computer Methods in Applied Mechanics and Engineering*, 199:417–429, 2010. doi:10.1016/j.cma.2009.07.006.

[91] J. Mosler and M. Ortiz. An error-estimate-free and remapping-free variational mesh refinement and coarsening method for dissipative solids at finite strains. *International Journal for Numerical Methods in Engineering*, 77(3):437–450, 2009. doi:10.1002/nme.2428.

[92] J. Mosler, O. Shchyglo, and H. M. Hojjat. A novel homogenization method for phase field approaches based on partial rank-one relaxation . *Journal of the Mechanics and Physics of Solids*, 68:251–266, 2014. ISSN 0022-5096. doi:10.1016/j.jmps.2014.04.002.

[93] S. Nemat-Nasser and M. Hori. *Micromechanics: overall properties of heterogeneous materials.* Elsevier, 1999.

[94] S. Nemat-Nasser and R. Kapoor. Deformation behavior of tantalum and a tantalum tungsten alloy. *International Journal of Plasticity*, 17(10):1351–1366, 2001. doi:10.1016/s0749-6419(00)00088-7.

[95] E. Nesterova, B. Bacroix, and C. Teodosiu. Experimental observation of microstructure evolution under strain-path changes in low-carbon IF steel. *Materials Science and Engineering: A*, 309–310:495–499, 2001. doi:10.1016/s0921-5093(00)01639-7.

[96] W. Oliferuk, W. A. Świactnicki, and M. W. Grabski. Rate of energy storage and microstructure evolution during the tensile deformation of

austenitic steel. *Materials Science and Engineering: A*, 161(1):55–63, 1993. doi:10.1016/0921-5093(93)90475-t.

[97] A. Onuki. Ginzburg-Landau Approach to Elastic Effects in the Phase Separation of Solids. *Journal of the Physical Society of Japan*, 58(9):3065–3068, 1989. doi:10.1143/jpsj.58.3065.

[98] M. Ortiz and E. Repetto. Nonconvex energy minimization and dislocation structures in ductile single crystals . *Journal of the Mechanics and Physics of Solids*, 47(2):397 – 462, 1999. ISSN 0022-5096. doi:10.1016/S0022-5096(97)00096-3.

[99] M. Ortiz and L. Stainier. The variational formulation of viscoplastic constitutive updates. *Computer Methods in Applied Mechanics and Engineering*, 171(3–4): 419–444, 1999. doi:10.1016/s0045-7825(98)00219-9.

[100] M. Ortiz, R. A. Radovitzky, and E. A. Repetto. The computation of the exponential and logarithmic mappings and their first and second linearizations. *International Journal for Numerical Methods in Engineering*, 52(12):1431, 2001. doi:10.1002/nme.263.

[101] M. Ortiz and E. P. Popov. Distortional Hardening Rules for Metal Plasticity. *Journal of Engineering Mechanics*, 109(4):1042–1057, 1983. doi:10.1061/(asce)0733-9399(1983)109:4(1042).

[102] F. Parvizian, A. Güzel, A. Jäger, H.-G. Lambers, B. Svendsen, A. Tekkaya, and H. Maier. Modeling of dynamic microstructure evolution of EN AW-6082 alloy during hot forward extrusion. *Computational Materials Science*, 50(4):1520–1525, 2011. doi:10.1016/j.commatsci.2010.12.009.

[103] H. Petryk. Thermodynamic Stability of Equilibrium in Plasticity. *Journal of Non-Equilibrium Thermodynamics*, 20(2):132–149, 1995. doi:10.1515/jnet.1995.20.2.132.

[104] H. Petryk. Thermodynamic conditions for stability in materials with rate-independent dissipation. *Philosophical Transactions of the Royal Society A: Mathematical, Physical and Engineering Sciences*, 363(1836):2479–2515, 2005. doi:10.1098/rsta.2005.1584.

[105] M. P. Pietryga, I. N. Vladimirov, and S. Reese. A finite deformation model for evolving flow anisotropy with distortional hardening including experimental validation. *Mechanics of Materials*, 44:163–173, 2012. doi:10.1016/j.mechmat.2011.07.014.

[106] A. Rajagopal, P. Fischer, E. Kuhl, and P. Steinmann. Natural element analysis of the Cahn–Hilliard phase-field model. *Computational Mechanics*, 46(3):471–493, 2010. doi:10.1007/s00466-010-0490-4.

[107] E. Rauch, J. Gracio, F. Barlat, A. Lopes, and J. F. Duarte. Hardening behavior and structural evolution upon strain reversal of aluminum alloys. *Scripta Materialia*, 46(12):881–886, 2002. doi:10.1016/s1359-6462(02)00073-8.

[108] M. Ristinmaa, M. Wallin, and N. S. Ottosen. Thermodynamic format and heat generation of isotropic hardening plasticity. *Acta Mechanica*, 194(1-4):103–121, 2007. doi:10.1007/s00707-007-0448-6.

[109] P. Rosakis, A. Rosakis, G. Ravichandran, and J. Hodowany. A thermodynamic internal variable model for the partition of plastic work into heat and stored energy in metals. *Journal of the Mechanics and Physics of Solids*, 48(3):581–607, 2000. doi:10.1016/s0022-5096(99)00048-4.

[110] M. Schmidt-Baldassari. Numerical concepts for rate-independent single crystal plasticity. *Computer Methods in Applied Mechanics and Engineering*, 192(11–12): 1261–1280, 2003. ISSN 0045-7825. doi:10.1016/S0045-7825(02)00563-7.

[111] D. Schneider, O. Tschukin, A. Choudhury, M. Selzer, T. Böhlke, and B. Nestler. Phase-field elasticity model based on mechanical jump conditions. *Computational Mechanics*, 55(5):887–901, 2015. doi:10.1007/s00466-015-1141-6.

[112] D. Schrade, R. Müller, D. Gross, M.-A. Keip, H. Thai, and J. Schröder. An invariant formulation for phase field models in ferroelectrics . *International Journal of Solids and Structures*, 51(11–12):2144–2156, 2014. ISSN 0020-7683. doi:10.1016/j.ijsolstr.2014.02.021.

[113] B. Shi and J. Mosler. On the macroscopic description of yield surface evolution by means of distortional hardening models: Application to magnesium. *International Journal of Plasticity*, 44:1–22, 2013. doi:10.1016/j.ijplas.2012.11.007.

[114] B. Shi, A. Bartels, and J. Mosler. On the thermodynamically consistent modeling of distortional hardening: A novel generalized framework. *International Journal of Plasticity*, 63:170–182, 2014. doi:10.1016/j.ijplas.2014.05.008.

[115] O. Sigmund and J. Petersson. Numerical instabilities in topology optimization: A survey on procedures dealing with checkerboards, mesh-dependencies and local minima. *Structural Optimization*, 16(1):68–75, 1998. doi:10.1007/bf01214002.

[116] M. Šilhavý. *The Mechanics and Thermodynamics of Continuous Media*. Springer Science + Business Media, 1997. doi:10.1007/978-3-662-03389-0.

[117] J. C. Simo and F. Armero. Geometrically non-linear enhanced strain mixed methods and the method of incompatible modes. *International Journal for Numerical Methods in Engineering*, 33(7):1413–1449, 1992. doi:10.1002/nme.1620330705.

[118] J. C. Simo and M. S. Rifai. A class of mixed assumed strain methods and the method of incompatible modes. *International Journal for Numerical Methods in Engineering*, 29(8):1595–1638, 1990. doi:10.1002/nme.1620290802.

[119] J. Simo. Numerical analysis and simulation of plasticity. In *Numerical Methods for Solids (Part 3) Numerical Methods for Fluids (Part 1)*, pages 183–499. Elsevier BV, 1998. doi:10.1016/s1570-8659(98)80009-4.

[120] J. Simo and T. Hughes. *Computational Inelasticity.* Springer-Verlag, 1998. doi:10.1007/b98904.

[121] J. Simo and C. Miehe. Associative coupled thermoplasticity at finite strains: Formulation, numerical analysis and implementation. *Computer Methods in Applied Mechanics and Engineering*, 98(1):41–104, 1992. doi:10.1016/0045-7825(92)90170-o.

[122] R. Smit, W. Brekelmans, and H. Meijer. Prediction of the mechanical behavior of nonlinear heterogeneous systems by multi-level finite element modeling. *Computer Methods in Applied Mechanics and Engineering*, 155(1):181 – 192, 1998. ISSN 0045-7825. doi:10.1016/S0045-7825(97)00139-4.

[123] L. Stainier and M. Ortiz. Study and validation of a variational theory of thermo-mechanical coupling in finite visco-plasticity. *International Journal of Solids and Structures*, 47(5):705–715, 2010. doi:10.1016/j.ijsolstr.2009.11.012.

[124] I. Steinbach and M. Apel. Multi phase field model for solid state transformation with elastic strain . *Physica D: Nonlinear Phenomena*, 217(2):153 – 160, 2006. ISSN 0167-2789. doi:10.1016/j.physd.2006.04.001.

[125] I. Steinbach and M. Apel. The influence of lattice strain on pearlite formation in fe–c. *Acta Materialia*, 55(14):4817–4822, 2007. doi:10.1016/j.actamat.2007.05.013.

[126] I. Steinbach and F. Pezzolla. A generalized field method for multiphase transformations using interface fields. *Physica D: Nonlinear Phenomena*, 134(4):385–393, 1999. doi:10.1016/s0167-2789(99)00129-3.

[127] I. Steinbach. Phase-Field Model for Microstructure Evolution at the Mesoscopic Scale. *Annual Review of Materials Research*, 43(1):89–107, 2013. doi:10.1146/annurev-matsci-071312-121703.

[128] R. H. Stogner, G. F. Carey, and B. T. Murray. Approximation of Cahn-Hilliard diffuse interface models using parallel adaptive mesh refinement and coarsening with C^1 elements. *International Journal for Numerical Methods in Engineering*, 76(5):636–661, 2008. doi:10.1002/nme.2337.

[129] E. Svenning, M. Fagerström, and F. Larsson. Computational homogenization of microfractured continua using weakly periodic boundary conditions. *Computer Methods in Applied Mechanics and Engineering*, 299:1–21, 2016. ISSN 0045-7825. doi:http://dx.doi.org/10.1016/j.cma.2015.10.014.

[130] G. I. Taylor and H. Quinney. The Latent Energy Remaining in a Metal after Cold Working. *Proceedings of the Royal Society A: Mathematical, Physical and Engineering Sciences*, 143(849):307–326, 1934. doi:10.1098/rspa.1934.0004.

[131] R. Taylor. FEAP – A Finite Element Analysis Program, Version 8.4 User Manual. *University of California at Berkeley, Berkeley, CA*, 2013.

[132] C. Truesdell and W. Noll. The Non-Linear Field Theories of Mechanics. In *The Non-Linear Field Theories of Mechanics / Die Nicht-Linearen Feldtheorien der Mechanik*, pages 1–541. Springer Science + Business Media, 1965. doi:10.1007/978-3-642-46015-9_1.

[133] M. Wallin and M. Ristinmaa. Boundary effects in a phase-field approach to topology optimization. *Computer Methods in Applied Mechanics and Engineering*, 278: 145–159, 2014. doi:10.1016/j.cma.2014.05.012.

[134] M. Wallin, M. Ristinmaa, and H. Askfelt. Optimal topologies derived from a phase-field method. *Struct Multidisc Optim*, 45(2):171–183, 2011. doi:10.1007/s00158-011-0688-x.

[135] J. Wang, V. Levkovitch, F. Reusch, B. Svendsen, J. Huétink, and M. van Riel. On the modeling of hardening in metals during non-proportional loading. *International Journal of Plasticity*, 24(6):1039–1070, 2008. doi:10.1016/j.ijplas.2007.08.009.

[136] P. Wriggers and J. C. Simo. A general procedure for the direct computation of turning and bifurcation points. *International Journal for Numerical Methods in Engineering*, 30(1):155–176, 1990. ISSN 1097-0207. doi:10.1002/nme.1620300110.

[137] P. Wriggers, C. Miehe, M. Kleiber, and J. C. Simo. On the coupled thermomechanical treatment of necking problems via finite element methods. *International Journal for Numerical Methods in Engineering*, 33(4):869–883, 1992. doi:10.1002/nme.1620330413.

[138] Q. Yang. *Thermomechanical variational principles for dissipative materials with application to strain localization in bulk metallic glasses.* Phd thesis, California Institute of Technology, Pasadena, 2004.

[139] Q. Yang, L. Stainier, and M. Ortiz. A variational formulation of the coupled thermo-mechanical boundary-value problem for general dissipative solids. *Journal of the Mechanics and Physics of Solids*, 54(2):401–424, 2006. doi:10.1016/j.jmps.2005.08.010.

[140] W. Zhang and K. Bhattacharya. A computational model of ferroelectric domains. Part I: model formulation and domain switching . *Acta Materialia*, 53(1):185 – 198, 2005. ISSN 1359-6454. doi:10.1016/j.actamat.2004.09.016.

Curriculum Vitae

Personal Data

Name	Alexander Bartels
Date of Birth	May 29, 1984
Place of Birth	Warendorf, Germany
Nationality	German

Professional Occupation

02/2012 – 06/2017	Scientific Assistant, Institute of Mechanics, Technische Universität Dortmund University
09/2011 – 01/2012	Scientific Assistant, Lehrstuhl für Mechanik-Materialtheorie, Ruhr-Universität Bochum

University Education

08/2011	Academic Degree: Master of Science (M.Sc.) in Mechanical Engineering
10/2009 – 08/2011	Master studies of Mechanical Engineering, Ruhr-Universität Bochum
03/2009	Academic Degree: Diploma (Dipl.-Ing. (FH)) in Mechanical Engineering
10/2005 – 03/2009	Diploma studies of Mechanical Engineering, Fachhochschule Münster

School Education

06/2004	Abitur, Gymnasium Laurentianum, Warendorf

Publication series of the Institute of Mechanics

published to date:

2010/01 Palnau, V.: Implementierung eines netzfreien Diskretisierungsverfahrens und seine Anwendung auf die Scherbandanalyse. ISBN 978-3-921823-51-4

2010/02 Klusemann, B.: Application of homogenization methods and crystal plasticity to the modeling of heterogeneous materials of technological interest. ISBN 978-3-921823-53-8

2011/01 Hortig, C.: Local and non-local thermomechanical modeling and finite-element simulation of high-speed cutting. ISBN 978-3-921823-54-5

2011/02 Parvizian, F.: Modeling of microstructure evolution in aluminum alloys during hot extrusion. ISBN 978-3-921823-56-9

2011/03 Noman, M.: Characterization and model identification for the simulation of the forming behavior of ferritic steels. ISBN: 978-3-921823-55-2

2011/04 Kayser, T.: Characterization of microstructure in aluminum alloys based on electron backscatter diffraction. ISBN: 978-3-921823-57-6

2011/05 Bargmann, S.: Computational modeling of material behavior on different scales based on continuum mechanics. ISBN: 978-3-921823-58-3

2013/01 Waffenschmidt, T.: Modelling and simulation of adaptation and degradation in anisotropic biological tissues. ISBN: 978-3-921823-61-3

2015/01 Ostwald, R.: Modelling and simulation of phase-transformations in elasto-plastic polycrystals. ISBN: 978-3-921823-66-8

2016/01 Subramanian, M.: Phenomenological modelling and simulation of ferroelectric ceramics. ISBN: 978-3-921823-74-3

2016/02 Clausmeyer, T.: Evolution of plastic anisotropy in metals. ISBN: 978-3-921823-76-7

2016/03 Holtermann, R.: Computational multiscale modelling of grinding processes. ISBN: 978-3-921823-86-6

2017/01 Bartels, A.: Modelling of evolving microstructures at different scales. ISBN: 978-3-921823-93-4